THE UNIVERSITY OF MANITOBA

FLOW BEHAVIOR AND MICROSTRUCTURAL EVOLUTION DURING SUPERPLASTIC DEFORMATION OF AA8090 ALUMINUM-LITHIUM ALLOY

WENJIE FAN

A Dissertation Submitted to the Faculty of Graduate Studies
in Partial Fulfillment of the Requirements of the Degree of

DOCTOR OF PHILOSOPHY

Metallurgy Science Laboratory
Department of Mechanical and Industrial Engineering
Winnipeg, Manitoba

SUMMER 1998

THE UNIVERSITY OF MANITOBA

FACULTY OF GRADUATE STUDIES

*****

COPYRIGHT PERMISSION PAGE

FLOW BEHAVIOR AND MICROSTRUCTURAL EVOLUTION DURING SUPERPLASTIC DEFORMATION OF AA8090 ALUMINUM-LITHIUM ALLOY

BY

WENJIE FAN

A Thesis/Practicum submitted to the Faculty of Graduate Studies of The University of Manitoba in partial fulfillment of the requirements of the degree of DOCTOR OF PHILOSOPHY

ACKNOWLEDGMENT

I am indebted to my thesis advisor, Professor M. C. Chaturvedi, for providing me the opportunity to work under his guidance, and for his trust, patience, constant encouragement and complete support.

I am grateful to Dr. N. Richards for his many suggestions and keen interest in my work. I would like to express my sincere thanks to Dr. Naresh Goel for numerous thought provoking discussions and for his constant technical and moral support. I am thankful to Professor D. Thompson for his helpful advice. I would like to record my gratitude to Professor, A. K. Jena and Professor B. P. Kashyap for their encouragement and for their help in the preparation of the thesis.

Mr. John Van Dorp and Mr. Don Mardis patiently assisted me throughout the course of my work. I am thankful to both of them, and also Mr. Kim Majury. I would like to thank all my friends for their understanding and support.

I deeply appreciate the emotional support given to me by my parents, family, and especially my daughter, Helen.

ABSTRACT

Superplasticity in AA8090 Al-Li alloy has been a subject of extensive studies, due to its potential for commercial applications since last decade. However, the anisotropy and microstructural gradient existing in this material introduce additional complication in understanding the mechanisms for superplastic deformation and has resulted in a debate about the role of dislocation activity. This has necessitated a more detailed microstructural study, especially texture, than that is commonly required to understand the deformation mechanism in other superplastic materials. Attempt has been made in this investigation to achieve this by means of microsturctural characterization of specimens deformed in tension by using optical microscopy, TEM, SEM and orientation imaging microscopy (OIM).

The microstructural characterization of the as-received material showed that there were three distinct layers in the cross-section of the sheet. Pancake grains in the center layer of about 1/3 thickness with brass-type texture, and nearly equiaxed grains on either side of it of about 1/3 thickness with copper texture.

Tensile tests were conducted over a temperature range of 25 - 570°C and a strain rate range of $1x10^{-4}$ - $1x10^{-2}$/s. Optimum superplastic conditions were found in a temperature range of 500 - 530°C and in a strain rate range of $1x10^{-4}$ - $1x10^{-3}$/s. These deformation conditions yielded the maximum value of strain rate sensitivity index ($m \approx 0.5$) and the minimum value of instability parameter (I).

During superplastic deformation, there occurred grain growth, texture weakening and change in grain shape. The disappearance of initial microstructural gradient occurred at a strain of about 1.0. The relationship between grain size (d) and strain (ε) could be expressed as $d \propto \varepsilon^q$, with the value of exponent q ranging from 0.21 - 0.44 depending on the test temperature. The level of texture weakening increased with increasing strain, but did not appear to be influenced by the strain rate and test temperature within the superplastic region.

The samples representing the center and surface layer materials showed significant flow anisotropy, whereas full thickness sheet samples showed less anisotropy. The nature of anisotropy in the center layer was opposite to that exhibited by the surface layer material. For the center layer material, the highest and lowest flow stresses were observed in 90° and 0° orientations with respect to the rolling direction of the sheet, respectively. Such effects could be attributed to the type and volume fraction of textures which relate to the variation in Taylor factor.

The rule of mixture, applied to the flow properties of the center and surface materials to account for that of the full thickness samples, revealed a reasonably good agreement with the experimental stress-strain curves in the 0° orientation. However, there occurred deviations in other orientations, which could be explained by the difference in textural evolution during deformation.

The values of strain rate sensitivity index ($m \approx 0.5$) and activation energy ($Q_t \approx 84$ kJ/mol) suggest the importance of grain boundary phenomena during superplastic deformation, however, the texture evolution suggests the importance of dislocation mechanism. The constitutive relationship for superplastic deformation was modified to incorporate the effect of texture evolution. Analysis of the correlation of various parameters and superplasticity indicated that dislocations contribute to superplastic deformation directly rather than just to accommodate grain boundary sliding.

CONTENTS

LIST OF FIGURES

LIST OF TABLES

LIST OF SYMBOLS

$\dot{\varepsilon}$	Strain rate
ε	Strain
σ or σ_i	Stress (y = yield stress, crss = critical shear stress)
b	Burgers vector
d	Grain size
D_0	Diffusion coefficient
E	Young's modulus
I	Instability parameter
I_i	Texture intensity evaluated by the maximum intensity of a pole figure (t = full thickness, c = center material, s - surface material)
k	Boltzmann constant
K	Material constant when only the strain rate sensitivity is considered
K′	Material constant when only the strain hardening is considered
K″	Material constant when both strain rate sensitivity and strain hardening are considered
m	Strain rate sensitivity index
n	Stress component
n_s	Strain hardening exponent
p	Grain size exponent
q	Grain growth related time exponent
Q or Q_i	Activation energy (for: a = apparent, t = true, gb = grain boundary diffusion, l = lattice diffusion, v = volume diffusion)
Q_t	True activation energy
R	Gas constant
T	Temperature
T_m	Absolute melting temperature of a material

CHAPTER 1
INTRODUCTION

The development of new materials is becoming essential to meet the ever rising demand in modern age of scientific and industrial achievements. In aerospace industries, the thrust for achieving higher and higher speed, larger payload capacity, improved fuel economy and better landing capacities of aircrafts [1], has led to remarkable research and development output in material's field. Such demands of materials have led to a revival of interest in development and fabrication of Al-Li alloys since the seventies. Lithium is one of the two alloying elements in Al (the other element is beryllium but it is toxic) that can significantly decrease the density and simultaneously increase the elastic modulus, providing better specific strength [2]. However, the use of Al-Li alloys for aerospace applications faces competition by fiber reinforced plastic composites which are much lighter and also some of them have higher specific strength [3]. Therefore, there has been a consistent need to improve the properties of Al-Li alloys and explore the fabrication route which is more economical. Continued attempts to fulfill this goal have led to the emergence of several commercial Al-Li alloys, like 2090, 8090 and 2095, in a short time [4]. Compared with fiber composites, these Al-Li alloys offer aircraft manufacturers the advantages of lower cost and the opportunity for continued use of manufacturing processes and equipment developed for conventional Al alloys [5]. However, Al-Li alloys exhibit lower ductility at room temperature, which makes the fabrication of useful components difficult. Also, the presence of Zr in these alloys suppresses recrystallization and causes the grains to be elongated or banded with strong texture, leading to anisotropy in mechanical properties in Al-Li alloy

sheets. Fortunately, in line with the thermomechanical treatment developed by Rockwell group for 7xxx series of Al alloys [6], Al-Li alloys can be made superplastic [7]. As Al_3Zr particles inhibit grain boundary migration, their presence is beneficial in producing fine grained superplastic materials. Also, superplastic deformation provides additional benefits by reducing anisotropy in superplastically formed components. Therefore, a systematic study of superplastic behavior of a commercially produced Al-Li alloy should be of interest to both the academic and the industrial community. In line of this, an investigation of superplasticity in AA8090 Al-Li alloy was initiated with an emphasis on microstructures, microtextures and their evolution during deformation.

A large number of publications related to AA8090 Al-Li alloy have appeared because of its use in more product forms and in more diverse applications than any other Al-Li alloy [4]. In addition to excellent fatigue properties, good plane stress fracture toughness (like other Al-Li alloys), and weldability (like 2090), AA8090 Al-Li alloy demonstrates excellent cryogenic as well as elevated temperature properties. Recrystallization causes an outstanding plane-stress toughness. Unlike other Al-Li alloys, the engineering properties of this alloy are retained upto plate thickness of 10 - 15 cms. The first report on superplastically formed component based on 8090 Al-Li alloy appeared in 1982 [8]. Since then, the investigations on flow behavior and concurrent microstructural evolution in AA8090 Al-Li alloy have been extensively pursued [7-26]. The observations on superplastic behavior reported so far can be summarized as follows.

1. Superplasticity in AA8090 Al-Li alloy can be produced either by special thermomechanical treatment or by dynamic recrystallization, without a need of any special processing. The material, which has undergone prior static recrystallization, shows much less superplasticity than that subjected to dynamic recrystallization.

2. Depending upon thermomechanical treatment employed, there are low temperature (LTSP) and high temperature (HTSP) superplastic AA8090 alloys. While the former shows the maximum ductility (700%) at 350°C, the latter shows the same (1000%) at 500°C. At the same time, the LTSP material shows less cavitation and grain growth than the HTSP material.

3. The maximum value of strain rate sensitivity index, m, in HTSP material is ≥ 0.5 whereas it is 0.33 for LTSP material. Also, the activation energies for superplastic deformation in these two cases are 92 and 141 kJ/mol, respectively. Accordingly, the mechanisms of superplastic deformation in these two versions of AA8090 are suggested to be grain boundary sliding and dislocation creep, respectively.

4. Tensile test at constant cross-head speed results in greater ductility than at constant true strain rate. This is attributed to the gradual decrease in strain rate in the former case compensating the effect of concurrent grain growth during superplastic deformation.

5. In as-processed state, AA8090 Al-Li alloy possesses microstructural and mechanical anisotropy. There appear gradients in grain morphology and texture along the thickness cross-section of the sheet. This is reduced or even eliminated by superplastic deformation.

6. The mechanism of superplastic deformation in this alloy is a subject of debate. While there are opinions supporting the operation of conventional mechanisms based on grain

boundary sliding, the others suggest the importance of dislocation slip on the basis of texture evolution.

The commercially processed superplastic forming grade AA8090 Al-Li alloy sheet possesses very heterogeneous microstructure, including texture. The microstructure is comprised of nearly equiaxed grains with copper-type texture towards surface and elongated or pancake grains with brass-type texture in the center section of the sheet. The microstructure is found to remain unchanged during static annealing. The structure-property correlation in such a material is expected to be much more complex in comparison to the equiaxed materials. Although superplastic behavior has been reported extensively in this material, most of the studies have been devoted to the optimization of superplastic condition and qualitative description of microstructural evolution. Therefore, the aim of present investigation was to systematically study the flow properties and microstructural evolution, especially texture, in the surface and center layer materials separately and to integrate them in the full thickness sheet, in order to understand the mechanisms for superplastic deformation.

Superplasticity in general and in materials of non-equiaxed grain structure in particular are reviewed in Chapter II. The experimental procedures, which involved tensile tests, optical metallography, orientation imaging microscopy, TEM, SEM are described in Chapter III. The results emerging from this work are presented in Chapter IV. The analysis towards understanding the results is attempted and presented in Chapter V. Finally, the highlights of this research are summarized in Chapter VI.

CHAPTER 2
LITERATURE REVIEW

2.1. Introduction

Literature available on various aspects of superplasticity is vast, because of its academic and industrial importance. As recently reviewed by Sherby and Wadsworth [27], publications in this field are growing very rapidly during the last three decades. The recent trends of research on superplasticity are found to focus towards (i) thermomechanical-treatment to develop superplasticity in known commercial materials, (ii) development of new materials with superplastic properties, and (iii) superplastic forming and diffusion bonding. While more research is being done on these aspects, there are continued attempts towards improving our understanding of the basic phenomena of superplasticity and the nature of the associated microstructural evolution. Superplasticity is exhibited at elevated temperatures and at intermediate strain rates by the materials which contain stable fine equiaxed grains. However, most of the commercially rolled sheets possess fine grains and non uniform distribution of grain size, grain shape and texture, which makes the correlation between flow behavior and microstructure more complex, and so does the understanding of the deformation mechanism. AA8090 Al-Li alloy is one of a series of commercially important superplastic materials, which are quasi-single phase aluminum alloys and owe their superplasticity to a specific thermo-mechanical-treatment. This alloy is the result of research and development work to produce high strength and low density (high specific strength) materials for aerospace applications. In the as-processed state, this material contains a complex

microstructure and possess lower ductility at room temperature which limits its formability. However, when it is given appropriate thermomechanical treatment, the microstructure evolves towards the one which can give rise to superplasticity. The present literature review is an attempt to focus on those aspects of superplasticity which are relevant to understanding the structure-property correlations and micromechanisms of superplastic deformation in AA8090 rolled sheet material.

2.2. Superplasticity

Superplasticity is the ability of a polycrystalline material with a specific microstructure to exhibit, in a generally isotropic manner, very high tensile elongation prior to failure under certain conditions of temperature and strain rate. Historically, the earliest report of true superplastic deformation is generally attributed to the classic work of Pearson in 1934 on Pb-Sn and Bi-Sn eutectic alloys [28], although recently it was discovered that superplasticity was first shown by Bebgough in 1912 in an α/β brass [27]. The Bi-Sn eutectic, which is essentially brittle in the as-cast condition (about 5% elongation to failure), could be made superplastic to exhibit an elongation of 1950%. The pioneering work of Backofen and his co-workers at MIT on Zn-Al and Pb-Sn alloys showed the potential for utilization of superplastic forming through simple operations [29]. This is beneficial for the formation of products having complex shapes. Recently, the field of superplasticity has expanded dramatically as evidence has been forthcoming for the attainment of high tensile ductility in a very wide range of new and advanced materials, including mechanically alloyed metals, superalloys, ceramics, intermetallics, and both metal matrix and ceramic matrix composites [30].

2.2.1 Conditions for Superplastic Deformation

While the conditions for superplasticity of metallic materials are well established, the same for non-metallic fine-grained materials are less well defined. Described below are the prerequisites for the materials to exhibit superplasticity.

a. Deformation Conditions

(i) Strain rate sensitivity index (m) — Superplasticity requires the value of strain rate sensitivity index m, to be greater than 0.3. Such high values of m are observed at intermediate strain rates, normally in the range 10^{-5}-10^{-2}/s. These strain rates are much lower than those employed in conventional processes, which have positive exponents of strain rates. The strain rate range for superplasticity shifts towards higher values with an increase in temperature and a decrease in grain size. Successful attempts have being made to get superplasticity at higher strain rates by using mechanical alloying or other processing methods. For example, mechanically alloyed IN9021 (Al-4.0wt%Cu-1.5%wtMg-1.1wt%C-0.8wt%O with 4.1%Al_4C_3 and 1.2% Al_2O_3 dispersoids in volume fraction), was found to exhibit ductility of 1250% at a strain rate of 50/s. [31].

(ii) Temperature — Superplasticity is generally exhibited at temperatures higher than 0.5 T_m, where T_m is the absolute melting point. Higher temperature facilitates the deformation processes involved in superplastic deformation.

b. Microstructural Conditions

(i) Fine grain size — For metallic materials the grain size should be less than 10μm whereas for ceramics it should be less than 1μm. The presence of fine grains in a material provides more grain boundary area which improves the probability of the occurrence of grain boundary phenomena for superplasticity, like grain boundary sliding, grain boundary diffusion and grain boundary migration etc.

(ii) Grain shape — The grains should generally have equiaxed shape, although superplasticity is shown by the materials which do not have initially equiaxed grains that is attained by microstructural evolution in the early part of deformation. For example, in the as-cast state Al-Cu eutectic is not superplastic but with continued cycling of deformation over a range of strain rates at high temperatures, m increases to the value necessary for superplasticity [32].

(iii) Grain size stability — Since superplasticity is seen at elevated temperatures and intermediate strain rates, the initial fine grains may undergo substantial coarsening during superplastic deformation, which may impair superplastic property of the material. The grain size stability is achieved by making use of either second phase or precipitates in the material, which impede grain boundary mobility.

(iv) Nature of grain boundaries — The grain boundaries should have high angles, typically obtained by annealing of cold worked materials or by hot working. Grain boundary sliding,

which is the dominant process during superplastic deformation, takes place easily in the high angle grain boundaries [33].

2.2.2 Mechanical and Microstructural Characteristics

Tensile testing has been used extensively to study and evaluate superplasticity. Several aspects of tensile behavior under superplastic deformation conditions are described below.

a. The Normal Mode and the Superplastic Mode

Flow stress (σ) is a function of strain (ε), strain rate($\dot{\varepsilon}$), temperature (T), and microstructure (S) of the material. In general terms, stress may be expressed by the relation

$$\sigma = f(\varepsilon, \dot{\varepsilon}, T, S) \qquad (2.1)$$

Typical stress-strain curves of AISI 1040 steel at room temperature and at three strain rates are shown in Fig.2.1 [34].

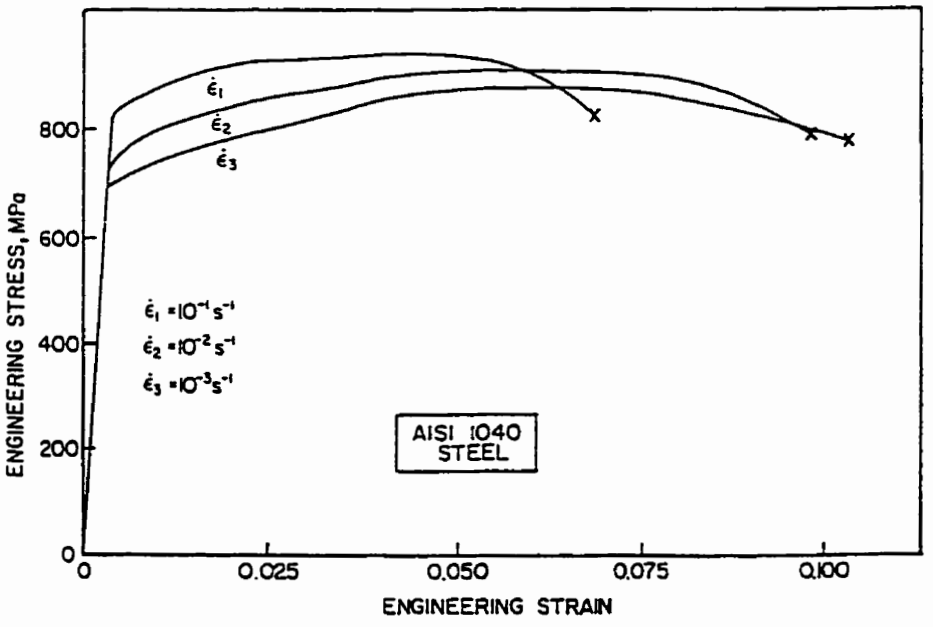

Fig.2.1. (Normal deformation mode) the effect of strain rate on the stress-strain curves for AlSi 1040 Steel at room temperature [34].

For this non superplastic material, it is evident that the stress increases with increasing strain as well as strain rate. Under such conventional mode of deformation, stress is a function of strain and strain rate, and equation (1) reduces to

$$\sigma = K'\varepsilon^{n_s}\dot{\varepsilon}^{m} \qquad (2.2)$$

where n_s is the strain hardening exponent, m is the strain rate sensitivity index, and K' is determined by temperature and microstructure of the material. In the normal deformation mode, the value of m is usually very small and may be close to zero in materials like Al. The value of n_s is usually large. As n_s is dominant and m is negligible, equation (2.2) reduces to

$$\sigma = K''\varepsilon^{n_s} \qquad (2.3)$$

where K'' is a constant. In this deformation mode, tensile samples normally fail by a neck formation and the resistance to necking is entirely due to strain hardening. Usually, deformation in the normal mode occurs at temperatures below 0.4 T_m.

Fig.2.2 [35] shows the stress-strain curves of a Sn-Pb alloy deformed at 273K and at two strain rates of 9.5×10^{-5} and 1.9×10^{-4}/s. The nature of these two curves is different from those shown in Fig.2.1 in the sense that stress is not a function of strain but, instead, the material flows at a constant stress level. That is, the strain hardening is negligible, which is characteristic of an ideal superplastic flow behavior. However, the steady-state flow stress increases with an increase in strain rate. As the strain hardening coefficient n_s equals zero in this case, equation (2.2) reduces to

$$\sigma = K\dot{\varepsilon}^{m} \qquad (2.4)$$

where K is a material constant depending upon test temperature and the microstructure of the specimen. In this mode, the resistance to necking is due to high strain rate sensitivity (m) of the material. The total elongation obtained under the condition of superplastic deformation is usually much higher than that obtainable in a normal deformation mode. The maximum ductility recorded to-date is about 8000% in a commercial bronze [36].

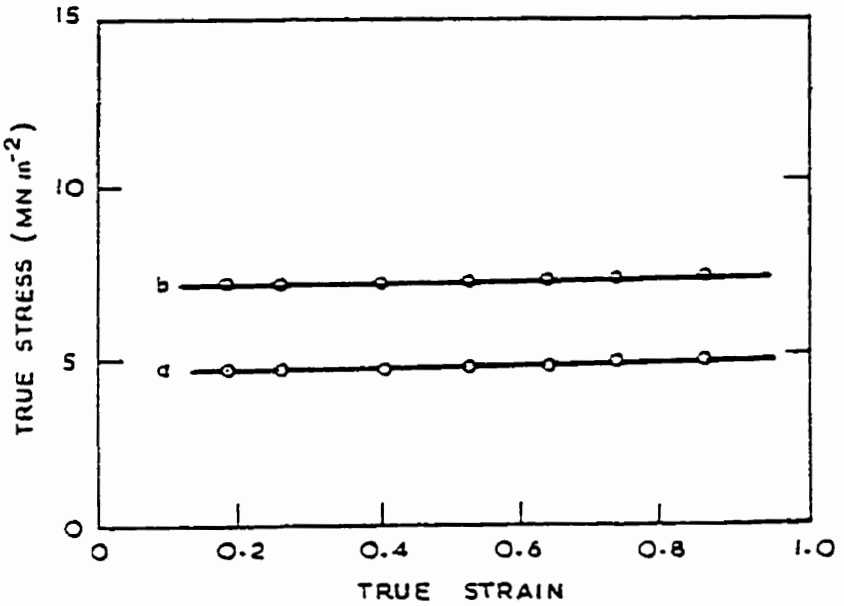

Fig.2.2. (Ideal superplastic deformation mode) the effect of strain and strain rate on the stress-strain curves for Sn-Pb eutectic at 30℃ and at strain rate of (a) $9.5x10^{-5}$ and (b) $1.9x10^{-4}$/s, respectively [35].

b. Nature of Stress-Strain Rate Curves in Superplastic Deformation Mode

In superplastic materials, the flow stress is particularly sensitive to the strain rate, temperature and grain size. The effect of temperature and grain size can be incorporated in the stress-strain rate relationship given by equation (2.4). In its normalized form, the constitutive relationship can be represented as [37],

$$\dot{\varepsilon} = \frac{AD_0Eb}{kT}\left(\frac{b}{d}\right)^p\left(\frac{\sigma}{E}\right)^n \exp\left(-\frac{Q}{RT}\right). \qquad (2.5)$$

Here $\dot{\varepsilon}$ is steady state strain rate, A is a dimensionless constant which depends on the creep mechanism, $D_0 \exp(-Q/RT)$ is the diffusion coefficient, E is the Young's modulus, b is the Burgers vector, d is the grain size, p is the grain size exponent, n (=1/m) is the stress exponent, k, R and T have their usual meanings. According to this relation there will be a unique value of flow stress for a selected combination of strain rate, test temperature and grain size.

As suggested by equations (2.4) and (2.5), the slope of the plot of $\ln\sigma$ vs. $\ln\dot{\varepsilon}$ gives the value of m. Similarly, the values of p and Q are obtained from the stress-strain rate plots for various grain sizes and at different temperatures, respectively. The $\ln\sigma$ vs. $\ln\dot{\varepsilon}$ plots over a large range of strain rates can be usually divided into different regions. Fig.2.3 [38] shows these regions, I, II and III, which is common for various superplastic materials. With an increase in test temperature or a decrease in grain size, flow stress decreases and the transition between regions II and III shifts towards higher strain rate. Fig.2.3 also shows additional regime (region 0) at very low strain rates. The typical values of m, p and Q are presented in Fig.2.3 along with a summary of micromechanisms and microstructural changes occurring in different regions. Here, Q_{gb} and Q_l are the activation energies for grain boundary and lattice diffusion, respectively. While regions I and III, representing the lower and higher strain rate ranges, have smaller values of $m \leq 0.3$, the value of m in region II, which is known

as the superplastic region, is greater than 0.3. As concluded by Langdon [39], there exists controversy about the exact nature of the stress-strain rate curves at lower strain rates (region 0 and I). Some group of investigators believe that the presence of region I is the result of excessive grain growth rather than a new regime of different deformation mechanism. Recently, in a number of publications Mohamed and his co-workers [40] have attributed the existence of region I to the threshold stress arising from the presence of impurities in the material.

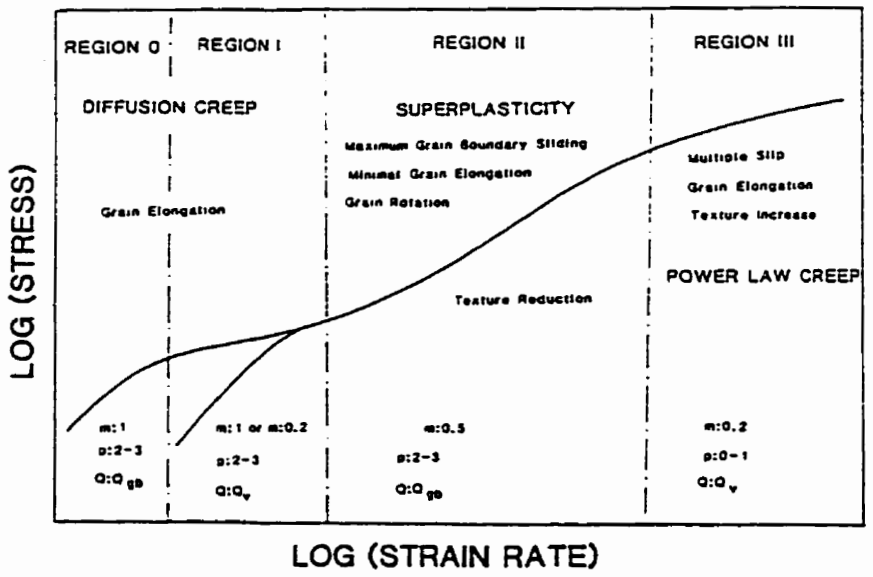

Fig.2.3. Schematic illustration of the strain rate dependence of flow stress in a superplastic material [38].

c. Effect of Strain Rate Sensitivity on Ductility

Sometimes, the slope of $\ln\sigma$ vs. $\ln\dot{\varepsilon}$ plot is found to vary continuously from the peak value at an intermediate strain rate to the lower values towards either region I or III. This is illustrated in Fig.2.4 for a Mg-Al alloy [41]. Such a variation in m also results in a similar effect of strain rate on ductility, as illustrated for Zn-22%Al alloy in Fig.2.5 [42]. Irrespective of the type of material, it is established that an increase in m leads to an increase in ductility as illustrated in Fig.2.6 [39]. Similarly, m increases with an increase in temperature and a decrease in grain size which, in turn, leads to an increase in ductility [35].

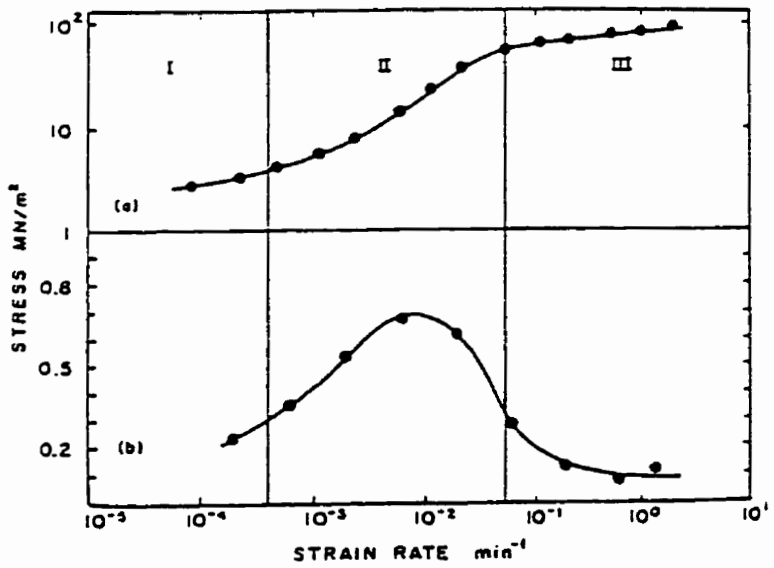

Fig.2.4. Strain rate dependence of (a) flow stress, and (b) m value for a Mg-Al alloy superplastically deformed at 350℃ [41].

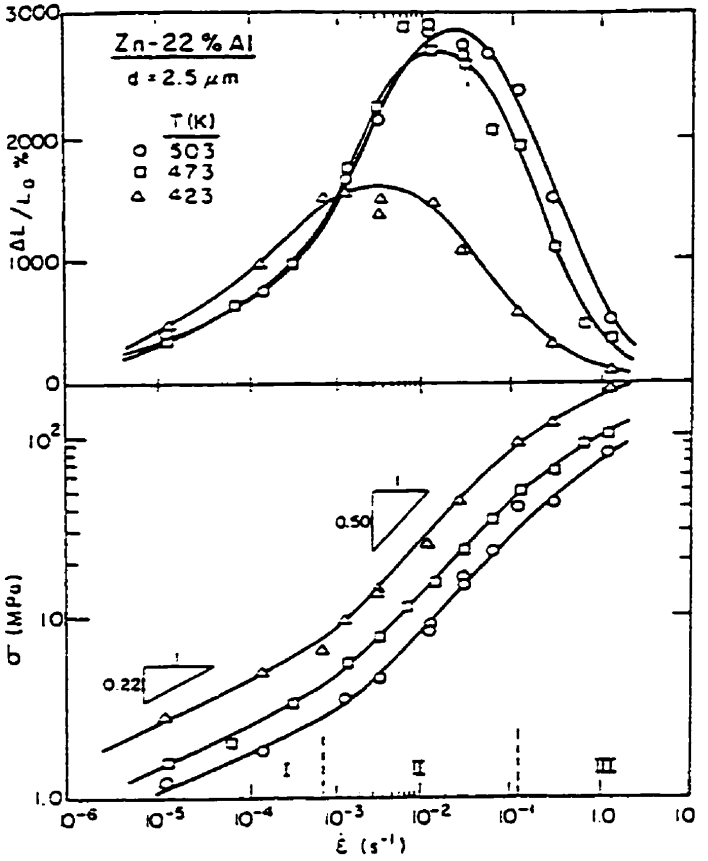

Fig.2.5. Elongation to failure (upper) and flow stress (lower) vs. initial strain rate for Zn-22Al at temperature range from 150 - 230℃ [42].

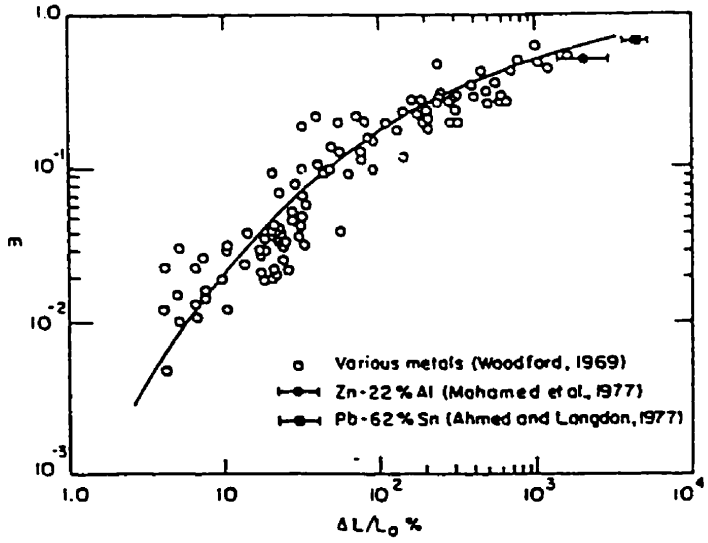

Fig.2.6. Strain rate sensitivity index vs. elongation to failure for various metals and the highly superplastic Zn-22Al and Pb-62Sn alloys [39].

d. Parameters of the Constitutive Relationship

The stress-strain rate data are obtained by differential strain rate tests, constant strain rate tests and stress relaxation tests. While, as described earlier, m is the slope of ln(stress) vs. ln(strain rate) plot, it is also determined by several methods [35], such as by the change in load values on changing the cross head speed during straining. The values of p and Q can be determined from the stress-strain rate data by making use of equation (2.5) in appropriate forms, viz.

$$p = n\left[\frac{\partial \ln(\sigma)}{\partial \ln(d)}\right]_{\dot{\varepsilon},T} = -\left[\frac{\partial \ln(\dot{\varepsilon})}{\partial \ln(d)}\right]_{\sigma,T} \qquad (2.6)$$

$$Q_t = -R\left[\frac{\partial \ln(\sigma^n / TE^{n-1})}{\partial (1/T)}\right]_{\dot{\varepsilon},d} = -R\left[\frac{\partial \ln(\dot{\varepsilon}TE^{n-1})}{\partial (1/T)}\right]_{\sigma,d} \qquad (2.7)$$

Once the values of m, p and Q are obtained, the same can be used to determine the magnitude of A in equation (2.5). The values of all these parameters, as typically shown in Fig.2.3, are then compared with the predictions of various theories to understand the mechanisms for deformation. The mechanisms for superplastic deformation are presented in the section 2.3.

2.2.3. Texture

The study of texture evolution during superplastic deformation provides information regarding the deformation mechanisms, because the final texture represents the cumulative effect of the entire thermal and mechanical history of the specimen. In spite of its importance, the studies on the role of texture in superplasticity literature are very limited in comparison to the other aspects of superplasticity. This may be mainly due to the non-availability of the facility and a lack of general interest in accepting this to be an important

parameter for understanding the mechanisms of superplastic deformation. However, some in-depth investigations performed by using texture measurements should contribute towards a better understanding of the subject. In fact, as far as the mechanism involving dislocations during superplastic deformation is concerned, texture information is very valuable because of its being a record of entire dislocation activity during the deformation process. This is not the case when other techniques, which only give the current structural details, are employed because the dislocations can easily disappear into grain boundaries at high temperature deformation.

Therefore, it is intended to provide a general background about textures and the related terminology in the appendix, which may be useful in appreciating the present work and the relevant literature available on texture evolution during superplastic deformation.

The study of texture evolution in rolled sheet materials has been the subject of several investigations in recent times, which will be summarized in section 2.4.6 by taking AA8090 Al-Li alloy as an example. Presented next is a general summary of texture studies during superplastic deformation.

Various observations on textures during superplastic deformation in quasi-single phase and two phase materials have been summarized by Edington et al [36], and Padmanabhan and Davies [35]. Although some of the observations and conclusions are questionable according to the latter authors, the following points provide an interesting background for understanding the mechanisms for superplastic deformation.

1. In microduplex alloys, texture evolution in the two phases can be quite different. While one phase can show extensive evidence of slip by appearance of new peaks of texture, the other phase may not undergo slip.
2. If the material does not have preferential orientation in the beginning, no texture is developed during superplastic deformation.
3. There occurs a texture weakening and randomization of orientation if the material contains texture at the beginning of superplastic deformation. Such textural evolution during superplastic deformation depends on strain rate sensitivity index, nature of phases present in the material and the sample orientation. The degree of texture weakening increases with increase in the value of m due to grain boundary sliding and grain rotation.
4. Occasionally, new peaks of texture were found during superplastic deformation when the starting structure was anisotropic.
5. At optimal strain rate for superplasticity, certain components of texture are more stable than others.

2.3. Mechanisms for Superplastic Deformation

Although superplasticity was initially considered to be associated with fine equiaxed grains, the process used for the production of these materials does not always lead to such an ideal microstructure. Quite often the microstructures of the materials processed for superplasticity contain elongated grains in one or two directions, banded structures and pancake grains etc., which are also seen to have a strong texture. Inspite of such heterogeneity in microstructures,

these materials are found to show satisfactory superplastic properties. While the mechanisms for superplastic deformation for the case of equiaxed grains have been studied in-depth, the instability of the second type of microstructure (pancake grains etc.) makes the development of suitable theories difficult. Nonetheless, this has been the subject of many investigations. For convenience and clarity the mechanisms for superplastic deformation in literature, reviewed here, are classified as for materials having (i) equiaxed grains, and (ii) non-equiaxed grains. The former will be referred as traditional superplastic materials whereas the latter will be referred as deformation induced continuous recrystallized materials (DICR).

2.3.1. Traditional and DICR Materials

In these two kinds of superplastic materials, the traditional materials are in the recrystallized state with microstructural features consisting of equiaxed grain structure and random orientation. The second group of materials are rolled sheets typically in unrecrystallized state with nonequiaxed grain structure and texture. The study of superplasticity on the first kind of materials, such as on Pb-Sn, Bi-Sn, Zn-Al eutectic and eutectoid materials, started early. However, extensive studies on the superplastic behavior of rolled sheet materials have been undertaken in recent years, as rolled sheet is one of the very important starting industrial materials.

If one compares the tensile behavior of these two kinds of materials during superplastic deformation, it would be difficult to see the difference. However, the microstructural evolution in these two kind of materials during superplastic deformation is different. In the

first kind of material, the microstructural evolution results in grain growth without any change in the initial microstructural characters, like grain shape and texture. The evolution of microstructure of the second kind of material results in changes in the initial characteristics. The initial microstructure of most of the rolled sheets consists of elongated or pancake shaped grains in the cross-section. The distribution of grain shape in cross-section in these materials may differ considerably from the surface to the center and the texture might also be non uniform through the cross-section. When the material is subjected to static annealing at the superplastic deformation temperature, grain growth occurs. The grain growth is associated with recovery, change of subgrain structures, dislocation structure and precipitates. However, grain shape and texture may not change significantly, meaning no discontinuous recrystallization (including the nucleation of new grains and their growth) occurs during static annealing. In contrast to this, during superplastic deformation, not only does the grain growth occur, but the grains also become equiaxed and the initial texture becomes weaker. After certain amount of strain, the material develops characteristics of a recrystallized product. The process is termed deformation induced continuous recrystallization (DICR). Therefore, for the first kind of material, here, the term used is "traditional superplastic material", and for the second kind of material the term of "DICR material" is used.

2.3.2. Theories of Superplastic Deformation for Traditional Materials

It has been clear for some time that grain boundary sliding (GBS) plays a major role in superplastic deformation of many alloys. For GBS to occur, extensive material transport must take place to maintain compatibility between the grains. Consequently, GBS and its

accommodation processes are generally included as part of the overall deformation mechanism. Various models have been developed to explain the experimentally determined constitutive relationship and the topological features observed during superplastic deformation. Although the newer models simply attempt to overcome the limitations of proceeding models for superplastic deformation, no single theory so far is able to account for all the observations. Gifkins [43] in the first international conference (1982) on superplasticity, had proposed the possibility of simultaneous occurrence of all the mechanisms in different zones of the superplastically deforming materials. Based on the accommodation processes, the available models for superplastic deformation can be classified [44] into two groups: (i) accommodation due to dislocation motion and (ii) diffusional accommodation. The group (ii) can be further classified into an accommodation process due to dislocation pile-ups (either inside the grains or in the interfaces) and due to motion of individual dislocations. The models for superplastic deformation have been the subject of several reviews [36, 45]. Presented in Table.2.1 is a summary of various models for superplasticity, which is a modification of the Table initially given by Neih et al (1997) [46].

Table.2.1 Summary of Proposed Models for Superplastic Deformation on Grain Boundary Sliding and Its Accommodation Processes

Models proposed by	Basic principle	Constitutive relationship
A. Slip accommodation (rate controlling)		
1. Dislocation pile-ups within the grains		
Ball and Hutchson [47] (1969)	Groups of grains slide as a unit. Unfavorably oriented grains obstruct the process. The stress concentration is relieved by dislocation motion in the blocking grains. These dislocations pile up against the opposite GB. The leading dislocation in the pile-ups can climb into GB and get annihilated.	$\dot{\varepsilon} = K_1(\frac{b}{d})^2 D_{gb}(\frac{\sigma}{E})^2$
Mukherjee [37] (1971)	Grains slide individually. Dislocations are generated by ledges and protrusions in GBs, traverse the grain, and are held up in pile-ups at opposite GBs. The rate of sliding is controlled by the climb of the leading dislocation into GBs.	$\dot{\varepsilon} = K_2(\frac{b}{d})^2 D_{gb}(\frac{\sigma}{E})^2$
2. Pile-ups in the interfaces (grain and/or phase boundaries)		
Muhkerjee [48] (1975)	This is a modification of his original model. GBS is rate controlled by dislocation motion in the GB by climb-glide process. The compatibility between the adjacent grains is achieved by diffusion controlled climb of lattice dislocations along the GBs. Thus, repeated accommodation is possible for the operation of GBS as a unit process.	$\dot{\varepsilon} = K_3(\frac{b}{d})^2 D_{gb}(\frac{\sigma}{G})^2$
Langdon [49] (1970)	GBS occurs by the movement of dislocations along, or adjacent to, the boundary by a combination of climb and glide. The strain rate due to sliding is proportional to σ^2/d. The various deformation mechanisms, including sliding, operate independently at lower stresses and/or smaller grain sizes. At constant but high stresses, the contribution of GBS to total strain increases with decrease in grain size, but this trend is reversed at lower stress levels.	$\dot{\varepsilon} = K_4(\frac{b}{d})D_L(\frac{\sigma}{E})^2$
Gifkins [50] (1976)	Sliding takes place by the motion of GB dislocations that pile up at triple points. The stress concentration is relaxed by the dissociation of the leading GB dislocation. The dissociated dislocations move along the adjoining GBs at triple point, or/and lattice in vicinity of GB. The split dislocations climb and glide until they meet each other and get annihilated.	$\dot{\varepsilon} = K_5(\frac{b}{d})^2 D_{gb}(\frac{\sigma}{E})^2$

Fukuyo et al [51] (1990)	The slip accommodation process for GBS involves the sequential steps of glide and climb. When the climb is the rate controlling step, the stress concentration at the lead of the pile-ups results in superplasticity (m = 0.5). When glide is the rate controlling step, however, m is equal to unity because there is no pile-up stress.	$\dot{\varepsilon} = K_6(\frac{b}{d})^2(\frac{D_{chem}}{b^2})(\frac{\sigma}{E})^2$
Kaibyshev [52] (1985)	Importance of changes in structure and properties of GBs at interaction with lattice defects is emphasized. Superplastic flow begins with the generation and motion of GB dislocations. Stress concentration due to pile-ups of GB dislocations in triple points initiates generation of lattice dislocations. These dislocations enter the GBs after traversing through the grain interior. Such absorption of dislocations by GBs result in the activation of GBS and diffusion. The application of the concepts of strain hardening and recovery describes the microscopic pattern of flow.	$\dot{\varepsilon} = K_7(\frac{b}{d})^2(\frac{\sigma-\sigma_0}{E})^2$
Gittus [53] (1977)	This is a theory for SPD in two phase materials. Piled-up GB dislocations climb away into adjacent disordered segment of the interphase boundary (IPB). Sources in the IPB introduce new dislocations to replace those that have climbed away from the head of pile-up. Sliding occurs at the IPBs as the dislocations in the pile-up glide toward the head of the pile-up. A threshold stress, due to the pinning interaction between IPB superdislocations and boundary ledges, are incorporated.	$\dot{\varepsilon} = K_8(\frac{b}{d})^2 D_{IPB}(\frac{\sigma-\sigma_0}{E})^2$
Nazarov [54] (1997)	Kinetics of relaxation of various non equilibrium dislocation ensembles formed in GBs was analyzed to develop models for superplastic flow. This involves series of mechanisms which are effective and operate at different levels of the applied stresses, different geometry of triple junctions and grain sizes. The common feature of these mechanisms is the back stress from accommodating GB dislocation arrays which impedes the main deformation process and determines the similar rate equations.	$\dot{\varepsilon} = K_9\frac{V_a D_{gb}\delta}{d^2}(\frac{\sigma}{G})^2$ where V_a is the atomic volume, δ is the width of grain boundary.
Perevezentsev et al [55] (1992)	Superplastic behavior results from the transition of a grain boundary into a special high-excited state, by destabilization of the atomic structure by fluxes of lattice dislocations. Such	$\dot{\varepsilon} = K_{10}(\frac{b}{d})^2 D_{gb}(\frac{\sigma}{G})^2$

	a state facilitates the occurrence of GBS. GBS is accommodated through cooperative local GB migration, emittance of lattice dislocations from bends and boundary junctions, and diffusion mass transfer.	
3. Accommodation by the motion of individual dislocations		
Hayden et al [56] (1972)	GBS is controlled by the rate of intergranular dislocation creep. Dislocations are nucleated at GB triple points and ledges, traverse individually in the grain by glide and climb and then finally climb to annihilation site in the opposite GBs. Proposed two constitutive relation for the relatively lower and higher temperature ranges.	$\dot{\varepsilon} = K_{11}(\frac{b}{d})^3 D_p(\frac{\sigma}{E})^2$ where D_p is diffusivity along dislocation pipe.
Spingarn and Nix [57] (1979)	Deformation occurs by intragranular slip along slip bands which are blocked by GBs. The strain at the boundaries is accommodated by diffusional flow. The slip band spacing decreases as the strain rate is increased. At very large stresses, the slip band spacing is taken to be equal to the subgrain size.	$\dot{\varepsilon} = K_{12}(\frac{b}{d})^3 D_{gb}(\frac{\sigma}{G})^2$
Arieli and Mukherjee [58] (1980)	The individual lattice dislocations in a narrow region near the interfaces climb directly into and/or along the interfaces. Multiplication of dislocations takes place during climb for making the process self-regenerative. At high stresses more dislocation arrive at the interfaces from the grain interior, the critical step then being the overcoming of the obstacles to their motion inside the grains. This involves glide and climb processes controlled by lattice diffusion.	$\dot{\varepsilon} = K_{13}(\frac{b}{d})^2 D_{gb}(\frac{\sigma}{G})^2$
B. Diffusional accommodation		
Ashby-Verall [59] (1973)	Superplasticity is treated as a transition region between diffusion accommodated flow, operative at low strain rates, and diffusion-controlled dislocation climb at high strain rates. Units of four grains must deform cooperatively in order to achieve a unit strain of 0.55. During this process, while the two adjacent neighboring grains are separated apart the other two grains come closer to each other. This involves a transient stage where two triple points of the four grains are replaced by a quadruple by Diffusional process, and finally the grain switching turns the original grain configuration in the	$\dot{\varepsilon} = K_{14}(\frac{b}{d})^2 D_{eff}(\frac{\sigma-\sigma_0}{E})$

	direction of tensile axis. At low strain rates, the specimen elongation is accomplished by grain rearrangement which in turn takes place by GBS. There arises threshold stress due to transient increase in grain boundary area during grain rearrangement process. At high strain rates, the specimen elongation is achieved by the change of the shape of individual grains.	
Padmanabhan [60] (1979)	Superplasticity can be shown by pure GBS without any accommodation process. Initially, atom-vacancy interchanges lead to GBS until the flow is blocked at an obstacle, e.g. ledges, triple points etc. The resistance to flow offered by the obstacle leads to the development of an elastic back stress. When this significantly exceeds the mean boundary shear stress, stress enhanced local diffusion results in atomic rearrangement. This process continues until the obstacles become more conducive to easy and continuous sliding. Finally, the steady state superplastic flow is attained when all the obstacles are smoothed out and GBS can take place without being accompanied by other process. Based on the atomistic calculations for grain/interphase boundary sliding, superplastic flow is controlled by GBS at a mesoscopic scale. In this case, GBS is accommodated by non-rate controlled diffusion and dislocation motion.	$\dot{\varepsilon} = K_{15}(\frac{b}{d})^2 D(\frac{\sigma}{E})^2$ where D may differ from D_L and D_{gb}.

2.3.3. Deformation Induced Continuous Recrystallization (DICR)

The early studies on superplasticity of unrecrystallized rolled Al alloy sheets were due to Watts in 1976 [61] on Al-Cu-Zr alloys, and due to Nes in 1978 on Al-Mn-Zr alloy [62]. According to these studies, an important feature of microstructural evolution during superplastic deformation in rolled sheet materials is that the microstructural changes from the initial unrecrystallized structure to the recrystallized structure. The former has non-equiaxed grain shape and strong texture, while the later has equiaxed grain shape and weakened texture. Because the recrystallized structure is reached through superplastic deformation, a term, ***deformation induced continuous recrystallization*** (DICR) is used to describe the process of microstructural evolution. DICR is used to emphasize the continuous process of microstructural evolution during superplastic deformation from an unrecrystallized rolled sheet material, rather than the process of nucleation of new grains and their growth which occurs during discontinuous recrystallization. There are a number of publications which report the behavior of DICR materials during superplastic deformation. Most of them deal with the investigation of Al alloys [10, 17, 18, 23, 24, and 61-79]. In the literature DICR has been attributed to (1) texture weakening, (2) increase in grain misorientation and (3) increase in the number of large angle grain boundaries.

Under superplastic deformation conditions, DICR is complete before a certain amount of strain. This is known as the first stage. During this stage the transition of microstructure from that of starting unrecrystallized specimen to that which is characteristic of the

recrystallized specimen, occurs continuously. It is found that during this stage alloys could be deformed at strain rates higher than 10^{-2}/sec [10, 17, 18, 64, 67, 68]. Since high angle boundaries are believed to have been developed during the first stage of deformation, the microstructure at the end of the first stage satisfies the requirements of deformation by traditional superplastic deformation mode. Therefore, deformation after the first stage is believed to be similar to that which occurs in traditional superplastic deformation materials, and is said to constitute the second stage. The strain rate in the second stage is similar to that of the traditional materials. According to the published reports [10, 18, 67], larger elongations have been obtained by using the two stage superplastic deformation mode than the constant strain rate mode. Typical proposed deformation mechanisms in DICR are outlined next.

(a) Subgrain coalescence

In a study of superplastic deformation behavior in a series of rolled Al-Cu-Zr alloys, Watts and co-workers [61] found that DICR took place during the early stages of deformation. The most noticeable feature found in their study was rapid subgrain growth coupled with an increase in misorientation between grains. They suggested that the dislocation walls with lowest angles dissociated by a combination of glide and climb, and the misorientation across the large angle subboundaries increased. A process akin to subgrain coalescence for static recrystallization took place during deformation. Dislocations and subgrain boundaries were found within the grains by TEM. The TEM samples were obtained by quenching the tensile specimens under load. The authors, however, did not discuss the details of the dislocation mechanism.

In the same alloy, the microstructure following superplastic deformation was also studied by other researchers by using TEM [74]. The TEM samples were obtained by the same technique as above. Both individual dislocations and dislocation networks were observed in the samples, and high dislocation densities were observed in some larger grains. Based on these observations, it was suggested that the process may occur either by the coalescence of adjacent boundaries or by slip/climb of dislocations to the opposite boundaries. It was further suggested that the dislocations will offer the greatest resistance to GBS. Therefore, dislocation motion should still be important at strain rates corresponding to superplastic deformation, at least as an accommodation mechanism.

(b) Subgrain boundary sliding

McNelley and coworkers [64, 79] carried out a series of studies on Al-Mg alloys, and measured grain misorientations by TEM in as-rolled, annealed and superplastically deformed samples. They found that (1) the low angle grain boundaries (1-5°) were dominant in the as-rolled material; (2) the grain misorientation increased a little, 2-7°, as a consequence of dislocation rearrangement after static annealing; and (3) the grain misorientation increased substantially to 10-30° after superplastic deformation. They suggested that the low angle grain boundaries behave the same way as the high angle grain boundaries even with misorientations less than 10° at the onset of superplastic deformation. This suggestion means that sliding of low angle grain boundaries takes place at the initial stage of superplastic deformation. The tendency of microtexture (measured by TEM) to become random was also

found. They believed that grain rotation occurred during superplastic deformation, which was associated with GBS. Dislocations observed within the grains were interpreted as an evidence of an accommodation mechanism for GBS. The absorption of such dislocations into boundaries had the effect of increasing misorientation between adjacent grains during superplastic deformation.

(c) Subgrain boundary migration

In a commercial Al-Cu-Zr alloy, Nes [62, 76] studied the DICR behavior by using TEM. He proposed that the development of high angle grain boundaries is a consequence of rapid subgrain growth during superplastic deformation. Grain misorientation was considered to be accommodated with increase in grain boundary migration distance. Thus, a high angle grain boundary could evolve from subgrain boundaries. The role of straining was to accelerate subgrain boundary migration (rapid grain growth), which allowed high angle grain boundaries to form in cases where subgrain growth during static annealing would be too low to develop high angle grain boundaries.

(d). Subgrain rotation, GBS and subgrain switching

Wert and coworkers [77] studied the microstructural evolution during superplastic deformation in Al-Zr-Si, Al-Cu-Zr-Si and Al-Li 2095 alloys by TEM. Both grain misorientation and microtexture were measured. The as-rolled microstructure in these three alloys was found to be similar. The alloys consisted of layers of grains parallel to the rolling plane. Only low angle grain boundaries were present within each layer, while adjacent layers

were separated by high angle grain boundaries. The increase in grain misorientation and the weakening of micro-texture during superplastic deformation were observed in all the three alloys, which were believed to be due to subgrain rotation during superplastic deformation. They suggested that at the start of superplastic deformation a significant fraction of the boundary area consisted of high angle grain boundaries, and sliding of these preexisting high angle grain boundaries might have led to an increase in misorientation through subgrain rotation. The subgrain rotation was suggested to be associated with GBS. In the process of deformation, the preexisting high angle grain boundaries played a key role in the misorientation evolution.

Later on, Lyttle and Wert [78] incorporated subgrain switching into their previous model. The mechanism of subgrain switching was derived from the grain switching model proposed by Ashby and Verrall [59]. They, thus suggested that the overall mechanism consists of subgrain rotation, subgrain switching and grain boundary sliding.

(e) ***Subgrain superplasticity***

Gandhi and Raj [80] analyzed different superplastic deformation behavior of various aluminum alloys which contained either low angle boundaries or high angle boundaries. They proposed a model for subgrain superplasticity, in which they considered a balance between the arrival and emission rates of dislocations at low angle boundaries during deformation. They predicted that the subgrain structure would be stable within a certain range of strain rates. However, if the strain rate was too slow then the arrival rate of

dislocations would exceed the emission rate, and the subgrain boundaries would gradually grow into high angle boundaries. If the strain rate was too high, then the emission rate would be faster and the low angle boundaries would annihilate into the crystal grains.

(f) Dislocation activity

Q. Liu et al [68] studied the microstructural evolution during superplastic deformation in an Al-Li alloy of near 2090 composition (Al-2.25Li-2.75Cu-1.10Mg-0.12Zr) by TEM. The grain misorientation development following the superplastic deformation was measured, and an increase in grain misorientation was observed during the initial stages of superplastic deformation. They separated the DICR itself into two stages. Subgrain boundary migration was thought to be easier in the first stage, and subgrain coalescence was suggested to have made a large contribution to the increase in grain misorientation during this stage. In the second stage, the generation and absorption of dislocations at grain boundaries were considered to result in a rapid increase in misorientation. They suggested that dislocation gliding within the grains can occur continuously to account for the observed strain during DICR, and higher the strain rate the faster the increase in misorientation during DICR.

Bate and his colleagues [23, 24] studied the microstructural evolution during superplastic deformation in an Al-Li AA8090 alloy by both tensile testing and deep drawing. Optical microscopy was used to study the microstructural evolution. Textural changes following the superplastic deformation were measured by X-rays and, the experimental data were analyzed by the orientation distribution function. The terms like banded and layered structure were

used to describe the starting microstructural characteristics in the central portion of the through thickness section of the rolled sheet. {110} <112> Brass texture was observed to be the preferential orientation in this position. The material in the top layers in the same section had a texture of {100} <110>, and consisted of reasonably equiaxed grains. The boundaries between layers were high angle boundaries and within such layer the boundaries were of low angle character. They studied both the full thickness and just the middle center layers of the material, in which the outer layers were removed from each side. The tensile tests were performed at 527°C at a strain rate of $1x10^{-3}$/sec. The results indicated that the flow stress of the center layer material was slightly higher than that of the full thickness material. But, the strain rate sensitivities for these two specimens showed no significant difference. Up to a strain of about 0.4, little change in the texture occurred. Between strains of 0.4 to 1.0, a considerable texture weakening took place. Based on these experimental results, they proposed the deformation process to be a combination of grain rotation and grain growth in the *absence of relative grain translation*, and this process was suggested to operate up to a strain greater than unity in the superplastic deformation regime. They also suggested that the interaction of lattice dislocations with grain boundaries was likely to be one of the most important aspects during superplastic deformation, and a further modeling of deformation micromechanisms operating during superplastic deformation was required. They gave a clear challenging argument that, on the basis of their experimental work, one of the currently dominant model viz. GBS may not be relevant, at least in some cases of deformation of material with high strain rate sensitivity. However, an alternative mechanism was not presented.

Z. Liu et al [63] examined the microstructures of the Al-Li 8090 alloy by TEM by using samples quenched after deformation. They found that dislocations formed at the triple junctions, grain boundary ledges and particles. The slip of such dislocations was quite active during the initial stages of deformation. During the middle stages of deformation, the dynamic recovery of interior dislocations occurred to form subgrain boundaries. Finally, although the dynamic recovery did not stop up to the failure stage, the accommodation mechanism by dislocation slip became more important. They suggested the dislocation slip to be the main mechanism of deformation during the early stages, and both dynamic recovery and dislocation slip to be part of the accommodation mechanism for GBS during superplastic deformation.

Pu et al studied the superplastic deformation behavior of an AA8090 alloy at a temperature of 350°C through a special thermo-mechanical treatment [26]. The microstructural examination was conducted by TEM by using the samples quenched under load. They observed that a great deal of dislocation interactions occurred in larger grains, the multiple dislocation slip systems were active, and these dislocations originated from different sources. They suggested that dislocation creep was involved in the deformation process and dislocations played an important role in the accommodation of GBS.

Liu and Chakrabarti [75] studied the microtexture evolution during superplastic deformation in a modified 7050 Al alloy by OIM technique (about OIM see section 3.5). Deformation

was conducted at 447°C and at a strain rate of $2x10^{-3}$/s. Both microstructural examination and microtexture measurement were carried out only in the mid-thickness of the longitudinal section. The as-received materials had heavily banded unrecrystallized microstructure with brass texture {110} <112>. Upon exposure to the test temperature without deformation, only recovery but no significant recrystallization occurred. The stress and strain curve at this deformation condition showed a peak at a true strain of 0.4. The microstructure in the gauge section was not noticeably different from that of the grip section before being strained to 0.4. At a strain of 0.4 recrystallized grains were observed, and at a strain of 0.75 the banded structure was replaced by a more equiaxed and uniform grain structure. At a strain of 1.3 the microstructure resembled the nearly equiaxed recrystallized fine grained structure. Texture weakening also occurred during deformation. The transition from brass texture to random orientation occurred between a strain of 0.4 - 0.7 and the transition was not abrupt but was gradual and progressive although there was a peak in the stress-strain curve. On the basis of these observations, they suggested that the early part of deformation was dominated by dislocation slip, and dynamic recrystallization occurred at the maximum stress, and after that grain boundary sliding and grain rotation became dominant.

From this brief review of microstructural evolution during superplastic deformation in DICR materials, it might be realized that there are several mechanisms available to explain the recrystallization of the initially unrecrystallized microstructure. The available mechanisms are presented in Table.2.2.

Table.2.2. Summary of existing mechanisms of DICR

Authors	DICR Mechanism	Refs
Watts et al.	*Subgrain Coalescence*	61, 74
McNelley et al.	*Subgrain Boundary Migration*	62, 76
Nes	*Subgrain Boundary Sliding*	64, 79
Wert et al.	*Subgrain Rotation / GBS*	77
Wert et al.	*Subgrain Rotation / GBS +Subgrain Switching*	78
Gandhi and Raj	*Subgrain Superplasticity*	80
Pu et al., Hales and McNelley, Brichnell and Edington	*Dislocation Activities as An Accommodation of GBS*	23, 24, 63, 68
Z. Liu et al., Q. Liu et al., Bates, Blackwell and Bates and Liu and Chakrabarti and	*Dislocation Activities Contributing to Deformation*	31,29,36,37, 75

2.4. Precipitation Behavior and Superplasticity in AA8090 Al-Li Alloy

2.4.1. Introduction

The earliest study on aluminum-lithium alloys might have been conducted in Germany in 1924 [81]. However, interest in Al-Li alloys and accelerated development of these alloys occurred in the seventies. The developmental work on Al-Li alloys was concerned with properties such as strength, fracture-toughness, modulus of elasticity, fatigue, corrosion, stress corrosion cracking resistance, and density. A number of review papers and conference proceedings on Al-Li alloys have been published [1, 5, 82, 83, 84]. Six international conferences on Al-Li alloys have been held. The first one was held in 1980 in USA [85] and the sixth one was in Germany in 1992 [86]. After the sixth conference, the subject of Al-Li alloys was merged into international conferences on Al alloys [87]. The developmental work led to the introduction of several commercial Al-Li alloys. These alloys rely on additions of copper, zirconium, and magnesium as essential alloying elements to obtain the desired combination of properties [88]. Table 2.3 gives typical chemical compositions of Al-Li alloys.

Table.2.3. Compositions of typical commercial Al-Li alloys

Alloys	Composition wt % (balance Al)	Reference
2090	2.4-3.0 Cu, 1.9-2.6 Li, 0.25Mg, 0.12 Zr	89
2091	1.8-2.5 Cu, 1.7-2.3 Li, 1.1-1.9 Mg, 0.10 Zr	89
8090	2.2-2.7 Li, 1.0-1.6 Cu, 0.6-1.3 Mg, 0.12 Zr	89
8091	2.4-2.8 Li, 1.8-2.2 Cu, 0.5-1.2 Mg, 0.10 Zr,	89
2095	5.55 Cu, 1.18 Li, 0.38 Mg, 0.15 Zr, 0.4 Ag	90
2195	4.0 Cu, 1.41 Li, 0.35 Mg, 0.13, Zr 0.4, Ag	91

Al-Li-based alloys are precipitation hardenable. The phase equilibria and precipitation reactions, that control the microstructure and hence the properties, are significantly different from those of the conventional alloys [92]. The effect of different alloying additions is to alter the phase equilibria and to modify the precipitation sequence.

The AA8090 alloy may possess moderate- to high-strength-levels and contain recrystallized or unrecrystallized grain structures, depending upon the type of temper used during heat treatment [93]. The alloy is available in sheet, plate, extruded, and forged products. In common with other Al-Li alloys, alloy AA8090 displays excellent resistance to fatigue crack growth and good plane-stress fracture-toughness [94]. Alloy AA8090 has also been shown to be weldable. It demonstrates excellent cryogenic properties as well as elevated-temperature properties up to 177°C. It has been used in more product forms and in more diverse applications than any other Al-Li alloy [89]. In addition, like other Al-Li alloys, AA8090 exhibits mechanical and microstructural anisotropy, which has been extensively investigated at ambient temperature [95, 96]. The precipitation-, anisotropic- and superplastic-behavior of this alloy are summarized next.

2.4.2. Aging Characteristics

As shown in Table 2.3, the AA8090 Al-Li alloy contains Li, Cu, Mg and Zr. The presence of these alloying elements leads to the formation of various precipitates which are listed in Table 2.4 along with their crystal structures.

Table.2.4 Phases encountered in Al-Li-Cu-Mg-Zr alloy systems [5]

Phase	Composition	Crystal Structure
δ′	Al_3Li	Ll_2
δ	AlLi	B_{32} (cubic)
θ′	Al_2Cu	tetragonal
T_1	Al_2CuLi	hexagonal
T_2	Al_6CuLi_3	icosahedral
T_B	$Al_{15}Cu_8Li_2$	cubic
β′	Al_3Zr	Ll_2
S′	Al_2CuMg	orthorhombic

The addition of zirconium results in the formation of a fine dispersion of fully coherent and ordered cubic β′ (Al_3Zr) particles (Table.2.4). The formation of β′ starts during the ingot solidification stage and the subsequent homogenization treatment. It is present as very fine and homogeneously distributed particles which are very effective in retarding grain boundary migration during annealing [96]. Therefore, the presence of β′ in this alloy suppresses static recrystallization and also the grain growth subsequent to dynamic recrystallization. The β′ dispersoids are unaffected by the solution-heat-treatment which is usually carried out at ~ 530°C [89].

The metastable ordered δ′ (Al_3Li) phase (Table.2.4) is the basic strengthening precipitate phase in this alloy. It nucleates homogeneously throughout the matrix [97, 98, 99]. Because β′ is isostructural with δ′, the former also acts as preferential site for the nucleation of the latter during artificial aging.

The addition of copper decreases the maximum solid solubility of lithium in aluminum at all temperatures [81]. Three copper containing phases, viz. θ′ (Al_2Cu) with tetragonal crystal structure, T_1 (Al_2CuLi) with hexagonal crystal structure, and T_2 (Al_6CuLi_3) with icosohedral symmetry (Table.2.4), may precipitate due to the addition of copper in Al-Li alloys. However, θ′ does not form in alloy 8090. T_1 is the predominant strengthening phase present after artificial aging to the near-peak-strength condition. T_1 nucleates heterogeneously on dislocations, low angle grain boundaries and substructural features. T_2 nucleates predominantly on high-angle grain boundaries. The formation of T_2 leads to the development of δ′ precipitate-free zones adjacent to the grain boundaries with concomitant reduction in ductility and fracture-toughness. T_2 phase is stable over a temperature range of 170-520°C [100].

The addition of magnesium also decreases the solubility of lithium in aluminum at all temperatures below 425°C [101]. Similarly, the solubility of magnesium in aluminum is drastically reduced by the presence of lithium. When magnesium is added to Al-Li alloys containing copper, precipitation of S′ (Al_2CuMg) occurs (Table.2.4). S′ phase has an orthorhombic crystal structure and has a tendency to nucleate heterogeneously on matrix dislocations, low angle grain boundaries, and other structural inhomogeneities. Unlike the case of T_1 precipitation, the heterogeneous precipitation of S′ does not result in precipitate-free zones along either low- or high-angle grain boundaries. However, the exact nature of the phase equilibria of the quaternary Al-Li-Cu-Mg alloys depends on the relative concentrations of all three alloying elements [102, 103].

The solution treatment temperature for AA8090 alloy is between 525 and 545°C [7]. In response to artificial aging after solution treatment, δ′ precipitates first; it has been observed even in the as-quenched condition [102]. S′ starts to precipitate at bout 200°C and then T_1 begins to form. Precipitation of T_2 starts at about 300°C [104]. Precipitation of S′ phase is very heterogeneous which results in stress concentration during subsequent deformation. In order to overcome this problem, the alloy is pre-stretched to about 4-6% after quenching but prior to artificial aging, which introduces dislocations into the matrix and ensures widespread nucleation of S′ precipitates with uniform distribution in the matrix [89]. In overaged tempers, the equilibrium δ (AlLi) with cubic crystal structure (Table.2.4) nucleates at high angle grain boundaries and this, in turn, also leads to the formation of δ′ PFZ at these boundaries. The AA8090 Al-Li alloy is found to exhibit a variety of microstructures and properties through the synergistic effects of the actual alloy composition, quenching rate, the amount of stretch prior to aging, the aging temperature and time, and the degree of recrystallization [89].

2.4.3. Anisotropy

As compared to the conventional high strength aluminum alloys, anisotropy in mechanical properties has been identified as one of the critical problems in the development of Al-Li alloys. In thick plates it manifests as low ductility in the rolling direction (RD) and transverse direction (TD) and low toughness in RD-ND or TD-ND orientations [105,106], here ND represents the normal direction. In 8090 sheet anisotropy manifests itself as the low yield stress in the off-axis (between the rolling and transverse) directions [20, 96, 107]. The

anisotropy is exhibited in mechanical properties like yield stress (20,108, 109], elongation to failure [96], elastic modulus [110, 111], and plasticity [110, 112]. Fig.2.7 [96] illustrates the variation in tensile properties as a function of orientation of the testing direction with respect to the rolling direction. However, a systematic study on the effect of anisotropy during superplastic deformation in AA8090 Al-Li alloy has not been carried out.

Single crystals are anisotropic, and their properties are strongly dependent upon orientation. However, in a polycrystalline material a random orientation makes the material isotropic. But, preferential orientation or texture in a polycrystalline material makes it like a quasi-single crystal and it exhibits anisotropy. Knowing the texture components of a polycrystalline material, it is possible to calculate the critical resolved shear stress in a given tensile direction. Various models have been proposed by Sachs [113], Taylor [114] and Bishop-Hill [115] to determine the average mechanical properties of polycrystalline materials from the data obtained from single crystals. Fig.2.8 shows the variation in Taylor factors (σ_{ys} /τ_{crss}) as a function of orientation for S, Cu and Bs texture components in f.c.c. metals. This calculation is based on the Taylor / Bishop-Hill model [116]. In addition to texture, Welch and Bunge [117] suggested that anisotropy in grain morphology, such as elongated grain shape, second phase particles and certain kind of grain boundaries can also contribute to mechanical anisotropy.

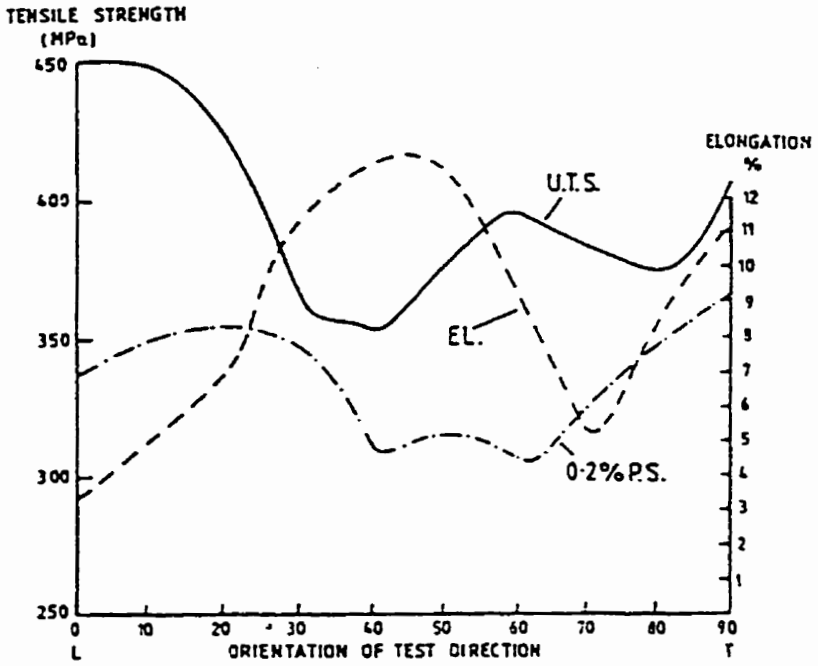

Fig.2.7. Anisotropy in tensile properties of a rolled 8090 alloy sheet at room temperature [96].

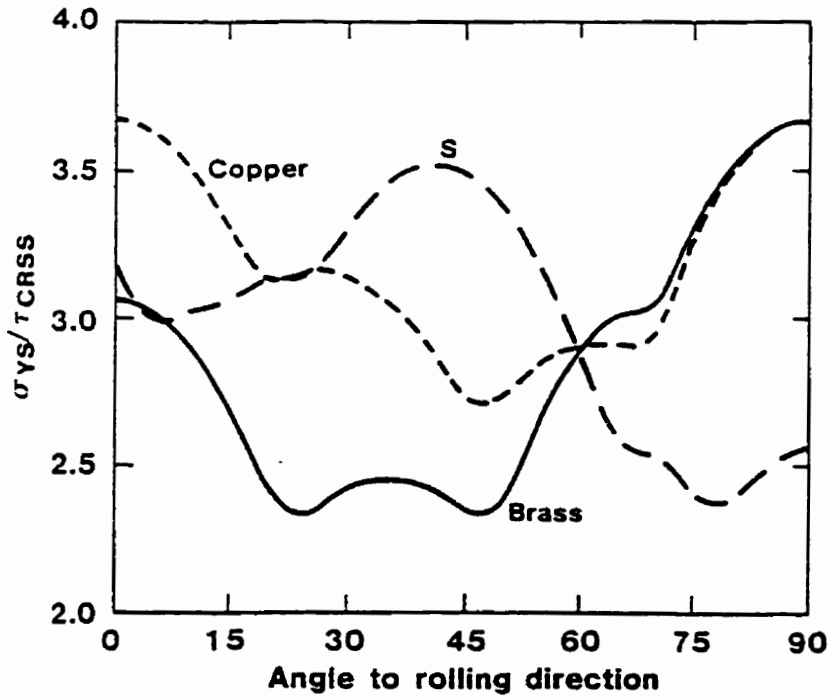

Fig.2.8. Variation of the factor of σ_{ys}/τ_{crss} as a function of orientation angle between tensile axis and rolling direction calculated by using Taylor/Bishop-Hill model [116].

2.4.4. Superplastic Deformation of AA8090 Al-Li Alloy

a. Ductility and Strain Rate Sensitivity Index

A number of investigations have been conducted to establish the stress-strain relationship, stress-strain rate relationship, nature of microstructural evolution including texture, and their correlations during superplastic deformation of rolled sheets of AA8090 Al-Li alloy [7-26]. D'Oliverira et al [22] obtained a maximum m value of 0.47 at 515°C and at a series of strain rates in the range 10^{-4}-10^{-2}/s. The microstructural development, which occurred during deformation, did not have a significant influence on the value of m. An m value of about 0.5 has been reported by several investigators [19, 23, 24, 26] at a strain rate of 10^{-3}/s in the temperature range of 500 to 530°C. However, larger values of m have also been reported, e.g., m = 0.6 at 520°C and strain rate of $1x10^{-3}$/s [16] and $2x10^{-4}$/s [22], m = 0.65 at 530°C and strain rate of $1x10^{-3}$/s, and m = 0.68 at 530°C and strain rate of $5x10^{-4}$/s [15]. In these investigations the maximum elongations corresponded to the maximum value of m, but the ductility was not much different. Ridley et al [12] showed the maximum ductility of about 700% at 520°C and strain rate of $2x10^{-4}$/s. However, the maximum ductility was improved by conducting tensile tests at (i) constant cross-head speed, instead of constant strain rate, and (ii) two stage deformation — first deformed at higher strain rate for recrystallization and then deformed at optimum superplastic condition. The maximum ductilities obtained were ~850% and >1600% under these two test conditions, respectively. In the latter case, the deformation was first conducted at an initial strain rate of $8.3x10^{-3}$/s, and then the strain rate was switched over to $2.5x10^{-3}$/s. Such a two stage deformation approach in AA8090 alloy has been employed by several of these investigators [7, 10, 17, 18] also.

At temperatures lower than 500°C, the value of m is usually observed to be less than 0.5. A value of about 0.3 was reported by Pu et al [26] at a strain rate of $1x10^{-4}$/s and at a lower temperature of 350°C in a specially processed material to exhibit low temperature superplasticity. The maximum ductility obtained in this case was 700%. Even the materials subjected to standard processing for superplasticity exhibit lower m values at lower temperatures, and sometimes at higher test temperatures also. In spite of significantly smaller values of m, obtained under these conditions, the ductility value still remains representative of superplasticity. For example, Amichi and Ridley [18] reported ductility of 450-500% corresponding to a value of m ~ 0.3 at 400°C.

Generally the value of m decreases with an increase in strain [22]. Blackwell and Bate [24] examined the nature of stress-strain curves and the m values in the center layer material as well as in the full thickness of the sheet, with tensile axis being parallel to the rolling direction. The flow stress of the center layer material was higher than that of the full thickness. The corresponding m values were 0.5 and 0.43, which showed no significant difference.

b. Effect of Temperature on Superplastic Behavior

Limited studies related to the effect of temperature on the nature of stress-strain and stress-strain rate curves, m, and ductility on AA8090 Al-Li alloy have been reported [7, 9, 15, 25, 26]. The stress-strain curves show an increase followed by a decrease in flow stress with

increasing strain. Only at larger strains ($\varepsilon \geq 1.0$) the flow stress tends to be independent of strain. The extent of flow hardening and flow softening is reported to decrease with increasing temperature [25]. An increase in ductility with increasing temperature was reported by Miller and White [7], over the temperature range of 510-545°C, and by Pu and Huang [25] over the temperature range of 300-525°C. For example, ductility of 440% was obtained at ~512°C whereas it was found to increase to 550% at 542°C [7]. While Ricks and Parson [15] have reported an increase in the value of m with increasing temperature, Lloyd [9] did not find any effect of temperature on the value of m. As a function of temperature, there appears to be some anomaly in relating ductility to the value of m.

The stress-strain rate curves at various temperatures have been reported [15, 25] to exhibit an extended region II and a tendency towards region I behavior at a strain rate lower than 10^{-4}/s. Pu et al [26] reported two values of activation energy for superplastic deformation, viz. 141 kJ/mol for higher temperature superplasticity and 92 kJ/mol for lower temperature superplasticity.

c. Effect of Grain Size on Stress-Strain Rate Relationship

Only Pu et al seems to have studied the effect of grain size on the stress-strain rate relationship in AA8090 Al-Li alloy [26]. They observed that the value of the grain size exponent, p, was ~2 for the high temperature superplasticity (525°C), and p~1 for the low temperature superplasticity (350°C) over the strain range of 0.2-0.6.

d. Strain Hardening during Superplastic Deformation

Strain hardening during superplastic deformation has been noticed in several studies [10, 12, 15, 18, 67]. They all agree that the source of hardening is grain growth during superplastic deformation rather than the conventional dislocation-related strain hardening. The value of strain hardening exponent (n_s) was reported [15, 18] to be about 0.4 during superplastic deformation of AA8090 Al-Li alloy. It was also suggested by them that strain hardening contributed to the stability of large elongation which was also responsible for a decrease in the value of m with increasing strain. Such hardening also resulted in the shifts of the peak towards lower strain rates in the plot of m vs. strain rate at higher strain levels [12]. Since the strain rate continuously decreases in a constant cross-head speed type of test, the effect of strain hardening (in reducing the magnitude of m) is compensated by the shift in the position of maximum m value towards lower strain rate. This results in higher ductility when the alloy is deformed at a constant cross-head speed instead of at a constant true strain rate. For example, ductility of 850% was reported by deforming at an initial strain rate of 3.3×10^{-4}/s, which is larger than the value of 500% obtained at a constant true strain rate of 4×10^{-4}/s [12].

2.4.5. Microstructures and Their Evolution during Superplastic Deformation

a. Microstructure Prior to Deformation

In the as-received cold rolled sheet material banding parallel to the rolling direction [9, 112] and elongated grains [118] have been reported. TEM examination of the rolled sheet showed a high density of dislocations and the presence of particles of T_2 phase and of the type Al-Cu-Fe and Al-Cu-Ti [119]. The precipitates of T_1, S′ and T_2 were also reported [23].

Conducting a superplastic deformation the material is first heated to the deformation temperature and maintained for a period of time to stabilize the microstructure. In several investigations, when the specimens were heated to 520 to 530°C for about 20 minutes, the original elongated, aligned or banded grain structures were found to be still present [7, 12, 16, 23, 24, 26]; which probably represents the retention of the initial grain morphology. While the small precipitates of δ′, S′ and $T_{1,}$ existing in the as-received material, dissolved completely during pre-heating, the large particles remained undissolved [23, 24]. However, when the test temperature was raised to above 550°C, these particles also dissolved completely, which caused significant grain coarsening [16, 17].

b. Microstructural Evolution during Superplastic Deformation

A significant change in grain shape during superplastic deformation has been reported. Superplastic deformation around 525°C and at a strain rate of $1x10^{-3}$/s caused the equiaxed grains, close to the top surface, to remain equiaxed whereas, the elongated grains in the center layers changed to nearly equiaxed shape [23, 24]. As such, equiaxed grains were found in many studies at the end of superplastic deformation [7, 15, 16,18, 20, 21, 24]. According to some studies, the significant changes in grain morphology occurred at strain levels of 0.4 [7], 0.5 [21], $0.5 < \varepsilon < 1.0$ [24], and $\varepsilon > 0.6$ [16]. It may be concluded from these studies that the strain level at which the transition in the microstructural state occurs is normally dependent on strain rate and temperature conditions.

Grain growth was found to be a common occurrence during superplastic deformation of AA8090 alloy sheet. In one case [6], the grain size changed from 6 to 12 μm at a strain of 1.0, when deformed at 520°C and at strain rate of $1x10^{-3}$/s. The decrease in strain rate was found to increase the grain size further. Pu et al [26] found that, during deformation at 525°C and at a strain rate of $2x10^{-4}$/s the average grain size increased from 5 to 22 μm at a strain level of 500%. Lloyd [9] and Miller and White [7] noted occasional large grains at the surface due to Li depletion.

TEM observations of samples deformed at 515°C and at strain rate of $1x10^{-3}$/s did not reveal dislocations [7, 15]. However, dislocations and subgrains were observed in a sample deformed at 350°C and at a strain rate of $1x10^{-4}$/s. Pu et al [26] suggested that the observed dislocations helped to accommodate grain boundary sliding. Precipitates of T_2 phase were found at grain boundaries upon superplastic deformation [15], but Gandhi et al [17] did not find any deterioration due to this on superplastic formability.

Many investigations have shown that failure of this material during superplastic deformation is caused by interlinkage of cavities and their subsequent transformation into cracks [7, 9, 10, 12, 17, 26]. However, superimposed hydrostatic pressure of about 60% of the flow stress [7, 9, 10, 12, 17] was shown to suppress the formation of cavities. The significant level of cavitation was found to start at the strain of about 1.0 [7, 9, 18] and the cavity volume fraction was dependent on the processing route and the orientation of the sample [7].

Table 2.5 Texture component in the 8090 Al-Li rolled sheet

Location in thickness CS	Texture component	Reference
Not specified	{110}<112	16
Not specified	{110}<112> and {4 4 11}<11 11 8>	15
Not specified	{110}<112> and {123}<634>	21
Not specified	{112}<111>	96
Surface	{001}<110> and {225}<554>	23
Surface	{001}<110>	24, 119, 112, 120
Surface	{112}<111> and {110}<112>	119
Center	{110<11√2>	23
Center	{110}<112>	14, 20, 24, 112, 120
Center	{110}<322>	119

2.4.6. Texture in AA8090 Al-Li Alloy

A number of investigators [14, 15, 16, 20, 21, 23, 24, 85, 112, 119, 120] have examined the texture in the as-worked AA8090 Al-Li alloy. Except in a few reports, the locations in the sheet at which the texture was measured, were not specified. Table 2.5 summarizes the texture components that have been observed in this alloy. Examination of the Table shows that the textures in the center and surface section are distinctly different. Generally, the texture in the center layer material is of brass-type, whereas the texture in the surface layer material is of copper-type.

Static annealing during heating and soaking at test temperature, prior to superplastic deformation, does not seem to have much effect on the texture present in the as-received material [15, 16, 21, 23, 24]. However, texture weakening during superplastic deformation has been reported in these investigations, but no new texture components were observed.

The significant texture weakening were reported at $\varepsilon = 0.5$ [21] and at $0.75 < \varepsilon < 1.0$ [14, 20] at the same test conditions of 530°C and a strain rate of $5x10^{-4}$/s. Blackwell and Bate have reported [24] texture in both the center and surface layers to become weak and similar during superplastic deformation over $0.4 < \varepsilon < 1.0$ at a temperature of 527°C and a strain rate of $1x10^{-3}$/s.

Bowen and Hirsch have reported [14] the effect of two orientations on texture weakening during superplastic deformation at a temperature of 530°C and a strain rate of $5x10^{-4}$/s. Upon deformation to strain of about 1.0, it was found that the sample pulled in the transverse direction showed less texture weakening than that pulled in the rolling direction. At the same time, the sample pulled in rolling direction showed a little shift in the texture direction from <112> to <111> [20].

2.5. Scope of Present Work

The review of the literature shows that superplastic deformation of rolled AA8090 Al-Li alloy sheet has been extensively investigated since 1982 because of its commercial importance. However, these studies were generally concentrated on exploring the deformation conditions (strain rate and temperature) to establish the optimum conditions for superplasticity, viz. the maximum strain rate sensitivity index and ductility. Except for the phenomenon of cavitation, a systematic study on concurrent microstructural evolution, and its relation with flow behavior seems to be lacking. Unlike many other superplastic materials having fine equiaxed grains, AA8090 Al-Li alloy contains microstructural gradient in terms of grain morphology and texture across the thickness section. The presence of such microstructural features complicates the understanding of the mechanisms operative during superplastic deformation. Therefore, there exists a clear need for investigating different aspects of superplastic behavior of this alloy in detail to improve the understanding of the role of different deformation mechanisms over a range of strain rates and temperatures. The consideration of the microstructural gradient of the AA8090 Al-Li alloy, grain structure and microtexture in different locations in the thickness section of the sheet, was the focus of this investigation. Especially, the microtexture of various samples taken from different locations in the thickness section was characterized by means of the newly developed electron back scatter diffraction (EBSD) and orientation imaging microscopy (OIM) techniques. The following were specific aims of the present investigation.

1. To characterize the microstructural evolution during superplastic deformation, with reference to the starting microstructure, by using optical metallography, TEM, SEM and OIM;
2. To investigate the effect of strain, strain rate and temperature on the texture evolution during superplastic deformation;
3. To correlate the concurrent microstructural evolution to the optimum conditions for superplasticity;
4. To individually evaluate the flow property and microstructural evolution in materials from different locations in thickness section of the sheet, and the possibility of composite-like flow behavior in the material with microstructural gradient;
5. To assess the anisotropy and its relation to texture;
6. Finally, to clarify the contribution of dislocation activity to superplastic deformation through texture measurements.

CHAPTER 3.
EXPERIMENTAL PROCEDURES

3.1. Material

The SPF grade AA8090 alloy received from Alcan in the form of a 1.8 mm thick sheet was used in this investigation. The nominal composition was Al-2.5Li-1.4Cu-1.2Mg-0.11Zr in wt%. The as-received material was used as such without any further heat treatment.

3.2. Tensile Test

The mechanical behavior of the material was studied by tensile testing. In this section, the selection and preparation of samples are sequentially described.

3.2.1. Sample Selection

Microstructural characterization of the material showed (see Chapter 4) that roughly 1/3 of the thickness of the material next to the surface had nearly equiaxed grains, while, the central 1/3 contained pancake shaped grains. Also, it is well known that the tensile properties of rolled sheets vary as a function of orientation relative to the rolling direction. In order to separate the effects of grain structure and rolling direction, tensile samples were made from different locations, as well as with tensile axis being a specific orientation with respect to the rolling direction of the sheet.

A. Original Sheet

Tensile samples were machined from the original sheet so that the thickness of the sample was the same as that of the as-received sheet material. The tensile axis of the samples was oriented at four pre-determined angles from the original rolling direction of the sheet. As illustrated in Fig.3.1 these directions were 0°, 30°, 45° and 90°.

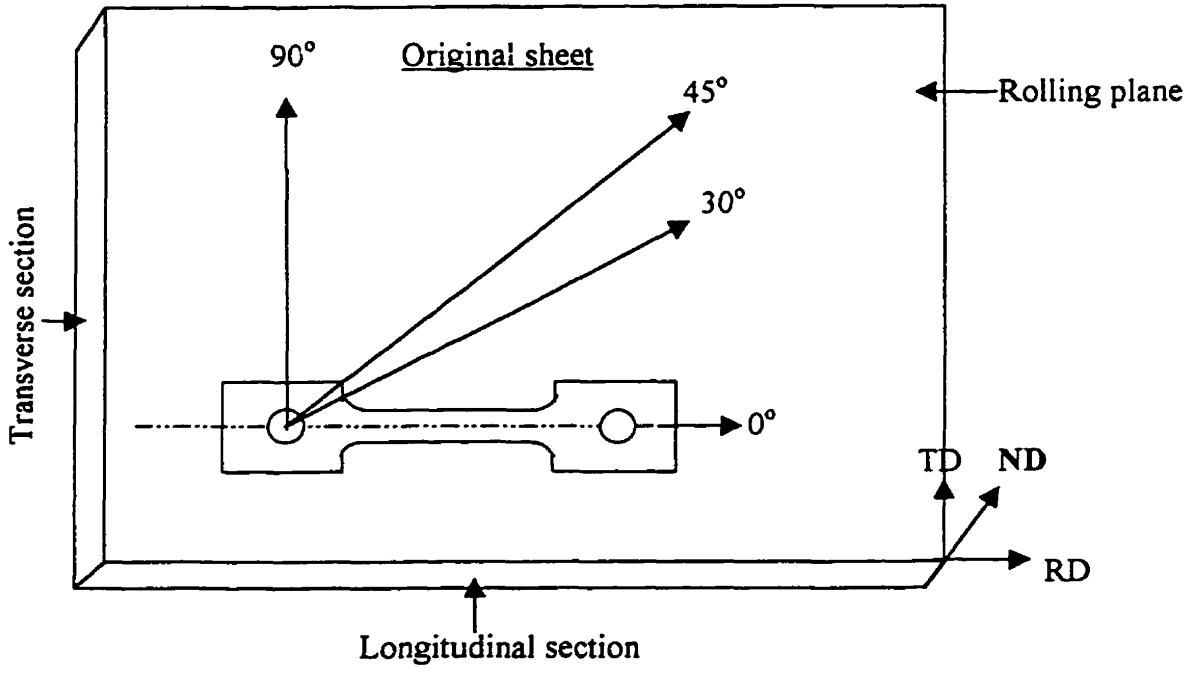

Fig.3.1. Schematic illustration of tensile samples orientated to have different angles between the tensile axis to the sheet original rolling direction.

The samples were designated in the following manner:

W0: Sample tensile axis at 0° to the original rolling direction of the as-received sheet,

W30: Sample tensile axis at 30° to the original rolling direction of the as-received sheet,

W45: Sample tensile axis at 45° to the original rolling direction of the as-received sheet,

W90: Sample tensile axis at 90° to the original rolling direction of the as-received sheet.

Where, W represents the whole thickness.

B. Surface Part of the Original Sheet

Tensile samples were prepared from the top 1/3 thickness of the as-received sheet by removing the rest 2/3 of the sheet. Such surface sheet, which was about 0.6 mm thick, was made by chemical milling by Bristol Aerospace Limited, Winnipeg, Canada, using a proprietary alkaline etchant Turco4181. As illustrated in Fig.3.1, tensile axes of the various surface material samples were at the same angle with the original rolling direction as those of the whole sheet samples.

S0: Surface sample with tensile axis at 0° to the original rolling direction of the as-received sheet

S30: Surface sample with tensile axis at 30° to the original rolling direction of the as-received sheet

S45: Surface sample with tensile axis at 45° to the original rolling direction of the as-received sheet

S90: Surface sample with tensile axis at 90° to the original rolling direction of the as-received sheet

Where, S represents the surface material of the whole thickness sheet.

C. Central Part of the Original Sheet

The central 1/3 part of the as-received sheet was prepared by removing the top and bottom 1/3 of the sheet, also through chemical milling by Bristol Aerospace Limited, and tensile samples were prepared from this central section. The orientations of these tensile samples with respect to the rolling direction were the same as that of the surface and whole thickness samples. The samples were designated in the following manner.

C0: Center sample with tensile axis at 0° to the original rolling direction of the as-received sheet

C30: Center sample with tensile axis at 30° to the original rolling direction of the as-received sheet

C45: Center sample with tensile axis at 45° to the original rolling direction of the as-received sheet

C90: Center sample with tensile axis at 90° to the original rolling direction of the as-received sheet

Where, C represents the central part material of the whole thickness sheet.

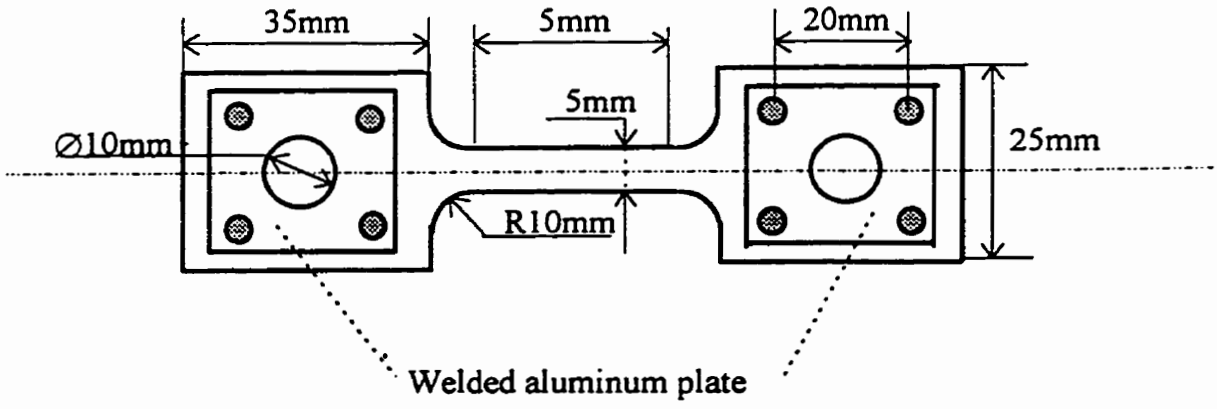

Fig.3.2. Schematic illustration of the dimension of the tensile sample.

3.2.2. Sample Preparation

Fig.3.2 illustrates the dimensions of the tensile samples. The dimensions of the tensile samples were determined by considering the tensile test setup, i.e. the furnace, the load cell, possible elongation and the distance available for the movement of the cross-head of the machine.

For making the tensile samples, strips closed to the sample width were first cut from the sheets in accordance with the pre-determined orientation. Tensile samples were then cut to size from these strips. To avoid deformation around the gripping pin holes during the test, small aluminum sheet pieces were spot welded to both sides of the sample shoulders as shown in Fig.3.2. Before tensile testing, each tensile sample was mechanically polished on all four sides of the gauge length. The polishing was done by using a series of sand papers, and finished with the 600 grade paper.

3.2.3. Test Setup

Tensile tests were performed in a screw driver Instron universal testing machine. The machine was modified by the addition of a microcomputer so that constant strain rates could be achieved. The testing temperatures were controlled by a three-zone split furnace. For each of the test temperatures, three zones of the furnace were first adjusted by using a test sample on which three thermocouples were spot welded to observe the temperature in the gauge section the sample. The furnace was adjusted to keep the temperature of the sample in the gauge section constant within ± 1°C. The load cell was installed at the fixed cross-head

which was at the lower end of the machine frame, so that the load cell was below the furnace rather than on the moving rod above the furnace. Such an installation of the load cell avoided heat input to the load cell by radiation from the furnace. All the tests were carried out at a fixed temperature with a pre-determined constant strain rate. Load and elongation of the sample were recorded by the microcomputer attached to the Instron machine.

It was observed that when furnace was put around the testing chamber, its temperature dropped by 30°C. Therefor, for performing a test, the furnace was first heated to a temperature that was about 30°C higher than the test temperature. Then a test sample was loaded and the furnace was put in place. It took about 15 min. for the sample to reach to the test temperature. However, to make the temperature of the sample uniform and to make the furnace attain equilibrium, the testing system was kept static for 5 more minutes before starting the test. All tests were conducted in air and were performed until failure. The furnace was then removed and the failed sample was allowed to cool in air. Whenever it was required to stop deformation of a sample at a specific strain for the purpose of microstructural examination, the load on the deforming sample was promptly removed then the sample was allowed to cool in air.

In order to retain the microstructural characteristics of the samples corresponding to the testing temperature, some of the deformed samples were obtained in the following manner. When the sample was deformed to a pre-determined strain, the load was removed and the sample was quenched by introducing a mixture of argon and water. The process was

completed within 100 microseconds. The quenching was conducted by a specifically designed in-situ quenching facility illustrated in Fig.3.3. There were two considerations in designing this in-situ quenching facility. (i) Ideally, direct examination of deformation microstructure during deformation should be conducted, especially if the dislocations were involved in the process, but it is impossible to directly examine the microstructure of a bulk material at high temperature. However, to freeze the deforming microstructure and then examine it is one of the indirect methods. The latter requires an extremely rapid cooling of the deforming sample from the high temperature. (ii) At the moment of quenching, the sample needs to be stress free to avoid external sources of dislocation generation. Therefore, the time gap between the two actions on the deforming sample, viz. fast cooling and the release of tensile stress, should be as short as possible. This resulted in the design of this in-situ quenching facility.

One of the two key units of this facility is the water supply, in which two pipes extended into the water chamber with holes on them. A symmetry in the flow of water from these two pipes was used to avoid any possible external stress on the sample at the moment of quenching. Cold water mixed with argon under a proper pressure established the cooling rate to be higher than 1000°C/s. The other key part is the stress release unit. A holder with grooves connected to the pull rod and a metal fork sliding through the grooves was made. The action of release was controlled by a solenoid. By measuring the time for water to reach the sample, the real gap between quenching and releasing of the load on the sample could be controlled by an electric timer to less than 100 micro seconds.

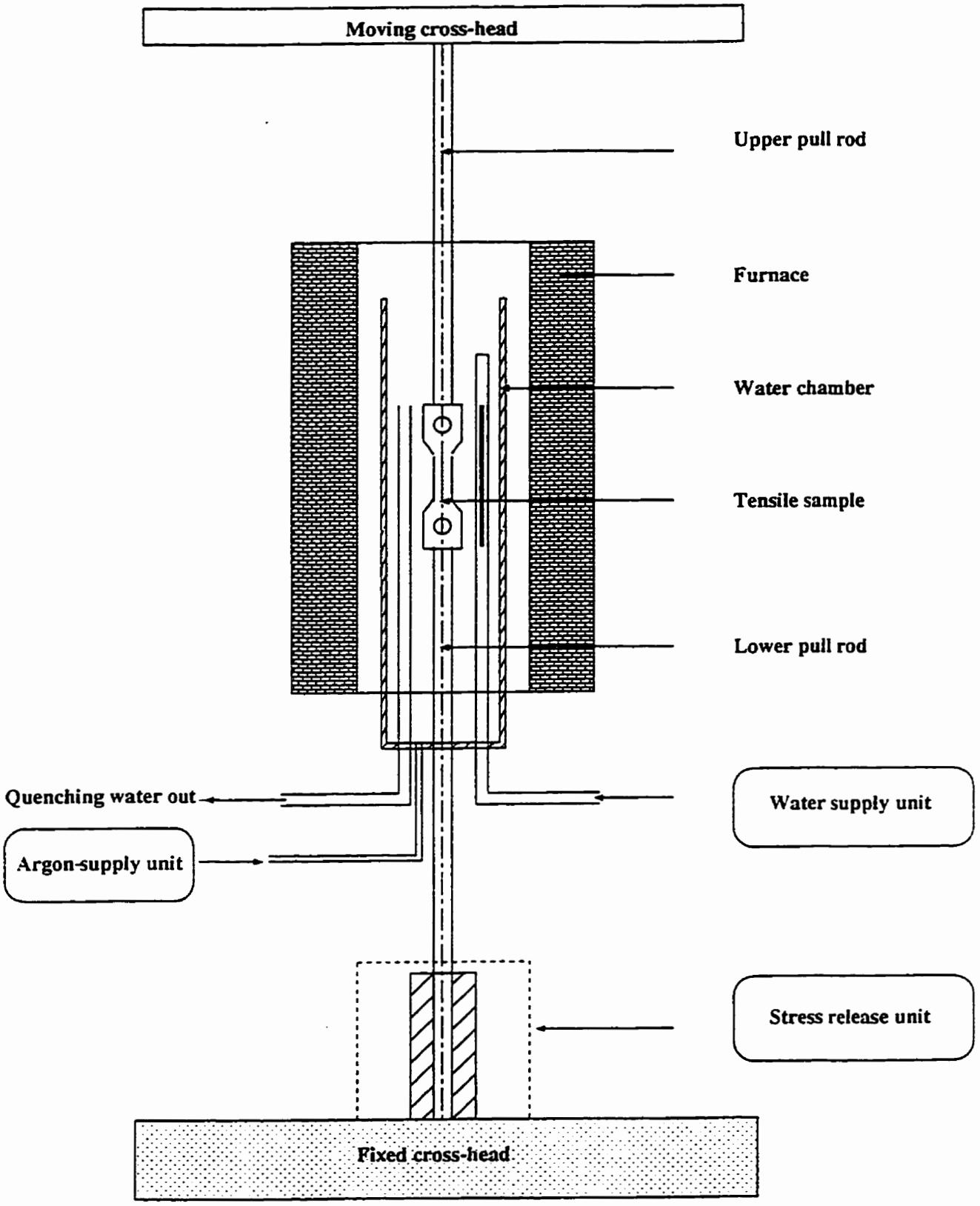

Fig.3.3. Illustration of in-situ quenching facility.

3.3. Optical Characterization

Optical metallography was used for microstructural characterization of the samples in various conditions. The optical samples were first mechanically polished and then chemically etched by Keller's reagent (Table.3.1.). A Leitz TAS Plus Image Analyzer was used to evaluate the grain size.

Table.3.1. The etching reagent being used

composition	HF	HCL	HNO_3	Still water
volume (ml)	2	3	5	190

3.4. TEM Characterization

More detailed microstructural examination was carried out by using TEM. The TEM examination was performed in a JEOL 2000FX operating at 200KV. To observe the through thickness subgrain structure of the starting sample, thin foils of longitudinal section of the sheet were made. The difficulties in making these thin foils were overcome in the following manner. A 0.5 mm wide strip was cut from the longitudinal section of the sheet. The strip was glued to a metal block and mechanically polished to a thickness of 200 μm. A 3 mm diameter punch was used to cut a 3mm x 1.8 mm piece from the thinned strip. The thin foil was then made by electropolishing. For this, the piece was placed in the specimen holder of the electropolishing machine and it was covered by a 3mm diameter Platinum foil disc with a small hole of about 0.5 mm diameter in its center. The thin foils of deformed samples, prepared by the in-situ quenching facility, were made from the rolling plane of the sheet. All the thin foils were finally prepared by electropolishing in a 25% nitric acid and 75% methanol solution cooled to -20°C, with an applied potential of 17V.

3.5. Orientation Imaging Microscopy (OIM) for Determination of Microtexture

Orientation imaging microscopy (OIM) (OIM is a trade mark of TexSEM Laboratories (TSL) Inc.) [121], a SEM-based imaging technique, has been commercially developed recently for analyzing the crystallographic structure of materials. It is proving to be a rich source of information for describing the spatial distribution of crystallographic features on the submicrometer to millimeter scale.

Principally, OIM is based on the electron back-scatter diffraction (EBSD) phenomenon [122], also referred to as back-scatter Kikuchi diffraction (BKD). The electron back-scatter diffraction patterns are formed in the SEM when a stationary probe is focused on the specimen. Initially, the incident beam is scattered elastically through large angles within the specimen, so that electrons diverge from a point source just below the specimen surface and impinge upon crystal planes in all directions. The subsequent elastic scattering of electrons by the crystal planes form arrays of Kikuchi cones whenever the Bragg condition is satisfied, which are viewed as the intense Kikuchi bands or Kikuchi diffraction pattern. Inelastic scattering events also occur and these contribute to a diffuse background.

Fig.3.4 illustrates the essential elements of the instrumentation necessary to obtain the electron back-scatter diffraction patterns [123]. An electron beam is incident on the specimen. A phosphor screen is placed close to the specimen to collect the back-scattered electrons. A normal to the screen drawn from the point of electron incidence must subtend an angle greater than 70° and less than 120° with the incident beam. The diffraction patterns

in the manner of Kikuchi bands are generated from the upper surface of the specimen. The phosphor screen is viewed by using a low light sensitive television camera. The video images are captured digitally into the frame storage of a computer for on-line indexing of the patterns. Fig.3.5 is an example of a electron back-scatter diffraction pattern obtained from an AA8090 Al-Li alloy sample used in the present study.

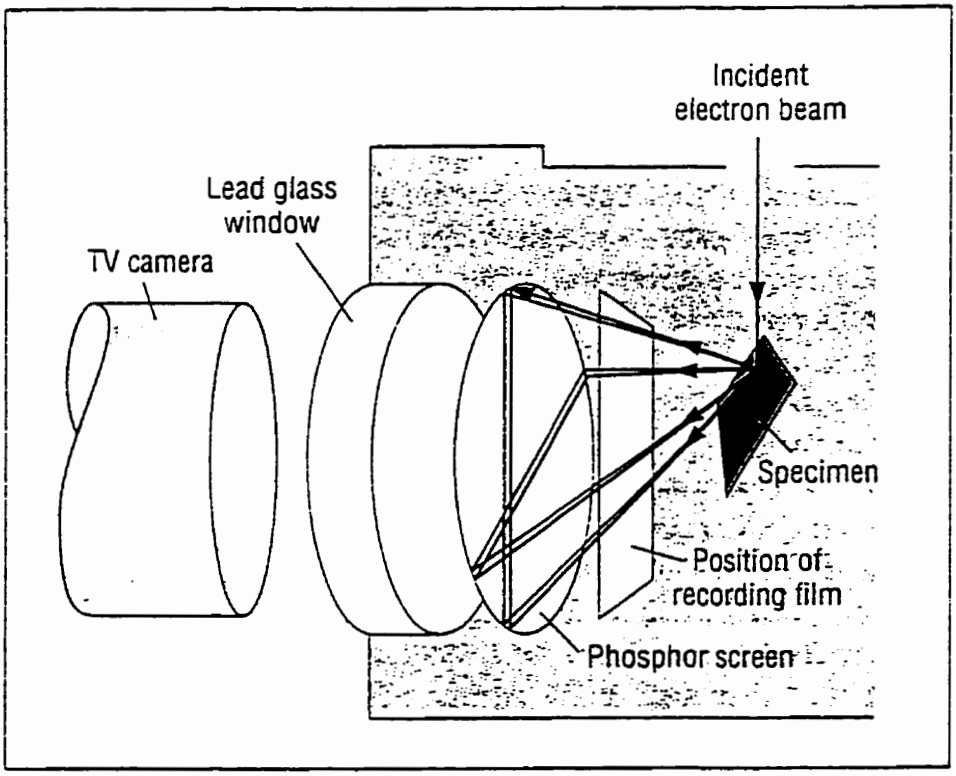

Fig.3.4. A Schematic illustration of the essential elements of OIM

OIM uses automated diffraction pattern analysis to obtain crystallographic data on a point-by-point basis over a selected area of the sample. The points are typically arranged in a regular grid and either the electron beam of the SEM is programmed to step to each point in turn, or the beam is held stationary and the specimen stage is programmed to traverse beneath it. The resultant data set include x-y coordinates (the real magnitude in the sample), local lattice

orientation, pattern quality, and a confidence index. From these data, OIM images, pole figures, orientation distribution function, grain misorientation distribution, etc. can be produced [124].

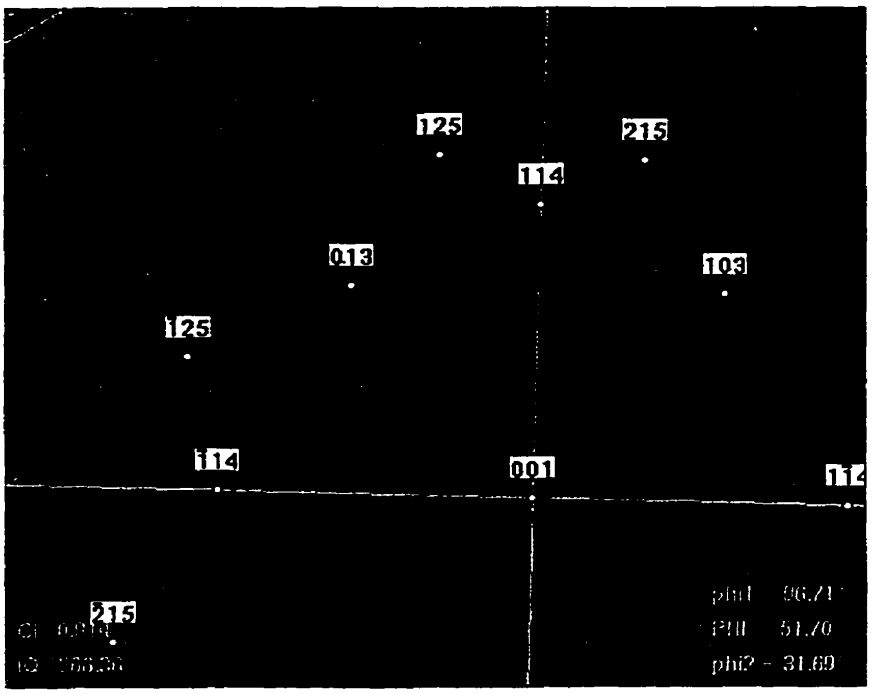

Fig.3.5. An example of a diffraction pattern obtained from AA8090 alloy.

Practically, the spatial resolution of this technique depends on the beam size of the SEM, and the orientation precision is about 1°. In addition to the normal operation of SEM, two aspects are essential to obtain reliable results. The first is that the angle between the incident beam and the specimen surface be small, i.e. 10-30° in order to minimize the amount of signal which is absorbed and to maximize that which is diffracted. The second is the specimen preparation. The beam/specimen interaction depth is approximately 10nm and this layer must be relatively strain free and clean for patterns to be generated.

In the current study, a Silicon Graphics computer based OIM manufactured by TSL was used with software OIM 2.0. The SEM was a JEOL 840 with a minimum beam size less than 1 μm. Beam-control was used to establish data scan. The normal to the specimen surface was at 70° relative to the incident beam. The selected scan grid was smaller than the grain size of the measured sample, and the scan area included at least 200 grains. The samples for OIM measurements were the same as those used for optical metallography. They were mechanically repolished and then electropolished in order to yield stress-free surface to produce high quality diffraction patterns. The electropolishing solution and conditions were the same as those used to prepare TEM thin foils. All the OIM scans were conducted on the longitudinal section for both undeformed and deformed samples.

CHAPTER 4.
RESULTS

The experimental results will be described in the following sequence:

1. Microstructural characterization of the as-received AA8090 Al-Li alloy sheet includes grain structure, precipitates, texture, and their distribution in through thickness cross-section. These establish the presence of microstructural gradient in this material as well as microstructurally composite-like nature of this material.

2. Effect of static annealing on microstructure including grain structure and texture upon annealing at 530°C and 570°C. These observations suggest that static annealing has no influence on the microstructural gradient existing in the as-received material, although grain coarsening does occur.

3. Tensile behavior of the full thickness sheet includes stress-strain relations, strain hardening, the value of strain rate sensitivity index, activation energy, and the effect of specimen orientation on flow behavior. These establish the optimum superplastic deformation condition for this material, and indicate a smaller level of anisotropy in the full thickness sheet material than in the surface or the center materials.

4. Microstructural evolution during deformation of full thickness sheet includes the microstructural characterization of grain size and shape, cavities, precipitates, dislocations and texture as influenced by strain, temperature and strain rate. In contrast to static annealing, deformation has reduced the microstructural gradient and weakened the texture.

5. Deformation behavior of the surface and center materials includes the effect of specimen orientation on flow property and texture. The results show significant flow stress anisotropy

compared with the full thickness sheet. The difference in texture development in different oriented samples brings out the direct involvement of dislocations during superplastic deformation of the AA8090 Al-LI alloy. A detailed description of these results is presented next.

4.1. Microstructural Characterization of As-received Material

4.1.1. Microstructures

Due to the difficulty in etching, it was not possible to reveal the microstructural features of the as-received material by conventional optical metallographic techniques. Therefore, the microstructural characterization was carried out by the OIM technique. Figure.4.1.1 (a-c) show the microstructures obtained by this technique, (a) in the rolling surface, (b) in the surface layer of the longitudinal section, and (c) in the center layer of the longitudinal section (see Fig.3.1 for the designation of various sections of the sheet). The contrast between grains in the images obtained by OIM is determined by the quality of diffraction patterns generated by the grains. Good quality patterns can be obtained from perfect grains, but can not be obtained from locations close to grain boundaries and deformed regions. The quality is also influenced by the size of the electron beam relative to the size of grains. The contrast in Fig.4.1.1 is poor because of residual stresses present in the rolled sheet specimens and the smaller grain size compared with the size of the electron beam. However, the OIM images show that the microstructures consist of nearly equiaxed grains at the rolling surface as well as in the layers in the longitudinal section close to the sheet surface. Elongated and banded grains are seen in the center layers of the longitudinal section. It was not possible to measure the grain size with certainty, due to the poor quality of the OIM images.

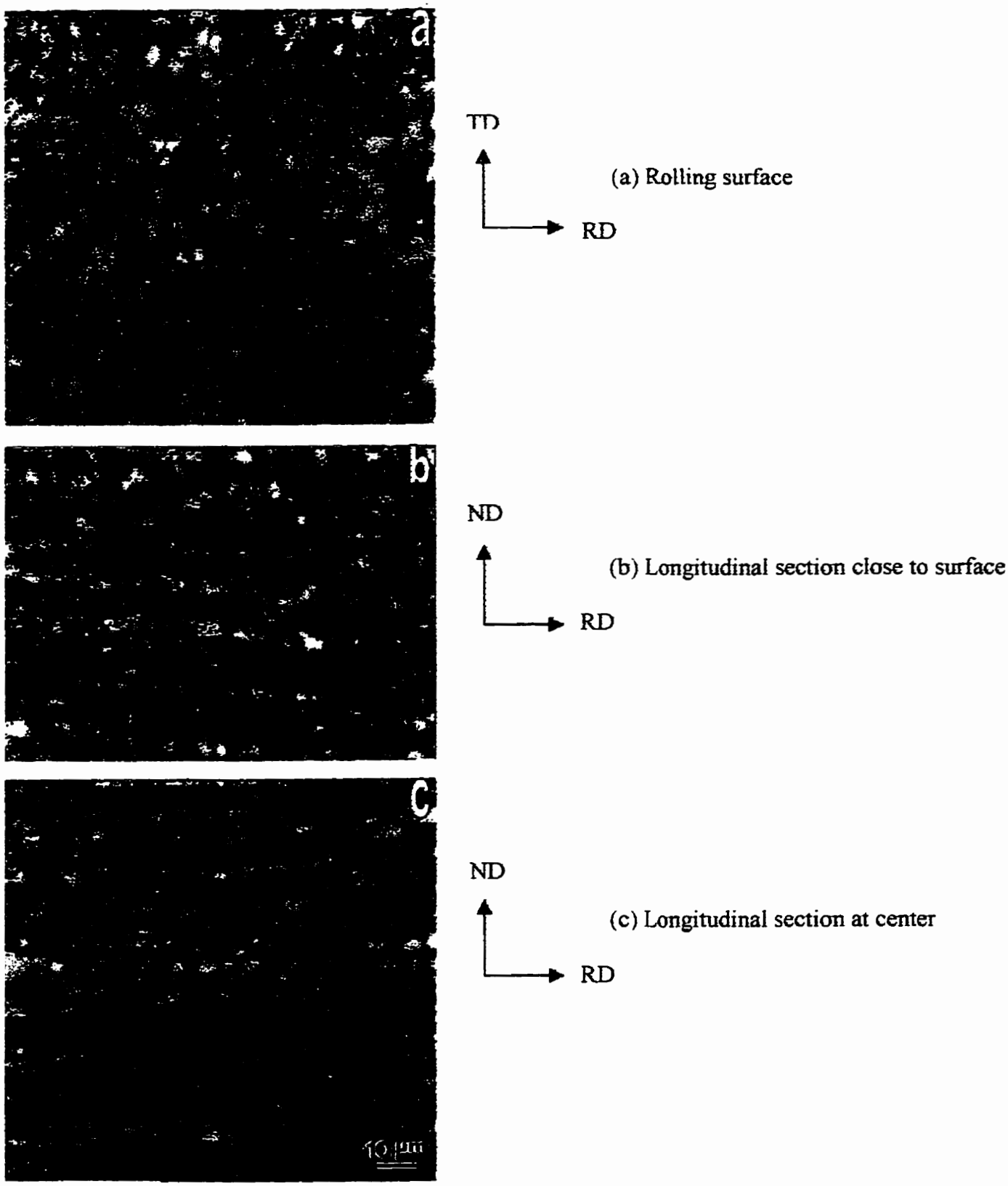

Fig.4.1.1. OIM images from as-received sheet material.

4.1.2. Precipitates and Substructures

TEM was used to characterize the precipitates and the substructure of the material. Thin foils of the surface and center layer materials of the sheet were made separately. The thin foils of the surface material were prepared by grinding off material from the opposite surface, leaving the surface material with a final thickness of about 200 μm. Whereas thin foils of the center layer material were obtained by grinding off both the rolling surfaces of a sheet sample and also leaving a thickness of about 200 μm, and finally using the electricpolishing technique described in Chapter 3.

TEM examination of the surface layer revealed the presence of at least two types of large precipitates, shown in Fig.4.1.2. At higher magnification, these precipitates were found to

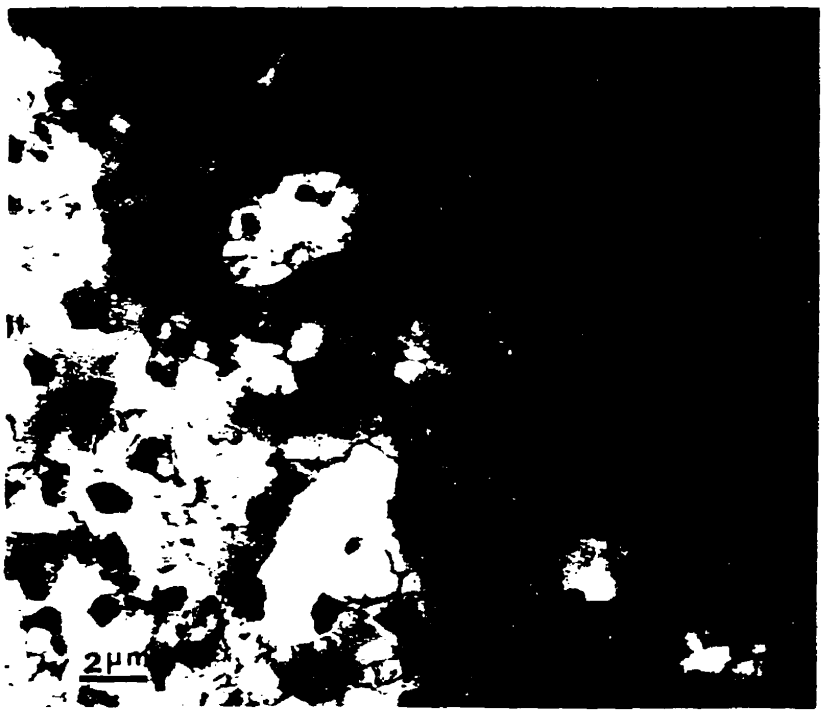

Fig.4.1.2. Microstructure (TEM) in the surface material of the as-received material.

be more distinct as illustrated in Fig.4.1.3(a). The microanalysis was carried out by energy dispersive x-ray spectroscopy (EDS). A typical energy dispersive X-ray spectrum of the precipitates, marked A in Fig.3.1.3(a), is shown in Fig.4.1.3(d). By semi-quantitative analysis carried out by Noran-TMF software, the compositions of this precipitate were found to be about 25at% Si, 2at% Mg and the rest Al, which suggest it to be Si-rich Al phase. Its micro-diffraction pattern is shown in Fig.4.1.3 (c), which suggests it to have a cubic crystal structure.

The microanalysis through EDS spectrum of the phase marked B in Fig.4.1.3(a) is shown in Fig.4.1.3(e), revealing its compositions to be approximately 14at% Cu, 9at% Mg and 75at% Al. The diffraction pattern of this precipitate, Fig.4.1.3.(b), shows a fivefold symmetry corresponding to that of the quasicrystal T_2 (Al_6CuLi_3), which has been also reported by Williams and Howell [92]. The average size of T_2 phase was estimated to be about 1 μm. In addition to these two kinds of phases shown in Fig.4.1.3, Fig.4.1.4 shows another kind of rod/cubic shaped precipitate marked by D. The analysis of the EDS spectrum shown in Fig.4.1.4.(c) suggests it contain about 15at% Fe, 80at% Al and some Mg, Cu and Si. Its diffraction pattern shown in Fig.4.1.4.(a) suggests this phase have a large lattice parameter and a complex crystal structure which could not determined unambiguously. Thus, the precipitates marked by A and D are rich in Si and Fe, respectively.

Fine precipitates were also observed within the grains. An example of this can be seen in Fig.4.1.4. The presence of these precipitates was further confirmed by the micrographs taken at higher magnifications.

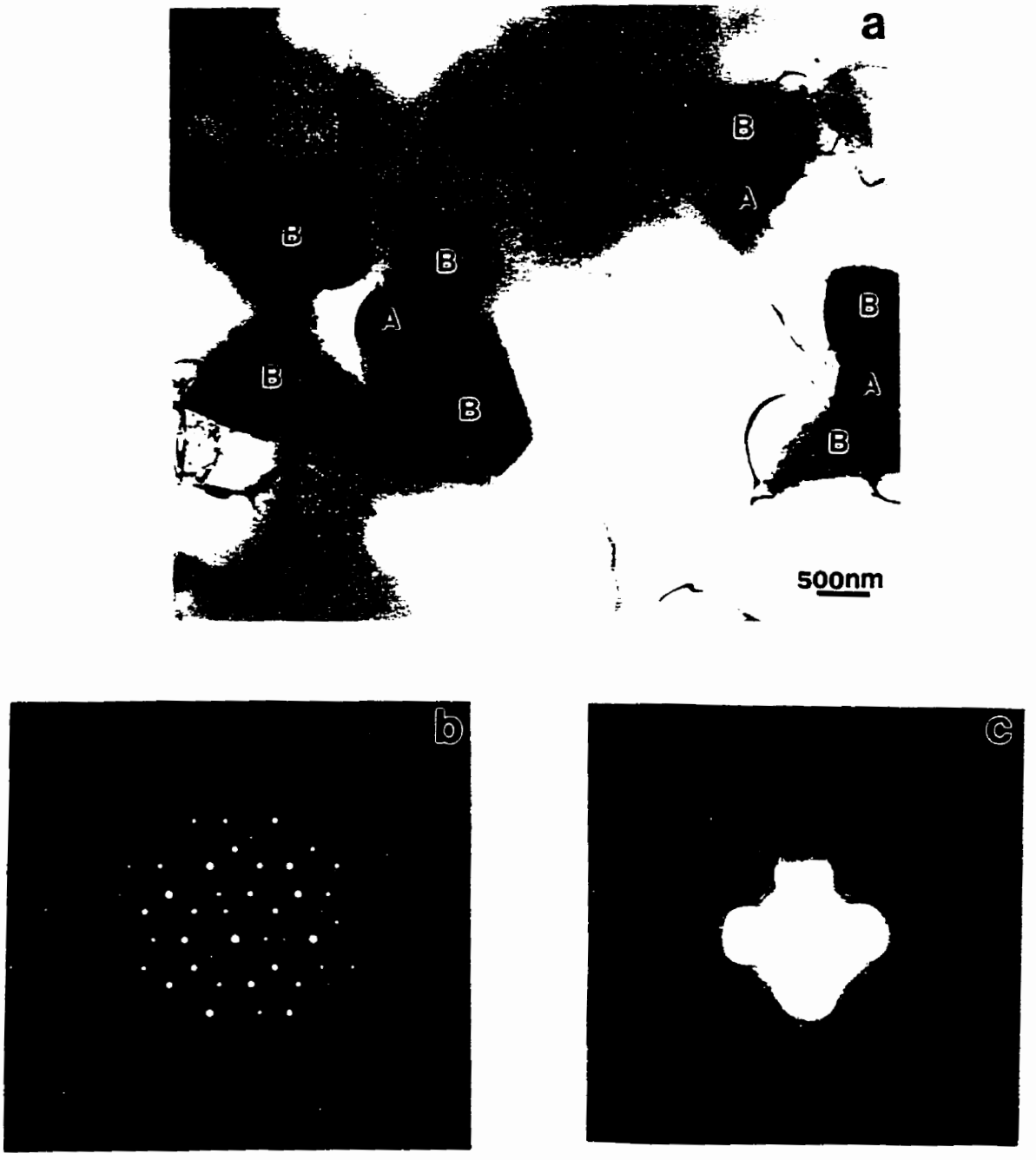

Fig.4.1.3. T_2 and Si-rich phases in the surface material of the as-received sheet. (a) bright field micrograph in which the precipitates marked A are the Si-rich phase and B are the T_2 phase; (b) diffraction pattern of the T_2 phase, and (c) diffraction pattern of the Si-rich phase, continue—

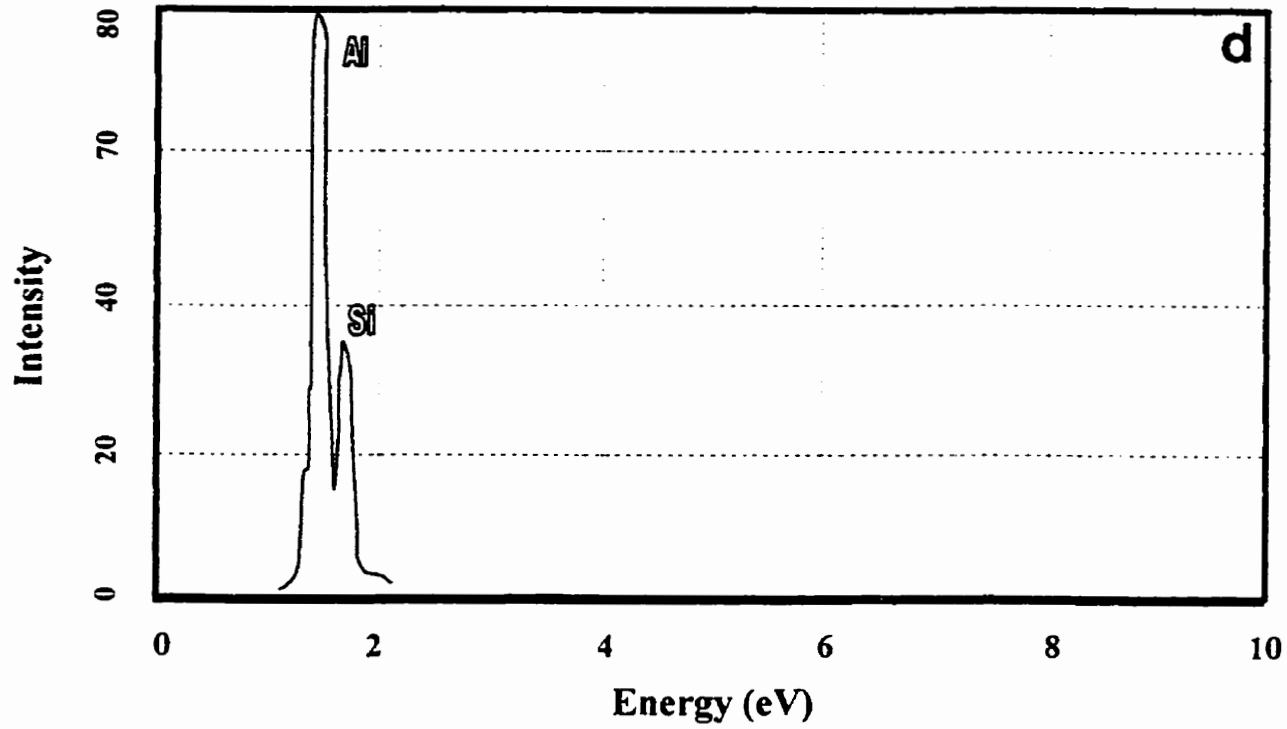

Fig.4.1.3(d). A typical energy dispersive spectrum of the Si-rich phase.

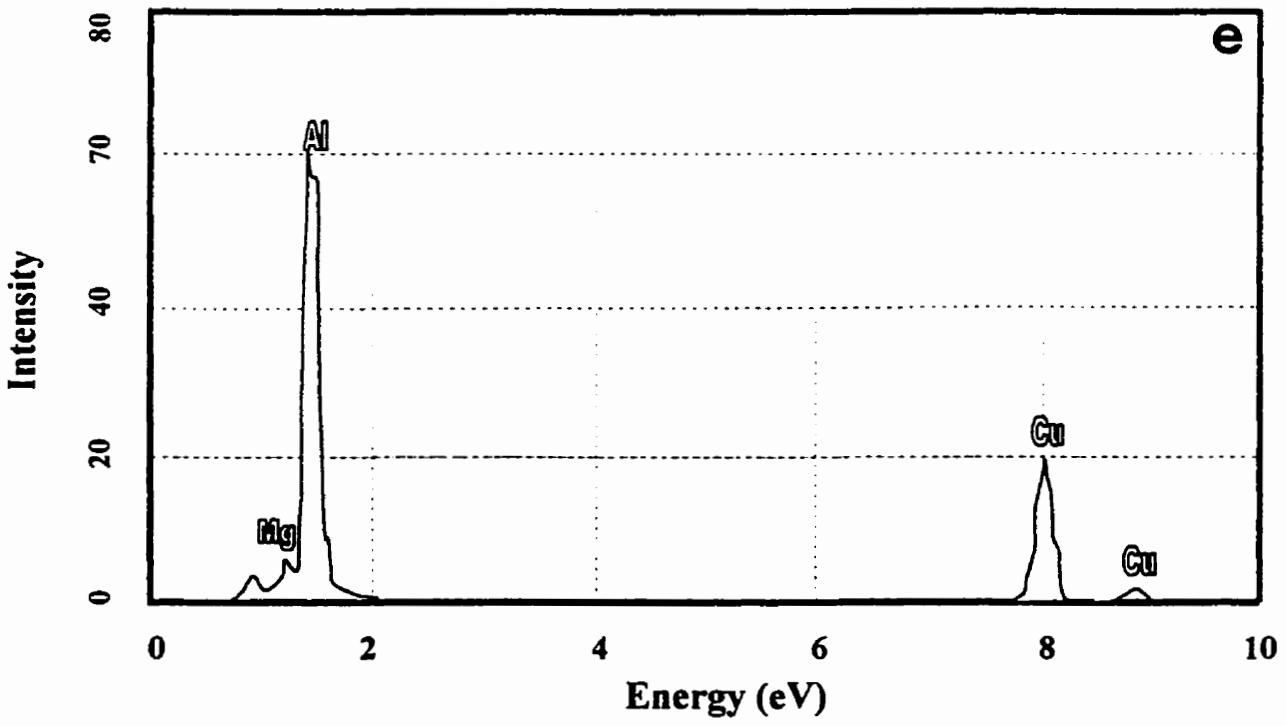

Fig.4.1.3(e). A typical energy dispersive spectrum of the T_2 phase.

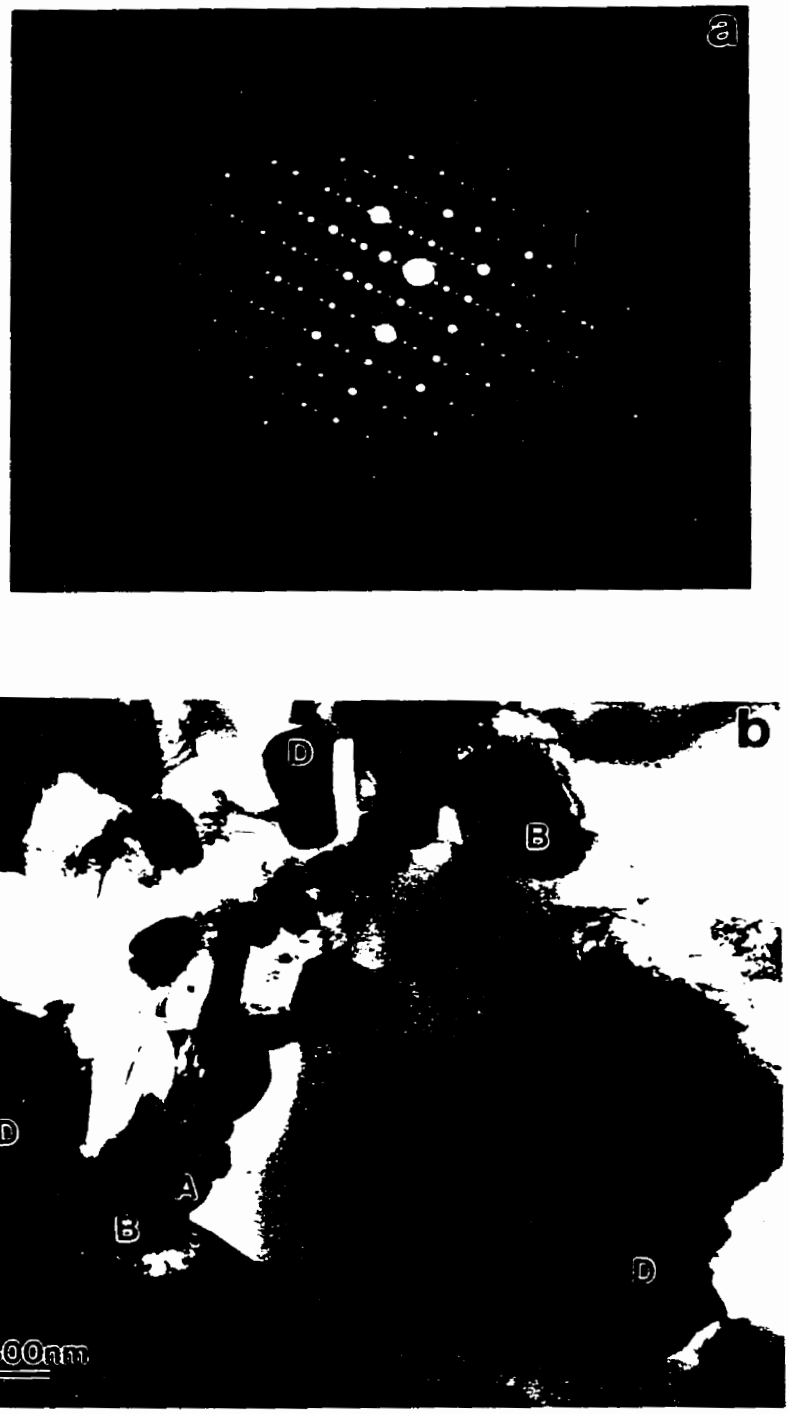

Fig.4.1.4. T_2, Si-rich and Fe-rich phases in the surface material of the as-received sheet:, (a) diffraction pattern of the Fe-rich phase marked D in (b) bright field micrograph in which the precipitates marked A is the Si-rich phase, B is the T_2 and D is the Fe-rich phase continue—

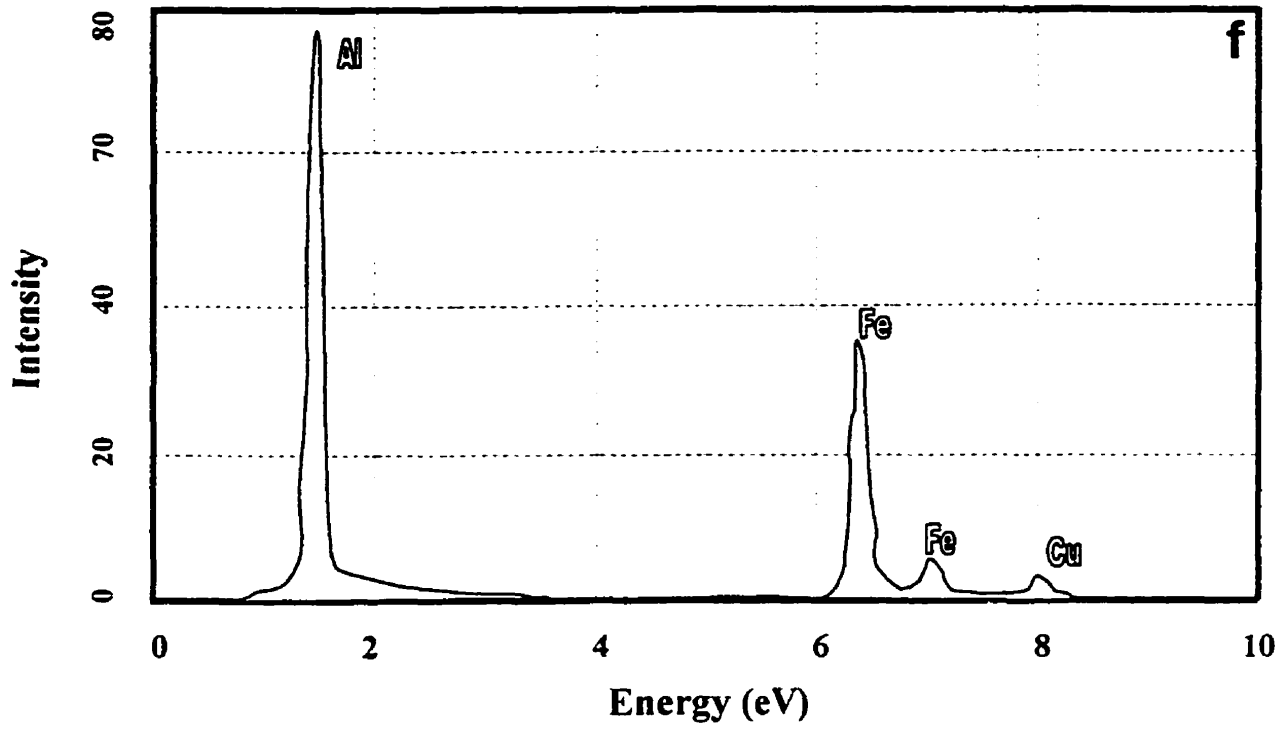

Fig.4.1.4(c). A typical energy dispersive spectrum of the Fe-rich phase.

A dark field micrograph of these precipitates is shown in Fig.4.1.5(a), which taken with the (010) superlattice reflection as shown in Fig.4.1.5(b) of the [110] selected area diffraction pattern. As marked in the micrograph, the darker spots surrounded by the white rings are the β' (Al_3Zr) phase; the white rings are the δ' (Al_3Li) phase which seem to have nucleated on the β' phase, as was reported in an Al-Li ally by Quist and Narayanan [89]; the bulky white phases at the grain boundaries are likely to be the δ (AlLi) phase, the same was also reported by Quist and Narayanan [89]. The β' precipitates, having about 0.1μm size, are seen to be uniformly distributed. All the precipitates found in the surface layer material were also observed in the center layer material, and their distribution, morphology and size were similar. These similarities are demonstrated in the TEM microstructures of the surface and center materials presented in Fig.4.1.2 and Fig.4.1.6, respectively.

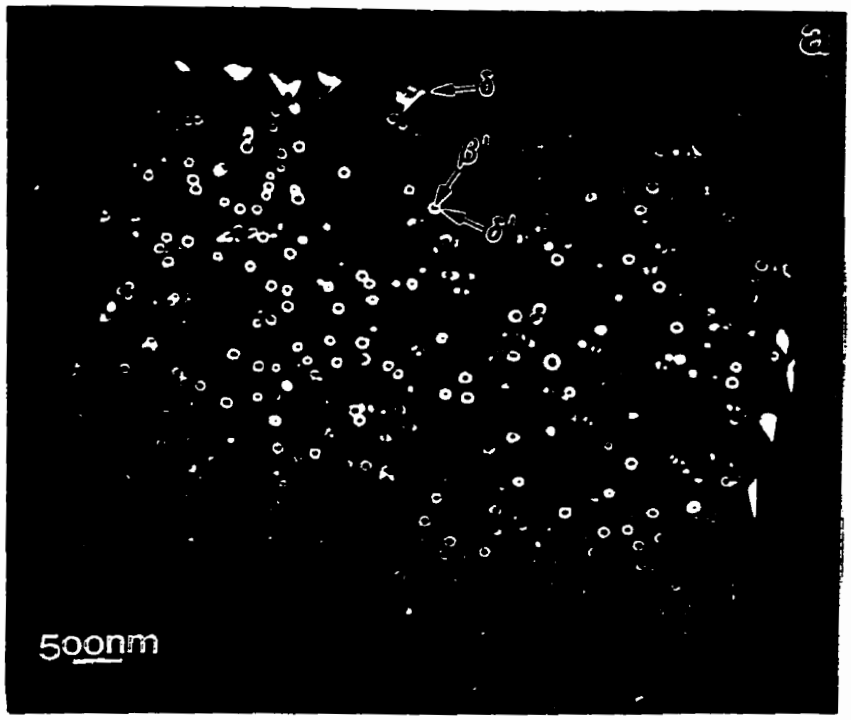

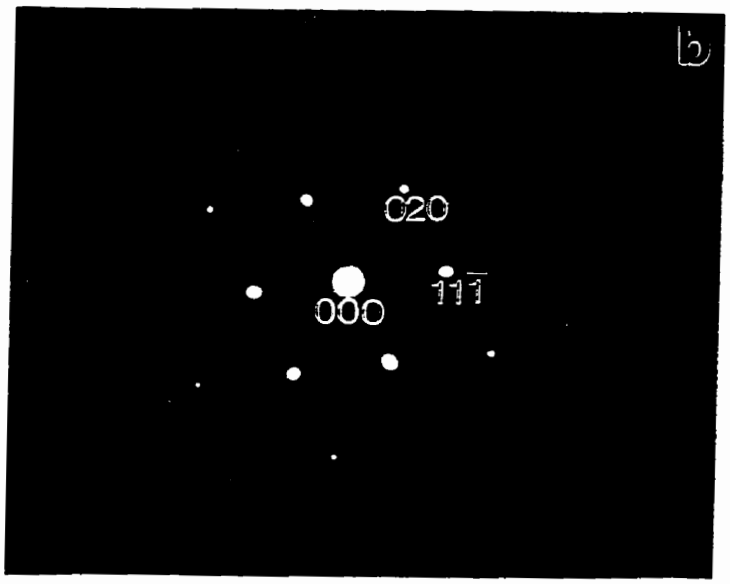

Fig.4.1.5. Precipitates of β', δ' and δ in a surface material of the as-received sheet(a) dark field micrograph in which all these phases are marked, (b) [110] diffraction pattern.

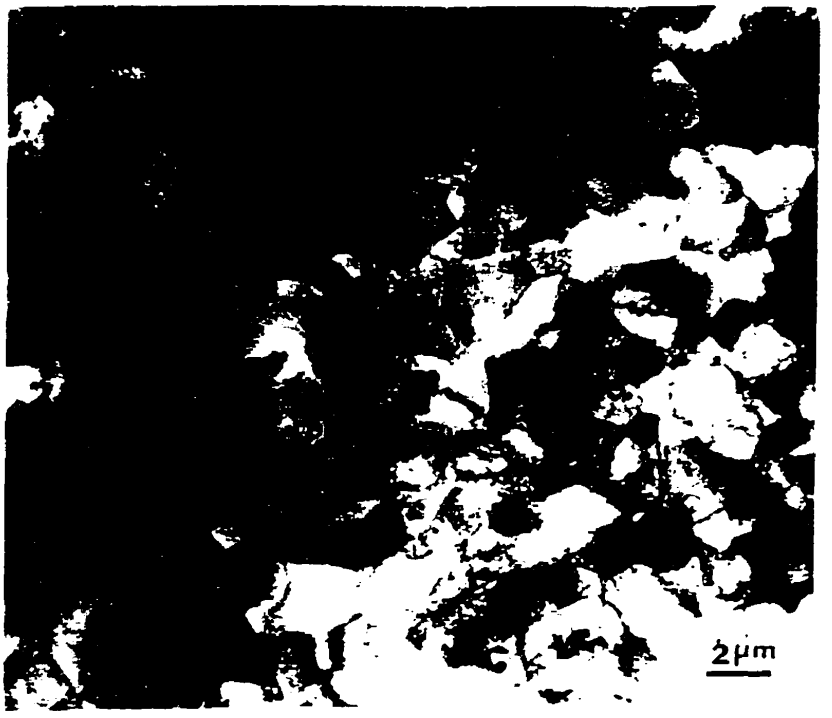

Fig.4.1.6. Microstructure (TEM) in a center layer of the as-received material.

4.1.3. Texture

The texture in a rolled sheet can vary in different locations of its thickness cross section. In order to determine if a texture gradient was present in the as-received material, textures were measured by the OIM technique at several locations on the longitudinal section (Fig.3.1) of the sheet sample as a function of thickness. Fig.4.1.7 schematically illustrates the locations from where the OIM images were obtained. The location A is next to the surface, E is at the center and B, C and D locations lie in between A and E. In each location, the instrument measured the orientations of all the grains in the entire area defined in Fig.4.1.7, each area was 80 μm along RD and 200 μm along ND, and produced OIM images and plots of pole figures (PFs).

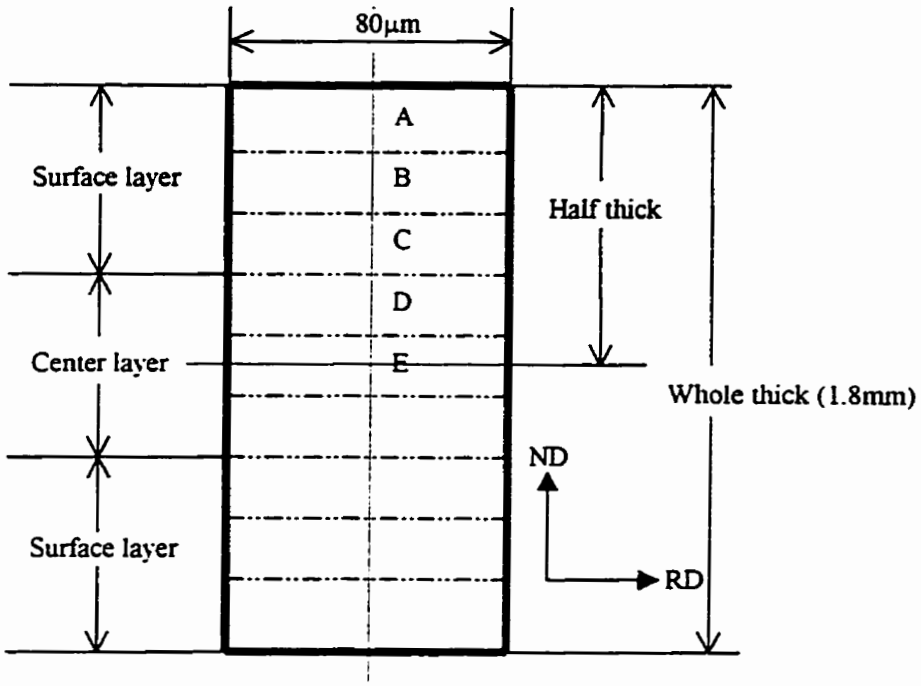

Fig.4.1.7. Schematic illustration of five equally divided locations in half thickness of the sheet longitudinal section at which OIM measurements were made.

Fig.4.1.8 shows the OIM images (a-e) and the corresponding PFs (a'-e') in the five locations, A to E. In rolled commercial purity aluminum, the major texture components have been observed to be copper (Cu) {112} <111>, S {123} <634> and brass (Bs) {110} <112> [125]. These are shown in Fig.A7 in the Appendix. From these it may be noted that the copper and S components tend to overlap and can not be separated easily. Comparison of PFs in Fig.4.1.8 with those in Fig.A7 shows that, at locations A and B, which correspond to the surface layer, the texture is copper-type with a mixture of S and Cu components. Whereas, the texture in the center layer at D and E was primarily brass-type with a mixture of brass and S. The transition from copper-type to brass-type textures is seen at C which was located approximately between the surface and the center layers.

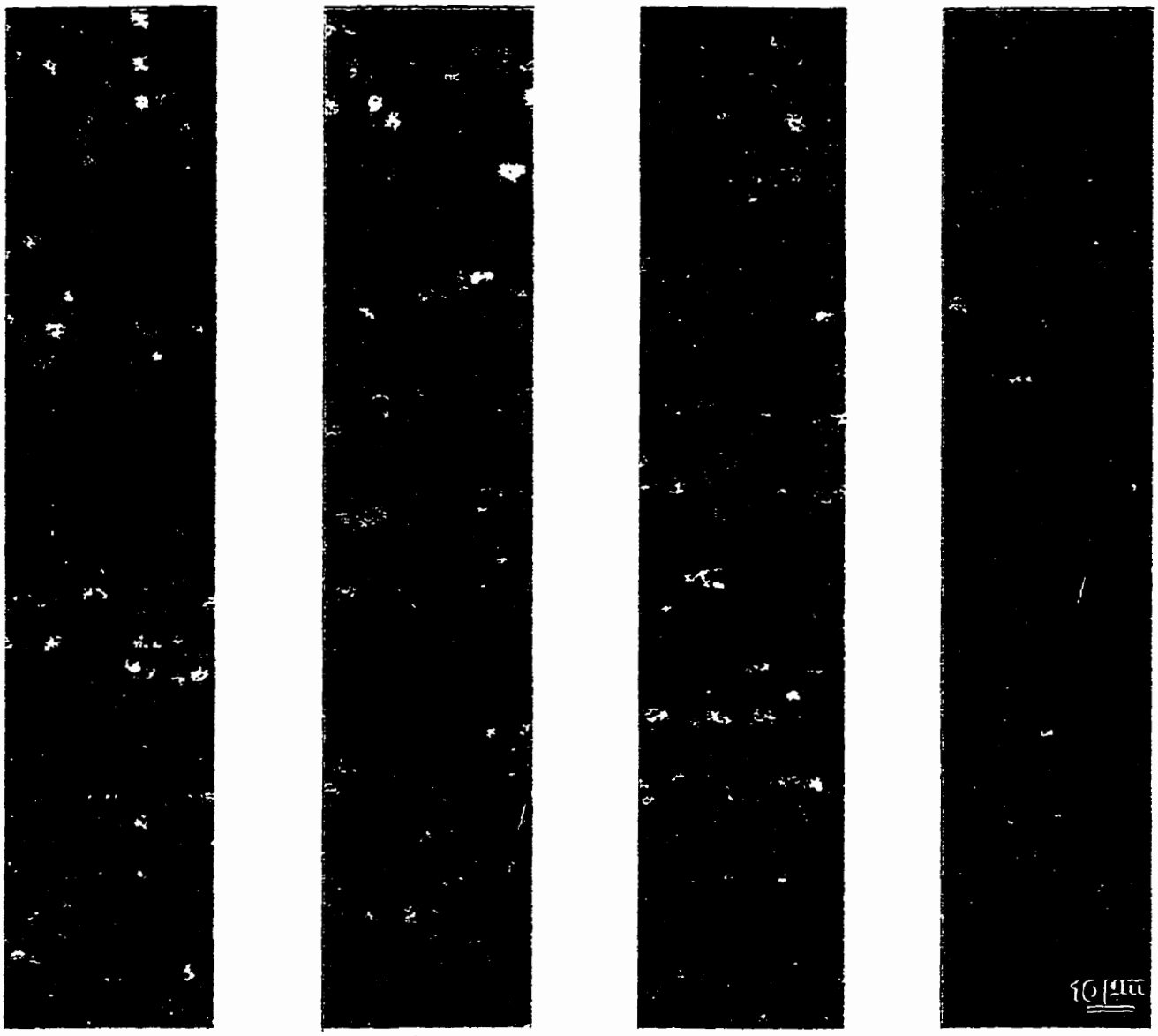

Fig.4.1.8. OIM images(a-e) and PFs(a'-e') of the as-received material in five equally divided locations in half thickness of the sheet longitudinal section, continued —

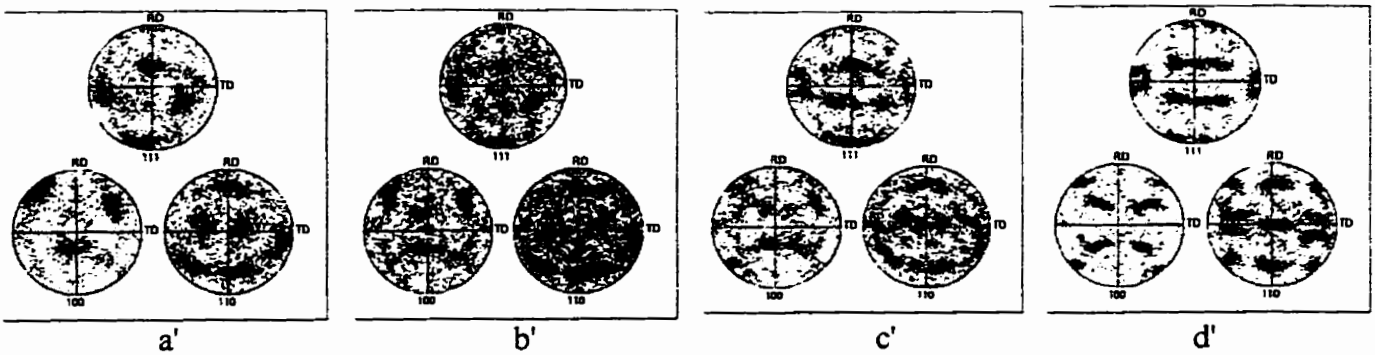

a' b' c' d'

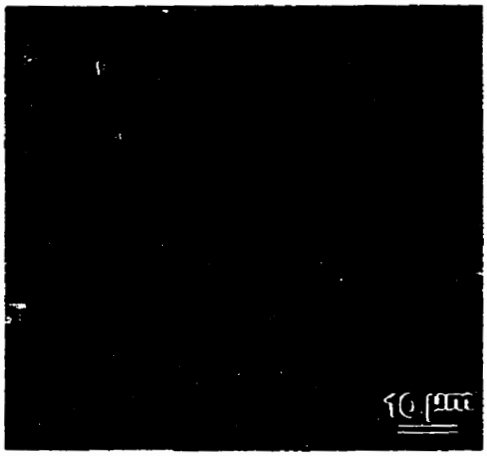

e

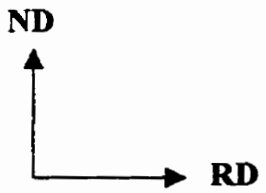

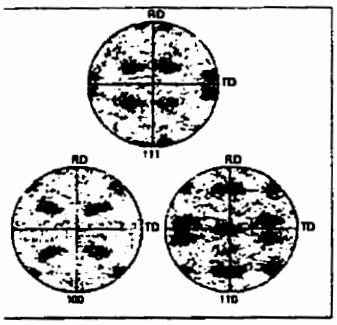

e'

Fig.4.1.8. OIM images(a-e) and PFs(a'-e') of the as-received material in five equally divided locations in half thickness of the sheet longitudinal section.

With the help of the software provided by the manufacturer of the OIM, TSL, it was possible to give a specific color to a set of grains having a specific orientation. In Fig.4.1.8 the two symmetrical components of the brass texture are colored red and green, while the Cu texture components are colored blue and pink (S is mixed with them). The grains which do not have these textures and have random orientations are colored yellow. The OIM images show that in the center section the brass texture components are dominant. The two symmetrical brass texture components are seen in alternate layers of grains parallel to the rolling direction. There are no yellow colored grains. Thus, all the grains in the center section are strongly textured. In contrast, although the copper texture is dominant in the surface layer it contains grains of all orientations, i.e. Cu (blue and pink), Bs (red and green) and random (yellow). There is a slight tendency to form layered grains in the surface section, but, this is not as prominent as in the center section. A number of green and red grains, representing Bs textures, are also seen in layer A, but they gradually increase from the surface towards the center reaching almost 100% in layer E.

In summary, in the as-received state the material contained nearly equiaxed grains in the surface layers and fine elongated grains in the center layers. A texture gradient was observed along the thickness cross-section with copper-type texture in the surface layer and brass-type texture in the center layer.

4.2. Effect of Static Annealing on Microstructure and Texture

The as-received microstructure may undergo some changes during heating and soaking at the testing temperature prior to the onset of deformation. Therefore, the specimens were subjected to somewhat equivalent static annealing, and their microstructure was examined and is described next, which was considered to be the initial microstructure, i.e. microstructure at the onset of deformation.

4.2.1. Annealing at 530°C

As will be discussed later, the optimum temperature for superplastic deformation of this material was found to be 530°C. Therefore, the specimens of the as-received sheet were annealed at 530°C for 20 minutes and air cooled. The 20 minutes correspond to the heating and soaking time prior to the onset of deformation during tensile testing as was described in Chapter 3. The stress relief by annealing and the precipitation during cooling made it possible to reveal microstructure by optical metallography, which was not possible with the as-received material. Microstructures of the rolling surface, the longitudinal section and transverse section were examined. The micrographs taken from various locations are presented in Fig.4.2.1 as a three-dimensional composite to clearly represent the variation in microstructure along the through thickness direction. As shown in this figure, nearly equiaxed grains were present in both the rolling surfaces of the sheet as well as in the longitudinal and transverse sections close to both the surfaces. Elongated grains were present in the center layer along both the rolling and the transverse directions, which suggests that the grains were of pancake shape.

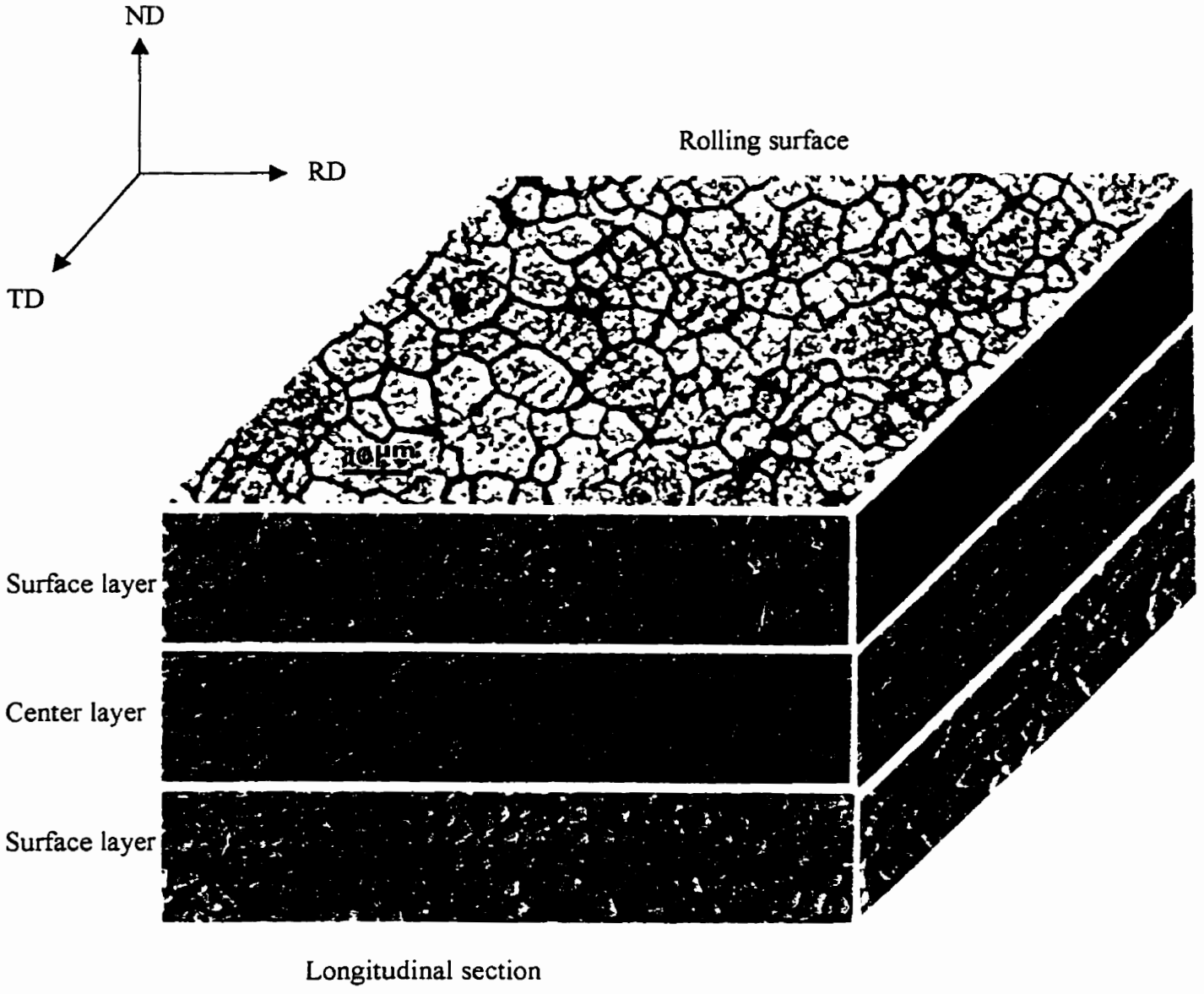

Fig.4.2.1. Three dimensional composite microstructure (optical) of the sheet after annealed at 530°C for 20 minutes

Comparison of the micrographs in Fig.4.2.1 with that in Fig.4.1.1 shows the pancake shape grains to be present in the center layer in both the cases, viz. as-received as well as after annealing. This suggests that recrystallization did not occur during static annealing, although the grains became coarser as a result of annealing. The average grain size after static annealing was ~ 4.2 μm in the surface layer material, and in the center layer the grain width increased to about 3 μm and they were about twice as long.

The TEM examination revealed that the precipitates of T_2, δ′ and δ, which were present in the as-received material (Figs.4.1.3-4.1.5), dissolved completely upon annealing at 530°C for 20 minutes as shown in the TEM micrographes of Figs.4.2.2 and 4.2.3. The Si-rich and Fe-rich phases, however, remained in the material, but their volume fractions and sizes, quantitatively seems to have been reduced. Fig.4.2.2 taken from the surface layer material and Fig.4.2.3 from the center layer, which were viewed along the normal direction (ND), suggest that almost equiaxed subgrains were present. However, when the center layer was examined with the foil normal in the transverse direction, i.e. viewed in the longitudinal section, the subgrains were seen to be elongated along the rolling direction, an example of which is shown in Fig.4.2.4. Therefore, the grains/subgrains in the center layer were of pancake shape.

Fig.4.2.2. Microstructure (TEM) in the surface material of a sample after annealing at 530℃ for 20 min.

Fig.4.2.3. Microstructure (TEM) in the center material of a sample after annealing at 530℃ for 20 min.

Fig.4.2.4. Microstructure (TEM) in the center material of a sample after annealing at 530℃ for 20 min viewing in longitudinal section.

Figure.4.2.5 gives the OIM images and PFs in five locations (a to e) in the longitudinal section. Comparison of OIM images and PFs in Fig.4.2.5 with those of the as-received material in Fig.4.1.8 shows that annealing resulted in grain growth, better quality OIM images and sharper PFs. However, the texture is noted to remain unchanged, suggesting that recrystallization had not occurred during annealing. Results of quantitative analysis of texture components are shown in Fig.4.2.6 (a)-(c), in which (a) is the distribution of volume fraction of texture components in location B, and (b) is in location E. A plot of the variation in volume fraction of various texture components as a function of distance from the surface to the mid-thickness of the sheet is shown in Fig.4.2.6(c). It is seen that the volume fraction of various texture components in the section near to the surface increase in the sequence of Goss, Brass, Cubic, Cu and S. However, in the center section it increases in the sequence of Goss, Cubic, Cu, S and Brass with only very small difference between the volume fractions of the first three components. It also is seen in Fig.4.2.6 (c) that S component is distributed somewhat uniformly, Cu is dominant in the surface section and Brass is dominant in the center section. The transition of texture components from predominantly copper-type to predominantly brass-type seems to occur between the surface and the center section.

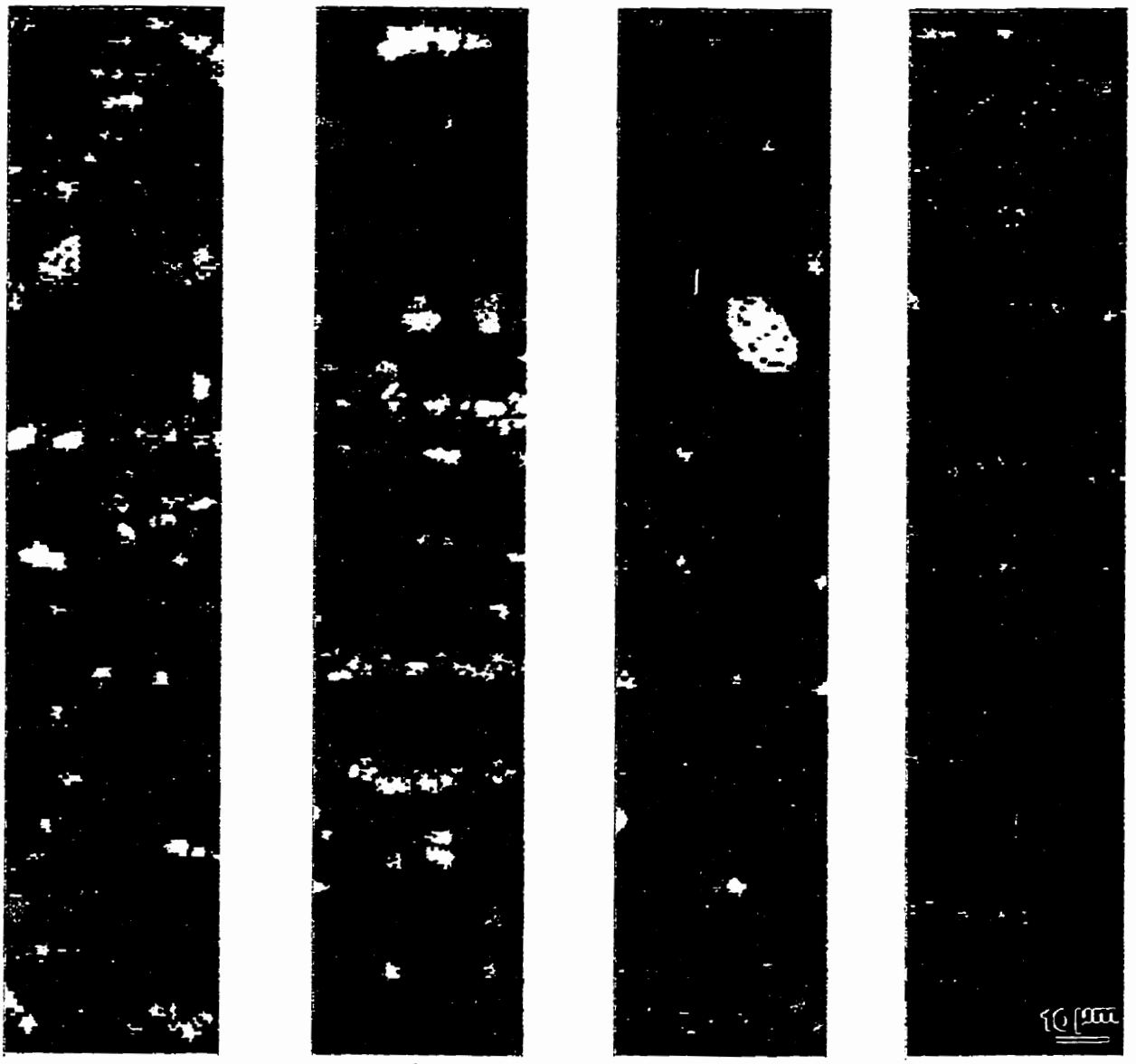

Fig.4.2.5. OIM images (a-e) and PFs (a'-e') of the material after annealing at 530 ℃ for 20 minutes in five equally divided locations in half thickness of the sheet longitudinal section, continued —

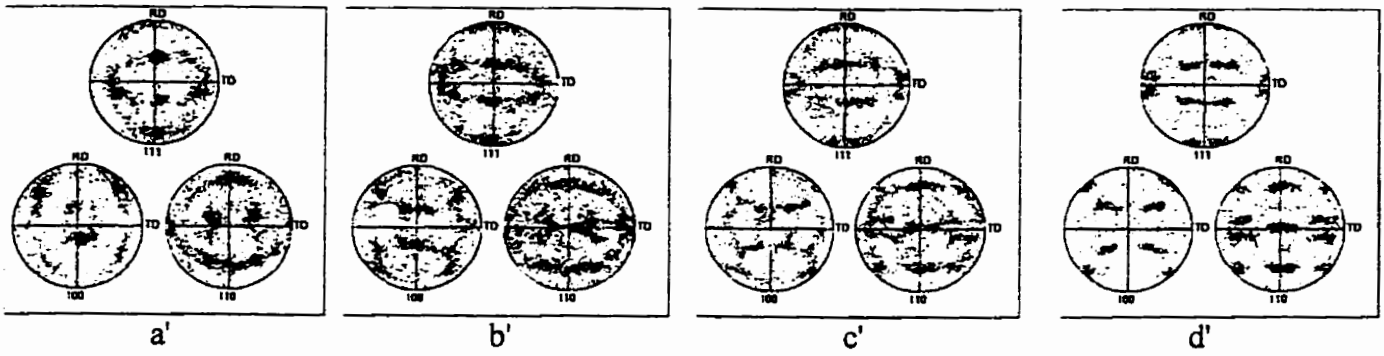

a' b' c' d'

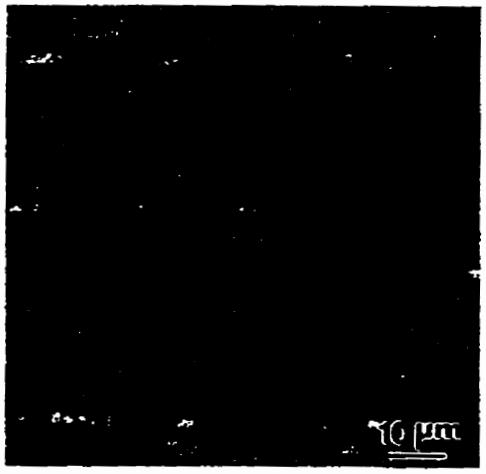

e

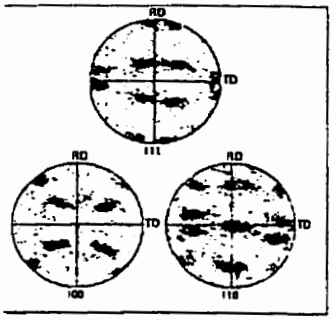

e'

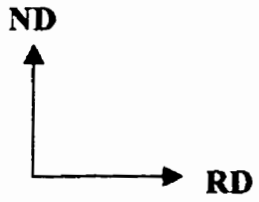

Fig.4.2.5. OIM images (a-e) and PFs (a'-e') of the material after annealing at 530℃ for 20 minutes in five equally divided locations in half thickness of the sheet longitudinal section.

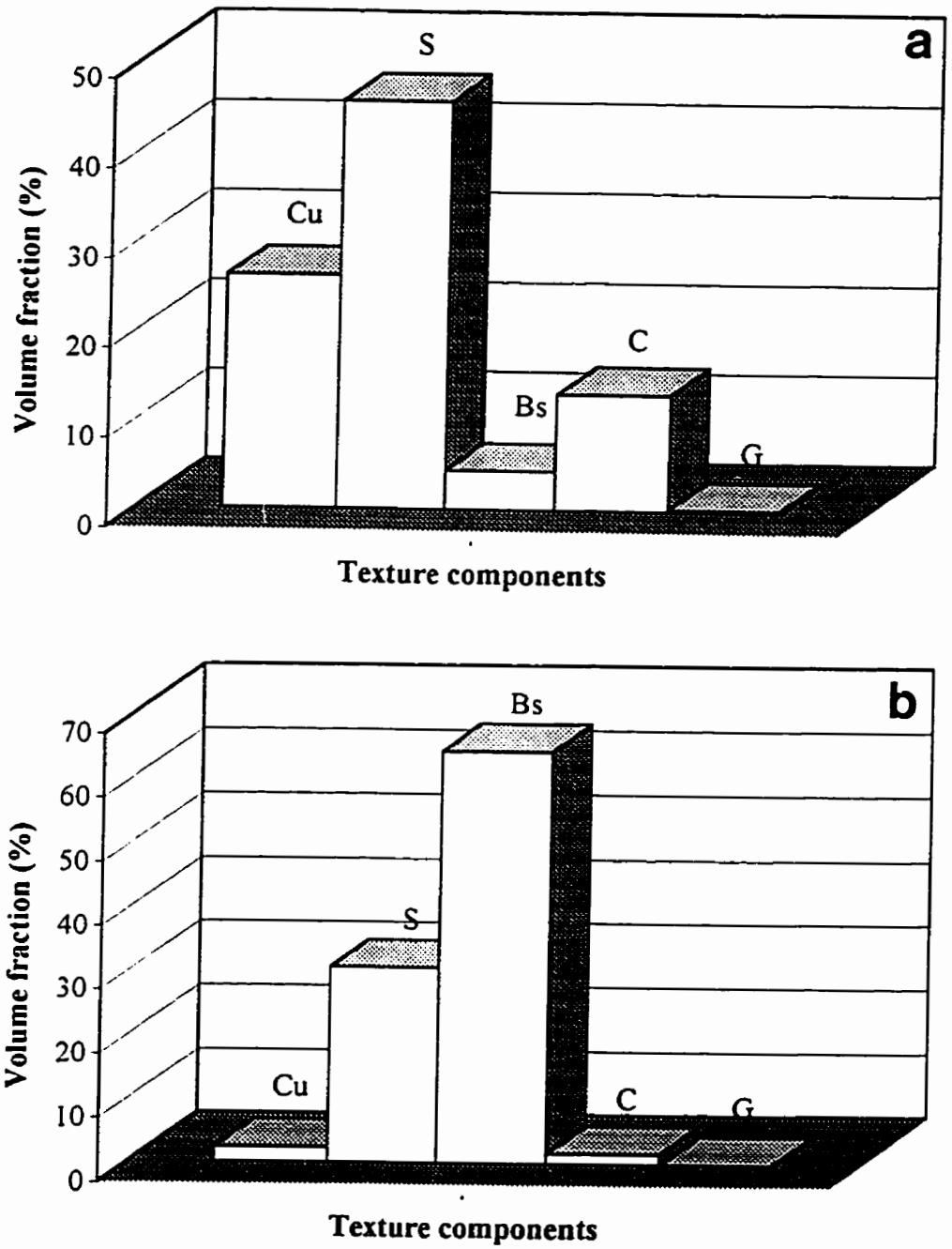

Fig.4.2.6. Volume fraction of main texture components of material annealed at 530℃ for 20 min in (a) the surface layer and (b) the center layer, continued —

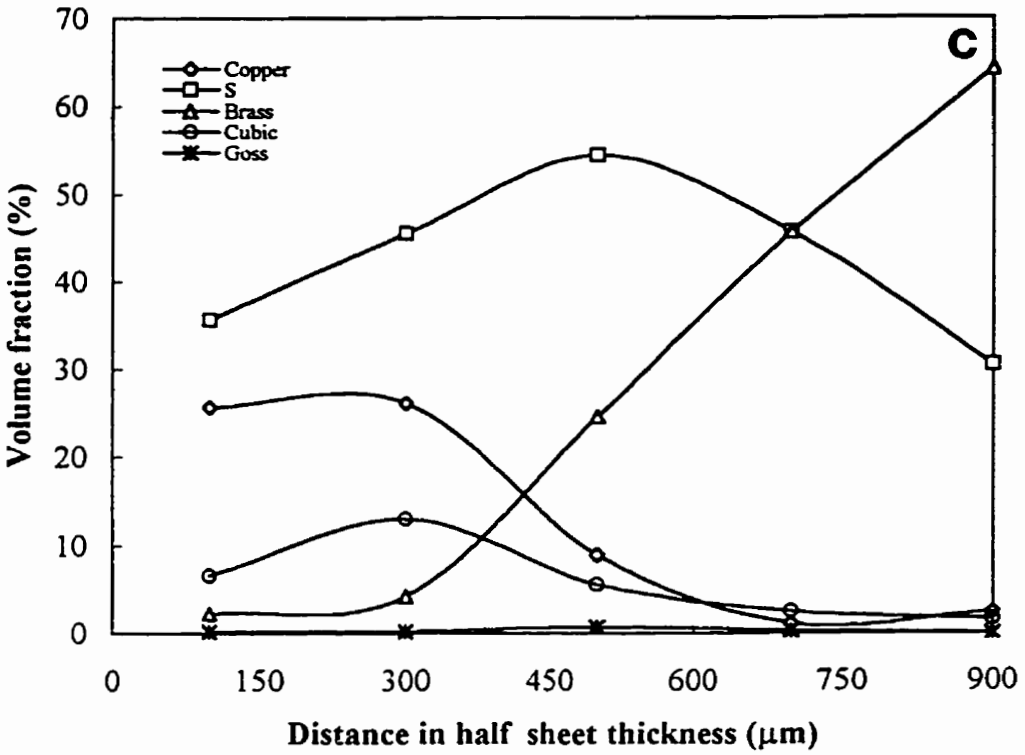

Fig.4.2.6(c). The distribution of volume fraction of texture components in the half thickness of the sheet longitudinal section.

4.2.2. Annealing at 570°C

Samples from the AA8090 sheet were also annealed at 570°C for 1 h in order to evaluate the changes in microstructure, texture and substructure, if any due to aggressive annealing. The purpose of this annealing was to simulate the structures that are commonly developed after prolonged annealing and concurrent straining after superplastic deformation.

Fig.4.2.7 shows a composite microstructure by using the same method as used for the specimen whose microstructure is shown in Fig.4.2.1. This microstructure shows a significant grain growth with the average grain size of about 14 μm. However, no change in the grain morphology was noted. TEM observations showed that the Si-rich and Fe-rich phases were still present, but their size had become larger. However, qualitatively, their volume fraction seemed to have decreased. Also, qualitatively, no change in the volume fraction of β′ was apparent. Fig.4.2.8 shows the OIM images (a-e) and the corresponding PFs (a′-e′) in the similar five locations as were used in the as-received material and the material annealed at 530°C for 20 minutes. Comparison of these OIM images and PFs in Fig.4.2.8 with those of the as-received (Fig.4.1.8) did not reveal any noticeable difference.

In summary, static annealing resulted in grain coarsening without any change in either the morphology of the grains or the texture, suggesting an absence of recrystallization. However, the T_2, δ′, and δ precipitates dissolved at these annealing temperatures, but the Si-rich and Fe-rich phases and β′ did not.

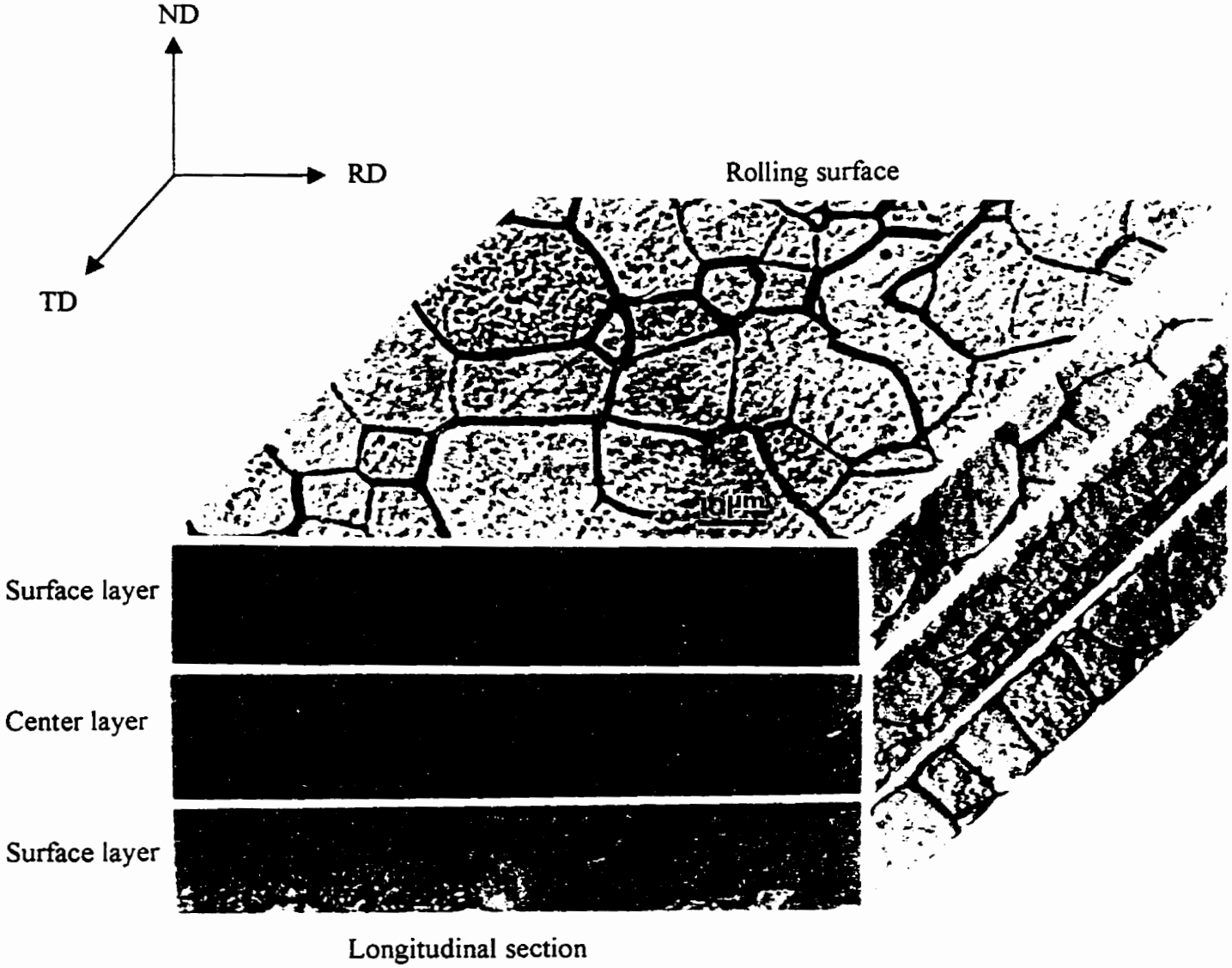

Fig.4.2.7. Three dimensional composite microstructure (optical) of the sheet after annealing at 570℃ for 1 hour.

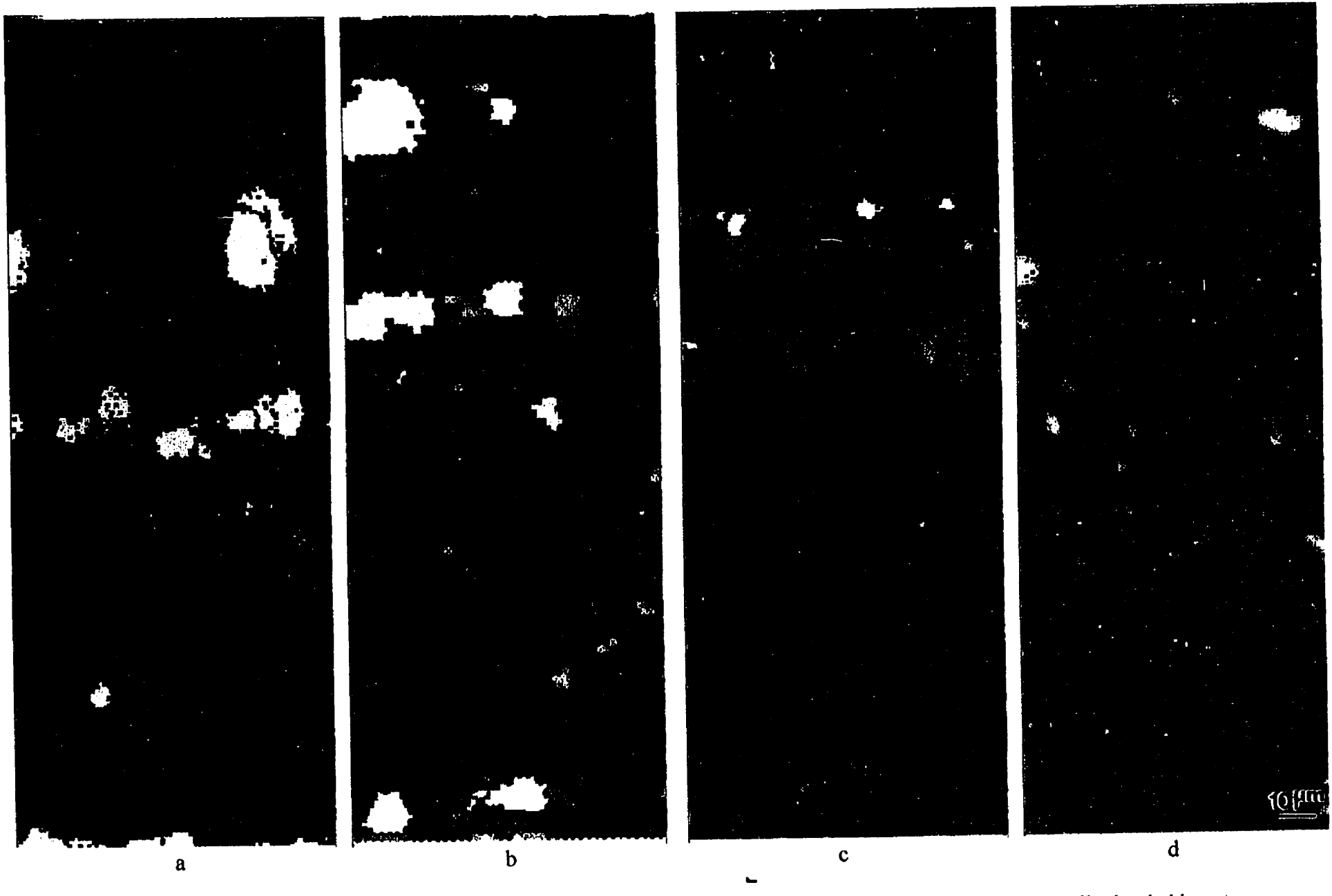

Fig.4.2.8. OIM images (a-e) and FPs (a'-e') of the material after annealing at 570 ℃ for 1 hour in five equally divided locations in half thickness of the sheet longitudinal section, continued —

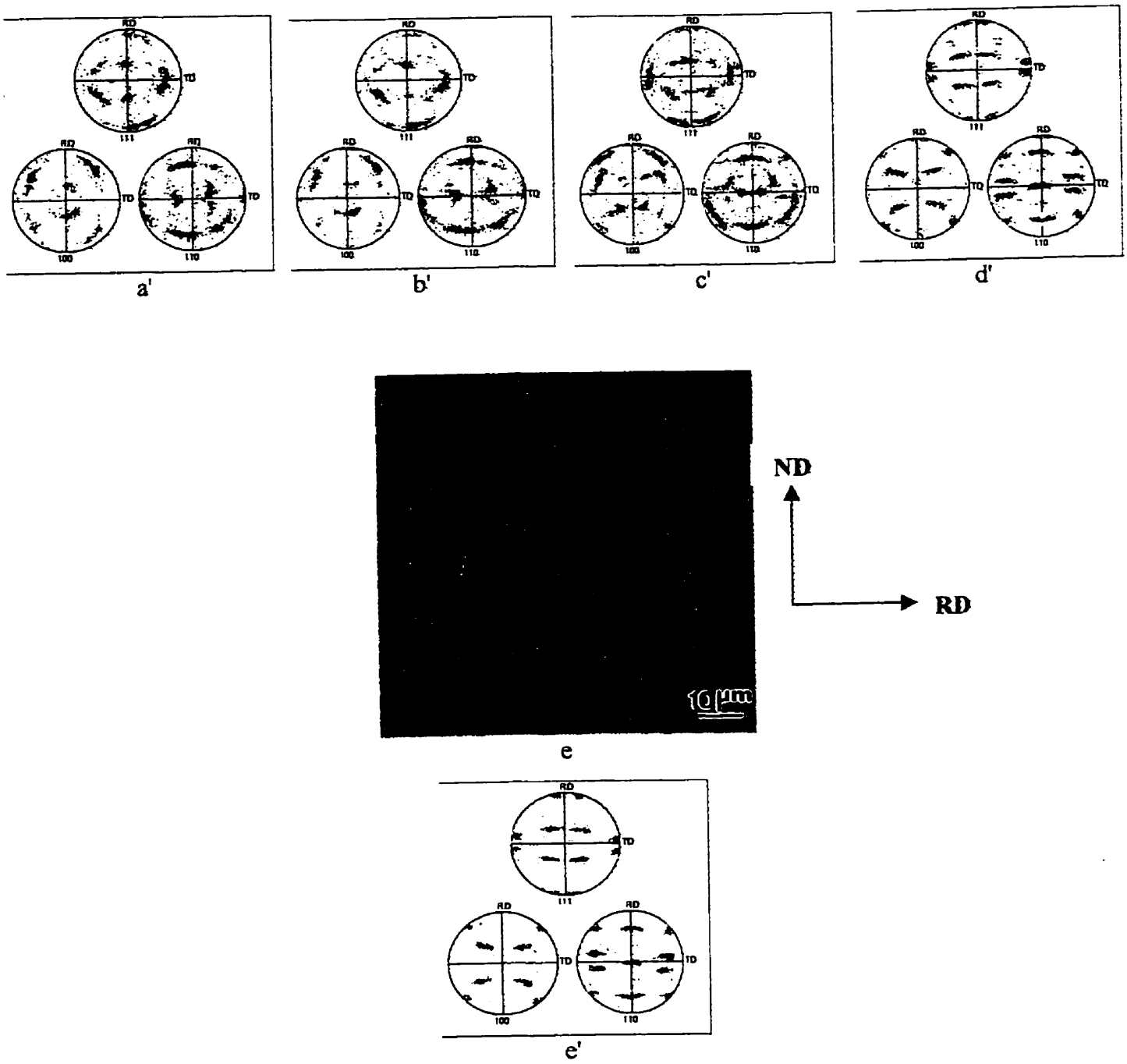

Fig.4.2.8. OIM images (a-e) and FPs (a'-e') of the material after annealing at 570℃ for 1 hour in five equally divided locations in half thickness of the sheet longitudinal section.

4.3. Tensile Behavior of the Full Thickness Sheet (sample W)

4.3.1. Stress - strain Relation

Tensile samples of the full thickness sheet, with the tensile axis parallel to the rolling direction, were deformed to failure at constant strain rates and temperatures. At each of the temperatures of 450, 500, 530, 550 and 570°C, the strain rates used were $1x10^{-4}$, $5x10^{-4}$, $1x10^{-3}$, $5x10^{-3}$, and $1x10^{-2}$/s. At 350°C they were $1x10^{-5}$, $5x10^{-5}$, $1x10^{-4}$, $5x10^{-4}$, $1x10^{-3}$. However, at two strain rates of $1x10^{-4}$ and $1x10^{-3}$, test temperature was extended to 210°C and 25°C. The combination of various test temperatures and strain rates are given in Tables.4.3.1 and 4.3.2, along with the observed values of maximum stress and % elongation.

The σ-ε curves, obtained at the constant strain rate of $1x10^{-4}$ and $1x10^{-3}$/s over the temperature range of 25°C to 570°C, are shown in Fig.4.3.1 (a) and (b), respectively. From Tables 4.3.1 and 4.3.2, and Fig.4.3.1, it is noted that at constant strain rates the flow stress decreases, whereas the ductility first increases then decreases with increasing temperature. The flow stress at the onset of plastic strain at the strain rates of $1x10^{-4}$ and $1x10^{-3}$/s were examined to determine their variation as a function of temperature. To eliminate the influence of variation in modulus (E) with temperature, the flow stresses were normalized against the value of E and plotted as a function of homologous temperature T/T_m, where T is the test temperature in K and T_m = 928K is the melting point of AA8090 Al-Li alloy [88].

Table.4.3.1. Maximum true stress (MPa) at various deformation conditions

Temperature (°C)	Strain rate (S^{-1})						
	$1x10^{-5}$	$5x10^{-5}$	$1x10^{-4}$	$5x10^{-4}$	$1x10^{-3}$	$5x10^{-3}$	$1x10^{-2}$
25			275.4		288.6		
210			140.3		180.3		
350	14.40	20.70	22.51	32.80	37.28		
450			6.66	11.11	15.30	27.52	30.31
500			3.81	8.13	11.13	19.39	24.05
530			3.49	6.76	10.45	19.31	23.10
550			3.45	6.53	8.68	15.30	18.25
570			3.45	5.90	7.59	13.33	15.50

Table.4.3.2. The maximum plastic elongation (ductility) at various deformation conditions

Temperature (°C)	Elongation [true strain / engineering strain (%)] Strain rate (S^{-1})						
	$1x10^{-5}$	$5x10^{-5}$	$1x10^{-4}$	$5x10^{-4}$	$1x10^{-3}$	$5x10^{-3}$	$1x10^{-2}$
25			0.09/ 9.4		0.08/ 8.3		
210			0.35/ 41.9		0.32/ 38		
350	1.39 / 300	0.76 / 114	0.79 / 120	0.53 / 70	0.44 / 55		
450			1.41 / 310	1.47 / 335	1.37 / 294	1.35 / 286	1.15 / 206
500			2.08 / 700	1.73 / 464	1.62 / 405	1.37 / 294	1.31 / 271
530			1.84 / 530	1.81 / 511	1.76 / 481	1.50 / 348	1.29 / 263
550			1.86 / 542	1.98 / 624	1.75 / 475	1.39 / 301	1.48 / 339
570			1.64 / 416	1.51 / 353	1.52 / 357	1.56 / 376	1.30 / 267

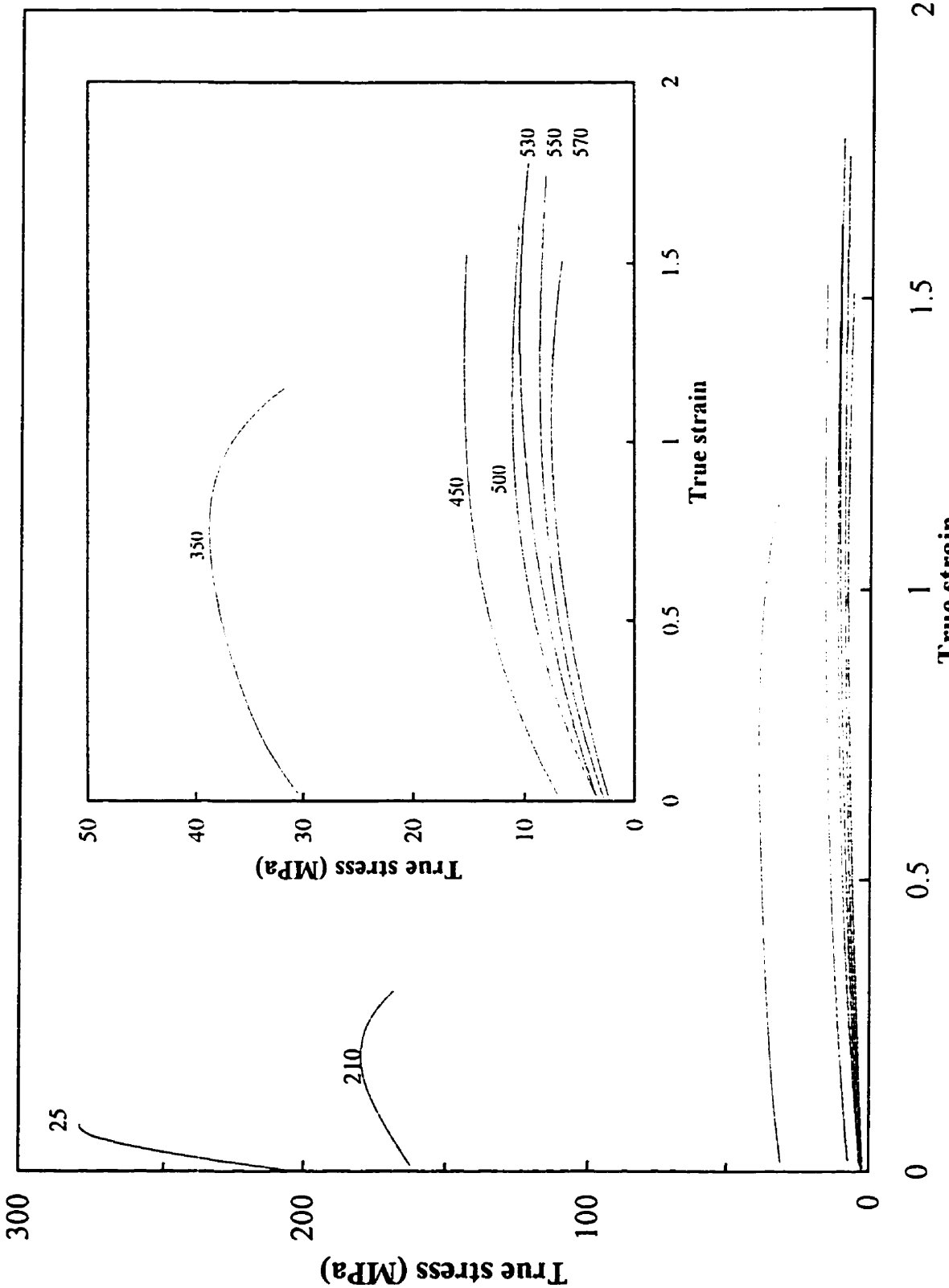

Fig.4.3.1(a). The relationship of stress-strain at temperatures from ambient to 570℃ and at a constant strain rates of $1x10^{-3}$/s.

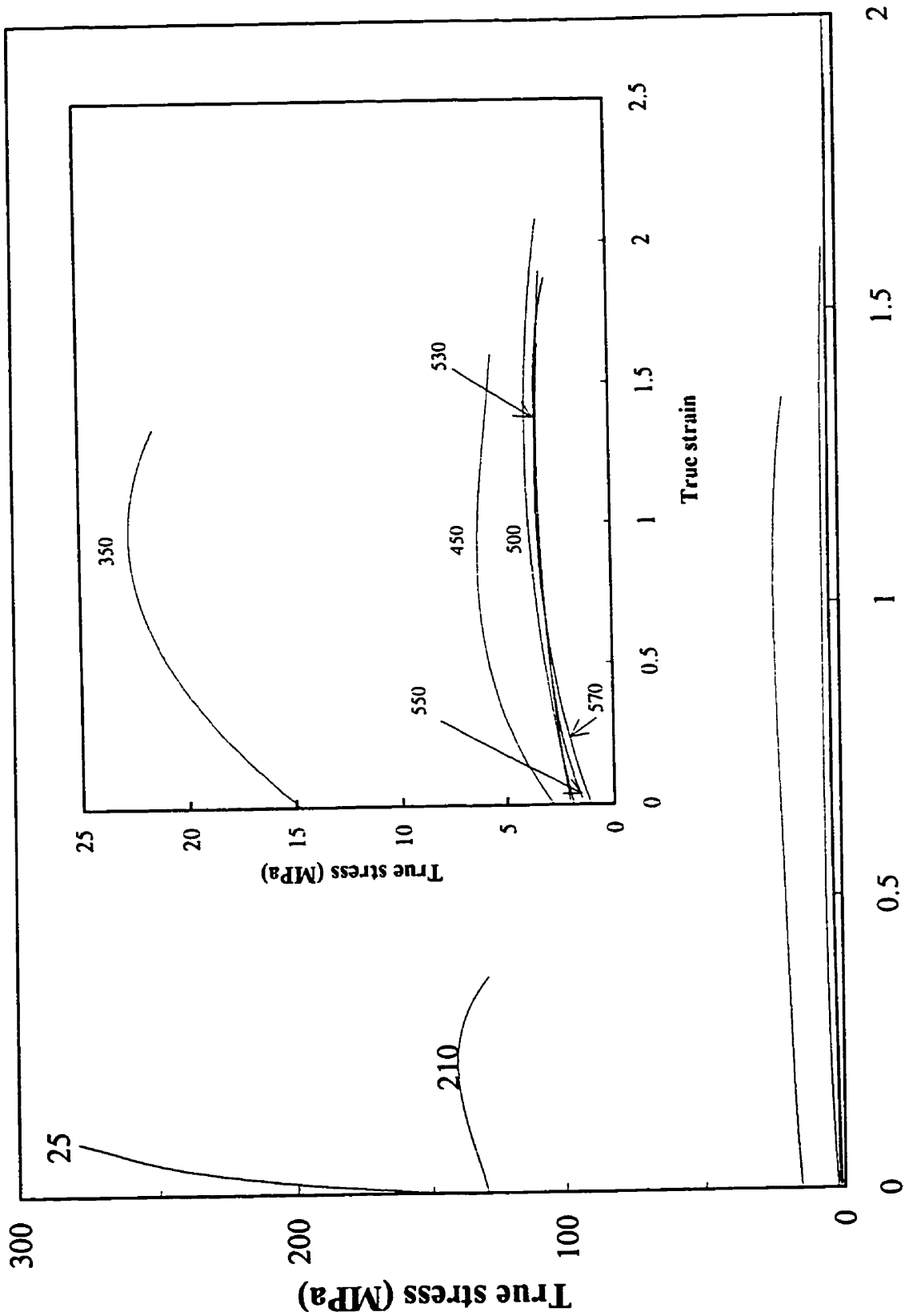

Fig.4.3.1(b). The relationship of stress-strain at temperatures from ambient to 570℃ and at constant strain rate of $1x10^{-4}$/s.

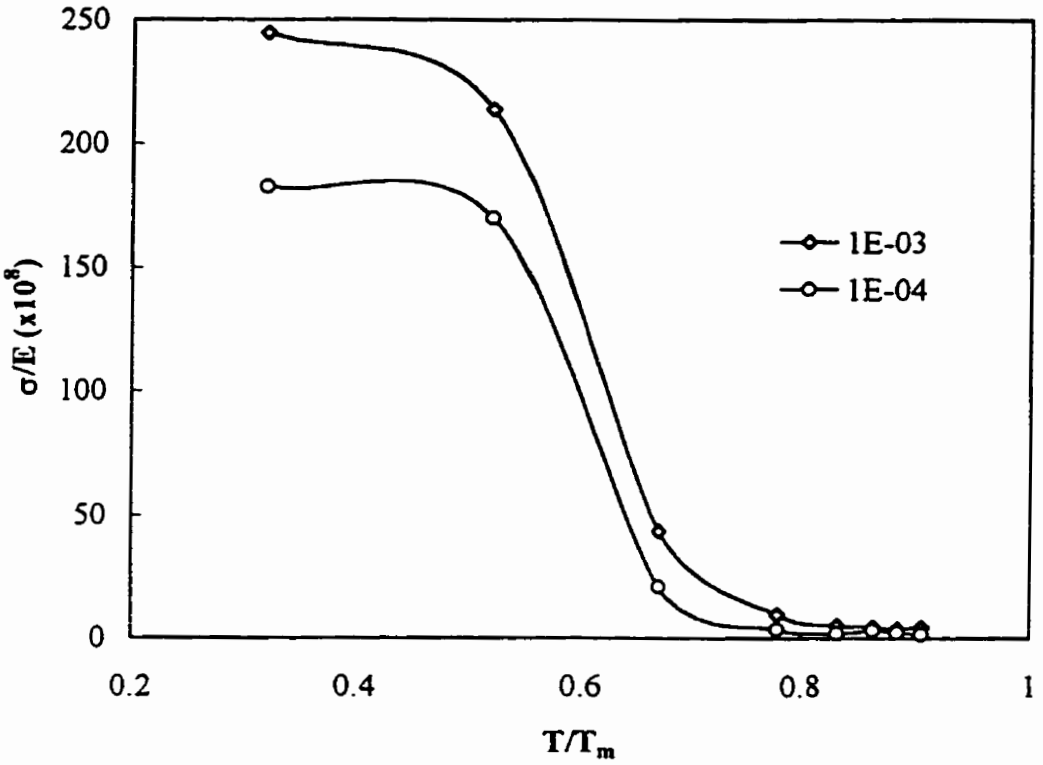

Fig.4.3.2. The relationship of normalized stress (σ/E) and temperature(T/T_m) at strain rates of $1x10^{-4}$ and $1x10^{-3}$/s, respectively.

These plots are presented in Fig.4.3.2. The values of E as a function of temperature were taken from Pu's work [26]. It was observed that these plots have two distinct athermal regions over ~ 0.3 to 0.5 T_m, and at a higher temperature above ~ 0.65 T_m the two are connected by a transition region. Over the entire temperature range the normalized stress is seen to be higher when the strain rate was higher.

Two typical sets of σ-ε curves, to illustrate the effect of strain rate on flow stress and ductility, are shown in Fig.4.3.3 at constant temperatures of 350°C (a) and 530°C (b), respectively. As is also observed in Table 4.3.2, the flow stress increases with increasing strain rate, whereas the reverse is true for the variation in ductility.

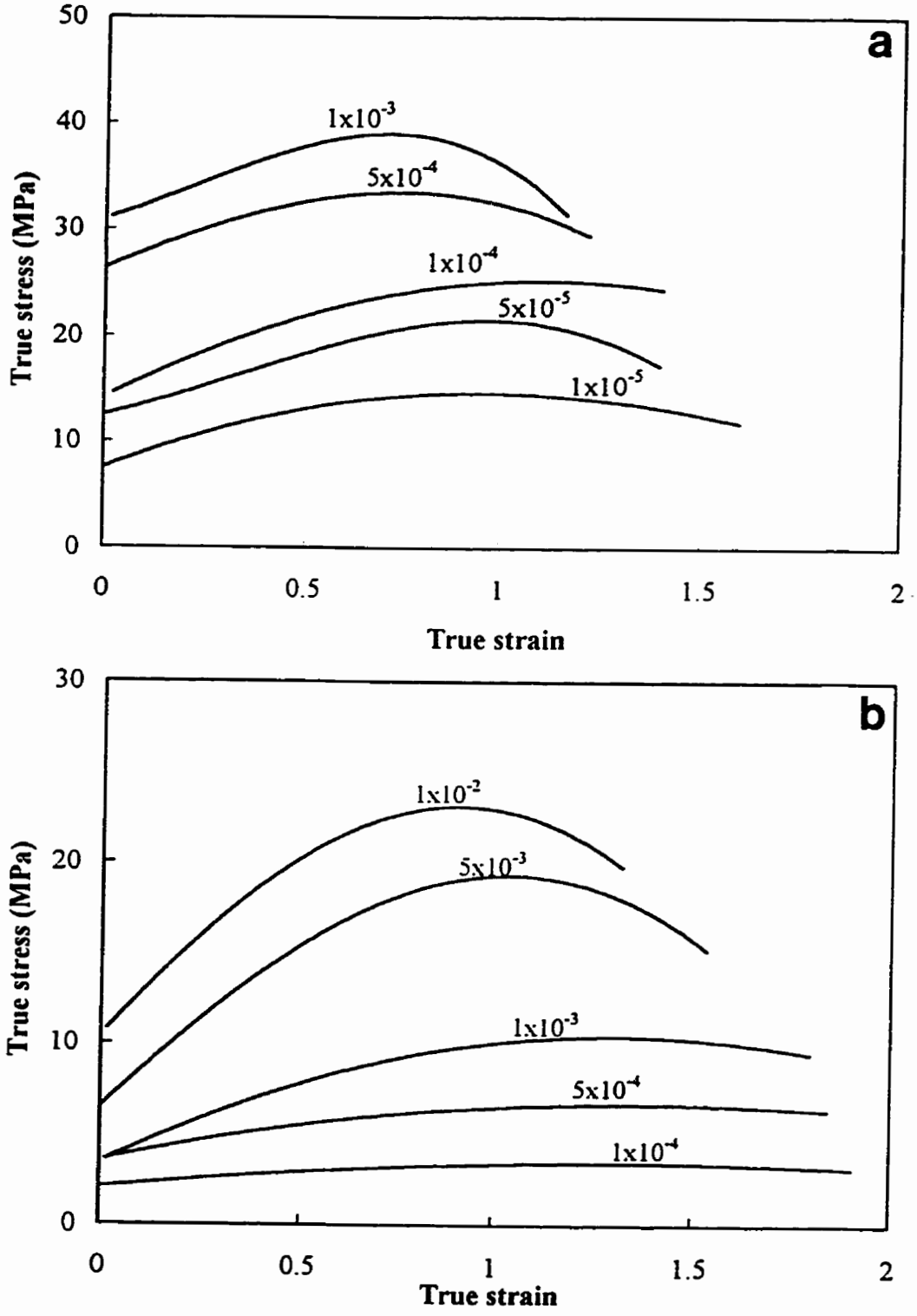

Fig.4.3.3. The relationship of stress and strain (a) at a temperature of 350℃ and a range of strain rates of $1x10^{-5}$ - $1x10^{-3}$/s, and (b) at a temperature of 530℃ and a range of strain rate of $1x10^{-4}$-$1x10^{-2}$/s.

4.3.2. Strain Hardening

The stress-strain curves presented in Figs.4.3.1, 4.3.3 show strain hardening to a varying extent. However, at higher temperatures the stress-strain curves tend to approach steady state at the strain level of ~ 0.75. When these σ-ε curves were re-plotted on a log-log scale as shown in Fig. 4.3.4, it is observed that the flow stress increases with increasing strain during the initial stage of deformation, although the increase seems larger at higher temperatures than that at lower temperatures, which is contrary to the expectation from the steady state nature of flow at elevated temperatures. In view of this, the strain-hardening behavior was analyzed and is presented next.

The σ-ε curves exhibiting conventional strain hardening can be expressed by the relationships of equation 2.3. Using this equation, the values of K'' and n_s can be determined from the log(σ) vs. log(ε) plot. The values of n_s, obtained from such plots at strain rates of $1x10^{-4}$ and $1x10^{-3}$/s and at various temperatures, are plotted as a function of temperature in Fig.4.3.5, in which four zones of strain hardening may be recognized. Zone I starts from room temperature and extends to about 300°C, in which strain-hardening exponent continuously decreases. Zone II begins approximately from about 300°C and extends to 500°C, in which the strain-hardening exponent continuously increases to a maximum value. In zone III from about 500°C to about 530°C, the strain-hardening exponent decreases. In zone IV, in the temperature range between 530°C and 570°C, strain-hardening exponent is seen to increase again.

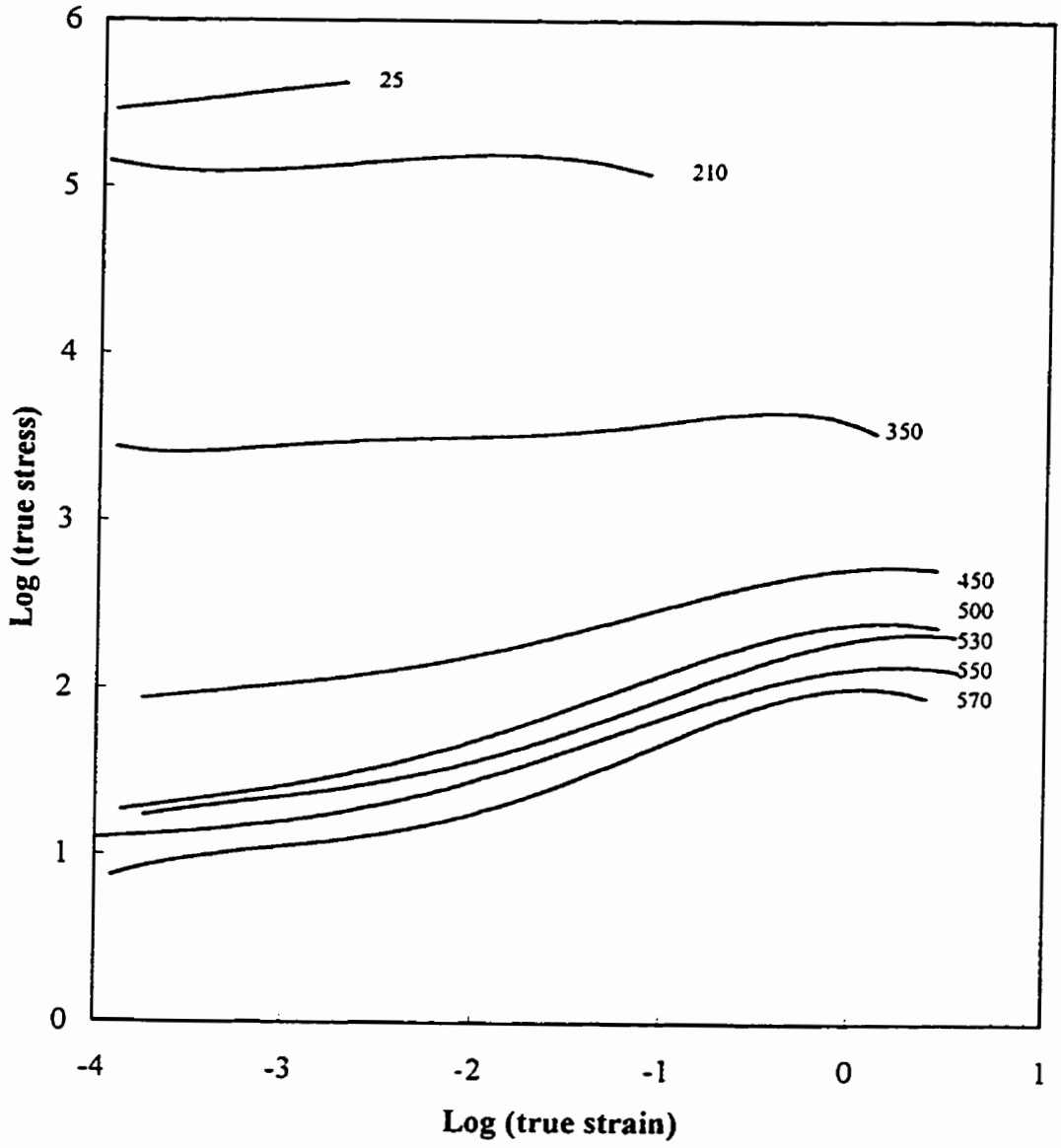

Fig.4.3.4. The relationship of stress and strain in natural log scale at a constant strain rate of $1x10^{-3}$/s and at a range of temperatures from ambient to 570℃.

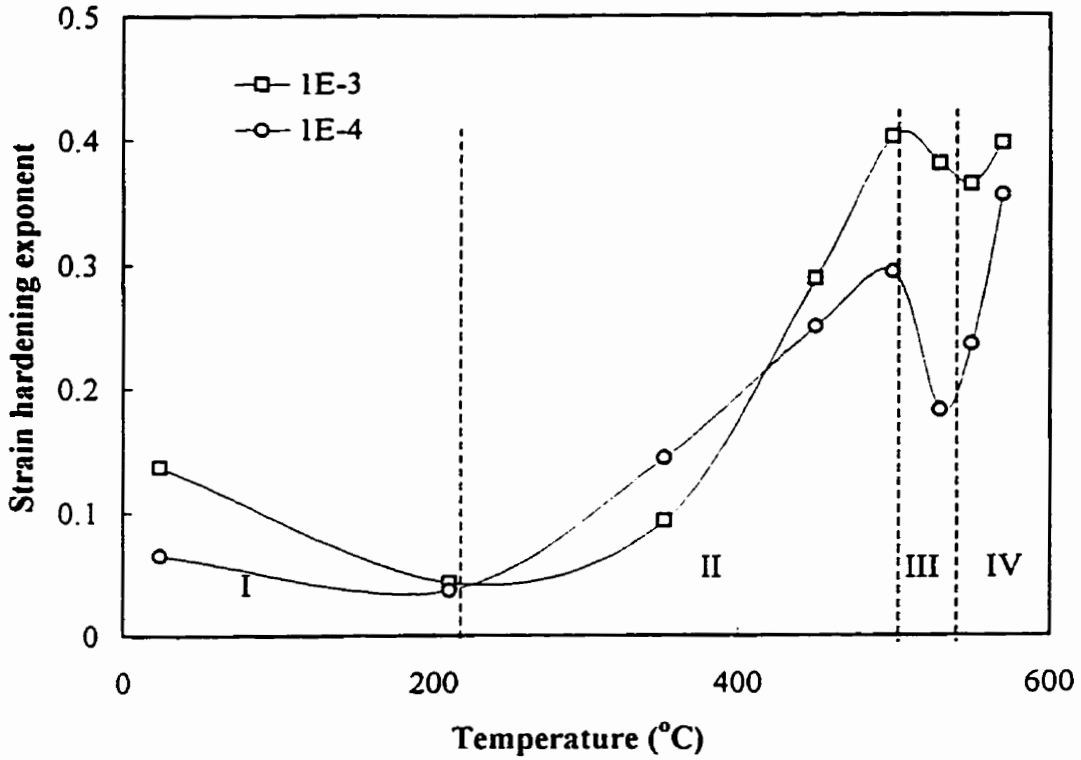

Fig.4.3.5. Changes in strain hardening exponent, (n_ε), with temperature from ambient to 570°C, at constant strain rates of $1x10^{-4}$ and $1x10^{-3}$/s, respectively.

4.3.3. Strain Rate Sensitivity Index (m)

At constant temperature and constant strain, the stress is related to the strain rate by the equation 2.4. A log(σ) vs. log($\dot{\varepsilon}$) plot is usually linear and its slope yields the value of m. Fig.4.3.6 (a) shows a set of log(σ) vs. log($\dot{\varepsilon}$) plots at strains of ε =0.3, 0.5, 0.7 and 0.9 obtained at 500°C at strain rate in a range of $1x10^{-4}$ and $1x10^{-2}$/s. At strain levels smaller than about 0.9, all the plots are observed to be linear having similar slopes. However, when the strains are greater than 0.9, the plots deviate from linearity on both sides of high and low strain rates. This is expected due to the changes in microstructure of the material following deformation, necking at high strain rates and formation of cavities at lower strain rates (see Fig4.4.4 in the next section).

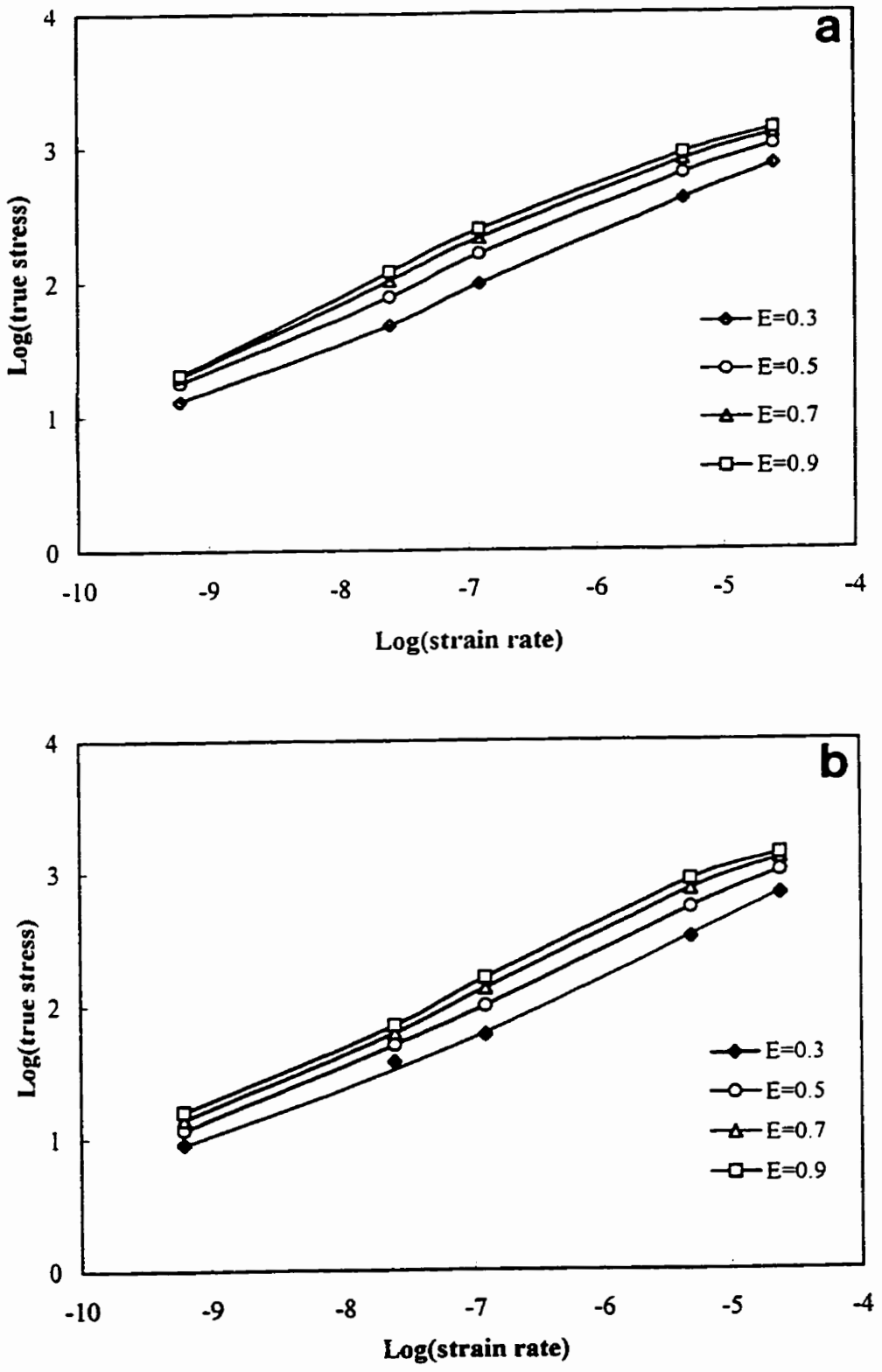

Fig.4.3.6. The relationship of stress and strain rate in natural log scale for different strain levels at temperatures of (a) 500℃ and (b) 530℃.

The same trend was observed at all other temperatures, as shown by the plots at 530°C in the same strain rate range of $1x10^{-4}$ and $1x10^{-2}$/s (Fig.4.3.6 (b)). Therefore, a strain of ε =0.7 was chosen to generate the log(σ) vs. log($\dot{\varepsilon}$) plots for all the deformation conditions. Fig.4.3.7 shows the log(σ) vs. log($\dot{\varepsilon}$) plots at the strain of ε = 0.7 for temperatures ranging from 350°C to 570°C. By least square curve fitting method, the slopes of the plots shown in Fig.4.3.7 were determined which are the values of the strain rate sensitivity at the testing temperature. Fig.4.3.8 shows the variation in strain rate sensitivity with temperature. The maximum value of m of about 0.5 was found at the temperature of around 500°C to 530°C.

The m values were also determined by strain rate change tests. In this test, the tensile test was first conducted at a strain rate of $\dot{\varepsilon}_1$ to a stress σ_1, which represents the stress for plastic flow, and then the strain rate was suddenly increased to strain rate $\dot{\varepsilon}_2$ which resulted in an increase in the flow stress to σ_2. From the following equation 4.3.1, the strain rate sensitivity was derived.

$$m = \log(\sigma_1 / \sigma_2) / \log(\dot{\varepsilon}_1 / \dot{\varepsilon}_2) \qquad (4.3.1)$$

For the test at 350°C, the strain rate $\dot{\varepsilon}_1$ was $1x10^{-4}$/s and the strain rate $\dot{\varepsilon}_2$ was $2x10^{-4}$/s. For the test at all other temperatures, the strain rate $\dot{\varepsilon}_1$ was $1x10^{-3}$/s and the strain rate $\dot{\varepsilon}_2$ was $2x10^{-3}$/s. The values of strain rate sensitivities obtained by this method are given in Fig.4.3.9(a), which also shows that the maximum value of 0.5 occurred at the temperature of about 530°C, very similar to that shown in Fig.4.3.8. Fig.4.3.9 (b) shows the change in ductility at the same deformation condition (Table 4.3.2). It is seen that the maximum ductility corresponds to the maximum value of m. (It is noted here that the m values obtained by both methods were apparent values because of grain growth during deformation.)

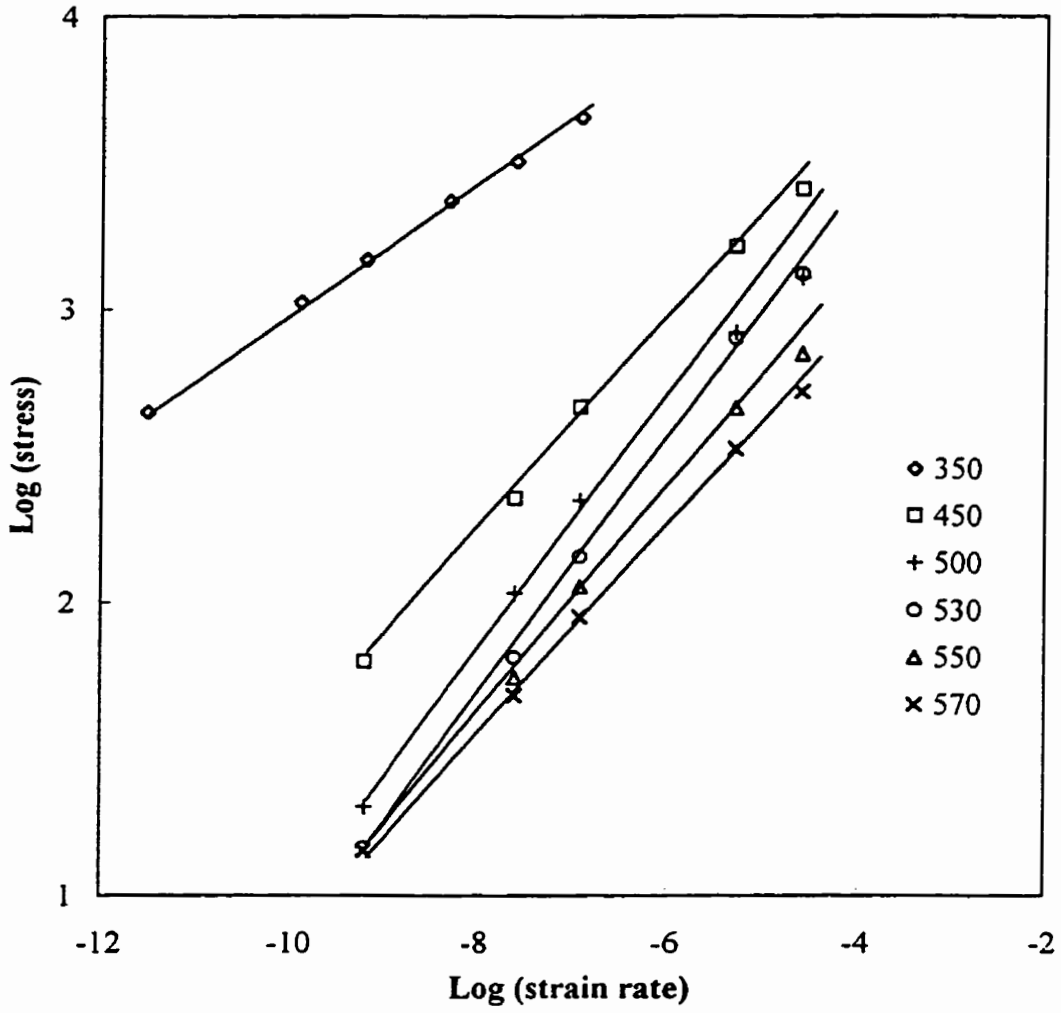

Fig.4.3.7. The relationship of stress and strain rate in log/log scale for a same strain level of 0.7 at a temperature range of 350 - 570℃.

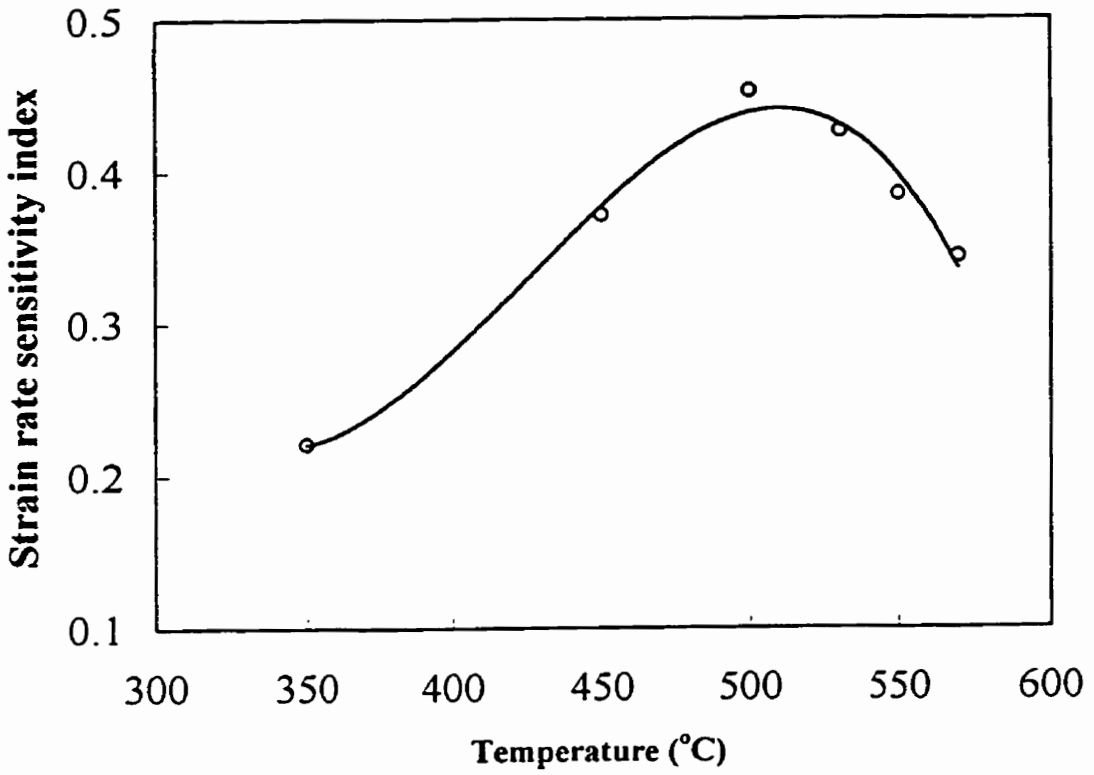

Fig.4.3.8. Changes of strain rate sensitivity index with temperature by data analysis.

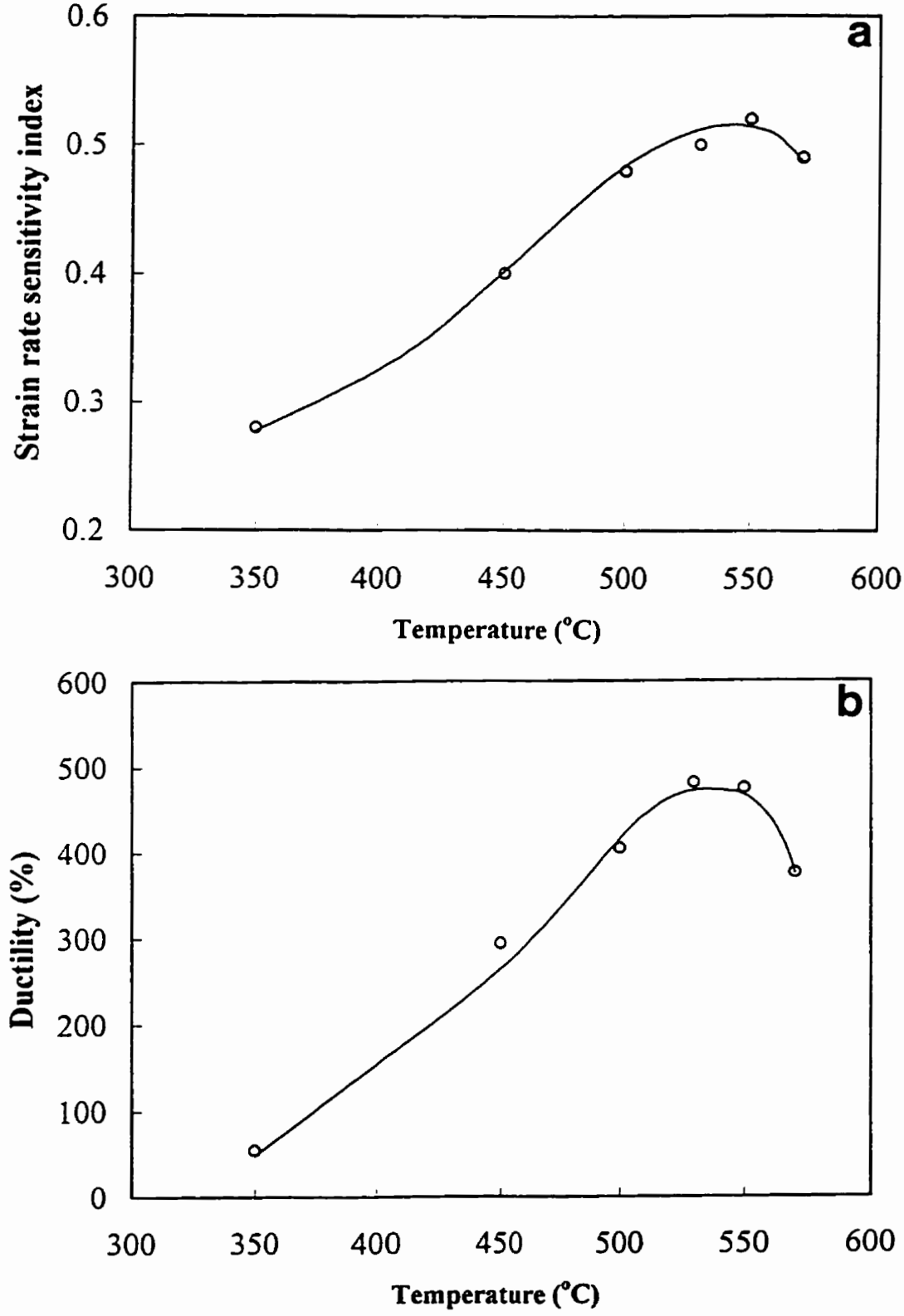

Fig.4.3.9. (a) Changes of strain rate sensitivity index with temperature by strain rate change test, and (b) maximum ductility.

4.3.4. Activation Energy (Q) for Superplastic Deformation

Activation energy for superplastic deformation was calculated by employing the following equations [38]

$$Q_a = nR\left[\frac{\partial \ln(\sigma)}{\partial(1/T)}\right]_{\dot{\varepsilon}} \qquad (4.3.2)$$

$$Q_t = R\left[\frac{\partial \ln(\sigma^n / TE^{n-1})}{\partial(1/T)}\right]_{\dot{\varepsilon}} \qquad (4.3.3)$$

where Q_a is the apparent activation energy, Q_t is the true activation energy, and as defined earlier in equation (2.5), n =1/m is the stress exponent, E is Young's modulus, T is the absolute temperature and R is the gas constant. The activation energies were calculated at selected strain levels and strain rates. For this purpose, the average value of n was taken from the data at different temperatures. The value of Q_a at the strain rate of $1x10^{-3}$/s, for example, was calculated to be 88.2 kJ/mol at strain = 0.3 and 78.3 kJ/mol at strain = 0.7, respectively. However, Q_a (at strain = 0.3) was found to increase to 110 kJ/mol with an increase in strain rate to $1x10^{-2}$/s.

True activation energy Q_t was also determined at various strain levels and strain rates. At the strain rate of $1x10^{-3}$/s, the value of Q_t was found to be 90.7 and 76.9 kJ/mol at the strain levels of 0.3 and 0.7, respectively. Thus, the average value of true activation energy was estimated to be ~ 83.8 kJ/mol.

4.3.5. Effect of Specimen Orientation on Tensile Behavior

(Samples W0, W30, W45, W60 and W90)

In order to examine the tensile anisotropy of the sheet material used in this investigation, test samples were prepared with angles, between tensile axis and the original rolling direction of the sheet, of 0°, 30°, 45°, 60° and 90°. As described in Chapter 3 and shown in Fig.3.1, these samples were designated W0, W30, W45, W60 and W90, respectively. The tensile tests were conducted under the optimum superplastic condition at the constant strain rate of $1x\ 10^{-3}$/s and at the temperature of 530°C. The stress-strain curves are presented in Fig.4.3.10. The figure shows the anisotropic behavior but does not suggest it to be very significant.

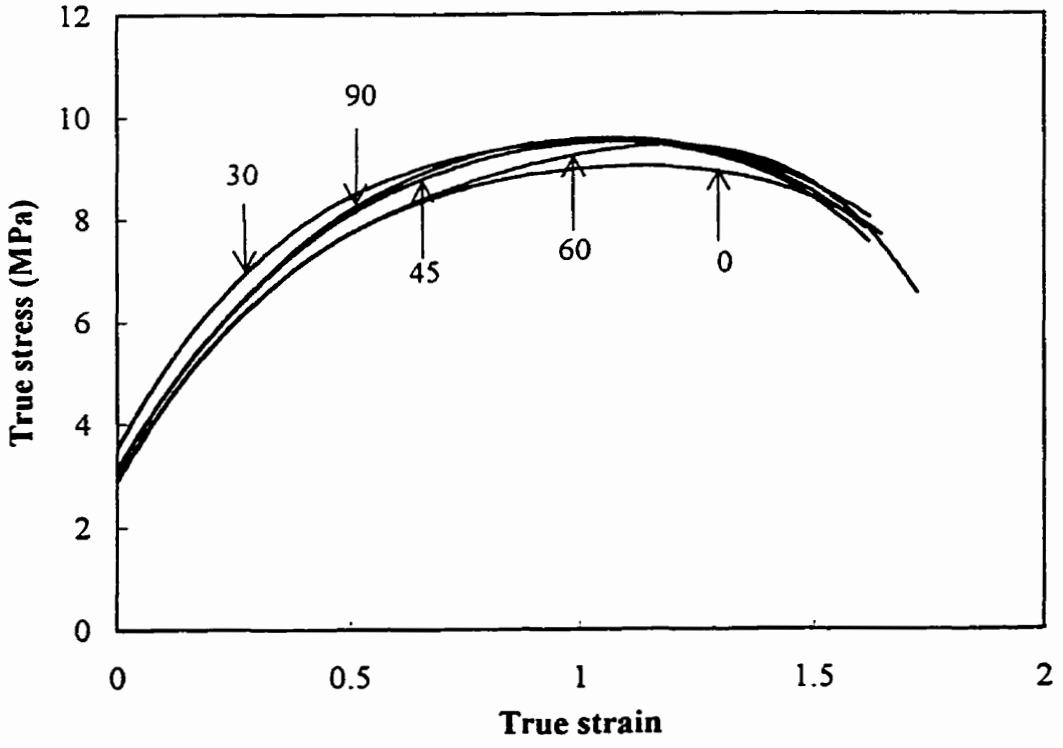

Fig.4.3.10. The relationship of stress and strain of samples with different orientations (0, 30, 45, 60 and 90°) between the tensile axis and the sheet original rolling direction.

4.4. Microstructural Evolution during Deformation of Full Thickness Sheet Material (W)

4.4.1. Grain Size and Shape

The grain size (d) of the tensile specimens was followed as a function of strain by terminating the tensile tests at the designated strain levels. All the measurements were made at the same strain rate of $1x10^{-3}$/s. The grain size in specimens tested at room temperature, 200°C and 350°C could not be measured accurately, as the grain boundaries were not clearly visible under optical microscope. However, the OIM examination of specimen tested at 350°C quantitatively indicated a small increase in the average grain size. The grain sizes in specimens tested between 450°C and 570°C could be measured reasonable easily. The 20 minutes of soaking time provided to specimens at the beginning of the tensile tests at these temperatures also made it possible for the grain boundaries to be revealed clearly by optical metallography.

Figure 4.4.1 (a-d) shows a series of optical micrographs taken from the center of the longitudinal section of samples deformed at 530°C and at the strain rate of $1x10^{-3}$/s to $\varepsilon = 0$, 0.5, 1.0 and 1.75. It is seen that along with grain growth grain shape also changes from the initially elongated to nearly equiaxed as shown in Fig.4.4.1(e). The elongated grains become almost equiaxed at a strain of about 1.0.

Figure 4.4.2 gives the plot of average grain size as a function of strain after deformation at the same strain rate of $1x10^{-3}$/s, but at different temperatures. It is seen that the average grain size increases with increasing strain, and also with an increase in temperature.

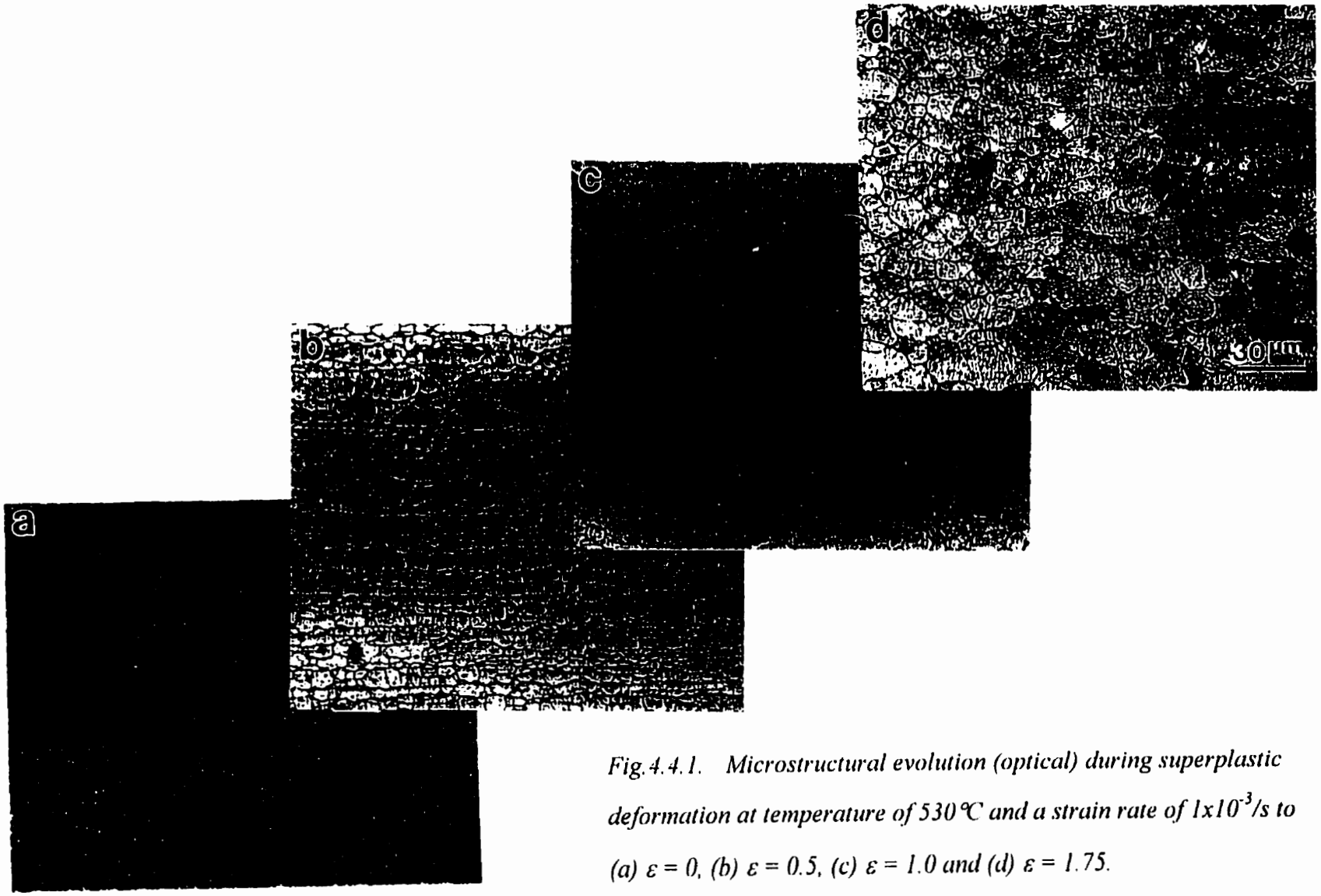

Fig.4.4.1. Microstructural evolution (optical) during superplastic deformation at temperature of 530℃ and a strain rate of $1x10^{-3}$/s to (a) $\varepsilon = 0$, (b) $\varepsilon = 0.5$, (c) $\varepsilon = 1.0$ and (d) $\varepsilon = 1.75$.

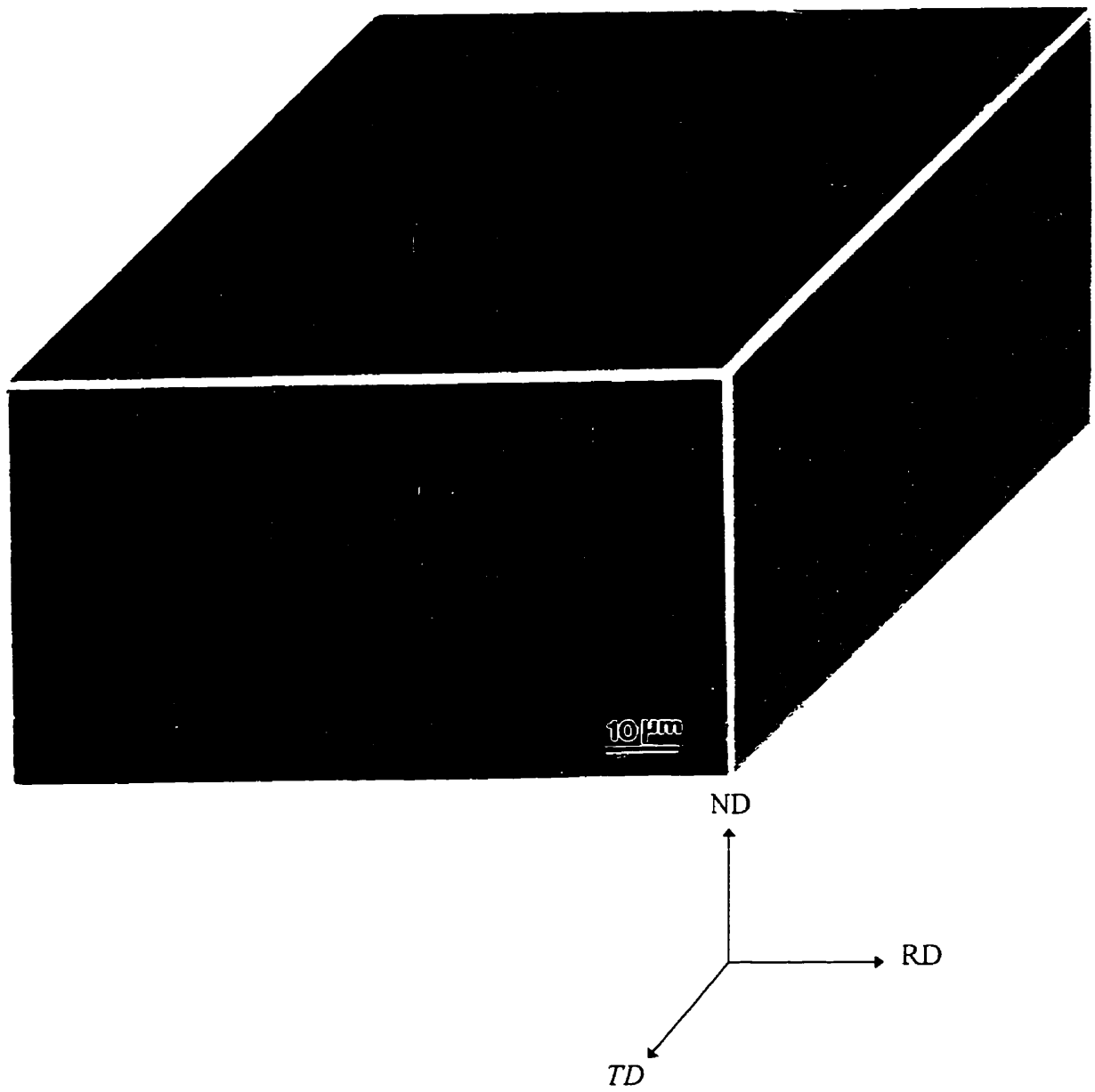

Fig.4.4.1(e). Three-dimensional microstructure (optical) of the sample deformed to $\varepsilon = 1.75$ at temperature of 530 ℃ and a strain rate of $1x10^{-3}/s$.

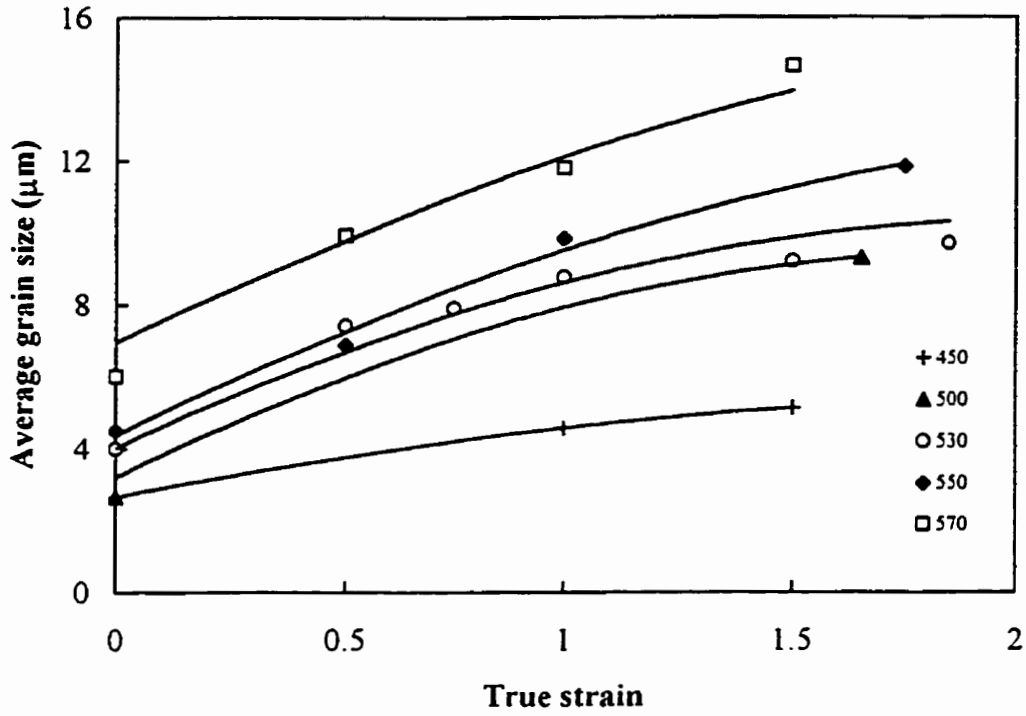

Fig.4.4.2. Grain growth represented by average grain size during deformation at a constant strain rate of $1x10^{-3}$/s and at various temperatures.

The variation in grain size as a function of strain is found to follow a relationship of the type:

$$d = K_d \varepsilon^q \qquad (4.4.1)$$

Here the proportionality constant K_d and the exponent q were calculated form the plots of ln(d) vs. Ln(ε), and these values at various temperatures are presented in Table.4.4.1.

Table 4.4.1. Values of K_d and q according to $d = K_d \varepsilon^q$ during SPD at $\dot{\varepsilon} = 1x10^{-3}$/s

Temperature (°C)	K_d value (μm)	q value
450	1.52	0.28
530	2.15	0.21
550	2.25	0.44
570	2.52	0.34

The increase in grain size could be due to two factors: (i) the increase that occurred in the absence of strain because of holding the sample at the test temperature, which may be denoted as static grain growth, (ii) the increase over this static value induced by the imposed strain and termed dynamic grain growth. The static grain growth was determined by measuring the grain size in the grip section of the deformed samples. Fig.4.4.3 shows the variation in grain size as a function of temperature in the grip and gage sections, respectively, upon straining to ε =1.0 at the strain rate of $1x10^{-3}$/s. Also included in the figure are (i) the grain sizes attained during heating to and soaking at the test temperatures prior to straining (represented by "start"), (ii) the difference between the grain sizes in the grip section and that prior to straining (represented by "static GG"), and (iii) the difference between the grain sizes in the gage section and the corresponding grip section (represented "dynamic GG"). A comparison of various curves in Fig. 4.4.3 shows that all of them exhibit a similar trend.

4.4.2. Cavities

Samples deformed at the temperature of 530°C and the strain rate of $1x10^{-3}$/s, were examined by SEM for cavities which were generated during deformation. Typical features of cavities at ε = 0.5, 0.75 and 1.0 are shown in Fig.4.4.4 (a-c). Very few cavities are seen in the sample deformed to ε = 0.5, but their size and number are seen to increase with further strain. These cavities are predominantly present at triple points but some are also seen along the grain boundaries.

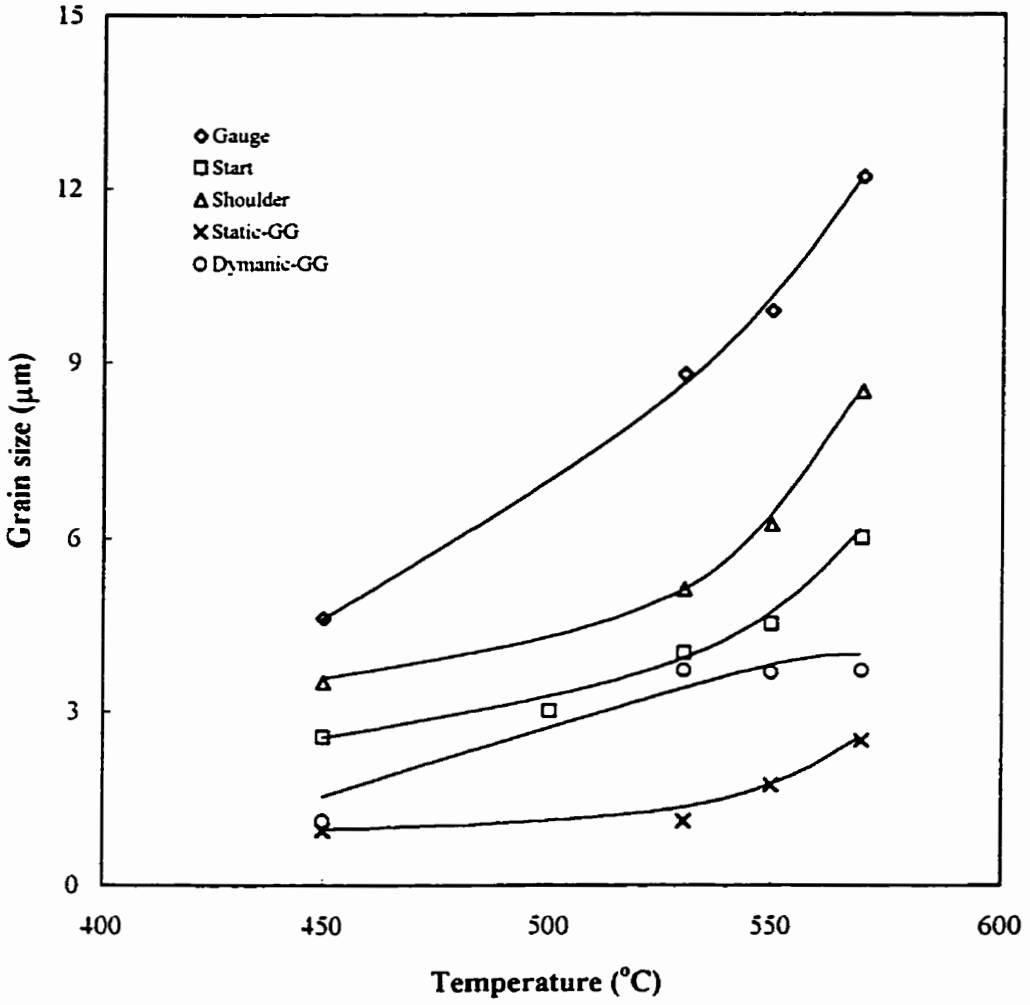

Fig.4.4.3. Grain growth in samples deformed to a same strain level of 1.0, at a constant strain rate of $1x10^{-3}$/s and at various temperatures.

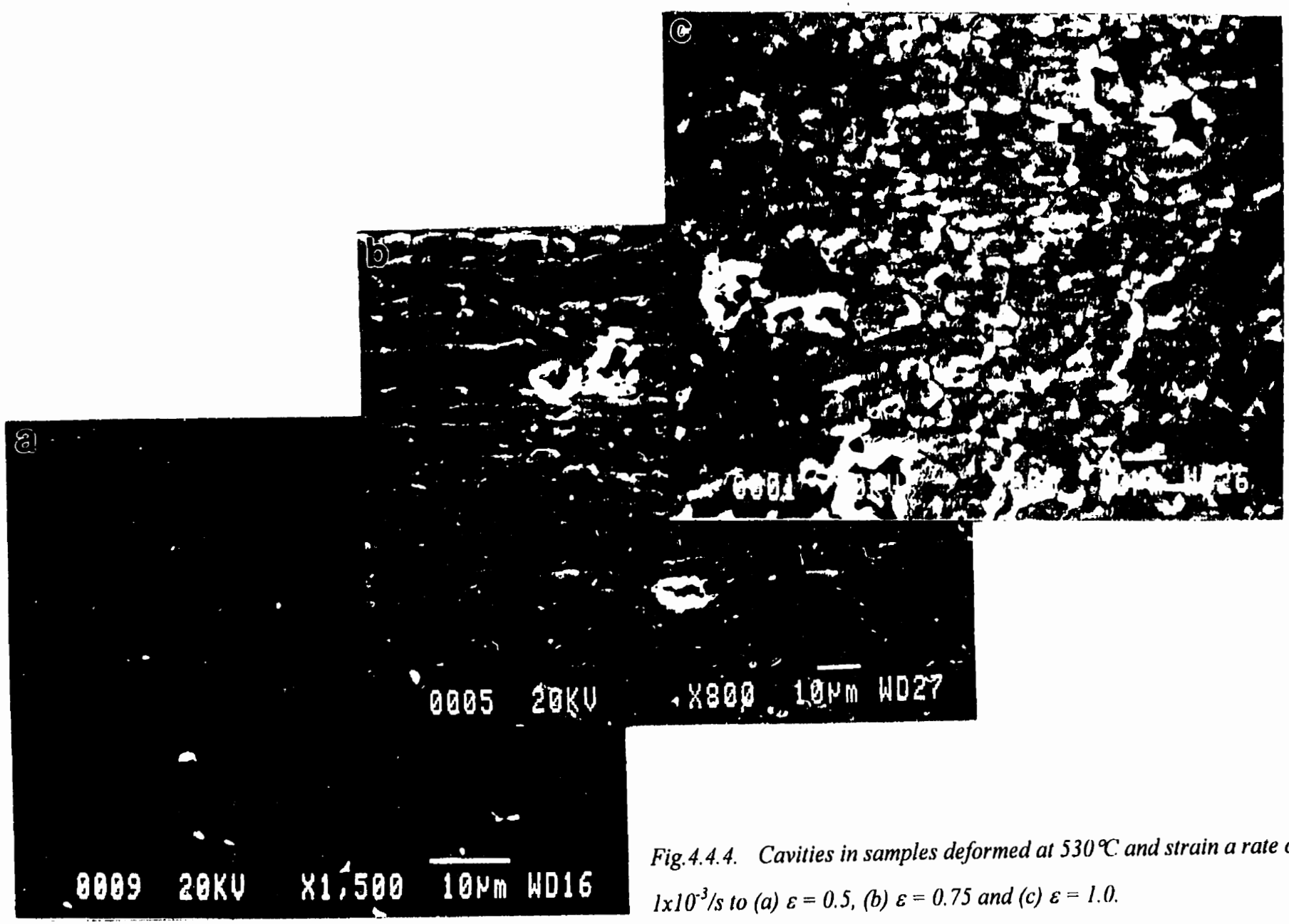

Fig.4.4.4. Cavities in samples deformed at 530℃ and strain a rate of $1x10^{-3}/s$ to (a) $\varepsilon = 0.5$, (b) $\varepsilon = 0.75$ and (c) $\varepsilon = 1.0$.

4.4.3. Precipitates and Dislocations

TEM observations were carried out on samples deformed at the same strain rate of $1x10^{-3}/s$ but at temperatures of 350°C, 500°C, 530°C and 570°C. All the samples were deformed to the same strain of $\varepsilon = 0.5$, and quenched by the in-situ quenching facility attached to the Instron testing machine (see Chapter 3). Thin foils of the center layer material were made by using the same technique as was used for making thin foils from the as-received and annealed materials. The normal of such thin foils was parallel to ND of the sheet. At the temperature of 350°C, T_2, β', Si-rich and Fe-rich phases were observed. A typical TEM microstructure is shown in Fig.4.4.5.

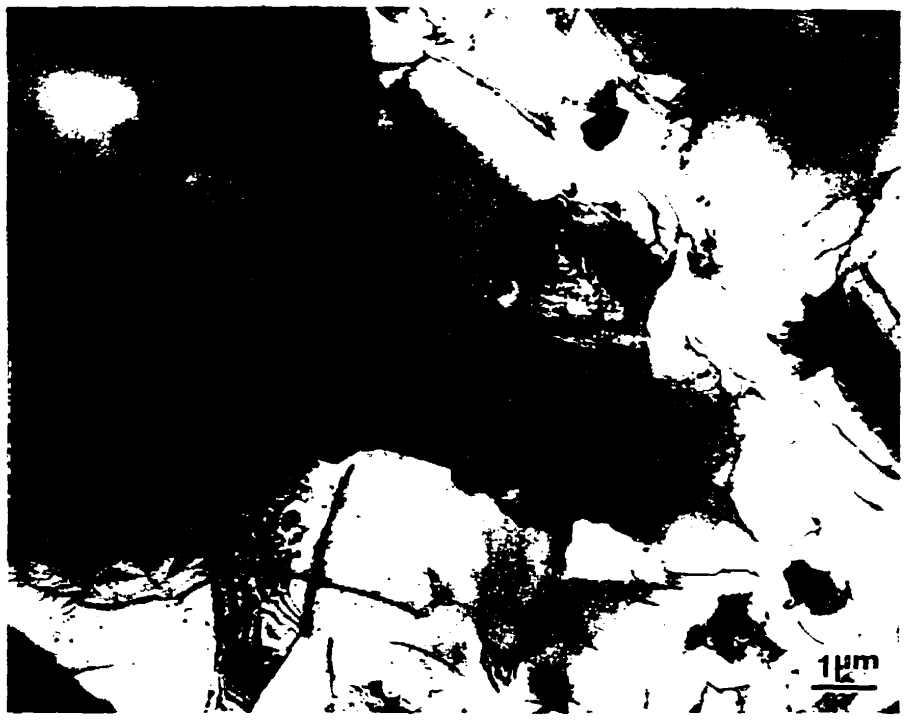

Fig.4.4.5. Precipitates in a sample deformed to strain of 0.5 at 350℃ and a strain rate of $1x10^{-3}/s$, marked by A is the Si-rich phase, B is the T_2 phase. and the little sports are β' phases.

However, when the testing temperature was higher than 500°C, T_2 phase was found to have dissolved, but β′, the Si-rich and Fe-rich phases were still present. Figure.4.4.6 was taken from the gage section of the sample deformed at 570°C. It shows β′ precipitates associated with dislocations, and a few Fe-rich precipitates are also observed. Dislocations, dislocation networks and dislocation tracks were observed not only in all the gage sections but also in the grip sections of the deformed samples. Figure 4.4.7 (a) gives an example of substructures developed in the gage section upon deformation at the temperature of 500°C. Calculation of thermal strain produced by the fast quenching indicated that a thermal shrinkage about 1.2% will be introduced in the quenched sample. This may be the reason that dislocations were observed in the grip section of the deformed sample which did not undergo tensile deformation. Therefore, it is difficult to achieve the goal of obtaining reliable direct experimental information about the role of dislocations during superplastic deformation at this time.

4.4.4. Effect of Strain, Strain Rate and Temperature on Textural Evolution

The variation in texture as a function of strain, temperature and strain rate was measured by OIM. All the measurements were made in the longitudinal section of the full thickness samples. In each of the samples the surface layer and the center layer were measured separately. The results of texture measurement made on the samples of the individual surface and the center materials will be given in next section (4.5).

Fig.4.4.6. Fe-rich phases at grain boundary in a sample deformed to strain of 0.5 at 570℃ and a strain rate of $1x10^{-3}$/s.

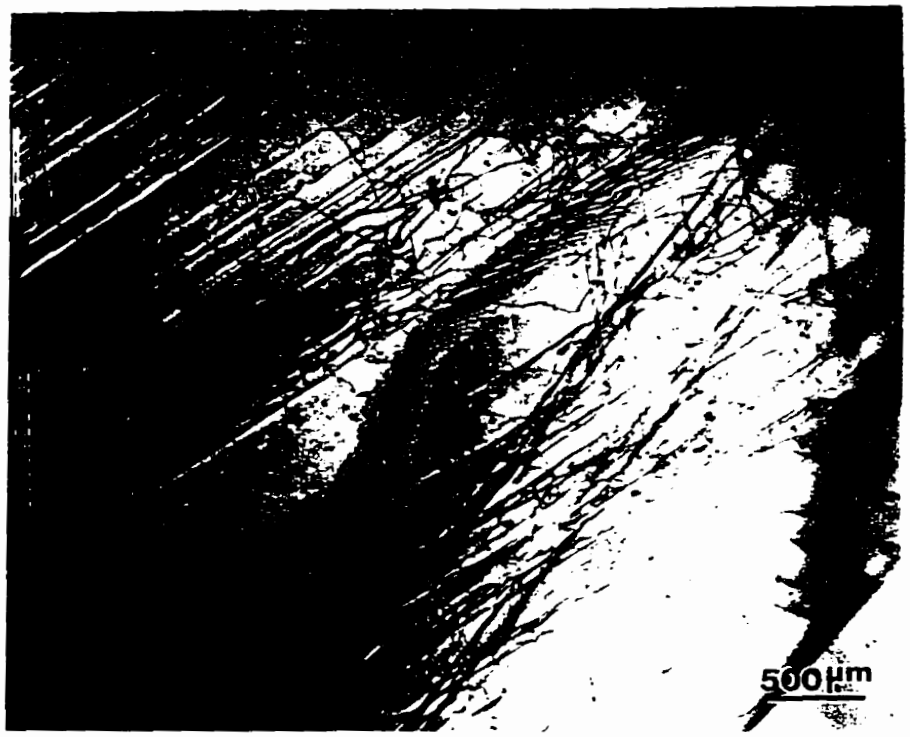

Fig.4.4.7. Dislocations, dislocation networks, and tracks in a sample deformed to strain of 0.5 at 500℃ and a strain rate of $1x10^{-3}$/s.

Figure 4.4.8A shows the stress and strain curve at 530°C and at the strain rate of $1x10^{-3}$/s. Fig.4.4.8B gives a series of OIM images and corresponding PFs from center layer of the samples deformed to $\varepsilon = 0.5$, 0.75, 1.0, 1.25, 1.5 and 1.75, respectively, which are marked a, b, c, d, e and f in the stress-strain curve shown in Fig.4.4.8A. As observed before, the grain size continuously increased and the grain shape gradually changed from the initially elongated to nearly equiaxed. Such transition in grain shape appears to have occurred between $\varepsilon = 0.75$ and $\varepsilon = 1.0$. It is also seen that the texture weakened continuously during the deformation to a nearly random orientation. As well, the transition from preferred orientation to random seems to have occurred between $\varepsilon = 0.75$ and $\varepsilon = 1.0$ where the PFs tended to become diffused.

The contour PFs corresponding to the discrete PFs in Fig.4.4.8B are given in Fig.4.4.9. It is seen that the separate intensity contours of the pole positions tend to overlap with increasing strain. By comparing the intensities of these PFs, the transition from textured to randomly oriented states may be considered to occur at strains between $\varepsilon = 0.75$ and $\varepsilon = 1.0$. Fig.4.4.10 shows the grain misorientation distribution as a function of strain from the same set of data as that shown in Fig.4.4.8. It is noted that at $\varepsilon = 0$, where the texture is strong, a large number of grains having small misorientation or low angle grain boundary are present. This is the characteristic of a textured material. The increase in grain misorientation with increase in strain implies that low angle grain boundaries showing small misorientation have evolved to high angle grain boundaries showing large misorientation. It is this evolution that results in the texture weakening. Figure.4.4.10 also shows that significant change of grain

misorientation have occurred at about ε = 1.0. Thus, both microstructural characteristics and grain misorientation features suggest that the texture tended to be randomized around ε = 1.0. All the texture characteristics found in the center layer were also observed in the surface layer. Fig.4.4.11 shows the continuous texture weakening in the surface layer. The trend of texture weakening exhibited by both the center and the surface layers is shown more clearly in Fig.4.4.12, where the maximum intensities of PFs obtained from PFs shown in Fig.4.4.9 and 4.4.11 are plotted against the strain.

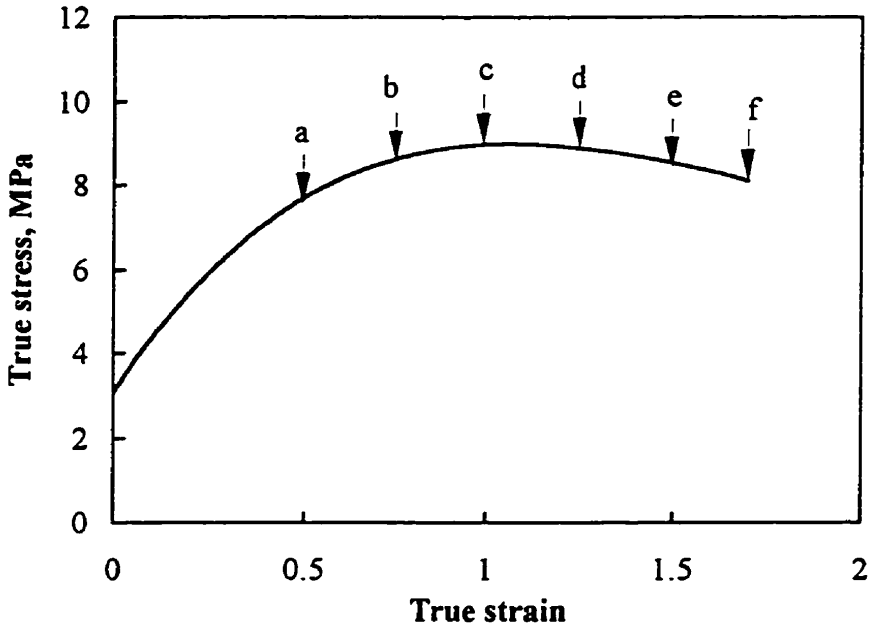

Fig.4.4.8A. The stress-strain curve at the optimum superplastic condition of 530℃ and the strain rate of $1x10^{-3}$/s.

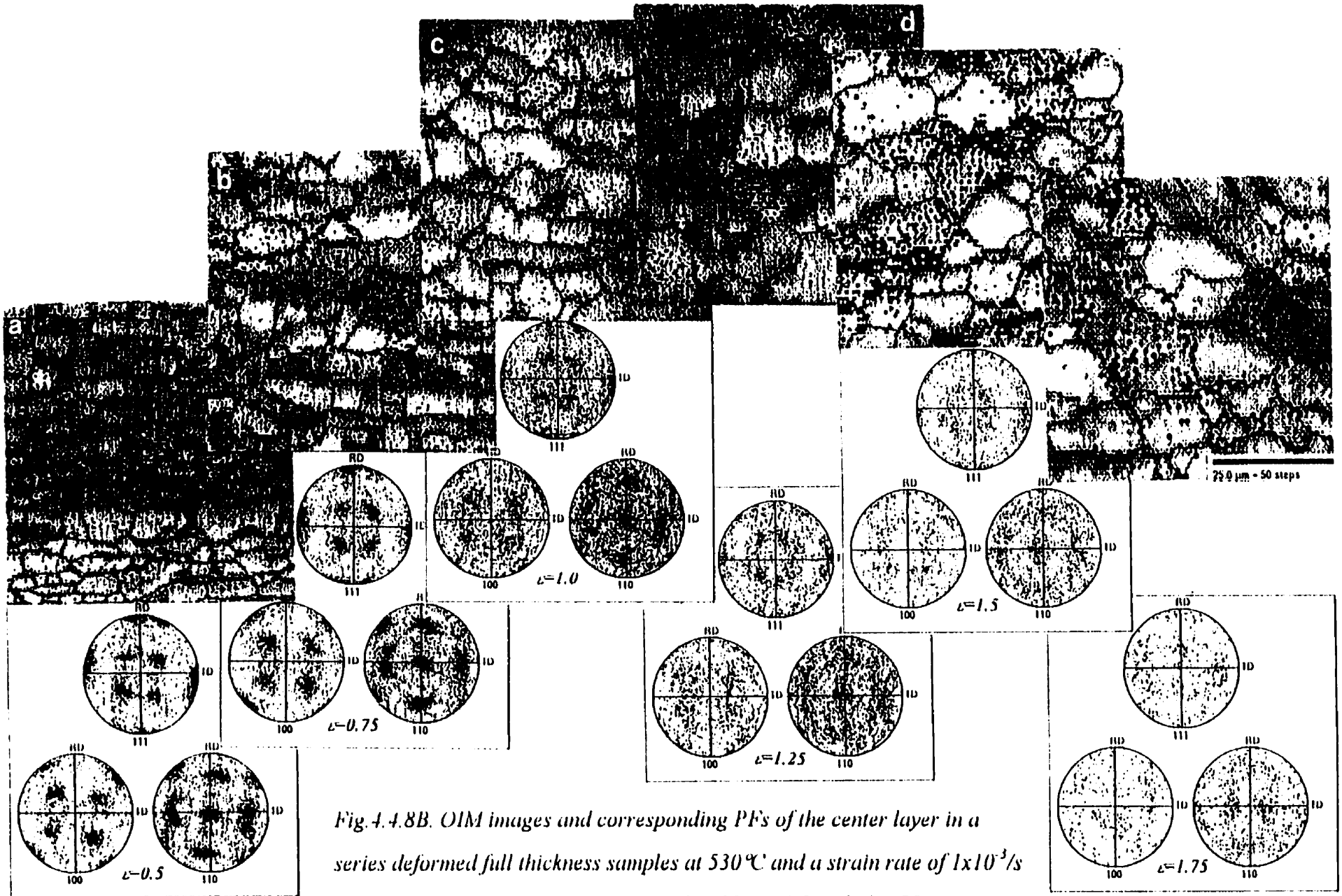

Fig.4.4.8B. OIM images and corresponding PFs of the center layer in a series deformed full thickness samples at 530℃ and a strain rate of $1x10^{-3}$/s to strains of (a) 0.5, (b) 0.75, (c) 1.0, (d) 1.25, (e) 1.5 and (f) 1.75.

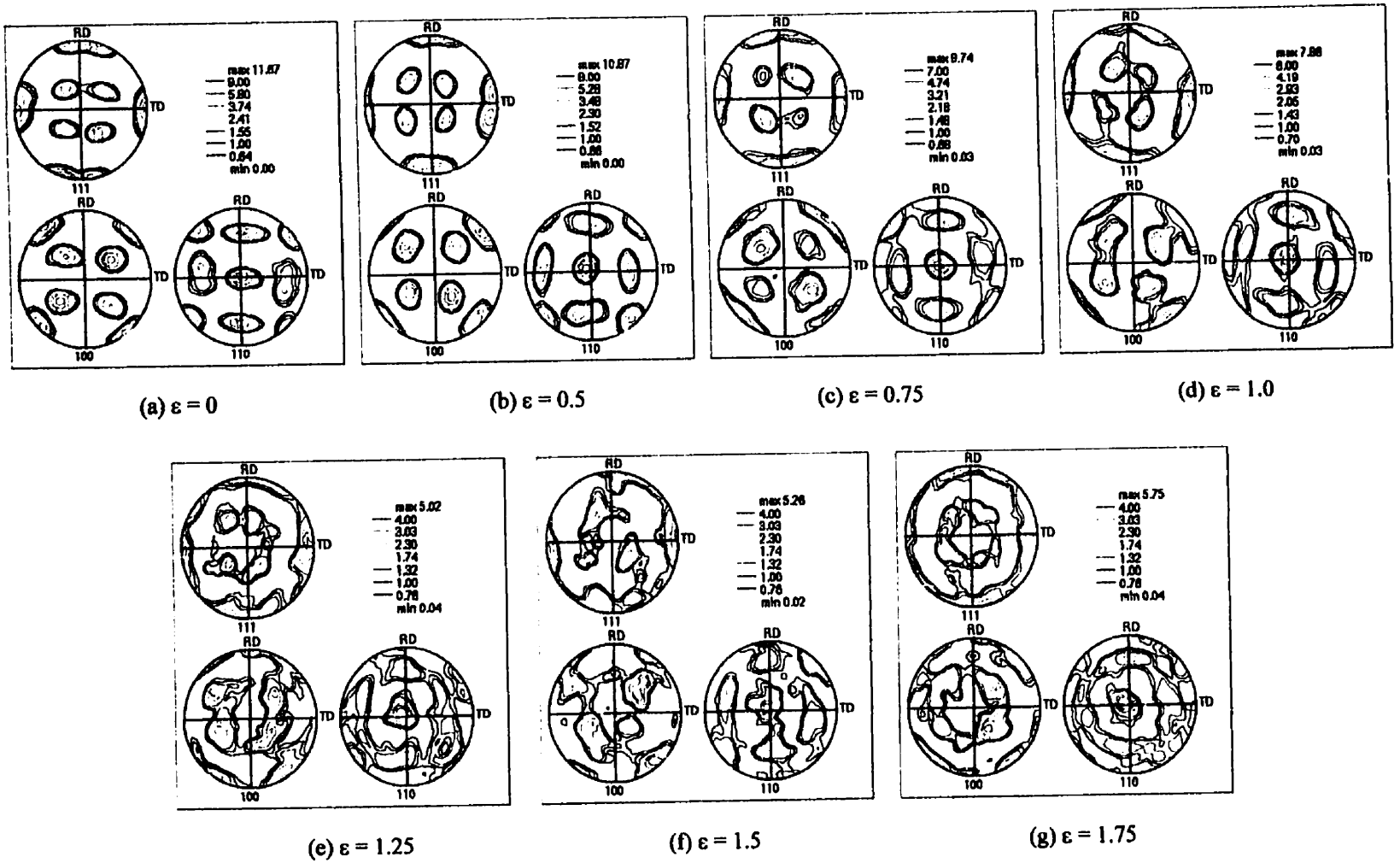

(a) $\varepsilon = 0$ (b) $\varepsilon = 0.5$ (c) $\varepsilon = 0.75$ (d) $\varepsilon = 1.0$

(e) $\varepsilon = 1.25$ (f) $\varepsilon = 1.5$ (g) $\varepsilon = 1.75$

Fig.4.4.9 Contour PFs of center layer in a series deformed samples at optimum superplastic condition of 530℃ and strain rate of $1x10^{-3}$/s to the strain levels of (a) 0, (b) 0.5, (c) 0.75, (d) 1.0, (e) 1.25, (f) 1.5 and (g) 1.75, respectively.

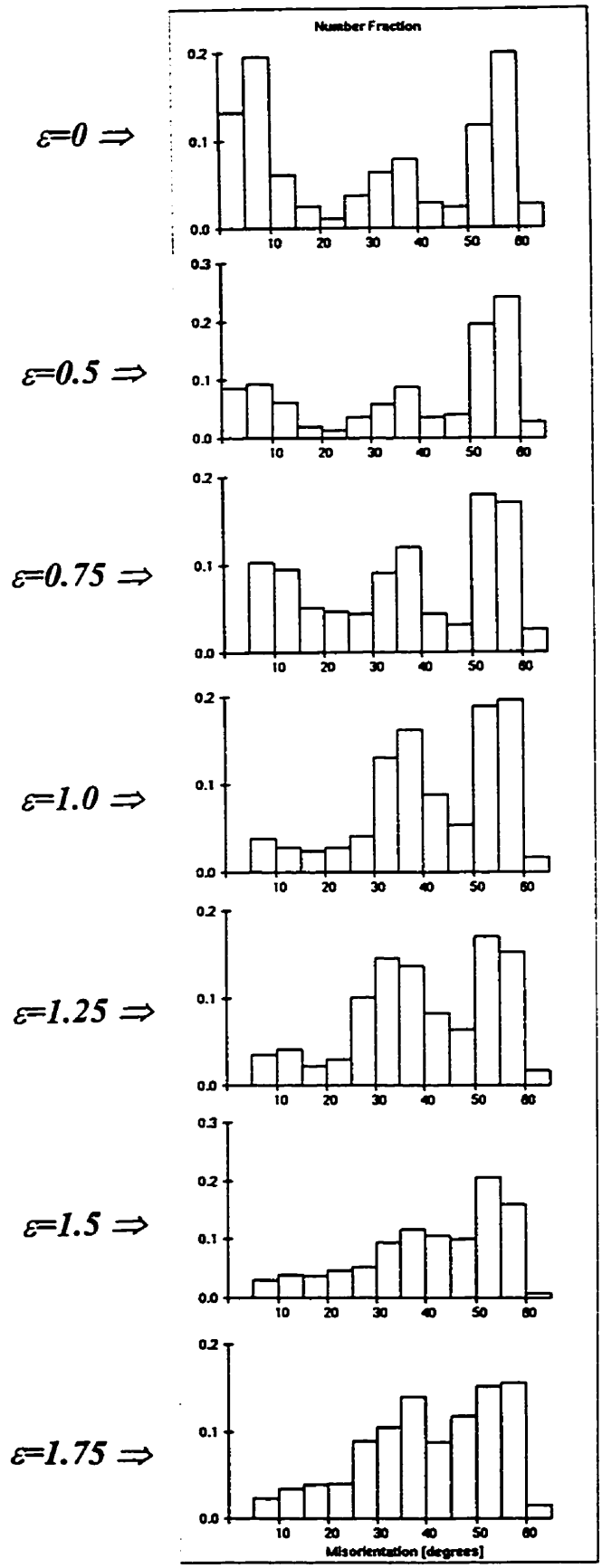

Fig.4.4.10. Misorientation distribution of the center layer in a series deformed full thickness samples at the optimum superplastic condition of 530℃ and the strain rate of $1x10^{-3}$/s to strains of (a) 0.5, (b) 0.75, (c) 1.0, (d) 1.25, (e) 1.5 and (f) 1.75.

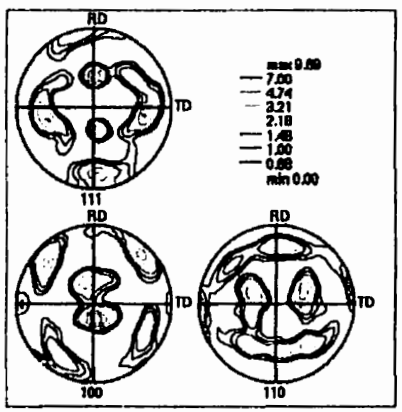

(a) ε = 0

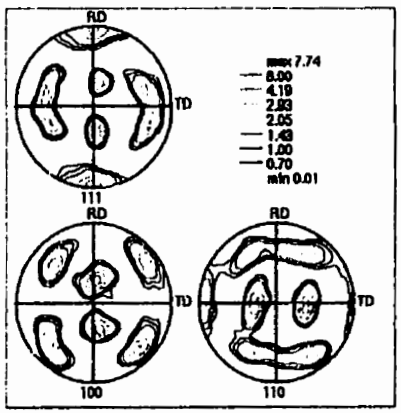

(b) ε = 0.5

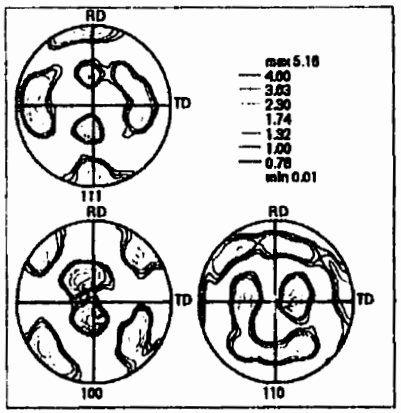

(c) ε = 0.75

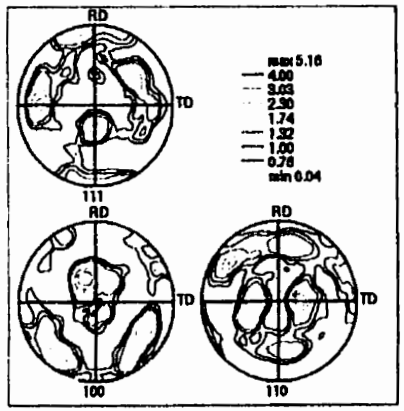

(d) ε = 1.0

Fig.4.4.11. Contour PFs of surface layer in a series deformed samples at the optimum superplastic condition of 530 ℃ and strain rate of $1x10^{-3}$/s to strain levels of (a) 0, (b) 0.5, (c) 0.75, and (d) 1.0, respectively.

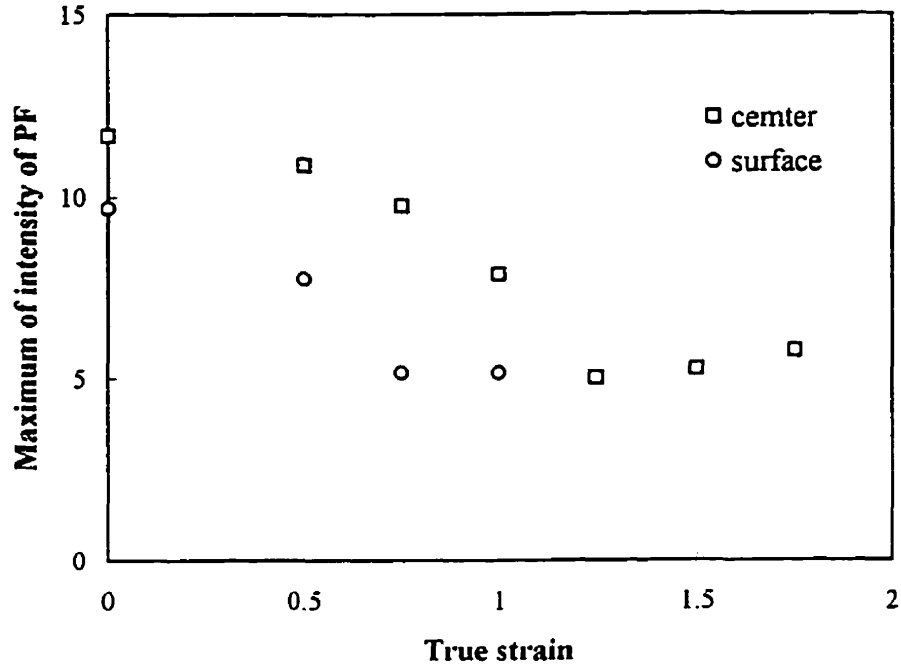

Fig.4.4.12. Changes of the maximum intensity of PFs following deformation in both the center and surface layers of the full thickness samples at the optimum superplastic condition of 530 ℃ and the strain rate of $1x10^{-3}$/s.

In order to study the effect of temperature on texture evolution during superplastic deformation, texture measurements were conducted on tensile specimens deformed at the same strain rate of $1x10^{-3}$/s and to a strain level of 1.0 at temperatures of 450 and 530°C. The texture was also measured on a specimen deformed at a lower temperature of 350°C to $\varepsilon = 0.55$ (the maximum strain that could be obtained) at the same strain rate, which showed only region III flow behavior. Fig.4.4.13 shows schematically the design of experimental study of the effect of temperature and strain rate on texture evolution. Figure.4.4.14 shows PFs from both the surface and center layers of the sample deformed at 450°C. A comparison of these PFs with those obtained from the sample deformed to the same strain at the same

strain rate but at temperature of 530°C (Fig.4.4.9 (d) and Fig.4.4.11 (d)), shows that the nature of texture weakening is similar in these two cases, but the rate of weakening in the center layer at 450°C is somewhat lower.

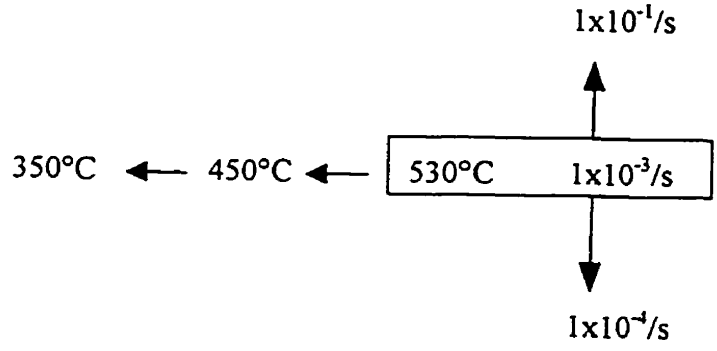

Fig.4.4.13. Illustration of experimental design for examining the effect of temperature and strain rate on texture evolution during deformation, with a reference of the optimum superplastic condition of 530 °C and the strain rate of $1x10^{-3}$/s.

The PFs obtained from the sample deformed at 350°C are shown in Fig.4.4.15. Comparison of these PFs with those from the sample deformed at 530°C ($\varepsilon = 0.50$), Fig.4.4.9 (b) and Fig.4.4.11 (b), shows that there is no texture weakening in the center layer. However, in the surface section, there is some texture weakening. The effect of temperature on texture evolution in the surface and center layers is summarized in Table 4.4.2.

Table. 4.4.2. Effect of temperature on texture evolution at optimum SPD strain rate (10^{-3}/s)

	Temperature		
Location	530°C	450°C	350°C
Surface	Continuous weakening	Weakening	low weakening rate
Center	Continuous weakening	low weakening rate	no weakening

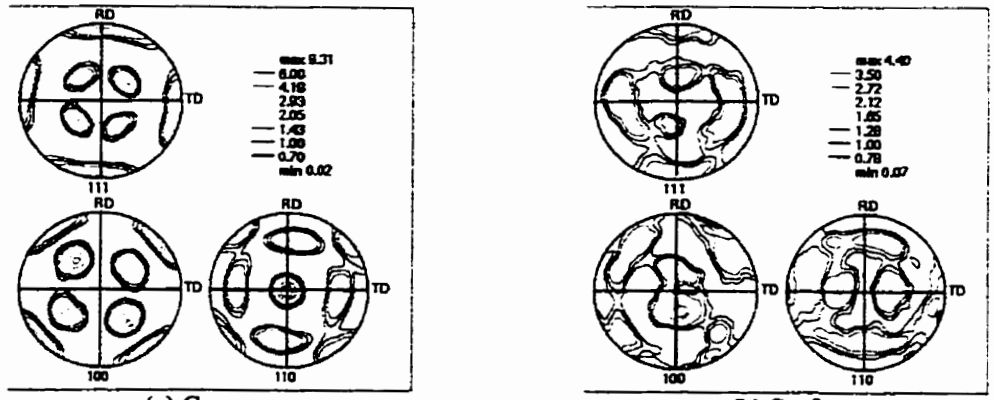

Fig.4.4.14. PFs of a full thickness sample deformed at 450℃ and a strain rate of $1x10^{-3}$/s to strain of 1.0 in its (a) center and (b) surface layers, respectively.

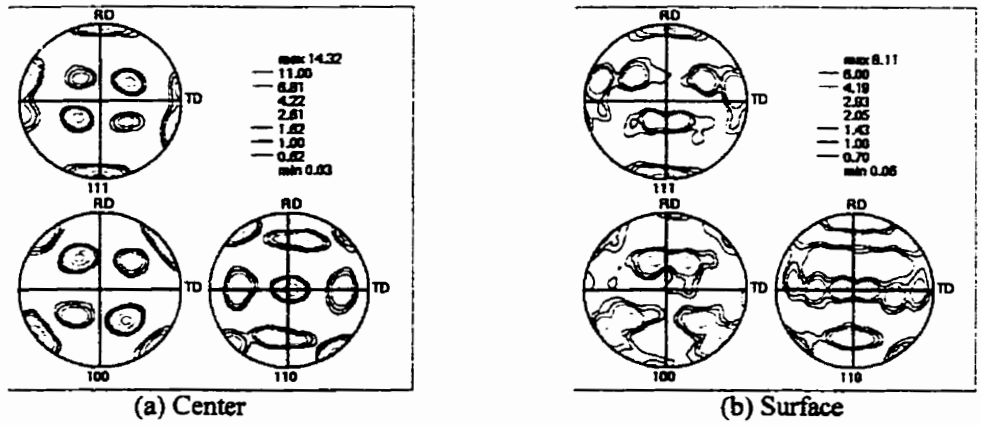

Fig.4.4.15. PFs of a full thickness sample deformed at 350℃ and a strain rate of $1x10^{-3}$/s to strain of 0.55 (which was the maximum elongation obtained at this condition) in its (a) center and (b) surface layers, respectively.

The variation in texture as a function of strain rate was investigated by deforming the specimens to selected strains at the strain rates of $1x10^{-1}$/s, $1x10^{-3}$/s and $1x10^{-4}$/s at temperature of 530°C. The PFs from the specimen deformed at 530°C at the highest strain rate of $1x10^{-1}$/s to $\varepsilon = 0.75$ (the maximum strain obtained) are shown in Fig.4.4.16. A comparison of these PFs with those deformed at the strain rate of $1x10^{-3}$/s, to the same strain level (Figs.4.4.9 (c) and 4.4.11 (c)), shows smaller degree of texture weakening in the center layer with increasing strain rate, however, in the surface layer some texture weakening occurred. The PFs obtained from the sample deformed at the lower strain rate of $1x10^{-4}$/s to $\varepsilon = 1.0$ at 530°C are shown in Fig.4.4.17. Comparison of these PFs with those deformed at the strain rate of $1x10^{-3}$/s, to the same strain level (Fig.4.4.9 (d) and 4.4.11 (d)), exhibits a similar texture weakening trend at both the strain rates. The effect of strain rate on texture evolution is summarized in Table 4.4.3.

Table 4.4.3. Effect of strain rate on texture evolution at temperature of 530°C

	Strain rate		
Location	$1x10^{-4}$/s	$1x10^{-3}$/s	$1x10^{-1}$/s
Surface	Weakening	Weakening	Weakening slow
Center	Weakening	Weakening	No weakening

Thus, there occurs texture weakening with increasing strain in superplastic region, but there does not appear to be any significant effect of temperature and strain rate. However, when deformed at higher strain rate or lower temperature, corresponding to region III, the texture weakening was noticed to be smaller in surface section, and no texture weakening in the center section.

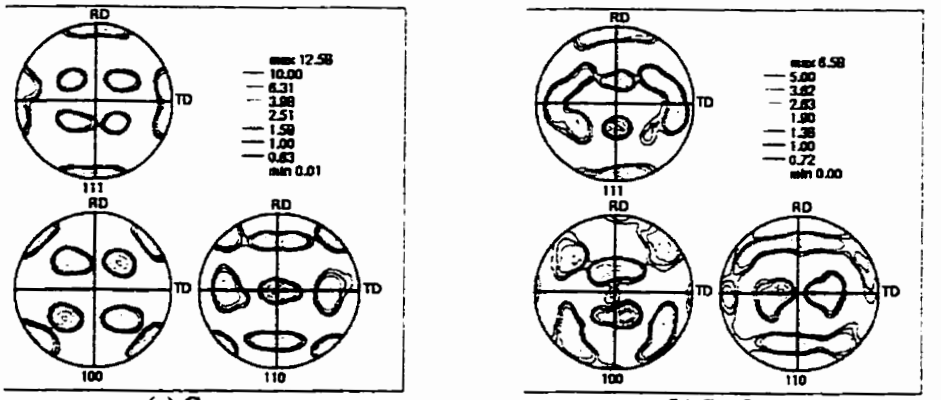

(a) Center (b) Surface

Fig.4.4.16. PFs of a full thickness sample deformed at 530℃ and a strain rate $1x10^{-1}$/s to strain of 0.75 (which was the maximum elongation obtained at this condition) in its (a) center and (b) surface layers, respectively.

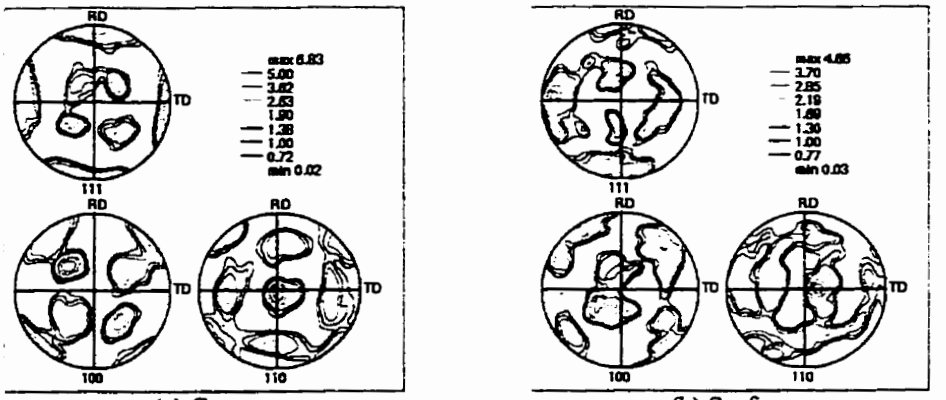

(a) Center (b) Surface

Fig.4.4.17. PFs of a full thickness sample deformed at 530℃ and a strain rate of $1x10^{-4}$/s to strain of 1.0 in its (a) center and (b) surface layers, respectively.

4.5. Deformation Behavior and Textural Evolution of the Surface (S) and Center (C) Materials

It was shown in section 4.1 that the sheet material may be considered to be made up of three layers, one center layer and two surface layers on either side of it. The grains in the center layer were pancake shaped and had brass–type textures. Whereas, the grains in surface layers were nearly equiaxed and had copper-textures. Therefore, tensile test specimens of the center and the surface materials were prepared form the full thickness sheet and were deformed under optimum superplastic condition of a temperature of 530°C and a strain rate of $1x10^{-3}$/s, in order to study the behavior of individual layers.

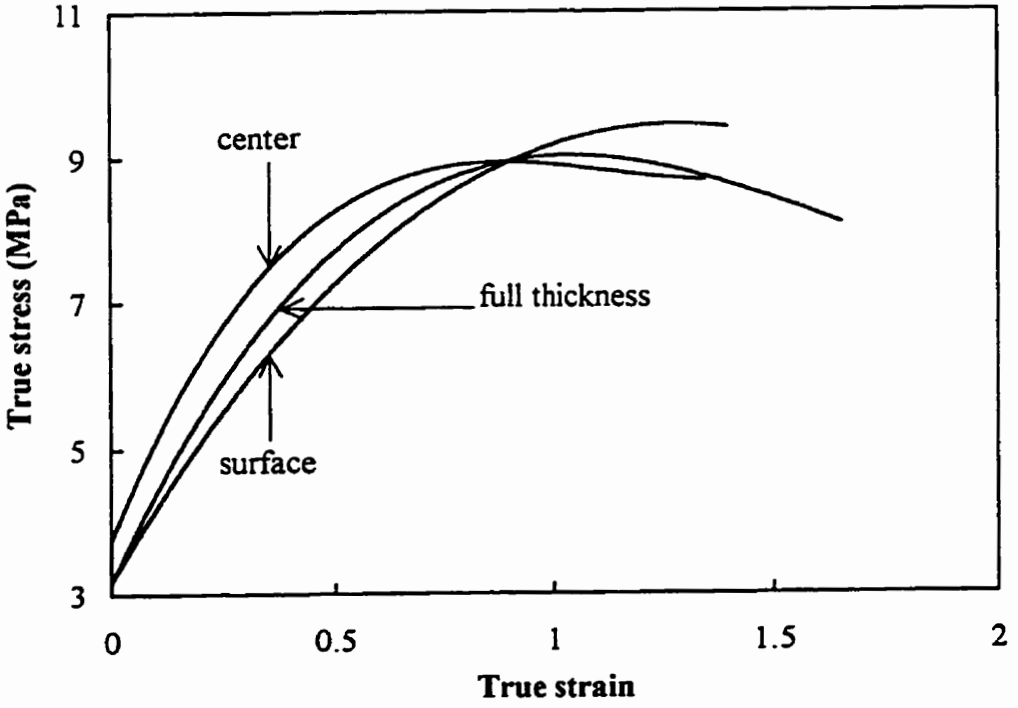

Fig.4.5.1. The relationship of stress and strain at deformation condition of 530 ℃ and a strain rate of $1x10^{-3}$/s from samples of the full thickness, the center and the surface materials.

4.5.1. Effect of Specimen Location on Tensile Behavior and Texture

Figure 4.5.1 shows the σ-ε curves obtained from the specimens of full thickness sheet (W0), the center (C0) and the surface materials (S0), with the tensile axis parallel to the sheet rolling direction. These curves are the average of 3 tests of each. It is seen that the flow stress of the center material is about 10-20 % larger than that of the surface material at a strain of about 0.4. Although the absolute difference in values is relatively small, the flow stress of the center material was consistently greater up to the strain of about 1.0, where these three curves reached the same level of flow stress. The flow stress of the full thickness specimen was between that of the center and the surface materials.

The textural changes in the full thickness specimens at selected strain levels at the optimum superplastic condition of 530°C and strain rate of $1x10^{-3}$/s, determined at the center and surface locations, have already been described in section 4.4 (Figs.4.4.9, 4.4.11 and 4.4.12). The textural changes in the specimens of the center (C0) and surface (S0) materials were also determined as a function of strain in the specimens deformed under the same condition of the temperature of 530°C and the strain rate of $1x10^{-3}$/s, to strain levels of 0.25, 0.5, and 1.0. The PFs of the center and the surface materials are shown in Fig.4.5.2 and 4.5.3, respectively. The trend of texture weakening in the center material is similar to that observed in the full thickness samples (Fig.4.4.9). Whereas, there are differences in the textural changes between the surface material and the full thickness specimens. Instead of continuously weakening observed in the latter, the former exhibits first an increase and then a weakening of texture.

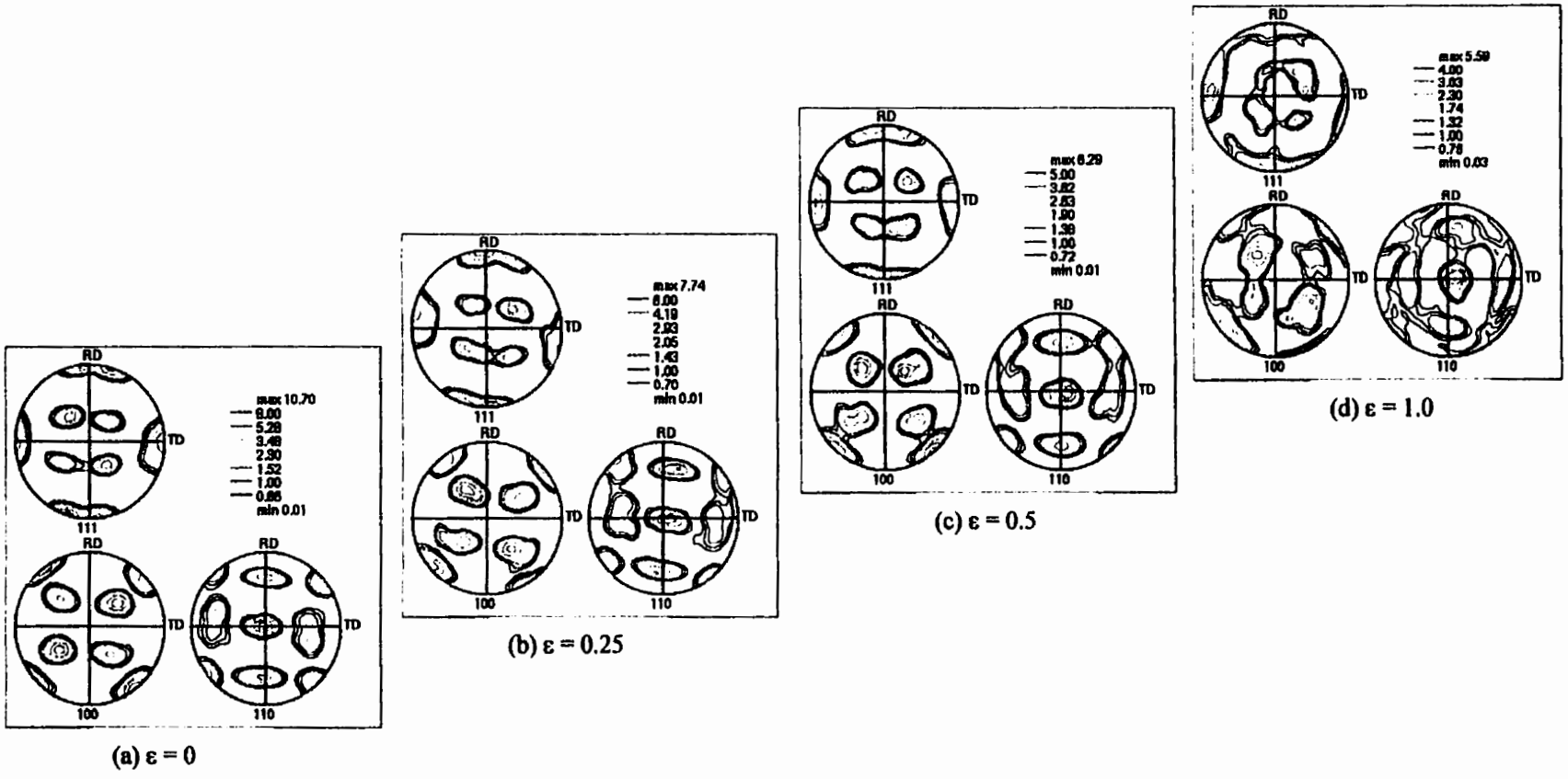

(a) ε = 0

(b) ε = 0.25

(c) ε = 0.5

(d) ε = 1.0

Fig.4.5.2. Contour PFs of center material deformed at 530℃ and a strain rate of $1x10^{-3}$/s to strains of (a) 0, (b) 0.25, (c) 0.5 and (d) 1.0.

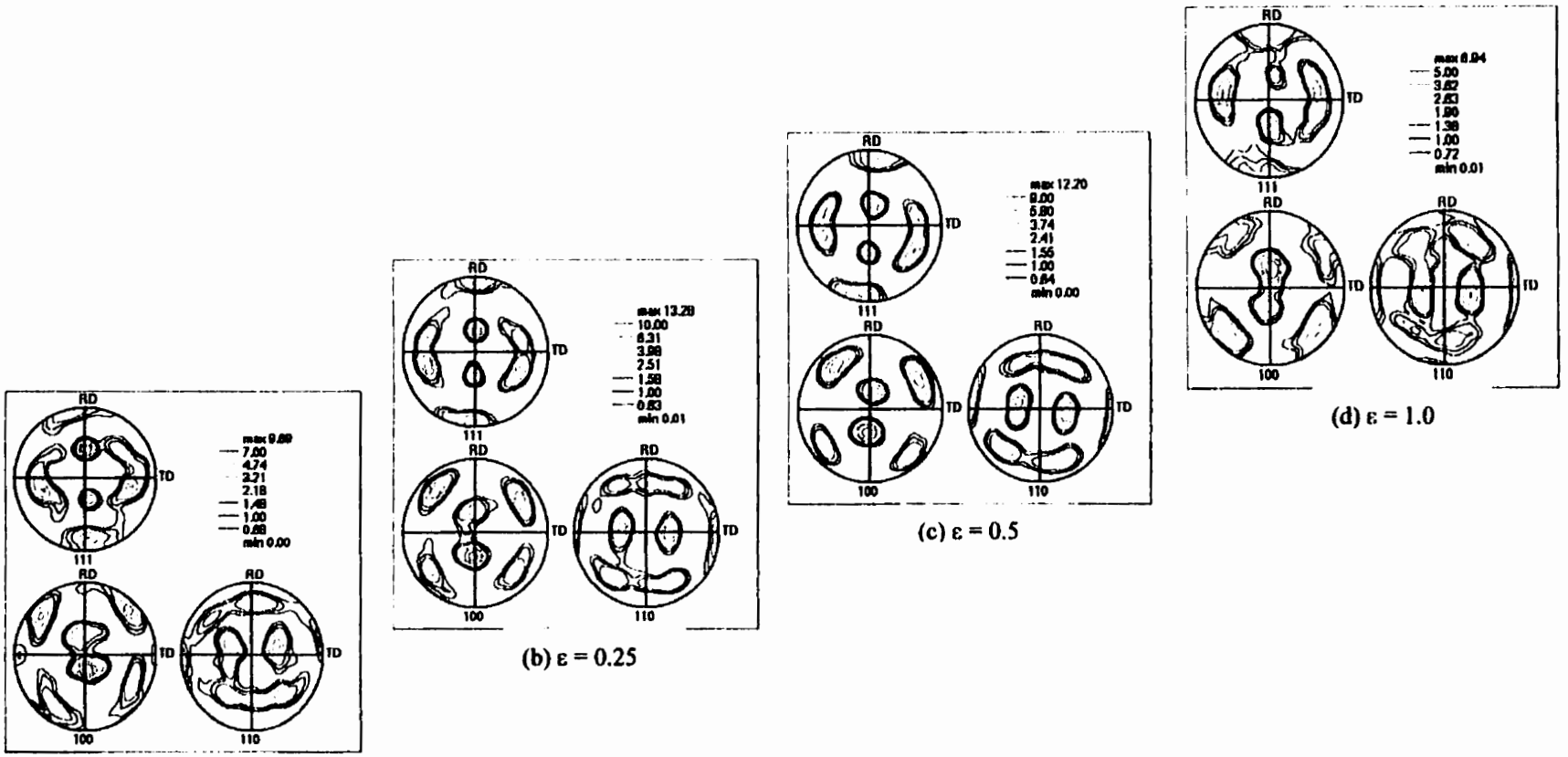

(a) ε = 0

(b) ε = 0.25

(c) ε = 0.5

(d) ε = 1.0

Fig. 4.5.3. Contour PFs of surface material deformed at 530℃ and a strain rate of $1x10^{-3}$/s to strains of (a) 0, (b) 0.25, (c) 0.5 and (d) 1.0.

Fig.4.5.4 shows changes in the maximum intensities of PFs as a function of strain in the separated center and surface materials. It is seen that although the process of textural changes is different during deformation in these two layers, a similar random orientation is reached when deformed to a strain of about 1.0.

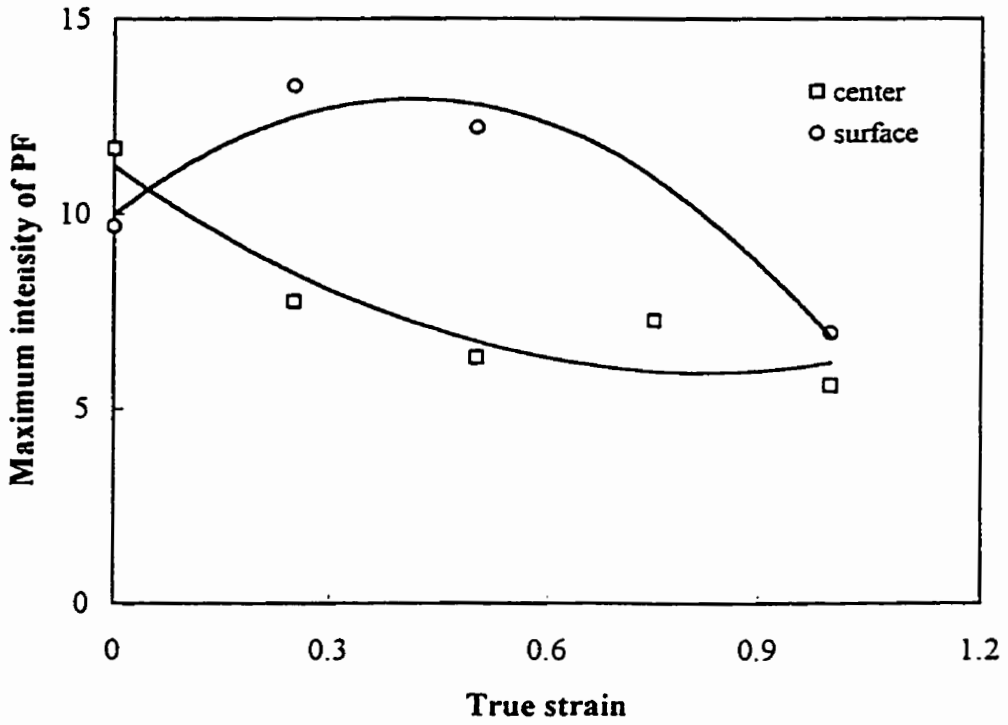

Fig.4.5.4. Changes of the maximum intensity of PFs following deformation in samples of both center and surface materials at 530℃ and a strain rate of $1x10^{-3}$/s.

4.5.2. Effect of Specimen Orientation on Tensile Behavior

Tensile specimens were prepared from the surface and center materials with tensile axis at 30, 45 and 90° orientations with respect to the rolling direction. As described in Chapter 3, these specimens were designated as S30, S45, S90, C30, C45, and C90, respectively. The σ-ε curves of the specimens of center material, having different orientations, are shown in Fig.4.5.5. They exhibit that, in the earlier part of deformation ($\varepsilon < 1.0$), the flow stress is maximum in the orientation of 90° and minimum in the orientation of 0°, and at larger strains the flow stress in all the orientations approach the same level.

Figure 4.5.6 presents the σ-ε curves for the specimens from the surface material at various orientations. The trend of flow behavior for this case is, however, opposite to that exhibited by the specimens from the center material. That is, the flow stress was maximum in the orientation of 0° and minimum in the orientation of 90°, and the flow stresses in different orientations do not approach the same value.

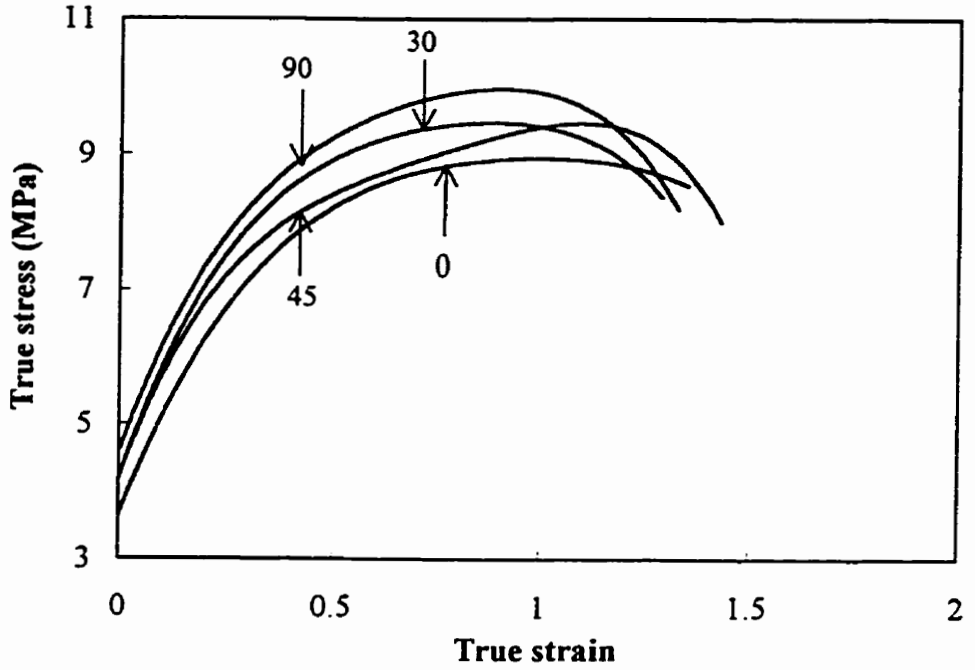

Fig.4.5.5. The effect of sample orientation on stress and strain relationship at deformation condition of 530℃ and a strain rate of $1x10^{-3}$/s in the center material with 0, 30, 45 and 90° between tensile axes and the sheet original rolling direction.

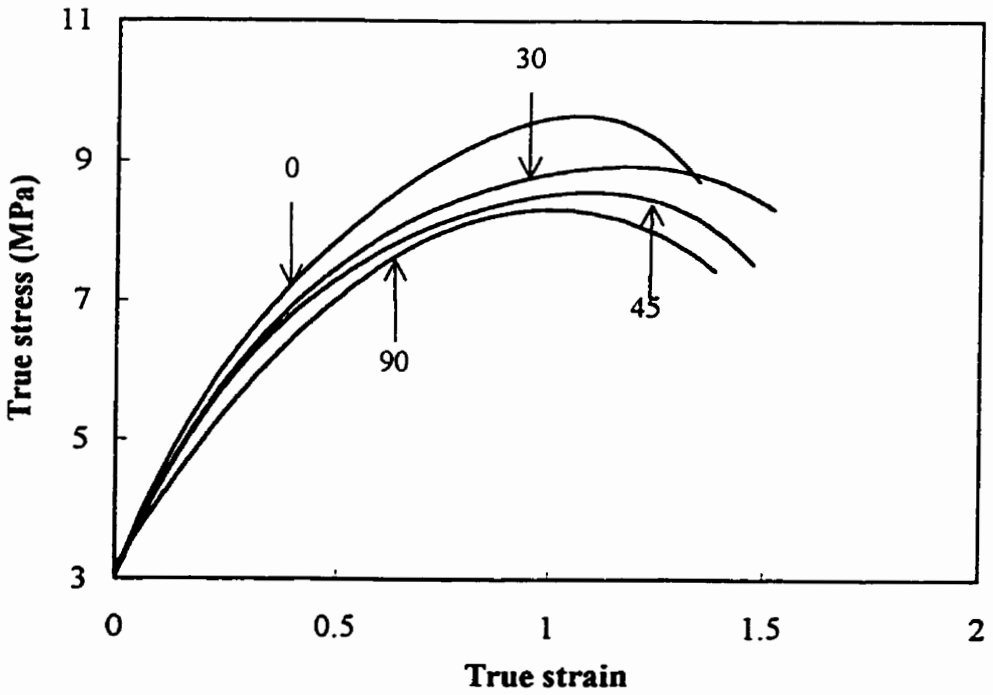

Fig.4.5.6. The effect of sample orientation on stress and strain relationship at deformation condition of 530℃ and a strain rate of $1x10^{-3}$/s, in the surface material with 0, 30, 45 and 90° between tensile axes and the sheet original rolling direction.

4.5.3. Effect of Specimen Orientation on Textures

The texture of the center and surface materials was determined after a strain of 1.0, under optimum superplastic conditions at a temperature of 530°C and a strain rate of $1x10^{-3}$/s. Fig.4.5.7 gives PFs from the samples of the center material. Irrespective of orientations, the results indicate that texture weakening occurs to a similar intensity without the creation of any new orientation. However, the results from samples of the surface material, Fig.4.5.8, show that although new texture is not created, the rate of texture weakening is reduced with an increase in the angle of orientation. This is also illustrated in Figure 4.5.9, which shows the changes in maximum intensities of PFs in samples from both the center and surface materials as a function of angles of orientation. Therefore, it may be concluded that for AA8090 Al-Li alloy with a microstructural gradient, the specimen orientation does not have an appreciable effect on texture weakening in the center material, but has an effect in the surface material during superplastic deformation.

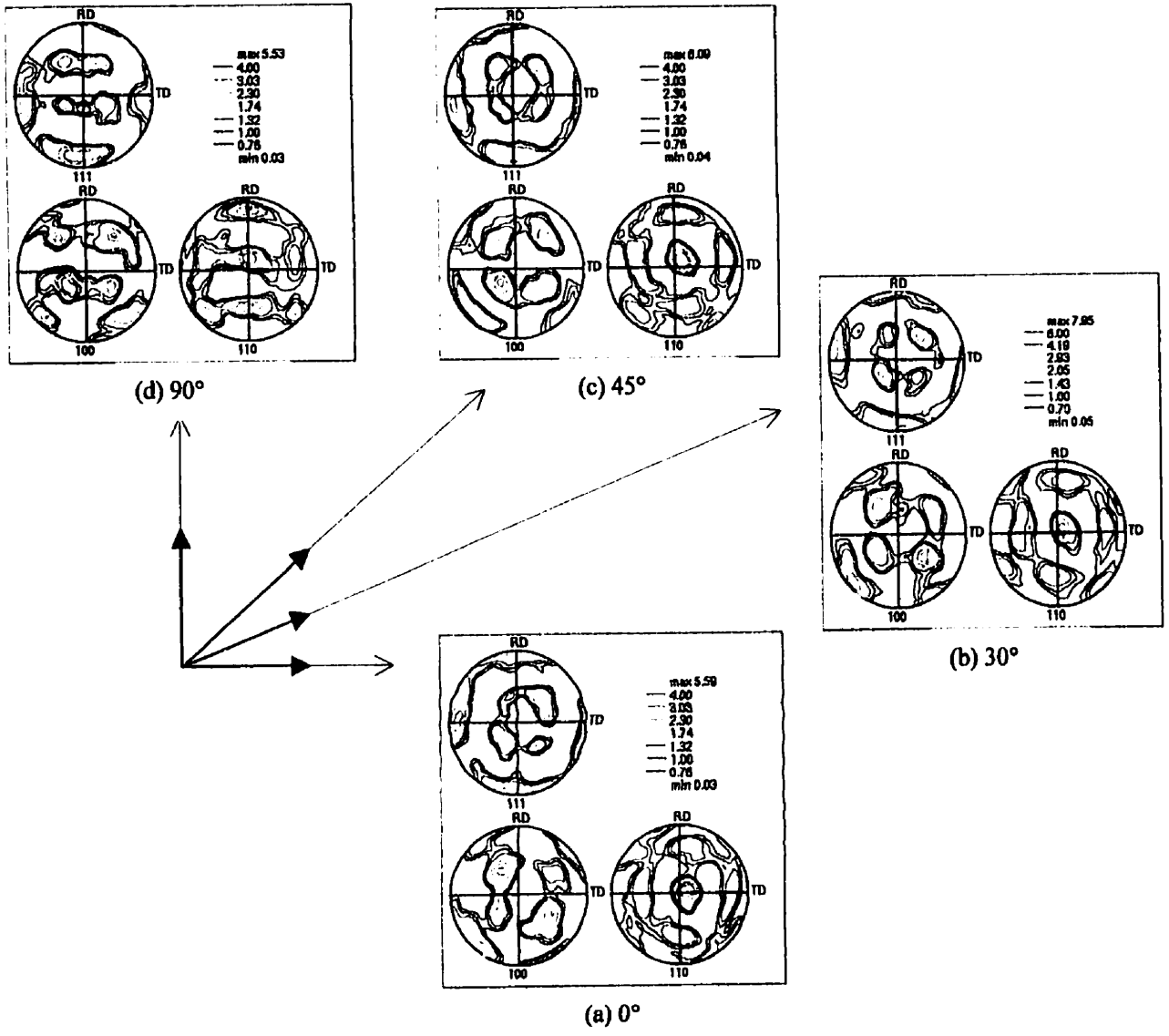

Fig.4.5.7. PFs of center materials with angles between tensile axis and the sheet original rolling direction of (a) 0°, (b) 30°, (c) 45° and (d) 90°, respectively, deformed at 530℃ and a strain rate of $1x10^{-3}$/s to a same strain of 1.0.

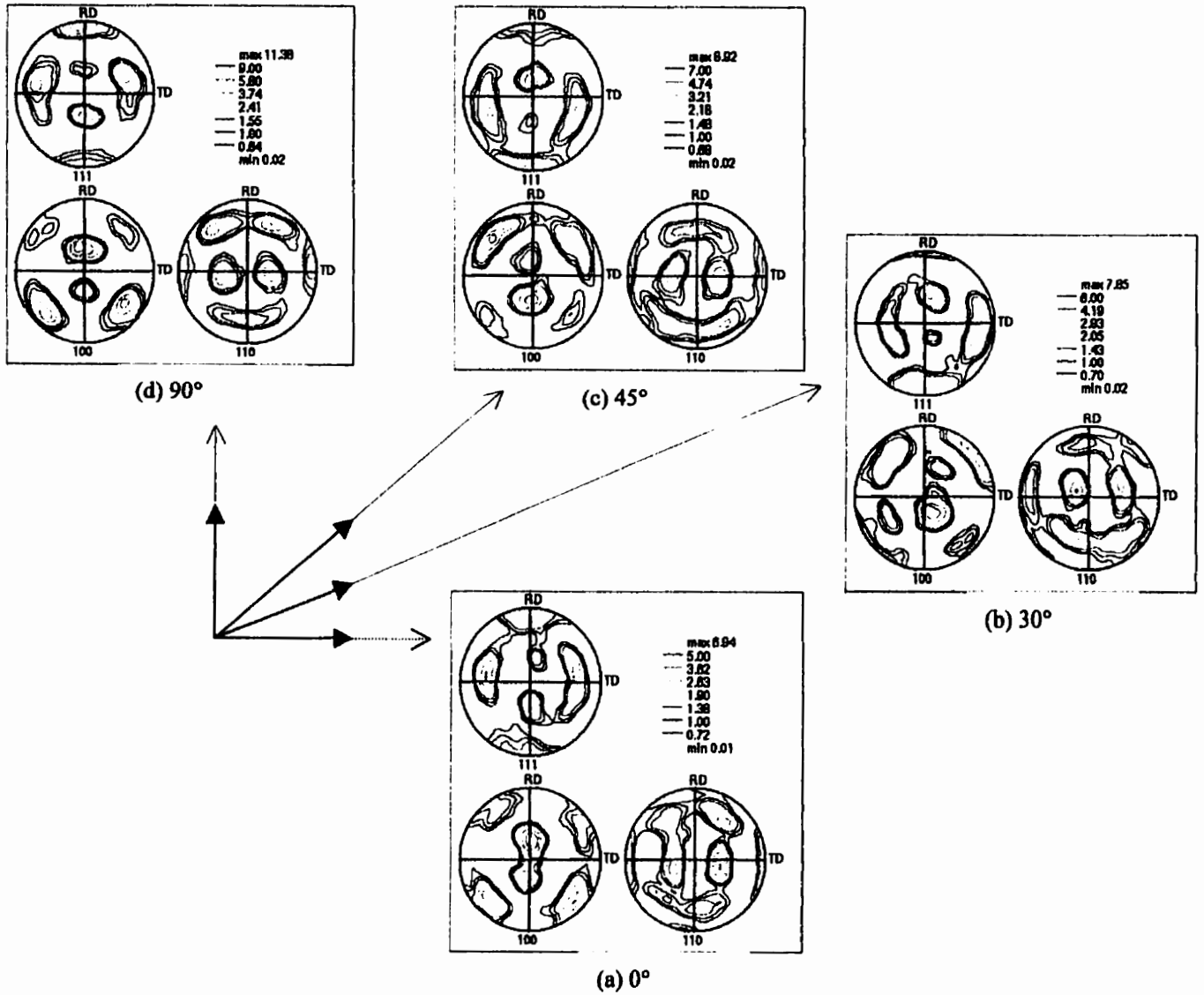

Fig.4.5.8. PFs of surface materials with angles between tensile axis and the sheet original rolling direction of (a) 0°, (b) 30°, (c) 45° and (d) 90°, respectively, deformed at 530℃ and a strain rate of $1x10^{-3}$/s to a same strain of 1.0.

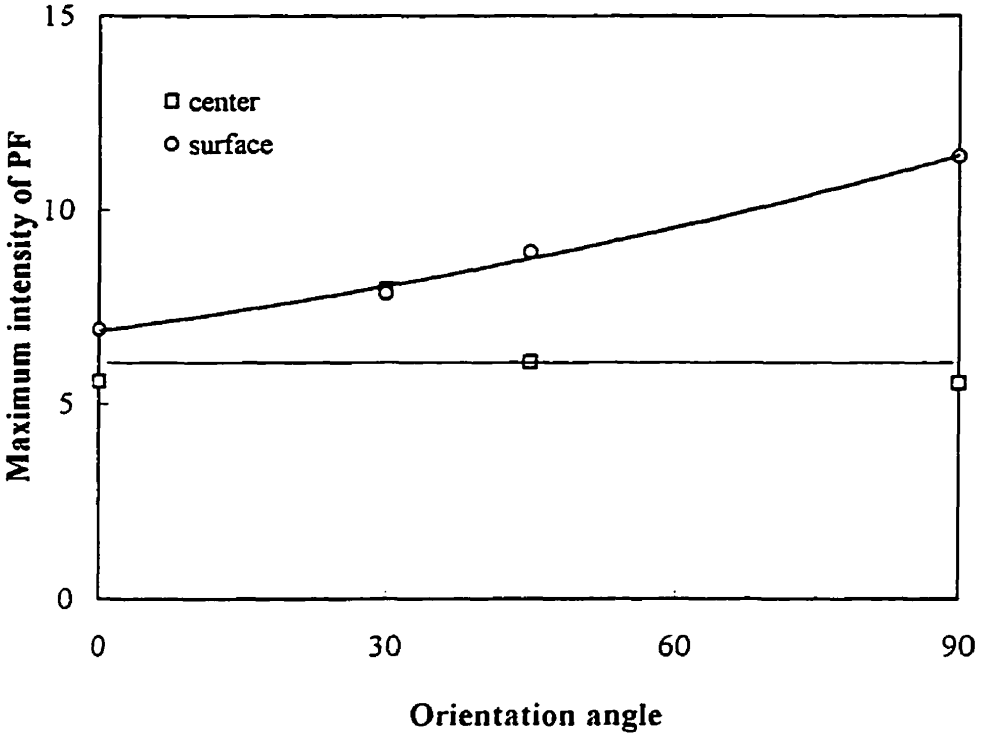

Fig.4.5.9. Effect of sample orientation on texture represented by the maximum intensity of PF for both the center and the surface materials with different orientations relative to the sheet original rolling direction deformed at 530℃ and a strain rate of $1x10^{-3}$/s to a same strain of 1.0.

CHAPTER 5
DISCUSSION

Results of studies on superplasticity in materials having fine equiaxed grains has been extensively reported in the literature. However, in as-worked state, many superplastic materials are known to have non-equiaxed microstructures, which evolve towards fine equiaxed grains after certain amount of deformation under superplastic conditions [9, 20, 23]. The as-received AA8090 Al-Li alloy used in the present study contained composite microstructure in the through thickness cross-section, having nearly equiaxed grains in the surface and pancake shaped grains in the center layers, which were elongated in both longitudinal and transverse directions (Fig.4.1.1). The alloy varied in texture from the surface towards center as well, that is, the surface had predominantly copper-type texture whereas the center had predominantly brass-type texture, with a continuous textural gradient from surface to center (Fig.4.1.8). No detailed and systematic study has been reported for superplastic behavior for such a complex microstructure from both grain morphology and textural point of view. Unlike the analysis of data obtained from materials containing fine equiaxed grains, the microstructure present in the AA8090 alloy would influence the flow behavior and the concurrent microstructural evolution by imparting the roles played by the varying grain size, grain shape, texture, and their distributions at different depths along the thickness direction of the sheet. Although the fine equiaxed grained material is well suited for understanding the mechanism for superplastic deformation, the study of present AA8090 alloy with its varying microstructure can help in understanding the behavior of other similar

commercial superplastic materials. In view of this, the analysis and discussion in this chapter are aimed to (i) bring out correlation between flow behavior and concurrent microstructural evolution, (ii) evaluate textural evolution and understand its relation with flow behavior, (iii) examine flow anisotropy and its relation with texture, (iv) integrate the microstructural and stress gradient to understand composite flow behavior, and finally (v) suggest an experimental constitutive relationship for a commercial material of this type.

5.1. Effect of Microstructural Evolution on Flow Behavior

5.1.1. Microstructural Evolution

The microstructure prior to straining retained its initial composite distribution of grain shape, grain size (Fig.4.2.1) and texture (Fig.4.2.6) during heating to the deformation temperature. No significant change was seen even after static annealing at 570°C for 1h, although the grains were noticed to be much coarser (Fig.4.2.8). The stability of texture and grain morphology during static annealing is attributed to the suppression of recrystallization through the presence of β′ (Al_3Zr) precipitates as has been reported by others [89]. However, deformation under superplastic condition was seen to help in microstructural evolution. As a result of this, the grain sizes, grain shape and texture tended to become the same with continued deformation. One such example is presented through a three dimensional representation of microstructure in a deformed sample in Fig.4.4.1 (d). The deformed microstructures revealed three distinct changes, viz. enhanced grain coarsening (Fig.4.4.3), elimination of grain directionality in the mid-thickness sections (Fig.4.4.8), and texture weakening (Fig.4.4.8, 4.4.9 and 4.4.11).

As presented in the Literature Review, section 2.3.3, one or more of the three microstructural changes are reported in different materials having similar starting microstructure [9, 20, 23]. Several proposed mechanisms for such microstructural evolution are listed in Table 2.2.

Due to the presence of second phase in micro-duplex alloys or dispersion of second phase particles in quasi-single phase alloys, the microstructures of superplastic materials are considered to be reasonably stable [36]. In these cases, the time exponent q in the kinetic expression $d \propto t^q$, where d is the grain size at time t and q is the time exponent, is known to be lower (q = 0.25 and 0.33) than that for single phase materials (q= 0.5) [126]. The values of q are even smaller (~0.1) in aluminum alloys [127]. However, superplastic deformation of AA8090 Al-Li alloy resulted in a significant grain growth (equation 4.4.1), with the value of q varying from 0.21 to 0.44 depending on temperature (Table 4.4.1). Such deformation induced grain growth has been reported [128] in a wide range of superplastic materials. The enhanced grain growth during SPD is attributed to grain boundary migration, which becomes necessary to accommodate stress concentration built up by grain boundary sliding [129].

A large number of superplastic materials contain grains elongated in one or two directions or a banded microstructure. Such materials exhibit grain growth, elimination of elongated grains, and their redistribution to homogeneously distributed equiaxed grains during superplastic deformation. The critical strain necessary for the material to exhibit equiaxed grains is reported to vary from $\varepsilon \sim 0.05$ to 0.80, depending on the type of material and the test

condition [128]. Since the as-received AA8090 Al-Li alloy was found to contain a combination of nearly equiaxed grains in the surface layers and pancake shaped grains in the center layers, the microstructural evolution will consist of grain coarsening in the former and both grain coarsening and evolution towards equiaxed grains in the latter.

The mechanisms of microstructural evolution during superplastic deformation, consisting of grain growth, grain shape and textural change, in rolled sheet of aluminum alloys have been discussed by different investigators (section 2.3.3). Most of the mechanisms essentially suggest coalescence, migration and sliding of subgrain boundaries, and coalescence, rotation, and switching of subgrains. Some of these mechanisms emphasize dislocation activity to be the source of these processes. A comparison of these mechanisms with the observed microstructural evolution in the present AA8090 alloy was made to examine whether they can explain all the three microstructural changes. Presented in Table 5.1 is the ability of these mechanisms to account for the observed microstructural changes. The ability of a particular mechanism to predict the microstructural evolution is marked by +, whereas its inability to predict is marked by - in the Table.

As seen, five of the mechanisms can explain the three observed microstructural changes, viz. grain growth, grain shape change and texture weakening. However, three of the mechanisms marked by * are similar. The reason for their being similar is based on the fact that, as far as the texture weakening is concerned, the subgrain rotation is essentially dictated by dislocation activity. Another mechanism, based on subgrain superplasticity, explains all the

three microstructural changes, but it is unlikely that subgrains would be retained at larger strains. It is evident from Fig.4.4.10 that the number of low angle subgrain boundaries decreases with increase in strain, therefore, subgrains are not stable during superplastic deformation. The mechanism involving discontinuous recrystallization is also, in principle, able to explain the three microstructural changes, but discontinuous recrystallization during deformation was not observed in the present investigation.

Table. 5.1. Applicability of various mechanisms to the observed microstructural features

Existing DICR mechanisms	grain growth	break down of banded structure	texture weakening
Subgrain coalescence	+	-	-
Subgrain boundary migration	+	-	-
Subgrain boundary sliding+GBS	+	+	-
**Subgrain rotation+GBS*	+	+	-
**Subgrain rotation+GBS+subgrain switching*	+	+	-
Subgrain superplasticity	+	+	-
**Dislocation activities*	+	+	-
Grain growth between bands	+	+	-
Discontinuous recrystallization	+	+	-

The texture weakening, where the orientation change gives an accumulated information about the process of deformation involving dislocation activity, suggests that mechanism based on dislocation activity might be more suitable for explaining the results observed from the present study. Nix [130], after critically analyzing various mechanisms of superplasticity, has concluded that slip must occur in some of the grains to account for grain rotation and changes in crystallographic texture. In the present study, textural changes were clearly observed and pancake shaped grains changed to equiaxed grains. Therefore, it is suggested that the

mechanism of superplastic deformation in AA8090 Al-Li alloy has an element of dislocation activity in it.

5.1.2. Effect of Superplastic Deformation on Texture Weakening

In the present study, deformation of AA8090 Al-Li alloy under superplastic condition was observed to lead to a significant texture weakening. This is in general in agreement with what is already known for a variety of superplastic materials [36]. The texture weakening is ascribed to grain rotation, which is facilitated during superplastic deformation as an accommodating step to grain boundary sliding.

Blackwell and Bate [24] have investigated the effect of strain and strain rate on texture evolution focused on the mid-thickness layer in AA8090 Al-Li alloy with a similar microstructure as was present in the material used in this study, and deformed at 527°C and at a strain rate of $1x10^{-3}$/s with tensile axis parallel to the rolling direction. According to their investigation, a slight increase in texture occurred in the early part of deformation ($\varepsilon = 0.25$), which was subsequently followed by continuous texture weakening. The texture weakening was independent of strain rate within the superplastic region, and they noticed a slight shift in orientation at a higher strain rate of $1x10^{-2}$/sec. This shift has not been observed in the current study.

Similar to the work of Blackwell and Bate and by using AA8090 Al-Li alloy, Bowen [14] also studied the textural evolution as a function of strain during superplastic deformation in

the center layers. He found a progressive decrease in the intensity of texture and a shift towards <111> with increasing strain in samples with tensile axis parallel to the rolling direction.

In another study, Liu and Chakrabarti [75] observed texture evolution by OIM in the mid thickness section of a 7050 alloy sheet deformed at 447°C and at a strain rate of $2x10^{-3}$/s. Although their material had pancake shaped grains, but not a composite type grain structure that was present in the alloy used in the current study. They found that texture weakening started to occur at a strain of about 0.4 and no noticeable change occurred prior to reaching this strain. A distinct texture weakening occurred between strains of 0.4 - 0.75. In all the above three studies, (viz. Blackwell and Bate, Bowen, and Liu and Chakrabarti) nearly equiaxed grains evolved following the texture weakening during superplastic deformation.

While, all these three studies were mainly limited to the effect of strain on texture evolution during superplastic deformation in aluminum alloys, in the present study, a systematic and detailed textural determination was conducted not only as a function of strain but also as a function of strain rate, covering the highest strain rate that the material could sustain, and temperature. In addition, by considering the texture gradient across the thickness section of the material, texture measurements were conducted in both the center and surface layers of the full thickness samples. Also, texture evolution was examined in the samples made of the surface and center materials individually. Finally, texture evolution was determined as a function of orientation between the original rolling direction and tensile axis in such separated materials.

As shown in Fig.4.4.12, texture weakening in the current investigation occurred continuously not only in the center layer of the full thickness material, but also in the surface layer at a temperature of 530°C and at strain rates of both $1x10^{-4}$ and $1x10^{-3}$/s (Table.4.4.3). This is similar to the result of the investigation of Blackwell and Bate, Bowen, and Liu and Chakrabarti. However, at a higher strain rate of $1x10^{-1}$/s, texture weakening occurred only marginally in the surface layers whereas there was no texture weakening in the center layers. The first two strain rates fall in the superplastic region whereas the last strain rate is beyond the superplastic region. The reason for the surface layers to exhibit some level of texture weakening, even at higher strain rate of $1x10^{-1}$/s (Table.4.4.3), may be associated with the presence of nearly equiaxed grains and their ability to undergo grain boundary sliding. On the other hand, the grains in the center layer had pancake shape, which may be less favorable for grain boundary sliding but more favorable for dislocation activity, which may further result in the absence of texture weakening. The decrease in temperature had a similar effect on texture evolution as the increase in strain rate, as shown in Table 4.4.2, and within the superplastic region there occurred a similar texture weakening at all the temperatures and strain rates. This suggests that the mechanism for superplastic deformation remains the same irrespective of temperature and strain rate in the superplastic region. The mechanism for such superplastic deformation involves an optimum combination of grain boundary sliding, diffusion and dislocation activity, which may be responsible for the observed similar texture weakening. When either the strain rate or temperature corresponds to region III, the optimum combination of various processes deviates to favor dislocation activity. As a consequence of this, no texture weakening is expected.

As presented in section 4.4.4, copper-type texture in the surface layer and brass-type texture in the center layers showed the same trend of continuous texture weakening (Fig.4.4.12), when the texture measurements were performed in the full thickness samples. However, intensities of the same copper texture showed a small increase first and they then decreased when the texture measurements were made in the separated surface material (Figs.4.5.3 and 4.5.4). This increase in texture intensity during the early part of deformation may be explained as follows. According to Nix [130], no grain rotation would be possible without activating intragranular slip in one or more grains. In the surface layers, the grains are nearly equiaxed and as such they can easily undergo grain boundary sliding without requiring much dislocation activity. Therefore, a significant texture weakening is not expected. Furthermore, the equiaxed grains undergo grain growth only, unlike pancake grains, which can cause texture sharpening following grain growth, as is commonly observed in commercial materials [131]. In the center layers, grains had pancake shape and they still showed superplasticity with $m \sim 0.45$ [24]. However, because of the non-equiaxed nature of grains, the optimum combination of deformation mechanisms would involve more dislocation activity which, in turn, will result in texture weakening.

5.1.3. Nature of Stress - Strain Curves

All of the stress-strain curves, irrespective of strain rate and temperature, exhibited an increase in flow stress with strain (Fig.4.3.1 and 4.3.3), although the extent of increase depended on deformation conditions. Up to 210°C, the intermediate temperature, the strain

hardening is suggested to be the main reason of strengthening. In this region, σ/E is nearly independent of temperature, which represents the athermal behavior due to long range stress fields opposing the movement of dislocations. These long range stress fields are suggested to be due to precipitates, grain boundaries and other dislocations [34].

The present study was mainly concentrated on superplasticity which prevails in the high temperature region. Usually, conventional strain hardening is not considered to be important under superplastic condition, instead, the flow strengthening exhibited during superplastic deformation is sometimes called as grain growth hardening. In the present investigation, grain growth was found to be significant at $T \geq 450°C$ (Fig.4.4.2). In addition to grain growth, there also occurred changes in grain shape, evolution of texture (Fig.4.4.8) and formation of cavities (Fig.4.4.4). The change from non-equiaxed grains towards equiaxed grains, and cavitation would lead to a decrease in flow stress with increase in strain. The former is considered to be important in the early part of deformation whereas the latter may become important at larger strains. The variation in flow stress of AA8090 Al-Li alloy in the present work was quantified as a function of strain through equation (2.3) over a large part of the strain, Fig.4.3.4, and the variation in n_s as a function of temperature is plotted in Fig.4.3.5. An attempt will be made next to understand the irregular variation in n_s as a function of temperature with the help of microstructural evolution.

The n_s vs. T plot in Fig.4.3.5 shows four regions. The decrease in n_s with increase in temperature in region I over $T = 25$ to $210°C$, appears to be due to the operation of thermally

activated process around 200°C. The increase in n_s with temperature in region II at ~350°C<T<~500°C can be ascribed to grain coarsening. The decrease in n_s with increase in temperature in region III at ~500°C<T<~530°C may be associated with the dissolution of precipitates, which reduces resistance to plastic flow. The microstructure developed during heating and soaking at 530°C for 20 minutes, prior to deformation, in fact shows (Fig.4.2.2) the disappearance of the precipitates present in the as-received state (Fig.4.1.4). Once the precipitates are dissolved, the grain boundary migration will be faster. Probably, it is the rapid grain growth that causes the observed increase in n_s with increase in temperature in region IV over T >~550°C. Cavitation may have effect on the flow behavior, but cavitation was not studied systematically in the present investigation. Kashyap and Chaturvedi (unpublished work) noticed that maximum cavitation occurred under optimum superplastic condition, which in fact corresponds to the temperature range in region III here, but the strain range is over that discussed here.

5.1.4. Correlation between Flow Behavior and Concurrent Microstructural Evolution

As discussed earlier, the microstructural evolution involves grain growth, change in grain shape, texture weakening and cavitation. Also, there is some evidence of dislocation activity during superplastic deformation of commercial materials like the one used here. However, a detailed study of dislocation activity could not be successfully conducted in this investigation because of the complications caused by fast quenching, which leads to about 1.2% shrinkage in the quenched sample. However, various stress-strain curves presented in Figs.4.3.1 show a continuous decrease in strain hardening rate with temperature. This is typical of the effect of

dynamic recovery occurring in the early part of the stress-strain curves of various materials undergoing dynamic recovery and recrystallization [132]. Therefore, the stress-strain curves in the present study suggest dislocation activity takes place during superplastic deformation. The effect of concurrent grain growth on the variation in flow stress with strain is analyzed next.

According to the various constitutive relationships for superplastic deformation (Table 2.1), the flow stress increases with an increase in grain size. At a constant temperature and strain rate, the relationship between flow stress and grain size can be written as

$$\sigma \propto (d)^{p/n} \qquad (5.1)$$

Here, p is the grain size exponent and n is the stress exponent. From most of the models for superplastic deformation, presented in Table 2.1, the values of both p and n are found to be equal to 2. For the AA8090 Al-Li alloy, p has been reported to be 2 [26] whereas n equals to 2 (m=0.5) as presented in section 4.4. Since grain size increases with increase in strain and so does the flow stress, it is possible to calculate the contribution of the increasing grain size to the flow stress by employing equation (5.1), and assuming that the stress at the onset of plastic strain corresponds to the grain size attained prior to superplastic deformation. That is, equation (5.1) can be re-written to relate the grain sizes d_0 and d_1 with stresses σ_0 and σ_1 at the onset of plastic strain (ε_0) and at any selected strain level ε, respectively:

$$\sigma_1 = (\frac{d_1}{d_0})^{p/n} \sigma_0 \qquad (5.2)$$

where p = n =2. For this purpose, the stress-strain curve (Fig.4.3.3b) and the grain size in the gage section as a function of strain (Fig.4.4.2), both at a constant strain rate of $\dot{\varepsilon} = 1x10^{-3}/s$

and T = 530°C were used. The calculated stress (σ_c) is plotted as a function of strain in Fig.5.1. Also included is the experimental stress (σ_e)-strain curve for comparison. It is seen that the concurrent grain growth is not able to fully account for the increase in flow stress with increasing strain. Similar difference between the experimental and calculated (on the basis of instantaneous grain size) stress-strain curves was reported [133] in the Al-Cu eutectic alloy, especially, at higher strain rates and lower temperatures, and the difference between these two flow stresses at the same strain level was attributed to dislocation activity. In AA8090 Al-Li alloy, the differential flow stress may also be the result of dislocation activity, but there does not appear to be any investigation to account for flow strengthening employing dislocation activity in the literature.

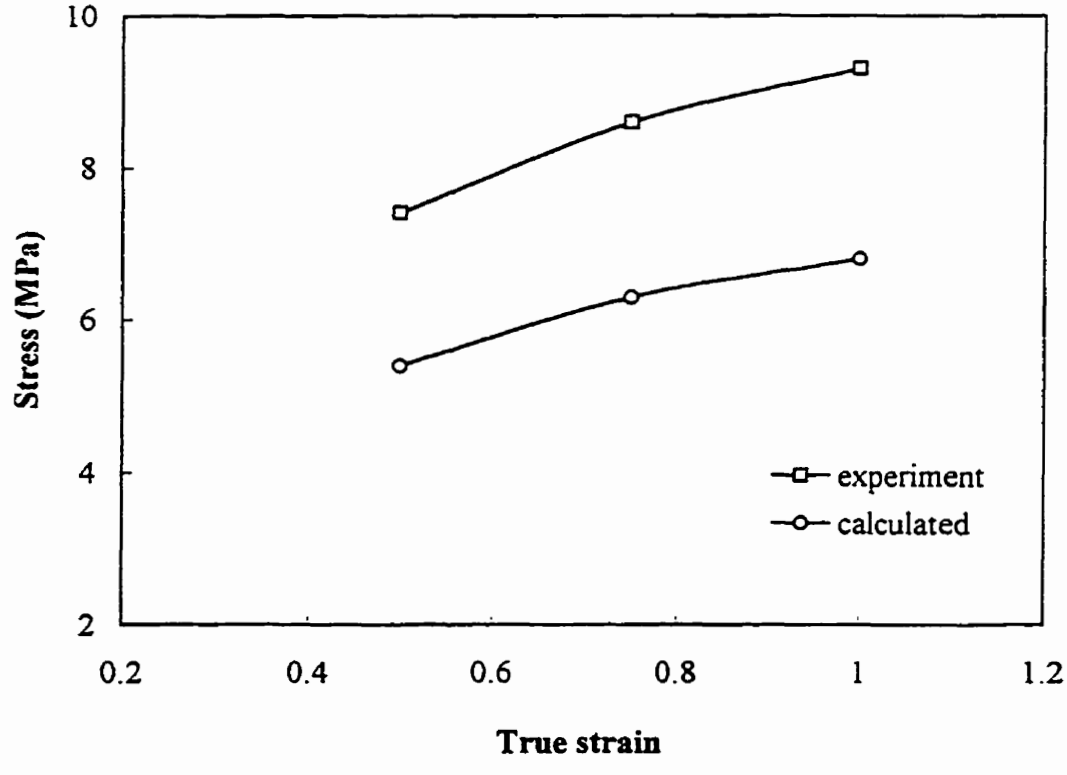

Fig.5.1. Comparison of flow stresses obtained from experiment and calculation.

Since texture is an accumulated measure of dislocation activity through a deformation process, it is possible to correlate texture intensity with the flow behavior. At selected strain levels, the increase in flow stress ($\Delta\sigma$), with reference to the stress at the onset of plastic strain, was calculated from the results at deformation condition of $\dot{\varepsilon} = 1x10^{-3}/s$ and T = 530°C. Corresponding to the same strain levels, the maximum average intensities of texture were also calculated for the full thickness sheet (I_t) by applying rule of mixture, viz. $\bar{I}_t = (1/3I_c + 2/3I_s)$, to the data obtained from the center (I_c) and the surface (I_s) materials. The plot between the values of $\Delta\sigma$ and $\bar{I}_t$, as shown in Fig.5.2, was observed to be linear, which reflects that an increase in flow stress is accompanied by texture weakening during superplastic deformation. This relationship can be also expressed by power law of type

$$\Delta\sigma = 19.21\ \bar{I}_t^{-0.65} \qquad (5.3)$$

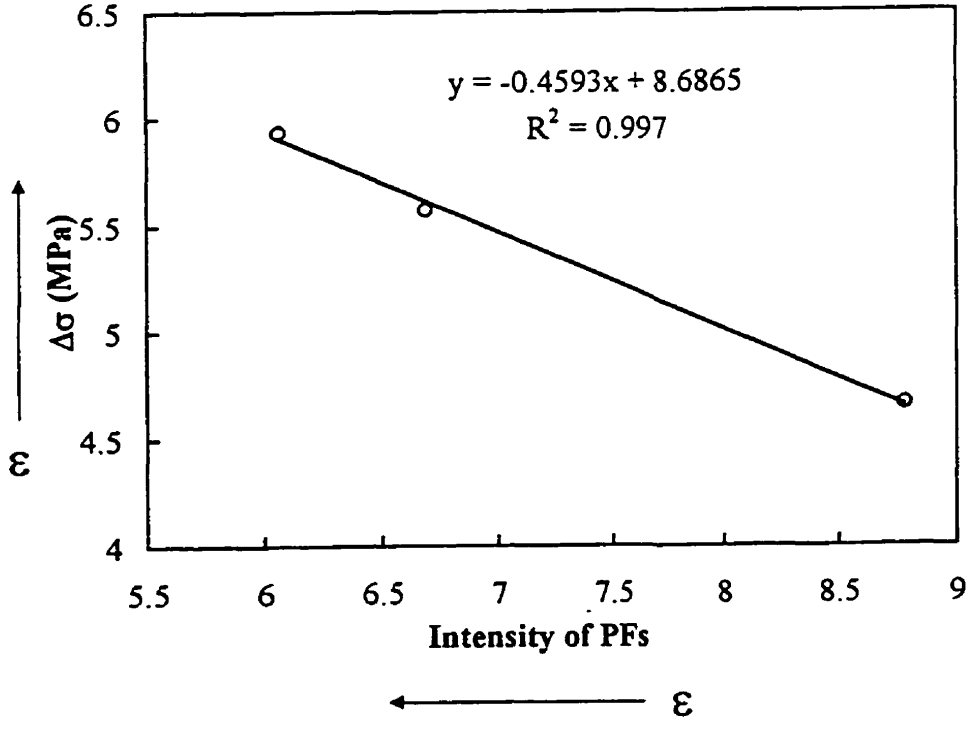

Fig.5.2. The relationship between $\Delta\sigma$ and $\bar{I}_t$. As marked by arrows in the figure the increase in $\Delta\sigma$ is related to the decrease in $\bar{I}_t$ following superplastic deformation.

Although it requires further work to understand the relationship between flow stress and texture during superplastic deformation (equation 5.3), it clearly indicates that dislocations play a important role beyond accommodating grain boundary sliding. Bate and his coworker [24] suggested the dislocation slip mechanism for superplastic deformation, whereas Pu et al [26] stressed the importance of grain boundary sliding. In view of these, the mechanism involving dislocation slip independently and its combination with grain boundary sliding appear to be more appropriate for superplastic deformation.

5.2. Optimum Superplastic Condition for AA8090 Al-Li Alloy

Generally, optimum superplasticity is exhibited under the strain rate, temperature and microstructural conditions (grain size) under which the value of strain rate sensitivity index (m) is maximum [35]. In several superplastic materials, the ductility has been shown to increase with increasing test temperature and decreasing grain size. In the present AA8090 Al-Li alloy, both the maximum ductility and the maximum m value were noted in the temperature range of 500-530°C (Fig.4.3.9), and the strain rate range of 10^{-4}-10^{-3}/s (Table 4.3.2). Similar optimum conditions have also been reported earlier for this material [12, 16]. By examining the ductility values in Table 4.3.2 and the nature of corresponding stress-strain curves (Figs.4.3.1, 4.3.3), as expected, it is observed that the maximum ductility occurs when deviation from steady state condition is minimum. For example, the maximum ductility of 700% was obtained at T = 500°C and at a strain rate of $1x10^{-4}$/s, at which the stress-strain curve shows almost a steady state. By examining the variation in several parameters during

superplastic deformation in the present study, it appears worthwhile to consider the interrelationship among them to account for the variation in ductility as a function of temperature. Ductility (δ) (Fig.4.3.10), strain hardening exponent (n_s) (Fig.4.3.5), strain rate sensitivity index (m) (Fig.4.3.8), strain exponent for grain growth (q) (Table 4.4.1), and grain size (d) attained at a constant strain level (Fig.4.4.3) are replotted as a function of temperature in Fig.5.3. Also included is the variation in the instability parameter I which is defined as [134]

$$I = \frac{1 - m - \gamma}{m} \qquad (5.4)$$

Here γ is the hardening parameter as defined by Hart [135], viz.

$$\gamma = \frac{1}{\sigma}\frac{\partial \sigma}{\partial \varepsilon} \qquad (5.5)$$

In the present work, $\partial\sigma/\partial\varepsilon$ was not calculated as such but, γ can be related to the strain hardening exponent as follows:

$$n_s = \partial \ln(\sigma)/\partial \ln(\varepsilon) = \varepsilon\,(1/\sigma)(\partial\sigma/\partial\varepsilon) = \varepsilon\gamma. \qquad (5.6)$$

Therefore,
$$\gamma = n_s/\varepsilon. \qquad (5.7)$$

Accordingly, I can be expressed as

$$I = \frac{1 - m - (1/\varepsilon)n_s}{m} \qquad (5.8)$$

As shown in Fig.5.3, ductility δ (a), m (c) and q (d) all increase first with temperature, attaining peak values at T~530°C, and then they decrease. The similarity between the variation in ductility and m as a function of temperature is in general agreement with the property of superplasticity. The decrease in ductility and m value beyond T~ 530°C can be

attributed to excessive grain growth, whereby the material loses its superplasticity. However, the concurrent increase in grain size, below the critical level (typically $d \leq 10\mu m$), is suggested to be beneficial to superplasticity. It has been reported that m increases with concurrent grain growth during superplastic deformation of IN744 microduplex steel [136]. This is because grain growth takes place by grain boundary migration which, in turn, is known to be essential to accommodate continued grain boundary sliding. This may also be the reason that ductility increases with increase in temperature in spite of grain growth (Fig.5.3d). The increase in strain hardening exponent (Fig.5.3b), typically in the temperature range of 350-500°C, can raise the magnitude of uniform strain, and so contribute to the improvement in ductility, when deformation involves significant dislocation activity. The importance of initial strain hardening in the development of superplastic ductility of an Al-Li alloy has been also emphasized by Ash and Hamilton [67]. As analyzed by them, the value of I, which combines both m and n_s, provides a good indication of relative tensile stability. By considering the values of m and n_s to evaluate I and plotting the same as a function of temperature at various strain levels, Fig.5.3f, leads to the following important implications. As seen in this figure, I decreases with increase in temperature, and reaches plateau or the minimum values at T = 500-530°C. One would expect the maximum ductility when I tends to be zero. Probably, this is the reason that the maximum ductility occurs around these temperatures.

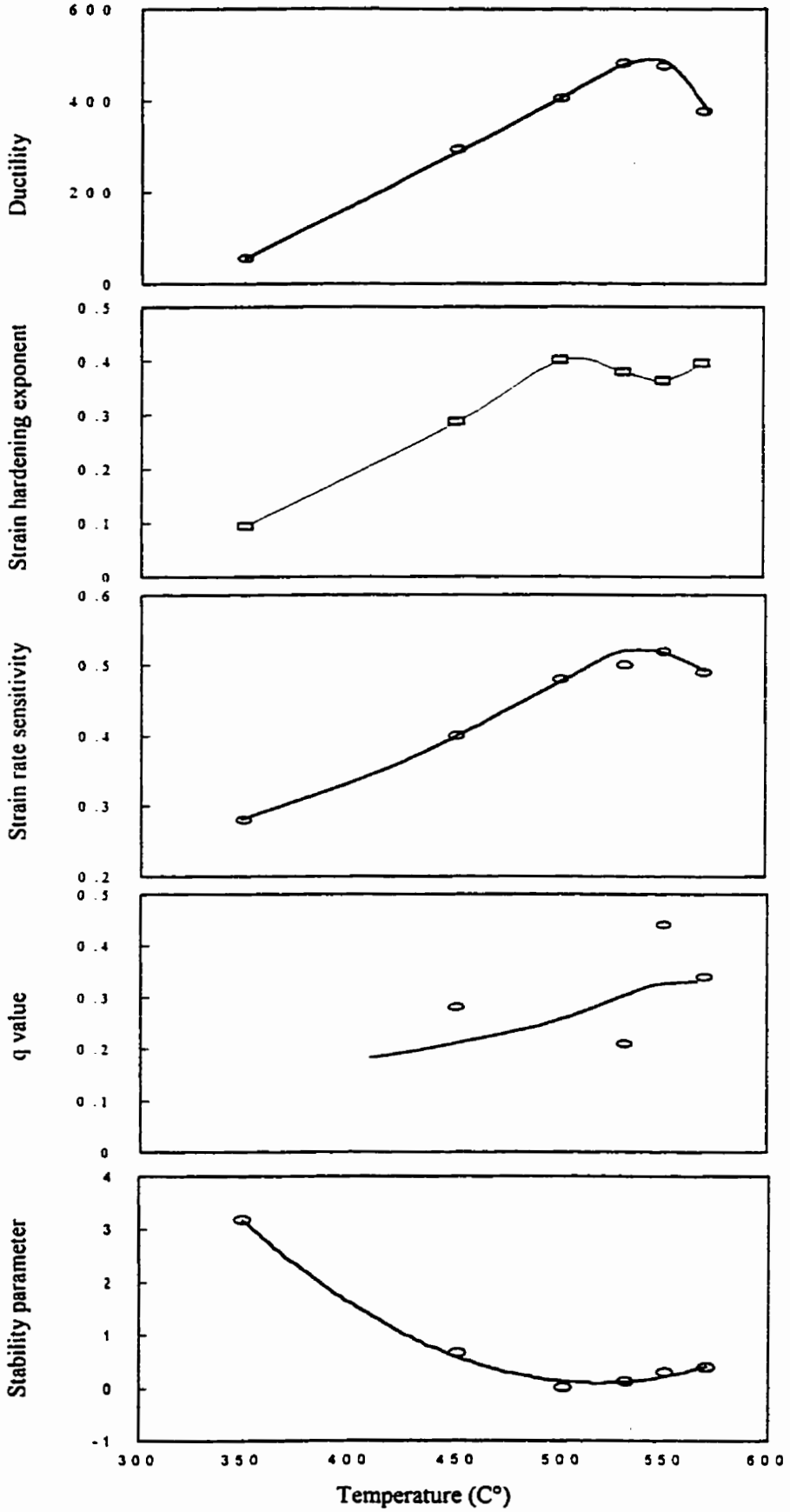

Fig.5.3. An indication of optimum superplastic temperature from several parameters, continue—

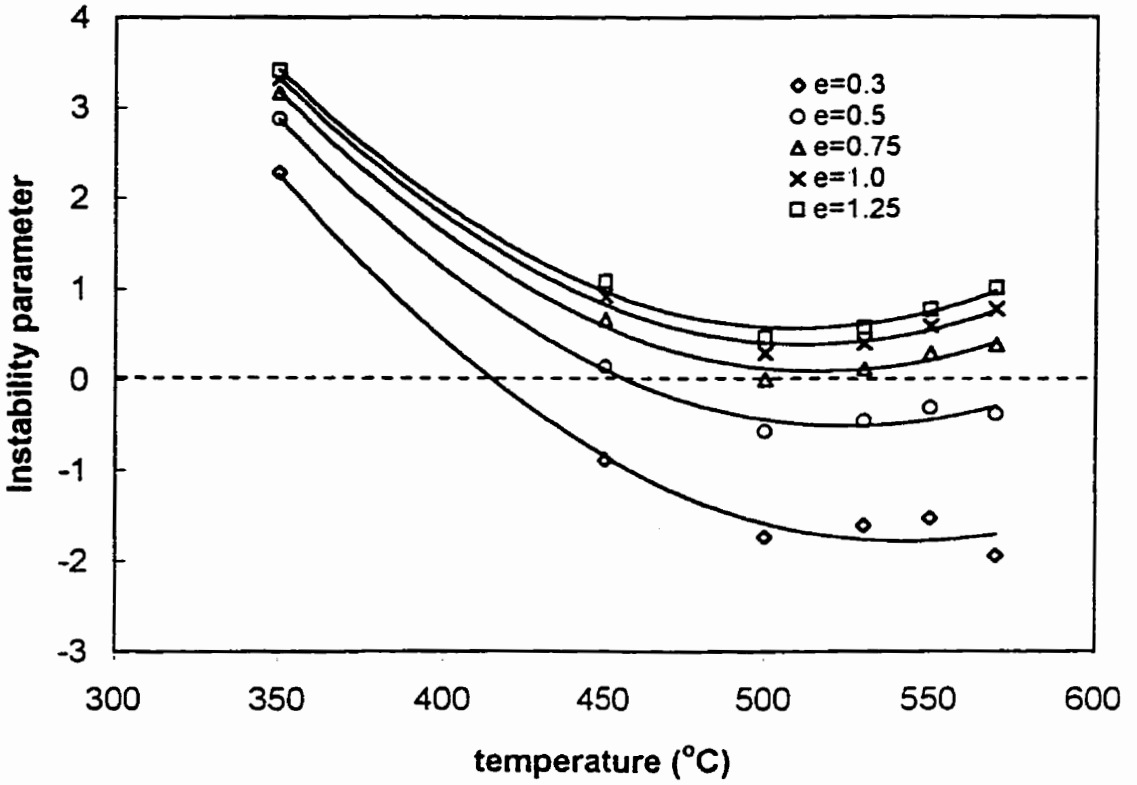

Fig.5.3f. Instability parameter (I) as a function of temperature for testing at a strain rate of $1x10^{-3}/s$.

The variation in I as a function of temperature at different strain levels delineates two distinct behaviors. (a) I becomes negative at smaller strains (typically $\varepsilon<0.75$) and at temperatures above ~400°C. (b) At larger strains ($\varepsilon>0.75$), I increases with increase in temperature subsequent to the initial decline without going to negative values. The decrease in I, at lower temperatures may be due to inhomogeneous deformation like necking, which is caused by preferential dislocation activity. This is supported by the fact that less texture weakening occurred in the surface layer and no texture weakening occurred in the center layer (Table 4.4.2) at T = 350°C.

The microstructural examination showed that both texture weakening and grain shape evolution became more pronounced at $\varepsilon = 0.75 - 1.0$, Fig.4.4.8. Therefore, this strain range may represent a transition in microstructural evolution during superplastic deformation. This may also indicate a transition in the nature of inter-dependence of concurrent microstructural state and the corresponding deformation mechanism. The coincidence of this transition strain with the inflection in the variation of I vs. T plot (Fig.5.3) suggests the existence of some correlation between I and the micromechanism for superplastic deformation, which was discussed earlier in section 5.1, that the earlier part of straining ($\varepsilon < 0.75$) is likely to be associated with dislocation activity (texture weakening), whereas the latter part of deformation is dominated by grain boundary sliding. This is similar to the observation of Liu and Chakarabarti [75] on 7050 Al alloy, although the transition they observed occurred between the strains of 0.4 - 0.75.

5.3. Anisotropy in Flow Behavior

The stress-strain curves of the center material (Fig.4.5.5.), surface material (Fig.4.5.6) and the full thickness sheet (Fig.4.3.12) showed some degree of anisotropy during superplastic deformation. In the center material, the 90° orientation showed the maximum flow stress whereas the 0° orientation showed the minimum, which is opposite to the trend shown by the surface material. These two opposite trends in the two sections of the same sheet individually, can be the cause for minimum anisotropy in the full thickness samples. The fact that higher flow stress exhibited in the 0° orientation than that observed in the 90° orientation in the full thickness samples, implies that the surface material dominates the flow behavior

because of its larger proportion; the full thickness consists of two sections of the surface material and one section of the center material.

Anisotropy during superplastic deformation in a large number of materials has been attributed to the presence of texture and/or elongated grains [36]. In the Pb-Sn eutectic alloy, anisotropy was eliminated at a strain of ~300% due to the break-up of the original directionality of the microstructure rather than due to the texture evolution [137]. On the other hand, the analysis of anisotropy in a superplastic duplex stainless steel by Song and Bate [138] led to the suggestion that the crystallographic texture may be more appropriate to explain the anisotropy during superplastic deformation. Although there exists evidence for some variation in texture during superplastic deformation of AA8090 Al-Li alloy [14], when deformed in the 0° and 90° orientations only, but, no systematic study appears to have been conducted to understand the flow anisotropy. However, anisotropy in this alloy has been extensively studied at room temperature [20, 95, 96, 108, 109, 110, 111, 112]. Such anisotropy is explained by the variation in Taylor factor (σ_y/τ_{crss}, where σ_y and τ_{crss} are the yield stress and critical resolved shear stress, respectively), associated with different texture components as a function of orientation (angle to rolling direction) [139]. Song and Bate in their study on superplastic duplex stainless steel found some similarities in the anisotropy observed at the low and high temperature deformation. Furthermore, as described in this investigation in section 4.4, there was texture weakening during superplastic deformation, but no change in the type of textures. Therefore, the anisotropy during superplastic deformation of AA8090 Al-Li alloy is analyzed below by utilizing the information available from the studies performed at room temperature.

From the literature, Fig.2.8, the values of σ_y/τ_{crss} were taken for Cu, S and Bs texture components at the angles of 0, 30, 45 and 90° to rolling direction. These values were used to calculate the average values of σ_y/τ_{crss} for the present AA8090 Al-Li alloy sheet according to the equation

$$\overline{M} = \frac{\sum v_i M_i}{\sum v_i} \qquad (5.9)$$

where at any given orientation, $\overline{M}$ is the average value of σ_y/τ_{crss}, M_i is the value of σ_y/τ_{crss} for ith type of texture component having volume fraction of v_i. The mean values of v_i for different textures in the surface and center materials were taken from the respective zones in Fig.4.2.6 (c). The values of σ_y/τ_{crss} thus calculated are plotted as a function of orientation angle in Fig.5.4.

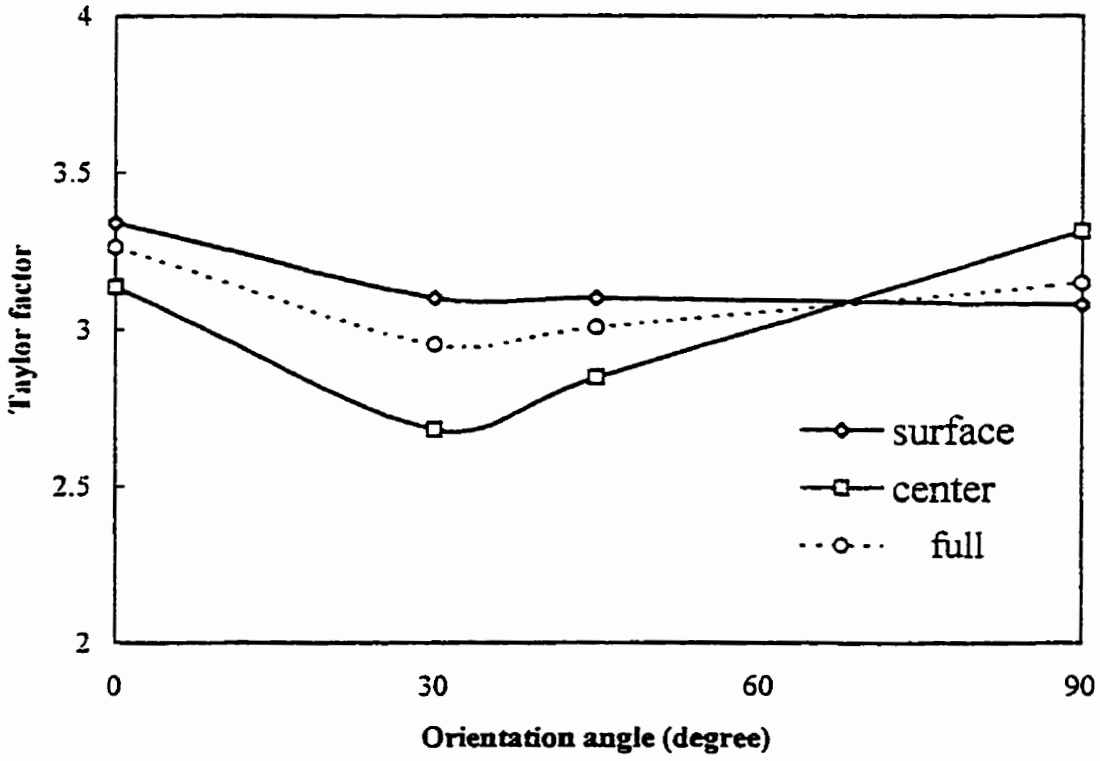

Fig.5.4. Calculated values of σ_y/τ_{crss} as a function of orientation.

Also included in this figure is the one for the full thickness sample, which is calculated by applying the rule of mixture to the values obtained for the surface and center materials. This will be discussed in the next section. Comparison of this figure with the stress-strain curves showing anisotropy, Figs.4.5.5 and 4.5.6, suggest many similarities — (i) $\overline{M}$ at 0° is less than that at 90° in the center material and so also is the trend for the variation in the flow stress at the corresponding orientations; (ii) $\overline{M}$ at 0° is more than that at 90° in the surface material and so also is the trend for the variation in flow stress at the corresponding orientations. Thus, the anisotropy in flow stress at 0 and 90° could be attributed to the presence of texture. However, the nature of variation in $\overline{M}$ as a function of orientation angle fails to explain the fact that $\overline{M}$ for the center material has lower values in the intermediate orientations (30 and 45°) whereas, in contrast, the magnitude of flow stress in these orientations is seen to be between that in the 0 and 90°. Probably, such a deviation may not be related to dislocation activity but may originate from the operation of other mechanisms for superplastic deformation. This further supports the suggestion made earlier that superplastic deformation in this material takes place by a combination of slip and other mechanisms, such as grain boundary sliding. Although Liu and Chakabararti [75] made the similar suggestion, as mentioned previously, they assumed another possibility of low angle grain boundary sliding, but it is unlikely and difficult to prove.

As shown in Figs.4.5.5 and 4.5.6, the stress-strain curves of specimens in different orientations tend to merge together for the center material, whereas the difference tends to widen in the case of surface material. However, no difference was noticeable in the grain

morphology and grain size in specimens of different orientations at $\varepsilon = 1.0$. The variation in maximum intensity in PF (I_c and I_s) in Fig.4.5.9 indicates that the texture weakening in the center materials with different orientations is similar and so also are the microstructures. This is suggested to be the reason that the stress-strain curves in different orientations tend to merge to a common stress level at large strain. In the surface material, the grain morphology and grain size for different orientations are comparable, the texture intensity suggests a different degree of weakening, Fig.4.5.9, depending on the orientation angle. Such a difference in texture is suggested to be the source of increasing anisotropy in flow stress in the surface material.

5.4. Composite-like Behavior of the Full Thickness Sheet

As seen in Figs.4.2.1 and 4.2.6(c), the microstructures in the center and surface layers were distinctly different. This variation in microstructure causes a significant difference in the flow properties of these two materials, Fig.4.5.1. When the full thickness sample is subjected to deformation, these two materials constituting a microstructurally composite material, deform under isostrain condition. Therefore, the flow stress of the full thickness sample should be related to the properties of the individual material. Since two thirds of the thickness (one third in each side) of the sheet belong to the surface material and one third represents the center material, the flow stress for the composite like full thickness sheet can be written by the rule of mixture, as follows:

$$\sigma_m = 1/3\ (\sigma_c) + 2/3\ (\sigma_s) \qquad (5.10)$$

Here, σ_m represents the calculated flow stress of the full thickness material by using the flow stresses of the center material, σ_c, and the surface material, σ_s. The values of σ_m thus calculated are plotted as a function of strain for different orientations, along with the plots of σ_c and σ_s in Fig.5.5. Also included for comparison are the experimental stress-strain curves of the full thickness material.

As seen in Fig.5.5, there is a reasonably good agreement between the calculated and experimental stress-strain curves for 0° orientation. However, when the orientation angle is changed, the calculated and experimental stress-strain curves are seen to be comparable only during the earlier part of the deformation, whereas, in the later part the calculated stress-strain curves are seen to deviate from the experimental ones and tend to reach close to that of the surface materials. On the other hand, the experimental curves tend to reach towards that of the center materials. The agreement between the calculated and the experimental stress-strain curves at 0° orientation may be attributed to the similarity in the texture intensities in the center and surface materials, Fig.4.5.9. Similarly, the deviation at other orientations could be due to the difference in the texture intensities between the two different materials. Furthermore, the following other two possibilities are suggested to explain the difference between the experimental and calculated stress-strain curves. First, the nature of variation in microstructural evolution in the center and surface layers continuously changes with progress in deformation, in which case the rule of mixture based on the initial microstructures may not be applicable. Second, in the case of composite microstructures, the deformation of the surface material can be constrained by the deformation of the center material.

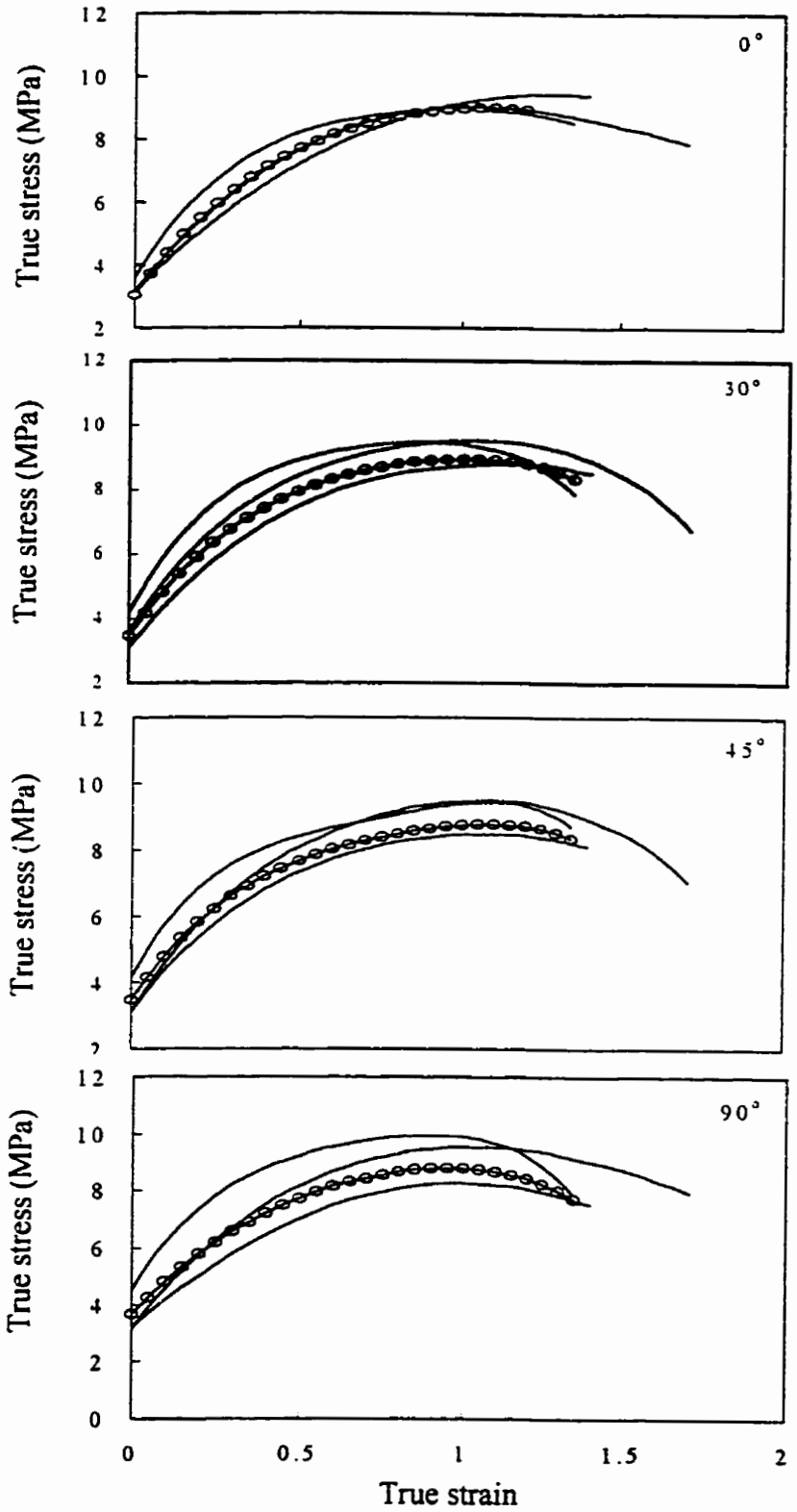

Fig.5.5. Comparison of composite-like flow behavior with the rule of mixture, in each of the figures the curve being of the highest stress level represents the center material, the one being of lowest stress represents the surface material, the intermediate represents the full thickness sheet, and the one with dots represents that calculated by the rule of mixture.

Probably, this is the reason that the nature of variation in texture is different for the same sections of the sheet material when measurements are conducted on specimens from (a) the surface or the center material individually (Fig.4.5.4), and (b) the surface or center layers in the full thickness sheet (Fig.4.4.12). It may be noted that the distributions of precipitates in both the center and surface layers were not different, and hence there will be no effect of this on the difference in the texture evolution of the two materials.

The mechanisms for superplastic deformation in the surface material may have some similarity as those discussed in the literature for the materials with fine equiaxed grains. However, the mechanisms for superplastic deformation of the center material could be different due to the presence of pancake shaped grains as well as texture. From the textural analysis in such microstructures, Bowen [20] suggested that grain boundary sliding and grain rotation can still be the dominant deformation mechanisms, but it will be feasible only in the plane of the sheet. Contrary to this, the microstructural examination in the present work, Fig.4.4.8, clearly revealed a change in grain shape from pancake to equiaxed during superplastic deformation. Therefore, the mechanism in the center material, at least, in the early part of deformation, should involve significant participation of dislocation activity, as suggested by the textural evolution in the present study. It may be noted that the nature of variation in flow stress for the full thickness samples (e.g. Fig.5.5) was comparable with the variation in Taylor factors (Fig.5.4) obtained from the rule of mixture. However, according to the Taylor factors, calculated as an average of different texture components (Fig.5.4), the flow stress for the surface material should be higher than that of the center material. But, as

seen in Fig.5.5, the flow stress for the center material is higher than that for the surface material. This suggests that the role of dislocations during superplastic deformation may be more complex than in conventional plastic deformation. However, it is not clear at this stage as to how to incorporate the slip mechanism in superplastic deformation, as was also pointed out by Bate and his coworker [24].

5.5 Constitutive Relationship for Superplastic Deformation

Since the stress-strain curves at various conditions of testing exhibit strain hardening (Figs.4.3.1 and 4.3.3), the determination of exact value of the various parameters for the constitutive relationship, which is meant for steady state conditions, is not possible. However, if it is assumed that the variation in flow stress with strain can be accounted for by the concurrent microstructural evolution, then appropriate corrections can be attempted to derive the parameters of the constitutive relationship for steady state. In the present study, the flow stress, at relatively higher temperatures and lower strain rates, tended to approach a steady state at strain levels of ~ 0.75. By considering this pseudo-steady state, the values of strain rate sensitivity index, m, and activation energy, Q_t, provide a reasonable guide for understanding the mechanism for superplastic deformation.

The value of m ~ 0.5 (n ~ 2) obtained in this study are comparable with that reported for this material by other investigators [12, 23]. This is also in agreement with the predictions of various theories (Table 2.1) proposed for explaining superplasticity. The average value of Q_t

~ 84 kJ/mol obtained in this study is also comparable with the activation energy of grain boundary diffusion 84 kJ/mol and also with that for dislocation pipe diffusion [140]. This value of Q_t is different from the value of 141 kJ/mol reported by Pu et al [26] for the high temperature superplasticity. But, it is close to the value of 92 kJ/mol reported [26] for the low temperature superplasticity. According to the present value of activation energy (84 kJ/mol), the mechanism for superplastic deformation of this material can be suggested to involve grain boundary sliding and dislocation slip as well. Since the previous discussion about evolution of texture during superplastic deformation gives strong evidence of dislocation slip, the mechanism is suggested to be as follows.

The deformation in the center material containing pancake grains may involve the dominance of intragranular slip, with limited grain boundary sliding. The deformation of the surface material is likely to be dominated by grain boundary sliding as a result of equiaxed grains present there.

Since in the present work no stress-strain rate data were obtained as a function of grain size, the exponent of inverse grain size (p) could not be determined. However, with the assumption that the increasing flow stress with strain is purely due to increase in grain size (d), an attempt to correlate the change in flow stress with the concurrent change in grain size can give some estimation of p. Accordingly, p was calculated by using the relationship

$$p = n\frac{\partial \ln(\sigma)}{\partial \ln(d)} \qquad (5.11)$$

where the values of σ (Fig.4.3.1) and d (Fig.4.4.2) correspond to the same strain level. The

values of p calculated at 530, 550 and 570°C at a constant strain rate $1x10^{-3}$/s, were found to be 1.5, 1.3 and 2.4, respectively, with an average of 1.7.

As shown in Fig.5.1, grain growth alone could not adequately explain the variation in flow stress with strain, but it is likely that additional strengthening resulted by dislocation activity resulting in texture modification. In view of this, the experimental constitutive relationship for superplastic deformation of AA8090 Al-Li alloy should incorporate not only the effect of grain size but texture as well. In this direction, a systematic and thorough study needs to be conducted. However, an attempt will be made to do preliminary analysis based on the results obtained in this study.

In spite of superplasticity shown by this material, flow stress is sensitive to not only the strain rate but also the strain. Equation 2.2 incorporates the effects of both strain and strain rate on flow stress, whereas equation 2.5 incorporates only the effect of strain rate, because under steady-state condition flow stress is independent of strain. By knowing the variations in flow stress and microstructural parameters, like grain size and texture, with strain, a relationship between stress and microstructures could be established. This enables to substitute the relationship between stress and strain in terms of microstructures, which can be directly employed in equation 2.5. By combining equations 2.2, 2.5 and 5.3 the tentative relationship for superplastic deformation of this material could be modified as:

$$\dot{\varepsilon} \propto \frac{I_t^{-0.65}\sigma^2}{d^{1.7}}\exp\left(-\frac{84kJ/mol}{RT}\right) \qquad (5.12a)$$

At a constant temperature, this equation can be rewritten as

$$\dot{\varepsilon} = \left[K_e \frac{I_t^{-0.65} \sigma^2}{d^{1.7}} \right]_T \qquad (5.12b)$$

where, the proportionality constant K_e depends on test temperature, other structural parameters and the mechanism for deformation. Here, the value of K_e was estimated to be 0.0016 by using experimental values of I_t, σ, and d at the test condition of 530°C and the strain rate of $1x10^{-3}$/s, which are summarized in Fig.5.6. In Fig.5.7, the plot of $K_e(\sigma^2/d^{1.7})$ vs. $1/I_t^{-0.65}$ gives a straight line whose slope represents the value of strain rate, and is found to be equal to 10^{-3}/s which is the same value at which the tests were conducted. That is there is some validity to the proposed constitutive relationship. However, a much more thorough analysis including different temperatures, strain rates and grain sizes need to be undertaken to fully validate it.

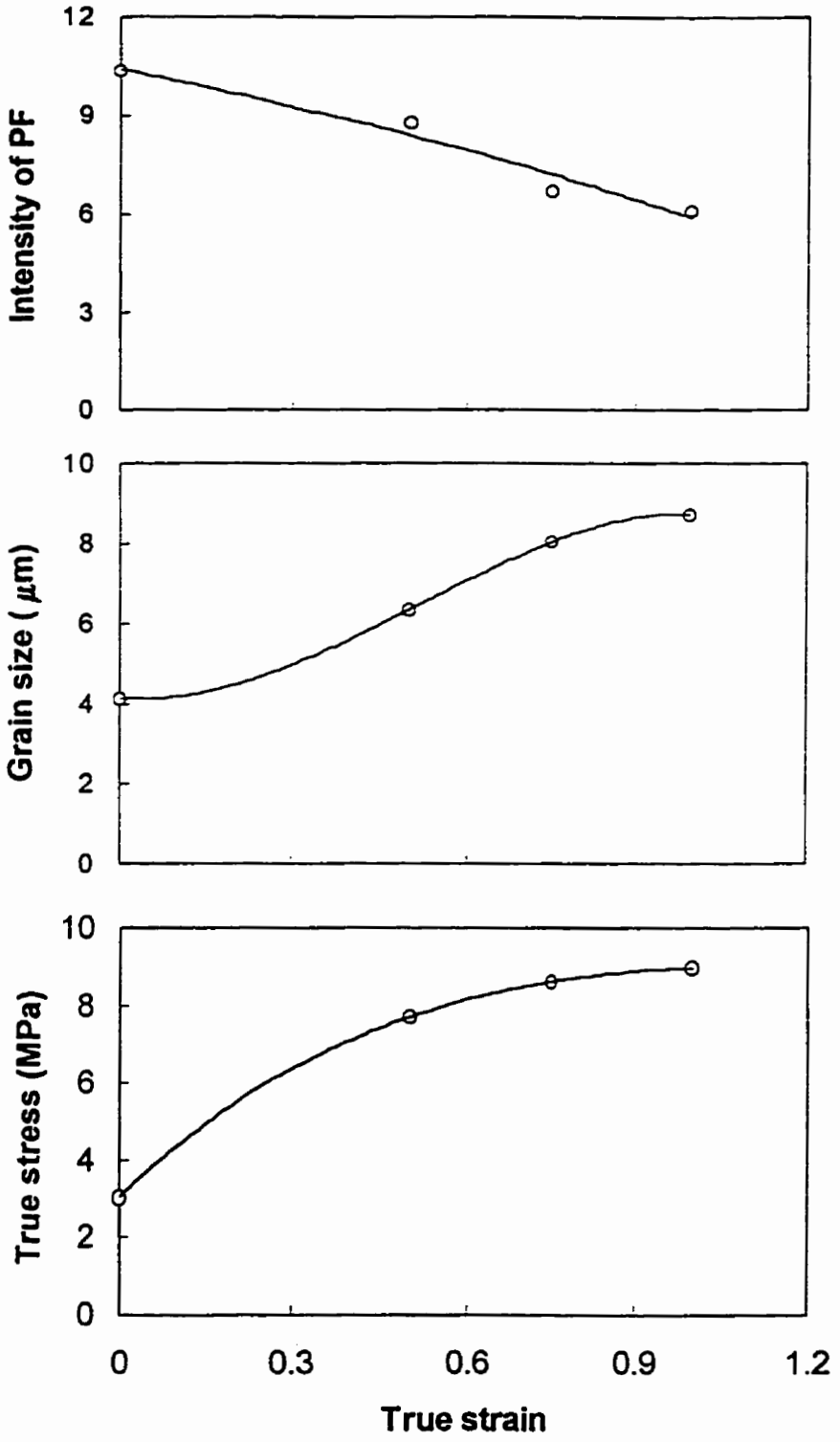

Fig.5.6. Summary of three parameters used in equation 5.12b, the intensity of the texture obtained by the rule of mixture, the average grain size and the flow stress, as a function of strain at deformation condition of 530 ℃ and a strain rate of $1x10^{-3}$/s.

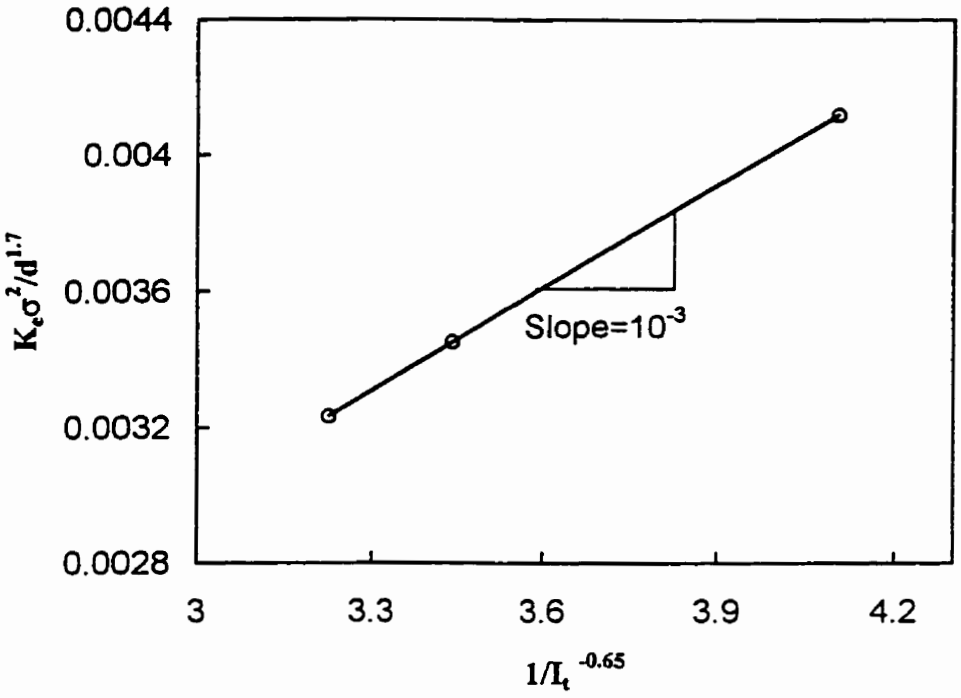

Fig.5.7. The relationship between $K_e(\sigma^2/d^{1.7})$ and $1/I_t^{-0.65}$ (K_e = 0.0016)

CHAPTER 6
CONCLUSIONS

The investigation on superplastic flow behavior of and concurrent microstructural evolution in AA8090 Al-Li alloy sheet, containing nearly equiaxed grains with copper-type texture in the surface section and pancake grains with brass-type texture in the center section, leads to the following conclusions.

1. Static annealing in the temperature range of 530 - 570°C did not affect the grain shape and texture but cause grain growth, indicating an absence of discontinuous recrystallization. This was the consequence of the presence of fine β′ (Al_3Zr) precipitates in the alloy.

2. The stress-strain curves obtained at strain rates ranging from $1x10^{-5}$ to $1x10^{-2}$/s, and temperatures ranging from 25 to 570°C, exhibited strain hardening to varying levels during the early part of deformation. The variation in strain hardening exponents with increasing temperatures exhibited four distinct regimes, which can be explained by the dominance of dislocation slip, grain growth, dissolution of precipitates and rapid grain growth for regimes I to IV, respectively.

3. The maximum ductility of 700% was obtained under temperature and strain rate conditions of 500°C and $1x10^{-4}$/s, respectively. The nature of variation in ductility as a function of temperature was seen to follow the same trend as exhibited by the variation in strain rate sensitivity index m.

4. The instability parameter (I), calculated from strain rate sensitivity index and strain hardening rate and which relates to the uniformity of deformation, was sensitive to temperature and strain levels. While, I decreased with increasing temperature below 450°C, the same approached a plateau (dI/dT = 0) at temperatures around 500-530°C. This is suggested to be one of the reasons for the maximum ductility obtained under this condition.

5. During superplastic deformation, the initial pancake grains in the center region changed towards equiaxed ones. Also, there occurred grain growth and texture weakening in both the center and surface sections. Such microstructural evolution accounted for the observed strain hardening.

6. Texture weakening occurred with increasing strain during superplastic deformation, and the magnitude of weakening within superplastic region was independent of strain rate and temperature. However, under non-superplastic condition of either strain rate or temperature the texture weakening was found to be much less in the surface region and almost absent in the center region.

7. The flow behavior of the full thickness sample could be reasonably explained by the flow properties of the separated center and surface materials according to rule of mixture. However, the concomitant texture evolution during superplastic deformation, depending on orientation, led to some difference in the experimental and expected flow stresses.

8. The stress-strain curves for various orientations were found to exhibit anisotropy in flow behavior, and the anisotropy was observed to be more prominent in the separated center and surface materials . Whereas the specimen oriented at 90° showed the highest flow stress and that oriented at 0° showed the lowest in the center material, the trend was reversed for the surface material. The difference in behavior of these two materials from the full thickness sheet can be attributed to the difference in their textural constituents.

9. The values of strain rate sensitivity index (m = 0.5) and activation energy for superplastic deformation (Q_t = 84 kJ/mol) support the predictions of several theories for superplasticity. However, the observed experimental dependence of flow stress and texture evolution led to a modified constitutive relationship.

10. Based on the grain structure and texture evolution during superplastic deformation, and their correlation with flow behavior, it is suggested that the mechanism for superplastic deformation in the early stage involves independent dislocation slip and grain boundary sliding. In the full thickness sheet, dislocation slip was dominant in the center section whereas grain boundary sliding was more favorable in the surface section.

CHAPTER. 7
FUTURE WORK

The mechanism deduced from this investigation emphasizes the occurrence of dislocation slip during superplastic deformation in addition to grain boundary sliding, which results in texture weakening. This dislocation activity is in addition to which occurs to accommodate the grain boundary sliding. This suggestion is reflected in the modified constitutive relationship by the inclusion of a texture parameter in it. However, from the present study only a limited amount of data was available to validate this constitutive relationship. Therefore, further research is needed to generate more data. The further tests planned are to:

1. Generate texture data as a function of strain for center and surface materials at the optimum superplastic condition;
2. Generate m, p, and Q values by changing grain size in the superplastic deformation range (temperature and strain rate);
3. Generate one set of data outside of superplastic range, either by reducing the test temperature or by increasing the strain rate.

The results of these test would be used to evaluate the validity of the constitutive equation proposed in this study.

APPENDIX
TEXTURE

A.1. Introduction

The property of a polycrystalline aggregate is determined by its microstructure. The microstructure of a polycrystalline material includes several items, like grain structure, second phase, interfacial features and dislocation structure. An additional component of the microstructure is the distribution of crystallographic orientation of individual grains. The crystallographic orientation of a grain may be different from those of others. All the grains may be oriented randomly, or may tend to cluster toward certain extent. When the orientations of the grains are non-random, the material is said to have a preferred orientation or texture. Texture of a polycrystalline material is a main source for anisotropy. At the same time, texture itself gives the information about the properties of the material and the processes responsible for its formation. From the point of view of dislocations, texture records the deformation history since a particular orientation state is the results of accumulated dislocation activity. Therefore, texture investigation has been considered to be a natural extension of metallography [141, 142]. Next, it is attempted to give a brief description about texture terms based on two reviews written by Bunge [143] and Mecking [144].

A.2. Texture Measurement

Diffraction of a polycrystalline material, by X-ray, neutron or electron, produces continuous Debye rings, if the grains in it are randomly oriented and they are of certain size. For a

material with preferred orientation, the distribution of orientation is no longer uniform. By analyzing the non-uniformity of the diffraction intensity, the preferred orientation in the material can be determined. X-ray diffraction is the traditionally and the most commonly used method to measure orientation distribution in a material. Recently, orientation imaging microscopy (OIM) has been developed. As has been described previously in section 3.5, it becomes a powerful tool in microstructural study of materials, especially for microtexture measurement [121, 122, 123, 124].

A.3. Presentation of Texture

a. Pole figures

A pole figure is a sterographic projection which shows variation in density of the poles at a given set of crystal planes in a material relative to the external reference directions. In case of rolled sheets, the projection plane is made parallel to the sheet surface or parallel to the sheet normal direction (ND), and the rolling direction (RD) and the transverse direction (TD) lie on this plane, which is shown in Fig.A1.

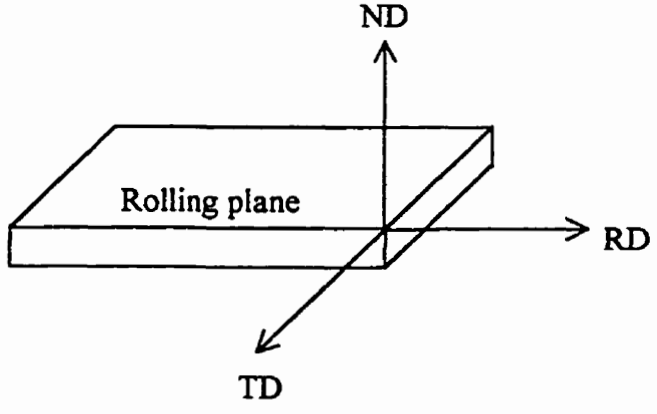

Fig.A1. Definition of orientations in a rolled sheet material.

Fig.A2(a) and (b) show (111) pole figures of two f.c.c. rolled sheet materials [143], copper and brass, respectively. They reveal that the poles are not randomly distributed, and most of the grains have orientations represented by the regions being of high (111) pole density.

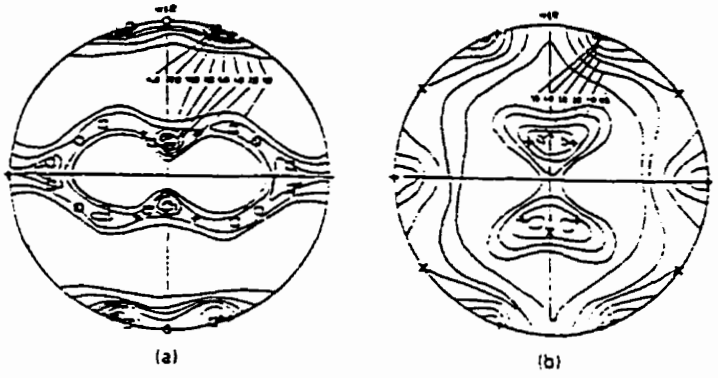

Fig. A2. (111) pole figures for Cu and brass after rolling at room temperature in (a) and (b) respectively. The symbols give the positions of the (111) poles of the main components, O:{112}<111>, □:{123}<634>, +{110}<112>, x {110}<100> [143].

Texture is often described by ideal orientation which is the orientation of a grain whose poles would lie in the high density region in the pole figure. For example, in case of cold rolled brass, if a single crystal with (110) parallel to the rolling plane is considered and the $[1\,\bar{1}\,2]$ is parallel to the rolling direction, the (111) poles of this crystal would lie approximately in the high density regions in the (111) pole figure as shown in Fig.A2(b) by the symbol +. Therefore, brass is said to have the (110) $[1\,\bar{1}\,2]$ texture. Ideal orientations or texture components, which are often found in Al alloys, are listed in Table A1 [145].

Table A1. Miller indices and Euler angles of most important orientations of Al and Al alloys after rolling and after recrystallization (approximate)

Orientation name	Miller indices {hkl}<uvw>	Euler angles			Type of texture component
		φ_1	Φ	φ_2	
C	{112}<111>	90	30	45	Rolling
S	{123}<634>	59	34	65	Rolling
B	{011}<211>	35	45	0/90	Rolling
Goss	{110}<100>	0	45	0/90	Rolling/recrystallization
Cube	{001}<100>	0	0	0/90	Recrystallization
$Cube_{RD}$	{013}<100>	0	22	0/90	Recrystallization
$Cube_{ND}$	{001}<310>	22	0	0/90	Recrystallization
R	{124}<211>	53	36	60	Recrystallization
P	{011}<122>	65	45	0/90	Recrystallization
Q	{013}<231>	45	15	10	Recrystallization

b. Orientation Distribution Function (ODF)

Sometimes, it is difficult to bring out the details of orientation distribution in a material when texture is presented as pole figures. However, with the development of improved data analysis by using computers, detail information of orientation distribution can be obtained from the calculated orientation distribution function. An orientation distribution function is defined as the volume fraction of grains in a material that have a given orientation. The data are then presented as a three dimensional orientation distribution function. Therefore, more details of orientation features in a material can be given.

The orientation between a grain in a polycrystalline material and the external directions is described by the orientation of the crystal coordinate system with respect to the sample

coordinate system. In order to find such orientation, the crystal coordinate system is brought to coincidence with the sample coordinate system, and then the crystal coordinate system is rotated in a certain sequence to bring back to the orientation of the crystallite. The angles, through which the crystal coordinate system is rotated, define the orientation of the crystallite in the sample. These angles are known as Euler angles. The sequence of rotations and the angular ranges are such that all possible orientations are covered [144]. Fig.A3 shows the definition of Euler angles ($\varphi_1, \Phi, \varphi_2$), in which K_A is the sample coordinate system and K_B is the crystal coordinate system.

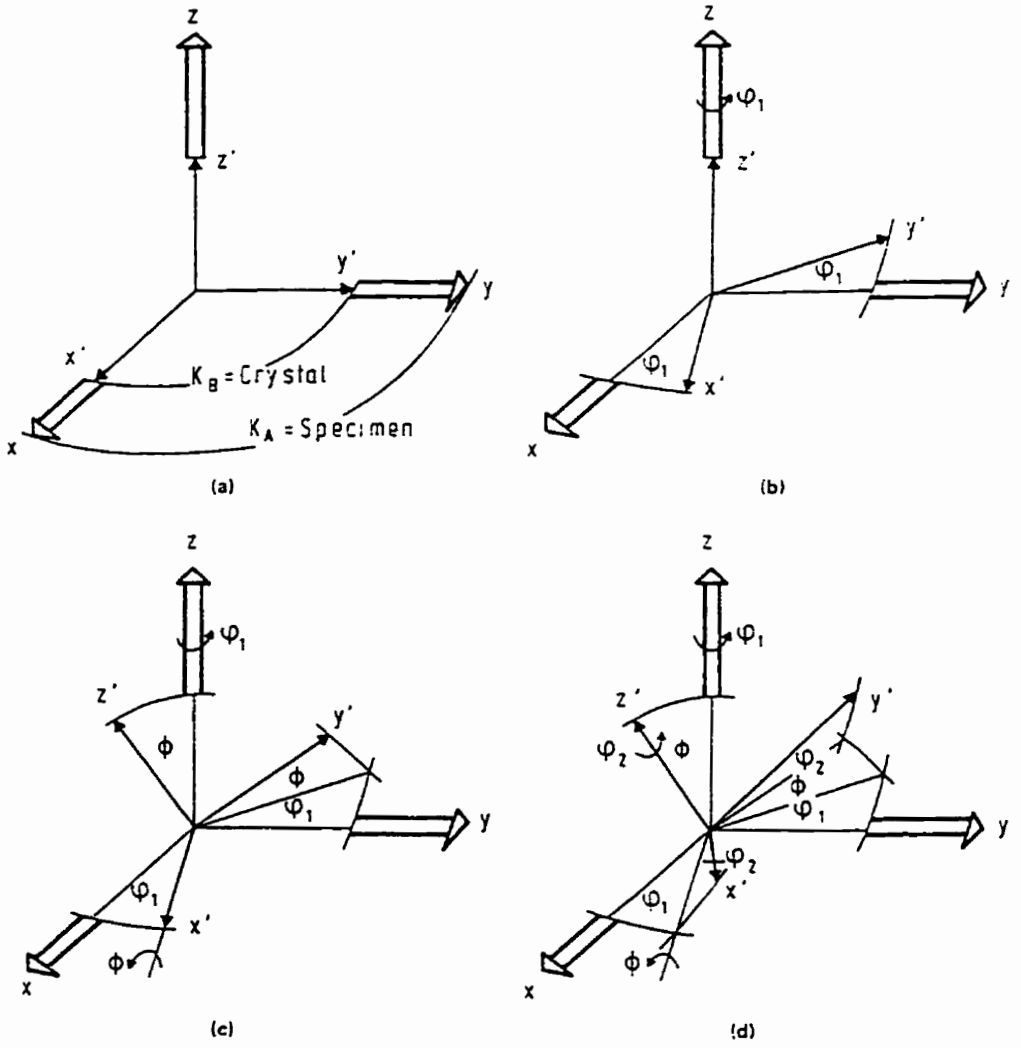

Fig. A3. Definition of the Euler angles [144].

These values of Euler angles are plotted in a Cartesian coordinate system which is called orientation space or Euler space. The orientation is usually obtained as a discrete distribution of points and is presented as equilevel contour lines in two dimensional sections containing φ_1, and Φ as variables with constant φ_2. Sections with 5 degree increment of φ_2 are often presented. Fig.A4 shows the stacked sections of ODF of a rolled Al alloy [146]. Fig.A5 shows a three dimensional picture of the same ODF [146], in which the distribution of orientation looks like a tube. This kind of orientation distribution is usually described by a term of orientation tube, and maximum density line in the tube is called skeleton line. Fig.A5 describes the common orientation feature of a rolled f.c.c. material. The α-fiber and β-fiber are usually used to describe the characteristics of the skeleton lines, and their changes with various variables.

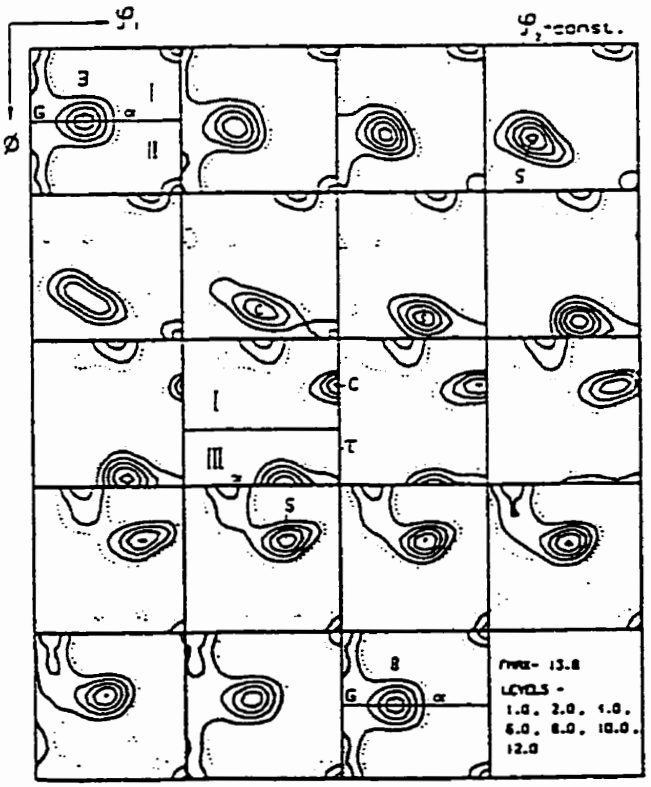

Fig.A4. Orientation distribution function of Al rolling texture in sections of Euler space [146].

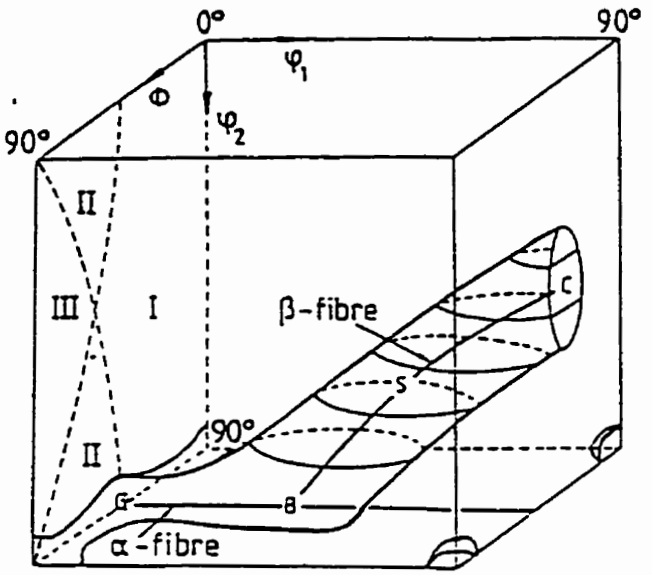

Fig.A5. Tubular distribution of orientation of Al rolling texture in the three dimensional Euler space, the orientation is same as Fig.4A [146].

Each point in Euler space can be associated the three Euler angles with a specific (hkl)[uvw] value. The figure showing the (hkl)[uvw] values in the Euler space for a given crystal system is know as the orientation chart. Orientation charts for cubic symmetry at constant φ_2 sections of Euler space are shown in Fig.A6 where only the important low integer values of the indices are shown [20]. By comparing the orientation charts with the sections of Euler space, one can identify the ideal orientations.

A.4. Rolling and Recrystallization Textures in f.c.c Materials

In f.c.c. rolled sheet materials, there are mainly two types of texture, copper type and brass type. The positions of the <111>, <110> and <100> poles of the main texture components in rolled f.c.c. materials are shown in Fig.A7 [143]. Details of distribution of orientations in these materials can be obtained form their ODFs.

In most of f.c.c. metals like Al and Cu, the dominant annealing texture is Cube (100)<001>. Usually, this texture appears a mixture with a number of other texture components, such as random orientation and parts of the rolling textures. However, the exact annealing texture depends upon the solute content of the alloy and the processing parameters such as annealing temperature, time, initial grain size and rolling reduction. The texture components that usually found in Al and Al alloys are shown in Table A1 by both Miller indices and Euler angles.

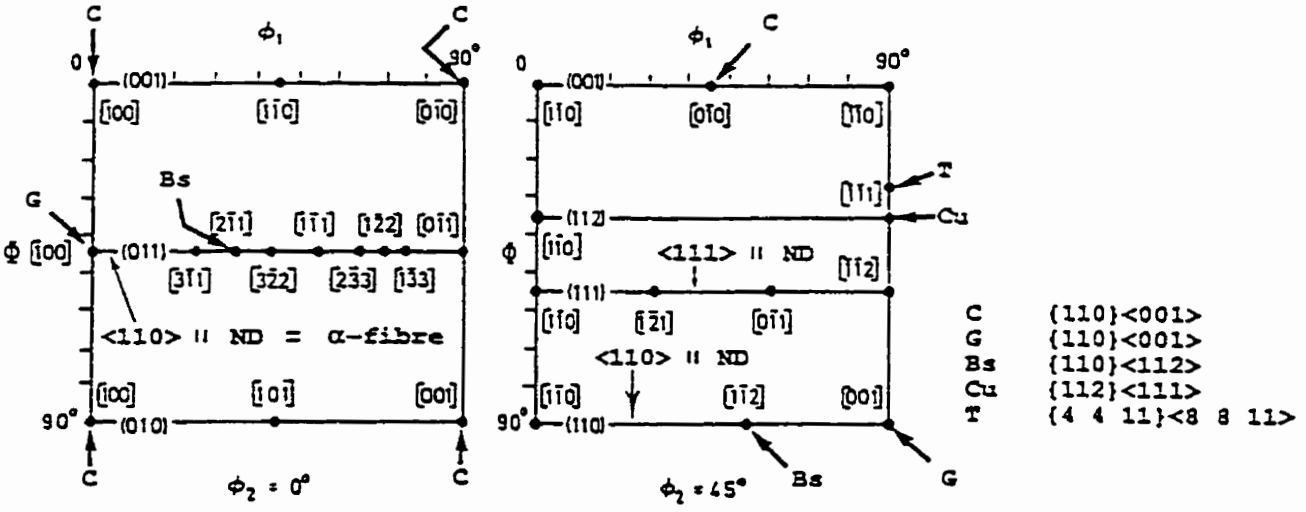

Fig.A6. Orientation charts of φ_2 = 0 and 45° sections through Euler space showing positions of various ideal orientations [20].

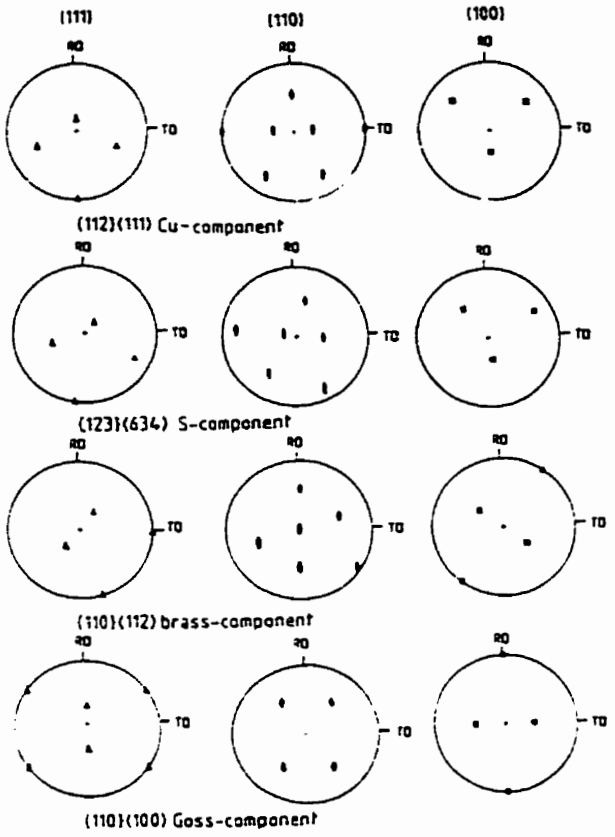

Fig.A7. Schematic illustration of pole figures of the positions of the <111>, <110> and <100> poles of the main components of the rolling texture in f.c.c. materials [143].

REFERENCES

1. Lavernia, E. J. and Grant, N. J., 1987, *J. Mater. Sci.*, **22**, 1521.
2. Sankaran, K. K. and Grant, N. J., 1980, *Mater. Sci. Eng.*, **44**, 213.
3. Jones, F. R., 1989, *Aluminum Alloys - Contemporary Research and Applications*, *Treatise on Mate. Sci. Technol.*, **31,** 605.
4. Quist, W. E., Harayanan, G. H. and Wingert, A. L., 1983, *Aluminum-Lithium Alloys II,* edited by Sanders Jr, T. H. and Starke Jr, E. A. (Warrendale, Metallurgy Society of AIME), 313.
5. Lavernia, E. J., Strivatstan, T. S. and Mohamed, F. A., 1990, *J. Mater. Sci.*, **25**, 1137.
6. Wert, J. A., Paton, N. E., Halmilton, C. H. and Mahoney, M .W., 1981, *Metall. Trans.*, **12A**, 1267.
7. Miller, W. S. and White, J., 1988, *Superplasticity in Aerospace II*, edited by. Heikkenen, H. C. and McNelley, T. R. (Warrendale, Metallurgical Society of AIME), 211.
8. Grimes, R., 1982, *Sheet Metal Industries,* **59**, 885.
9. Lloyd, D. J., 1986, *Can. Metall. Quart.*, **25**, 357.
10. Ghosh, A. K. and Gandhi, C., 1986, *Proc. 7th Inter. Conf. on Strength of Metals and alloys*, edited by McQueen, H. et al (Pergamon Press, Oxford), 2065.

11. McDarmaid, D. S. and Shakesheff, A. J., 1987, *Aluminum-Lithium IV,"* edited by Champier, G., Dubost, B., Miannay, D. and Sabetay, L. (France: Les Editions De Physique), 257.

12. Ridley, N., Liversy, D. W. and Pilling, J., 1987, *Aluminum-Lithium IV,* edited by Champier, G., Dubost, B., Miannay, D. and Sabetay, L. (France: Les Editions De Physique), 251.

13. Grimes, R., Miller, W. S. and Butler, R. G., 1987, *Aluminum-Lithium IV,* edited by Champier, G., Dubost, B., Miannay, D. and Sabetay, L. (France: Les Editions De Physique), 239.

14. Bowen, A. W. and Hirsch, J., 1988 *Proc. 8th Inter. Conf. on Textures of Materials* (Warrendale, Metallurgical Society of AIME), 549.

15. Ricks, R. A. and Parson, N. C., 1989, *Aluminum-Lithium Alloys V,* edited by Sanders T. H. Jr. and E. A. Starke E. A. Jr. (MCE, Birmingham, UK), 169.

16. Shakesheff, A. J., McDarmaid, D. S. and Gregson, P. J., 1989, *Aluminum-Lithium Alloys V,* edited by Sanders T. H. Jr. and E. A. Starke E. A. Jr. (MCE, Birmingham, UK), 635.

17. Gandhi, C., Bampton, C., Ghosh, A. K. and Anton, C. E., 1989 *Aluminum-Lithium Alloys V,* edited by Sanders T. H. Jr. and E. A. Starke E. A. Jr. (MCE, Birmingham, UK), 141.

18. Amichi, R. and Ridley, N., 1989, *Aluminum-Lithium Alloys V,* edited by Sanders T. H. Jr. and E. A. Starke E. A. Jr. (MCE, Birmingham, UK), 159.

19. Yoshida, H., Tanaka, H., Tsuchida, S., Tsuzaku, T. and Takahashi, A., 1989, *Aluminum-Lithium Alloys V,* edited by Sanders T. H. Jr. and E. A. Starke E. A. Jr. (MCE, Birmingham, UK), 179.

20. Bowen, A. W., 1990, *Mater. Sci. Technol.*, **6**, 1058.

21. Shakesheff, A. J., McDarmaid, D. S. and Gregson, P. J., 1991, *Mater. Sci. Technol.*, **7**, 276.

22. D'Oliveira, A. S., Bate, P. S. and Roberts, W. T., 1989, *Aluminum-Lithium Alloys V,* edited by Sanders T. H. Jr. and E. A. Starke E. A. Jr. (MCE, Birmingham, UK), 1001.

23. Bate, P. S., 1992, *Metall. Trans.*, **23A**, 1467.

24. Blackwell, P. L. and Bate, P. S., 1993, *Metall. Trans.*, **24A**, 1085.

25. Pu, H. P. and Huang, J. C., 1993, *Scripta Metall.*, **28**, 1125.

26. Pu, H. P., Liu, F. C. and Huang, J. C., 1995, *Metall. Trans.*, **26A**, 1153.

27. Sherby, O. D. and Wadsworth, J., 1988, *Superplasticity in Aerospace,* edited by Heikkenen, H. C. and McNelley, T. R., ASM, 3.

28. Pearson, C. E., 1934, *J. Inst. Metals*, **54**, 111.

29. Backofen, W. A., Turner, I. R. and Avery, O. H., 1964, *Trans. ASM*, **57**, 980.

30. Sherby, O. D., Nieh, T. G. and Wadsworth, J., 1994, *Mater. Sci. Forum*, **170-172**, 13.

31. Higashi, K., Okada, T., Muka, T., and Tanimura, S., 1991, *Scripta Metall.* **25**, 2503.

32. Suery, M. and Baudelet, B., 1978, *Rev. Phys. Appl.*, **19**, 53.

33. Gleiler, H. and Chalmers, B., 1972, *High-Angle Grain Boundaries, Prog. Mater. Sci.*, **16.**

34. Meyers, M. A. and Chawla, K. K., 1984, *Mechanical Metallurgy - Principles and Applications* (Prentice-Hall International Inc.), 572.

35. Padmanabhan, K. A. and Davies, G. L., 1980, *Superplasticity* (Springer, Berlin, Germany).

36. Edington, J. W., Melton, K. N. and Cutler, C. P., 1976, *Prog. Mater. Sci.*, **21**, 61.

37. Mukherjee, A. K., 1971, *Mater. Sci. Eng.*, **8**, 83.

38. Pilling, J. and Ridley, N., 1989, *Superplasticity in Crystalline Solids* (The Institute of Metals, London, England).

39. Langdon, T. G., 1982, *Metall. Trans.*, **13A**, 689.

40. Chaudhury, P. K. and Mohamed, F. A., 1988, *Acta Metall.*, **36**, 1099.

41. Lee, D., 1969, *Acta Metall.*, **17**, 1057.

42. Mohamed, F. A., Ahmed, M. and Langdon, T. G., 1977, *Metall. Trans.*, **8A**, 933.

43. Gifkins, R. C., 1982, *Superplastic Forming of Structural Alloys*, edited by Paton, N. E. and Hamilton, C. H. (Warrendale, Metallurgical Society of AIME), 3.

44. Arieli, A. and Mukherjee, A. K., 1980, *Metall. Trans.* **13A**, 717.

45. Kashyap, B. P. and Mukherjee, A. K., 1985, *Superplasticity,* edited by Baudelet, B. and Suery, M. (Publ. CNRS, Paris), 1419.

46. Nieh, T. G., Wadsworth, J. and Sherby, O. D., 1997, *Superplasticity in Advanced Materials* (Cambridge University Press).

47. Ball, A. and Hutchison, M. M., 1969, *Mater. Sci. J.*, **3**, 1.

48. Mukherjee, A. K., 1975. *Grain Boundaries in Engineering Materials*, edited by Walter J. L. et al (Claitor Publishing, Baton Rouge, LA), 93.

49. Langdon, T. G., 1970, *Phil. Mag.*, **22**, 689.

50. Gifkins, R. C., 1976, *Metall. Trans.*, **7A**, 1225.

51. Fukuyo, H., Tsai, H. C., Oyama, T and Sherby, O. D., 1991, *ISIJ International*, **31**, 76.

52. Kaibyshev, O. K., Valiev, R. Z. and Emaletdinov, A. K., 1985, *Phys. Stat. Sol. (a)*, **90**, 197.

53. Gittus, J. H., 1977, *Trans. ASME.*, 99, 244.

54. Nazarov, A. A., 1997, *Superplasticity in Advanced Materials*, edited by Langdon, T. G. (Trans. Tech. Publ.), 31.

55. Perevezentsev, V. N., Rybin, V. V. and Chuvil'deev, V. N., 1992, *Acta Metall.*, **40**, 895.

56. Hayden, H. W., Floreen, S. and Goodall, P. D., 1972, *Metall. Trans.*, **3A**, 833.

57. Spingarn, J. R. and Nix, W. D., 1978, *Acta Metall.*, **26**, 1389.

58. Arieli, A. and Mukherjee, A. K., 1980, *Mater. Sci. Eng.*, **45**, 61.

59. Ashby, M. F. and Verrall, R. A., 1973, *Acta Metall.*, **21**, 149.

60. Padmanabhan, K. A., 1979, *Mater. Sci, Eng.*, **40**, 285.

61. Watts, B. M., Stowell, M. J., Baikie, B. L. and Owen, D. G., 1976, *Metal Sci.*, **10**, 189.

62. Nes, E., 1978, *Mater. Sci.*, **13**, 211.

63. Liu, Z. Y., Cui, J. Z. and Bai, G. R., 1992, *J. Northeast Univ. Tech.*, **13**, 610.

64. Hales, S. J. and McNelley, T. R., 1988, *Acta Metall.*, **36**, 1229.

65. Ren. B. and Hamilton, C. H., 1988, *Superplasticity and Superplastic Forming*, edited by Hamilton, C. H. and Paton, N. E. (TMS), 121.

66. Srinivasan, M. N., Goforth, R. E. and Balasubramanian, R., 1992, *Mater. Character.* **29**, 397.

67. Ash, B. A. and Hamilton, C. H., 1988, *Scripta Metall.*, **22**, 277.

68. Liu, Q., Huang, X., Yao, M. and Yang, J., 1992, *Acta Metall.*, **40**, 1753.

69. Matsuki, K. et al, 1991, *Mater. Sci. Tech.*, **7**, 512.

70. Mahon, G. J. and Ricks, R. A., 1991, *Scripta Metall.*, **25**, 383.

71. Muramatsu, N. et al, 1989, *J. J. Inst. Light Metals*, **39**, 783.

72. Grimes, R. and Miller, W. S., 1984, *Aluminum-Lithium Alloys II*, edited by Sanders Jr, T. H. and Starke Jr, E. A. (Warrendale, Metallurgy Society of AIME), 153.

73. McNelley, T. R. and Kalu, P. N., 1991, *Light Weight Alloys for Aerospace Application II,"* 287.

74. Brichnell, R. H. and Edington, J. W., 1979, *Metall. Trans.*, **10A**, 1257.

75. Liu, J. and Chakrabarti, D. J., 1996, *Acta Metall.*, 12, 4647.

76. Nes, E., 1978, *J. Mater. Sci. Lett.*, **13**, 2052.

77. Gudmundsson, H., Brooks, D. and Wert, J. A., 1991, *Acta Metall.*, **39**, 19.

78. Lyttle, M. T. and Wert, J. A., 1994, *J. Mater. Sci.*, 3342.

79. McNelley, T. R., Lee, E. -W. and Grag, A., 1986, *Proc. Int. Conf. Aluminum Alloys —Physical and Mechanical Properties*, edited by Starke, E. A. Jr., Sanders, T. H. Jr. (EMAS, Warley West Midlands, UK), 1269.

80. Gandhi, C. and Raj, R., 1991, *Acta Metall.*, **39**, 679.

81. Silcock, J. M., 1959-1960, *J. Inst. Met.*, **88**, 357.

82. Starke, E. A. Jr., Sanders, T. H. Jr. and Palmer, I. G., 1981, *J. Met.*, 24.

83. Sanders, T. H., Jr. and Starke, E. A., Jr., 1982. *Acta Metall.*, **30**, 927.

84. Vasudevan, A. K. and Doherty, R. D., 1989, *Aluminum Alloys - Contemporary Research and Applications*, *Treatise on Mater. Sci. Technol.*, **31** (Academic Press Inc.)

85. Sanders, T. H., Jr. and Starke, E. A., Jr., 1980, *Aluminum Lithium alloys*, edited by Sanders T. H. Jr. and E. A. Starke E. A. Jr. (TMS-AIME).

86. Peters, M. and Winkler, P. J., 1992, edited *Aluminum Lithium Alloys VI.* (DGM, Oberursel, Germany).

87. Sanders, T. H., Jr. and Starke, E. A., Jr., 1994, edited *The 4th International Conference on Aluminum Alloys —Their Physical and Mechanical Properties* (The Georgia Institute of Technology, Atlanta, GA USA).

88. Sanders, T. H., Jr. and Starke, E. A., Jr., 1989, *Aluminum-Lithium Alloys V,* edited by Sanders T. H. Jr. and E. A. Starke E. A. Jr. (MCE, Birmingham, UK.), 1.

89. Quist, W. E. and Narayanan, G. H., 1989, *Aluminum Alloys - Contemporary Research and Applications*, *Treatise on Mate. Sci. Technol.*, **31**, 219.

90. Pickens, J. R., Heubaum, F. H. and Hramer, L. S., 1990, *Scripta Metall.*, **24**, 457.

91. Gayle, F. W., Tack, W., Swanson, G., Heubaum, F. H. and Pickens, J. R., 1994, *Scripta Metall.*, **30**, 761.

92. Williams, D. B. and Howell, P. R., 1989, *Aluminum Alloys - Contemporary Research and Applications*, *Treatise on Mater. Sci. Technol.*, **31**, 365.

93. Grims, R., Miller, W. S., Reynolds, M. A. and Gray, A., 1986, *Aluminum-Lithium Development, Applications and Superplastic Forming*, edited by Agrawal, S. P. and Kar, J. R. (ASM, Metals Park, Ohio), 38.

94. Miller, W. S., White, J., Reynolds, M. A., McDarmaid, D. S. and Starr, G. M., 1987, *Aluminum-Lithium IV,* edited by Champier, G., Dubost, B., Miannay, D. and Sabetay, L. (France: Les Editions De Physique), 151.

95. Singh, A. K., Saha, G. G., Gokhale, A. A. and Ray, R. K.. 1998, *Metall. Mater. Trans.*, **29A**, 665.

96. Palmer, I. G., Miller, W. S., Lloyd, D. J. and Bull, M. J., 1984, *Aluminum-Lithium Alloys II*, edited by Sanders Jr, T. H. and Starke Jr, E. A. (Warrendale, Metallurgy Society of AIME), 137.

97. Noble, B. and Thompson, G. E., 1971, *J. Met. Sci.* **5**, 114.

98. Williams, D. B., 1980, *Aluminum-Lithium Alloys*, edited by Sanders T. H. Jr. and E. A. Starke E. A. Jr. (TMS-AIME), 324.

99. Sanders, Jr., T. H. (1980) "*Aluminum-Lithium Alloys*", edited by Sanders T. H. Jr. and E. A. Starke E. A. Jr. (TMS-AIME), 63.

100. Cassada, W. A., Sheflet, G. J. and Starker, Jr. E. A., 1986, *Aluminum Alloys - Their Physical and Mechanical Properties*, edited by Starke, E. A. Jr., Sanders, T. H. Jr. (EMAS, Warley West Midlands, UK), 695.

101. Mondolfo, L. F., 1976, *Aluminum Alloys – structures and Properties* (Butterworth, London), 554.

102. Gregson. P. J. and Flower, H. M., 1985, *Acta Metall.*, **33**, 527.

103. Sainfort, P. and Dubost, B., 1987, *Aluminum-Lithium IV,* edited by Champier, G., Dubost, B., Miannay, D. and Sabetay, L. (France: Les Editions De Physique), 407.

104. Golvin, G. N. and Starker, E. A. Jr., 1988, *SAMPE Quarterly*, **19**, 10.

105. Miller, W. S., White, J. and Lloyd, D. J., 1987, *Aluminum-Lithium IV,* edited by Champier, G., Dubost, B., Miannay, D. and Sabetay, L. (France: Les Editions De Physique), 139.

106. Gokhale, A. A., Prasad, S. K., Kumar, V., Chakravorty, C. R., Leschiner, L. N., Mozharovshy, S. M. and Fridlyander, I. N., 1994, *Aluminum Alloys VI,* edited by Peters, M. and Winkler, P. J. (DGM, Oberursel, Germany), 428.

107. Reynolds, M. A. Gray, A., Creed, E. Jordan, R. M. and Titchener, A. P., 1984, *Aluminum-Lithium Alloys II,* edited by Sanders Jr, T. H. and Starke Jr, E. A. (Warrendale, Metallurgy Society of AIME), 57.

108. Bull, M. J. and Lloyd, D. J., 1986, *Aluminum-Lithium Alloys III*, edited by Baker, C., Gregson, P. J., Harris, S. J. and Peel, C. J. (The Institute of Metals, London), 402.

109. Barlat, F., Lege, D. J. and Warren, C. J., 1991, *Proc. Conf. Modeling the Deformation of Crystalline Solids* (TMS, Mew Orleans), 189.

110. Zeng, X. H. and Ahmad, M. and Ericsson, T., 1992, *Aluminum Alloys VI,* edited by Peters, M. and Winkler, P. J. (DGM, Oberursel, Germany), 1021.

111. Zeng, X. H. and Ericsson, T., 1996, *Acta Metall.*, **44**, 1801.

112. Engler, O., Mizera, J., Delecroix, M., Driver, J. and Lucke, K., 1992, *Aluminum Alloys VI,* edited by Peters, M. and Winkler, P. J. (DGM, Oberursel, Germany), 307.

113. Sachs, G., 1928, *Zur Ableitung einer fliessbedingung, Z. Ver. Dtsch. Ing.*, **72**, 734.

114. Taylor, G. I., 1934, *The Mechanism of Plastic Deformation of Crystals, Proc. R. Soc. London,* **145**, 362.

115. Bishop, J. F. W. and Hill, R., 1951, *Phil. Mag.* **42**, 414.

116. Fricke, W. G. Jr. and Przystupa, M. A., 1989, *Aluminum Alloys - Contemporary Research and Applications, Treatise on Mate. Sci. Technol.*, **31**, 563.

117. Welch, P. I. and Bunge, H. J., 1986, *Mater. Sci. Technol.*, 354.

118. Goncalves, M. and Sellars, C. M., 1987, *Aluminum-Lithium IV,* edited by Champier, G., Dubost, B., Miannay, D. and Sabetay, L. (France: Les Editions De Physique), 171.

119. Zeng, X. H., Ahmad, M. and Engler, O., 1994, *Mater. Sci. Technol.*, **10**, 581.

120. Schelb, W, Haszler, A. and Jager, H., 1992, *Aluminum Alloys VI,* edited by Peters, M. and Winkler, P. J. (DGM, Oberursel, Germany), 315.

121. Field, P. D. and Dingley, D. J., 1995, *Solid State Technol.*, **Nev.**, 91.

122. Dingley, D. J. and Randle, V., 1992, *J. Mater. Sci.*, **27**, 4545.

123. Dingley D. J. and Field, D. P., 1997, *Mater. Sci. Technol.*, **13**, 85.

124. Wright, S. I. and Kocks, U. F., 1996, *Proc. 7th Inter. Conf. Texture of Materials*, edited by Linag, Z., Zuo, L. and Chu, Y. (International Academic Publ.), 53.

125. Hansen, N. and Jensen, D. J., 1986, *Metal. Trans.* **17A**, 253.

126. HornBogen, K. and Koster, U., 1978, *Recrystallization of Metallic Materials*, edited by Haessner, F., Dr. Riederer Verlag GmbH, Stuttgat, 159.

127. Kashyap, B. P. and Tangri, K., 1987, *Z. Metallkde*, **78**, 876.

128. Kashyap, B. P., Arieli, A. and Muhkerjee, A. K., 1985. *J. Mater. Sci.*, **20**, 2661.

129. Hamilton, C. H., 1989, *Metall. Trans.*, **20A**, 2783.

130. Nix, W. D., 1984, Superplastic Forming, edited by Agrawal (Metals Park, Ohio, ASM), 3.

131. Hutchinson, W. B. and Nes, E., 1992, *Grain Growth in Polycrystalline Materials,* Edited by Abbruzzese and Brazzo (Trans. Tech. Publ.), 385.

132. Roberts, W., 1984, *Deformation, Processing, and Structure*, edited by Krauss (Metals Park, Ohio, ASM), 109.

133. Kashyap, B. P. and Tangri, K., 1987, *Metall. Trans.*, **18A**, 417.

134. Wilkinson, D. S. and Caceres, C. H., 1984, *Acta Metall.*, **32**, 1335.

135. Hart, E. W., 1967, *Acta Metall.*, **15**, 351.

136. Kashyap, B. P. and Murkherjee, A. K., 1983, *Proc. 4th Riso Inter. Symp. Deformation of Multi-phase and Particle Containing Materials*, edited by Blide-Sorenson et al (Rosklide, Denmark), 325.

137. Melton, K. N., Cutler, C. P. and Edington, J. W., 1975, *Scripta Metall.*, **9**, 515.

138. Song, J. L. and Bate, P. S, 1977, *Acta Metall.*, **45**, 2747.

139. Assaro, R. J. and Needleman, A., 1985, *Acta Metall.*, **33**, 923.

140. Humphreys, F. J. and Hatherly, M., 1995, *Recrystallization ad Related Annealing Phenomena* (Elsvier Sci. Ltd).

141. Chin, G. Y., 1973, *The Inhomogeneity of Plastic Deformation*, (Metals Park, Ohio, ASM), 83.

142. Hirsch, J. and Lucke, K., 1988, *Acta Metall.*, **36**, 2863.

143. Mecking, H., 1985, *Preferred Orientation in Deformed Metals and Rocks: An introduction to Modern Texture Analysis*, edited by Wenk, H. (Academic Press, Inc., London) 267.

144. Bunge, H. J., 1985, *Preferred Orientation in Deformed Metals and Rocks: An Introduction to Modern Texture Analysis*", edited by Wenk, H. (Academic Press Inc., London), 73.

145. Enger, O., 1996, *Mater. Sci. Technol.*, **12**, 859.

146. Hirsch, J. R., 1990, *Mater. Sci. Technol.*, **6**, 1048.

IMAGE EVALUATION
TEST TARGET (QA-3)

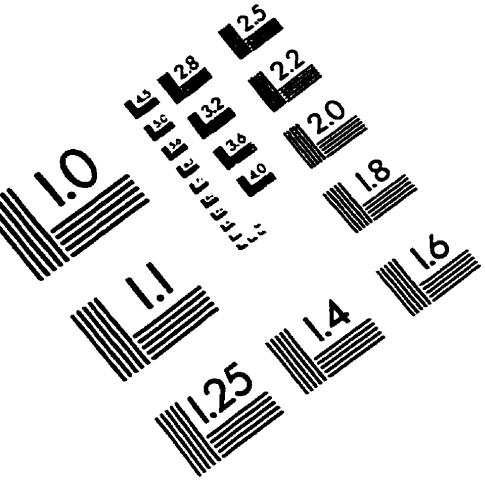

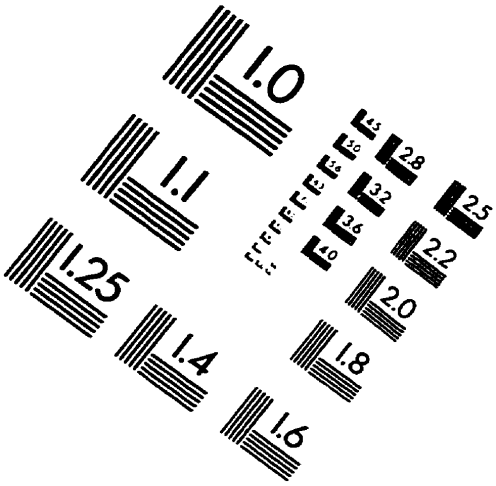

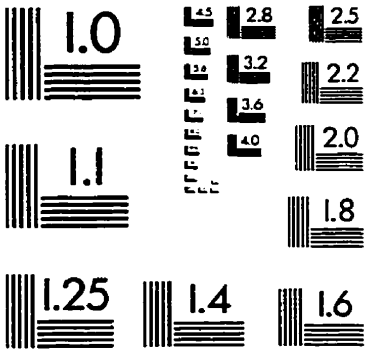

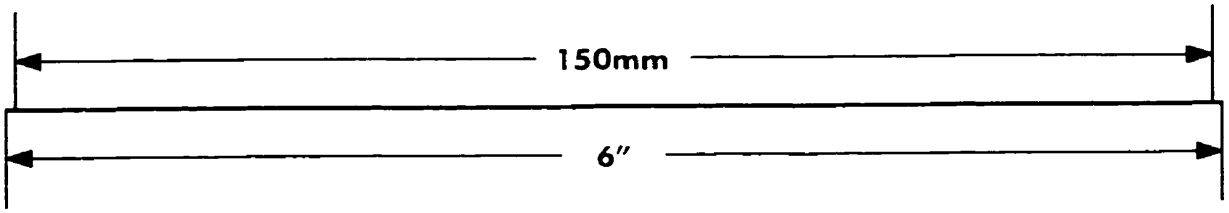

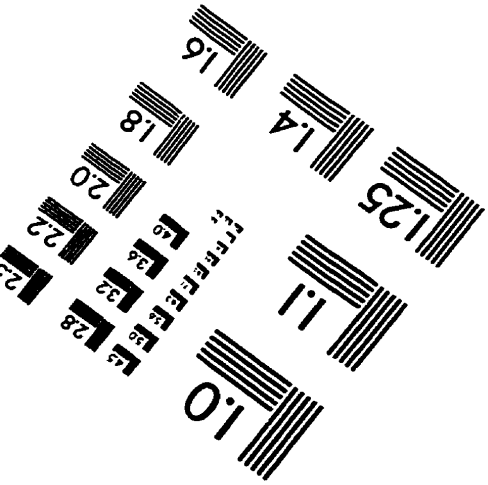

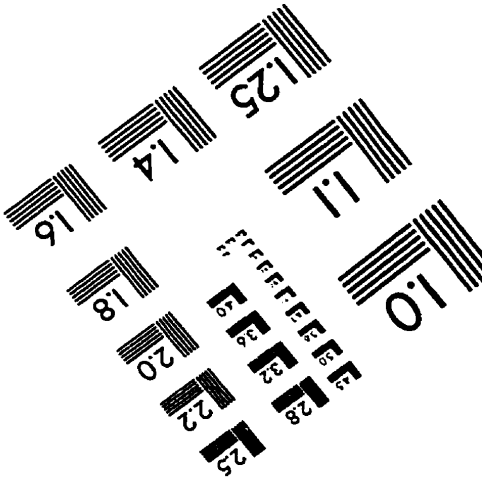

APPLIED IMAGE, Inc
1653 East Main Street
Rochester, NY 14609 USA
Phone: 716/482-0300
Fax: 716/288-5989